University of Warsaw
Faculty of Physics

Krzysztof M. Czajkowski

Impact of multiscale electromagnetic coupling on the properties of antenna-reactor complexes

Doctoral thesis supervised by
Dr hab. Tomasz J. Antosiewicz

Warsaw, February 2022

Abstract

Antenna-reactor complexes contain optical antennas, which are able to focus light into nanoscale volumes, and transition metal nanoparticles, which interact weakly with light, but exhibit high catalytic activity. Electromagnetic coupling in this system leads to enhanced optical absorption in transition metal nanoparticles, which facilitate prospect applications such as optical monitoring of phenomena accompanying catalysis and plasmon mediated photocatalysis.

In this thesis we provide a comprehensive theoretical study of electromagnetic coupling in antenna-reactor complexes occuring at three length scales present in this system: at the macroscopic level, the single antenna level and at the atomic scale. At the macroscopic scale the optical response of antennas is determined by coupling between them via multiple scattering. In experimental samples nanoantennas are distributed randomly on a dielectric substrate. Thus, we propose a T-matrix method based approach to describe the effective optical properties of such a layer. We show that in addition to antenna properties their minimal center-to-center distance is a key parameter determining electromagnetic coupling. The proposed approach enables formulating simple analytical expressions that may be used to optimize future devices based on amorphous arrays of nanoantennas.

At the single antenna level, we provide accurate models of both the nanoantenna and transition metal nanoparticle layer either by explicit modelling or using a gradient effective medium model developed by the author. This enables us to study absorption enhancement in transition metal nanoparticles and find useful guidelines for maximizing this effect in experimental samples. Also, the results tie changes of the properties of either the nanoantenna or transition metal nanoparticles to changes of the optical response of the system, which might be used to optically monitor the evolution of the system during catalysis.

Realistic modelling of phenomena occuring at atomic scales requires us to use time-dependent density functional theory. At this scale it is possible to credibly model plasmon formation and its subsequent dephasing that results in hot electron generation. We show that the presence of a nanoantenna leads to enhanced hot electron generation in the system compared to an isolated transition metal nanocluster and study the system parameters that determine this enhancement.

The study shows that antenna-reactor complexes form a promising platform for photonic enhancement of interaction of light with transition metal nanoparticles, which might lead to intersting applications in sensing and photocatalysis.

Streszczenie

Układ antena-reaktor zawiera antenę optyczną zdolną do skupiania światła w nanoskali oraz nanocząstki metali przejściowych, które słabo oddziałują ze światłem, ale wykazują się wydajną aktywnością katalityczną. Sprzężenie elektromagnetyczne w tym układzie prowadzi do zwiększenia absorpcji światła w nanocząstkach metali przejściowych, co umożliwia zastosowania takich układów optycznych do monitorowania zjawisk związanych z katalizą oraz przeprowadzenie fotokatalizy wspomaganej plazmonami.

W niniejszej pracy doktorskiej przedstawiono teoretyczne badania nad elektromagnetycznym sprzężeniem w układzie antena-reaktor zachodzącym w trzech skalach długości obecnych w tym układzie: w skali makroskopowej, na poziomie pojedynczej anteny i w skali atomowej. W skali makroskopowej sprzężenie elektromagnetyczne wpływa na odpowiedź optyczną przez wielokrotne rozpraszanie. W eksperymentalnych realizacjach układu, nanoanteny są rozmieszczone losowo. Z tego względu, opracowano model oparty na metodzie macierzy T aby opisać ich efektywne właściwości optyczne. Wykazano, że oprócz właściwości samych nanoanten, kluczowym parametrem określającym sprzężenie elektromagnetyczne jest minimalna odległość między środkami anten. Zaproponowane rozwiązanie umożliwia sformułowanie analitycznych równań opisujących ich własności optyczne, które można zastosować do optymalizacji przyszłych urządzeń opartych o amorficzne macierze nanoanten.

W celu modelowania własności pojedynczej struktury typu antena-reaktor zaproponowano realistyczny model zarówno samej nanoanteny jak i warstwy nanocząstek metali przejściowych. Model pozwala na modelowanie wprost, tj. przy użyciu metod numerycznych, albo za pomocą gradientowego modelu ośrodka efektywnego opracowanego przez autora rozprawy. Umożliwia to badanie wzmocnienia absorpcji i przedstawienie użytecznych metod maksymalizacji tego efektu w próbkach eksperymentalnych. Ponadto, wyniki wskazują na to, że zmiana właściwości zarówno anteny jak i nanocząstek metali przejściowych prowadzi do zmiany odpowiedzi optycznej, co można zastosować do optycznego monitorowania zmian układu podczas katalizy.

Realistyczne modelowanie zjawisk zachodzących w badanym układzie w skali atomowej wymaga zastosowania czasowozależnej teorii funkcjonału gęstości. W tej skali możliwe jest realistyczne modelowanie procesu powstawania i zaniku plazmonu, które prowadzi do generacji tzw. gorących nośników. W niniejszej rozprawie wykazano, że obecność nanoanteny wzmacnia generację gorących nośników w układzie antena-reaktor w porównaniu do nanoklastrów metali przejściowych i zbadano czynniki wpływające na obserwowane wzmocnienie.

Przedstawione badania wskazują na to, że układ antena-reaktor wykazuje potencjał do wzmacniania oddziaływania między światłem a nanocząstkami metali przejściowych, prowadząc do zastosowań czujnikowych oraz w fotokatalizie.

Preface

I would like to thank many people who supported me during this endevour. Without them this thesis would probably never be published.

First of all, to Dr. hab. Tomasz Antosiewicz, the supervisor of this thesis. We spent countless hours discussing the results and underlying physics.

To Prof. Rafał Kotyński who co-supervised me with Tomasz Antosiewicz during the first four years of my PhD studies at the Faculty of Physics, especially for always having time to discuss and creating a friendly environment to grow.

To Prof. Daniel Sanchez-Portal who hosted and supervised me during my two visits at the Material Physics Center in San Sebastian, Spain. Also, to Prof. Javier Aizpurua and all the kind fellow PhD students and postdocs from the Nanophotonics group and the B007 office at CFM. Special thanks goes to Marc Barbry, Peter Koval and Bruno Candelas for their support with the PyNAO code.

To Dr. Amos Egel for his support and expertise in the T-matrix method and the SMUTHI code. A true testimony to how much I've learned thanks to his advice is that I was able to both contribute to the development of the SMUTHI code and publishe papers on the T-matrix method, despite starting as an inexperienced SMUTHI user.

To Prof. Christoph Langhammer at Chalmers University of Technology in Gothenburg, Sweden for a fruitful collaboration.

To Prof. Bogdan Cichocki for sharing his experience and wide knowledge on how to tackle multiple interactions between randomly distributed nanoparticles.

To my fellow PhD students at the Nanophotonics FUW group – mgr Dominika Świtlik and mgr Maria Bancerek. Also, to my kind friends who shared this PhD experience with me – mgr Aliksandr Ramaniuk, mgr Jakub Kierdaszuk, and Dr. Arkadiusz Ciesielski.

To Kasia Dyl for support with administrative burdens.

To my family for love, patience and support. Without you I couldn't have stayed on the right track.

Contents

Chapter 1

Introduction to antenna-reactor complexes

Optical antennas, which are capable of concentrating the electromagnetic field in nanoscale volumes, enable substantial enhancement of interaction between light and matter located in the vicinity of the optical antenna. An archetypal example of such an antenna is a nanoparticle of a noble metal or a semiconductor with typical lateral dimensions between 1–100 nm. Herein, the role of the material, whose interaction with light is amplified by the antenna, is played by transition metal nanoparticles known for their ability to catalyze chemical reactions at their surface. In order for catalysis to take place efficiently, nanoparticles should have a large surface to volume ratio, what is achieved for sizes on the order of single nanometers. Such a system composed of a nanoantenna capable of concentrating the electromagnetic field and a nanoparticle or group of nanoparticles with catalytic properties is called an antenna-reactor system.

One expected result of enhanced interaction of light with catalytic nanoparticles through an optical antenna is amplification of the transition metal plasmonic activity. A surface plasmon is a collective excitation of electrons in the conduction band of a metal. It is typically observed in noble metals and enables localization of the electromagnetic field. It is also characterized by sensitivity to local surroundings, for example molecules adsorbed on the surface of the antenna or presence of other nanoparticles. As a consequence of the decay of a plasmon, light is scattered or absorbed. The latter process is a source of losses in plasmonic devices such as waveguides, but in the analyzed case of a catalytic nanoparticle, it is desirable. This is due to the fact that absorption of plasmons is accompanied by the generation of electron-hole pairs with energies much greater than those resulting from ambient temperature. These high energy carriers can be used, e.g.,

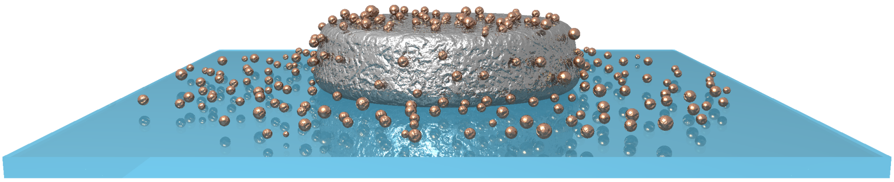

Figure 1.1: Schematic representation of antenna-reactor system. The plasmonic nanoantenna is decorated with smaller catalytic nanoparticles. The catalyst and antenna are separated by a thin layer of a dielectric. The system is supported by a dielectric substrate.

to increase the efficiency of reactions carried out on the surface of nanoparticles.

The scientific goal of the research presented in this doctoral dissertation is to understand the basic optical properties and electronic structure of antenna-reactor complexes composed of reactor nanoparticles made of non-noble catalytic metals and an optical antenna capable of increasing the density of optical states available for catalytic nanoparticles. Such a complex structure allows, on the one hand, to increase the efficiency of catalytic processes carried out on a catalytic nanoparticle, and, on the other hand, to detect various physical processes taking place during catalysis by means of an optical signal.

In the doctoral dissertation, the properties of the antenna-reactor system are studied theoretically and numerically using the methods of classical electrodynamics and quantum mechanics on many length scales that occur in experimental implementations of the system. This allows for the determination of rules and mechanisms governing the collective optical response, light absorption by individual components of the system, plasmon formation, electron transport and the generation of hot carriers. Solving the problem of describing the above-mentioned phenomena extends the basic knowledge of plasmon enhanced catalysis and plasmonic sensors of processes accompanying catalysis, and facilitates the design of nanostructures for these purposes.

1.1 Plasmon enhanced photocatalysis

Heterogenous catalysis is among the most important processes in the chemical industry. Catalysis increases reaction rate by adding a chemical, the so-called catalyst, that alters the reaction pathway and thus lowers its activation energy. In heterogeneous catalysis, the catalyst and reaction substrates are in different phase. Most typically, the catalyst is a solid, while the reagents are gases. It is estimated that around 90% of all chemicals are fabricated with heterogeneous catalysis.[1]

Most heterogeneously catalyzed chemical reactions require overcoming a high activation energy, which is typically provided by high temperature. The disadvantage of this approach is a reduction of catalyst durability and the need to provide a large amount of energy. For instance, the Haber-Bosch process, critical in production of ammonia - an important nitrogen fertilizer, consumes around 1% of world's industrial energy budget.[2] Thus, in the age of climate change, new, greener ways are sought for heterogeneous catalysis, that would require less extreme conditions and energy. Among such greener routes is photocatalysis, a process in which the reaction occurs in the presence of a catalyst and it is stimulated by light. Photocatalysis may use sunlight to lower energy consumption in a wide range of important reactions including hydrogen fuel production and organic synthesis. An example of photocatalysis inspiring this doctoral dissertation is one employing surface plasmons generated by plasmonic nanoparticles.[3,4] Reactions catalyzed by such nanoparticles in the presence of light can be carried out at reduced temperature. In some situations, the use of photocatalysis also leads to reaction pathways inaccessible by thermal activation, e.g. hydrogen dissociation on the surface of a gold nanoparticle.[5,6] Induction of chemical reactions on the surface of nanoparticles with light can also be used to synthesize plasmonic nanoparticles of a desired shape.[7]

The concept of plasmon-assisted catalysis usually involves the use of a noble metal nanoparticle as a catalyst. The limitation of this solution is the fact that, although they interact well with light, they are able to catalyze a relatively small number of important industrial processes. On the other hand, transition metals known for their good catalytic properties interact poorly with light.[6] This justifies the use of antenna-reactor systems in photocatalysis. As mentioned above, mutual coupling of nanoparticles composed of different materials allows obtaining both good optical and catalytic properties. The first experimental example of photocatalysis using such a system was the hydrogen photodissociation reaction on the surface of a dimer consisting of aluminum and palladium nanodisks.[8] It was demonstrated that the reaction occurred much more efficiently in the presence of an aluminum nanodisk and light. In particular, performance enhancement was present for one polarization direction, while for the orthogonal one this enhancement was absent. As the choice of polarization determined electromagnetic coupling magnitude between the antenna and catalytic particles, this confirmed the important role of coupling for catalytic activity enhancement. In another work,[9] the authors also showed that the efficiency of the reaction depends on the presence of a palladium nanoparticle and is the highest when the wavelength of the exciting light coincides with the wavelength corresponding to the plasmonic resonance of the dimer. They also demonstrated an increase in the selectivity for acetylene hydrogenation compared to conventional high temperature catalysis.

One of the observations made in the first work on antenna-reactor systems[6] was that the enhancement of catalyst activity depends on an increase of absorption of light in palladium. Its amplification is due to the presence of a concentrated electric field around the antenna. Therefore, it is important to design the system such that the reactor nanoparticles are located in areas of maximum electric field enhancement, so-called hot-spots. For a disk-shaped antenna placed on a substrate, they are located on the top of the disk and at the substrate-antenna border.[10] The size of the nanoparticle constituting the antenna is also important.[11] If too large an antenna is used, scattering will cause a large amount of energy to be radiated out into the far-field. In turn, a small antenna will be characterized by high absorption and coupling of light to nearby catalytic particles will be minimal. The scattering to absorption ratio of optical antennas can also be affected by their spatial distribution on a substrate.[12] Depending on the type of distribution (periodic or random) and the density of antennas, the scattered fields from the antennas interfere with each other and the incident field in different ways (with different phase relations). This affects mutual coupling and, as a result, is important for the optical properties of the system.[13,14] The geometry and material of the catalytic nanoparticle can also be complementarily manipulated, but it should be kept in mind that from the point of view of catalytic properties, it is important to maximize the surface, and therefore minimize the size of such a nanoparticle.[15]

The decisive effect of increasing the efficiency of a reaction using surface plasmon resonances is the formation of hot electron–hole pairs, which follows absorption of a plasmon. Experimental studies of carrier dynamics on the metal surface showed the existence of such hot carriers and established characteristic times associated with their formation and disappearance, but they are difficult to implement for nanoparticles.[16] While modeling using classical electrodynamics allows for effective determination of quantities such as electric field amplification or light absorbed in the photocatalyst, the prediction of effects associated with hot electrons is based on quantum mechanics.

1.2 Refractometric sensing with optical antennas

A key application of antenna–reactor systems discussed in this thesis is optical sensing. The idea behind optical sensing with resonant nanostructures is that the resonance energy is dependent on the distribution of refractive index of the surrounding environment.[17–19] Consequently, this sensing scheme is often called refractometric. The nanostructures are sensitive to bulk refractive index changes, but more importantly, they are also sensitive to minuscule local changes in their close vicinity that may occur due to various microscopic physical or chemical processes including e.g. molecule adsorption, presence of another nanoparticle

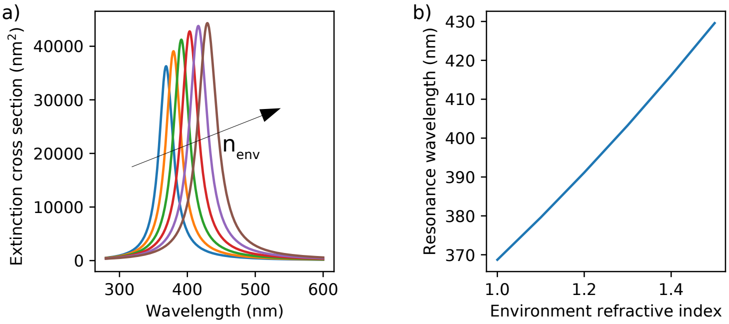

Figure 1.2: (a) Optical extinction cross section spectra for spherical silver nanoparticles with 10 nm radius calculated in quasi-static approximation. The refractive index of the environment ranges from 1.0 to 1.5. The peak wavelength increases with increasing environment refractive index. (b) Resonance wavelength depends almost linearly on the environment refractive index.

or a chemical reaction. Sensitivity towards nanoscale processes, which can be measured optically in the far field, makes nanostructures a promising platform for biosensing and material investigation. The quality of a refractometric sensor can be defined as the derivative of the resonance wavelength (λ_{res}) over the refractive index of the environment (n_{env})

$$B = \frac{\partial \lambda_{\mathrm{res}}}{\partial n_{\mathrm{env}}}, \tag{1.1}$$

with B being the sensitivity. Simulated optical spectra of silver nanoparticles are shown in Fig. 1.2a. With increasing refractive index of the environment n_{env}, the resonance wavelength increases. As presented in Fig. 1.2b, the dependence of the resonance wavelength on n_{env} is close to linear. Therefore, the sensitivity is calculated simply as the slope of the plotted dependence.

It is worth noting that in this work we deal only with factors that can be modified by changing the sensor material and topology, omitting several other significant factors such as functionalization towards a specific analyte, resolution of optical characterization etc.

An antenna reactor system, in which the reactor part of the system consists of one or more palladium nanoparticles can be extremely useful for studying and the detection of processes associated with catalysis. In the work by Larsson et al.[20] it was demonstrated that the location of the plasmon resonance depends on the coverage of the catalyst surface (platinum nanoparticles), allowing the kinetics of selected model chemical reactions to be studied. The main advantage of this approach is the ability to measure a simple optical signal (e.g. reflected or transmitted light) in real time while the catalytic process is occurring. Processes which can be monitored using such a plasmonic sensor include the so-called sintering of nanoparticles.[21] This is an adverse effect which shortens the life of the catalyst by gradual aggregation of nanoparticles into larger ones, reducing the efficiency of catalysis. After prior calibration consisting of measuring the spectral location of the plasmon resonance as a function of the size of catalytic nanoparticles, it is possible to study the sintering kinetics for varying ambient atmosphere and initial size distribution of nanoparticles.[22] A particularly sophisticated example of monitoring processes accompanying catalysis using the antenna-reactor system is an experiment conducted at the level of single catalytic particles. Specifically, a system consisting of a gold nanoparticle and a single palladium one enabled the study of the thermodynamics of palladium hydride formation in individual palladium nanoparticles of various shapes and sizes.[23]

Recently, dielectric nanostructures emerged as a lossless alternative for plasmonic ones and they are used as a novel platform for biosensing.[24] Dielectric materials are characterized by decreased optical losses leading to reduced heating. High-index dielectrics such as silicon and germanium are CMOS-compatible, making them a favorable choice for integrated devices and lab-on-chip systems.[25] Furthermore, a considerable advantage of dielectric nanostructures is also that they feature both magnetic and electric resonances providing more flexibility in terms engineering the optical response of the sensors. At the same time, the sensitivity of dielectric sensors is generally lower than for their plasmonic counterparts.[26] The key to improving these all-important properties for sensing applications is to exploit radiative coupling.[27]

1.3 Multi-scale light-matter coupling in antenna-reactor systems

The difficulty in modeling antenna-reactor system is the fact that it consists of many stochastically arranged elements of various sizes, whose properties are coupled together at different distance scales. Basic effects arising from near–field enhancement can be qualitatively described by models comprising a single antenna surrounded by a layer of catalytic nanoparticles separated from the antenna by a dielectric spacer layer. The presence of many antennas in the sample affects the measured spectral response of the system, as well as the ratio of scattering to absorption leading to discrepancies between a single antenna model and experimental results.[12–14] The shift of the resonance energy, width and amplitude is crucial when adapting the system to a specific light source (e.g. sunlight). The modified scattering to absorption ratio affects absorption of light in the layer of catalytic material, which justifies the study of multiple scattering in antenna arrays. In addition, we expect that coupling between the antennas also affects the sensitivity of the optical response to the processes around them.

The typical distance between antennas in a sample is on the order of several hundred nanometers. In contrast, the size of a catalytic nanoparticle and its distance from the antenna is on the order of single nanometers. This is the size at which quantum-mechanical effects associated with the atomic scale should be considered, which motivates the analysis of how these effects affect the optical properties of catalytic nanoparticles. The process of generating hot carriers should also be modeled at this scale, which is possible thanks to quantum mechanics calculation tools based on time-dependent density functional theory. This gives us a chance to understand the impact of small distance between particles on transport, optical properties, and the process of plasmon formation in this system.

The multi-scale approach to the problem of antenna-reactor modeling and close cooperation with international experimental and theoretical groups dealing with plasmonically assisted catalysis, sensors based on optical antennas and modeling of these systems, forms the basis of the innovative nature of the project. In the context of applications of the system in the detection of processes associated with catalysis, it is innovative to study the impact of nanoparticle size dispersion on the evolution of sensor signal evolution due to sintering of nanoparticles. The catalytic nanoparticle layer is modeled using an effective model, which avoids the need for simulations for many system configurations.

The principles of maximizing absorption presented in this dissertation are also innovative. For the first time, the material influence, thickness of the dielectric layer, as well as the size of catalytic nanoparticles on the distribution of absorption in the system between the antenna and reactors are considered in a systematic way. In comparison to earlier work by Antosiewicz and Apell,[15] a significant difference in the process of modeling the system is the inclusion of experimental data on distribution and sizes (based on electron microscopy images). In this case, the analysis is conducted with spatial resolution and split into different particle sizes, so many spatial configurations of the nanoparticle layer are simulated, and the absorption is calculated at the level of each nanoparticle. This is the most accurate absorption model of the antenna-reactor system using classical electrodynamics, but it describes only a single antenna covered with a layer of nanoparticles.

The collective response of many randomly distributed antennas is significantly different from a single particle response as discussed by Antosiewicz et al.[12–14] These works offer a description of the impact of radiation coupling on the spectral position and width of the resonance and the scattering to absorption ratio. Herein, we introduce significant extensions to the applicability of the effective model proposed earlier.[12–14] The first is to take into account higher-order and magnetic resonances, thereby allowing a description of dielectric structures. This is important in the context of the use of such structures as sensors for which the sensitivity mechanism is discussed in the scientific community. Modeling the sensitivity of the antenna-reactor system at the level of the collective response of many antennas has not been considered in previous works and the conclusions drawn from the extended model can also be related to the use of the antenna-reactor system as a sensor of catalytic processes. The second extension is the analysis of the scattering-to-absorption ratio for single- and multi-component antenna systems using an effective model, which is important for photocatalytic applications of the antenna-reactor system.

The antenna-reactor system has not yet been considered in the context of quantum mechanical effects. While the generation of hot carriers is mentioned as a mechanism of photocatalysis, a systematic analysis of this process in terms of quantum mechanics was not conducted. Therefore, quantum mechanical calculations for the Ag-Pd system are the first description of this type of antenna-reactor system. The use of a model that takes into account the atomic structure of the system and the effects of correlation and exchange can be considered particularly innovative. The system studied in this work is an example of generation of hot carriers in a non-noble metal, as well as a model system for studying the mechanism of the formation of hot carriers as a result of plasmon decay in a heterometallic system (i.e. consisting of various metals). These are supplemented by a study of the optical properties of catalytic and plasmonic nanoparticles using quantum mechanical methods.

The importance of the herein presented results for the development of the research field is primarily the development of basic knowledge regarding the optical properties of the antenna-reactor system and providing practical rules for designing these systems in terms of maximizing absorption and generation of hot electrons in transition metal nanoparticles with good catalytic properties. Study of transport of carriers and the mechanism of the formation of hot electrons in antenna-reactor systems with particular emphasis on quantum effects provides new methods of effective modeling as well as of analyzing the results of quantum mechanical calculations for the needs of multi-scale modeling of heterometallic systems.

1.4 Theses

The following theses are discussed and proven in this doctoral dissertation:

1. Nanoparticle density is an important parameter enabling tailoring of the optical response of amorphous arrays of nanoantennas for prospective ap-

plications.

2. Antenna-reactor complexes, including plasmonic core-shell nanoantennas, enable significant light absorption enhancement in transition metal nanoparticles; this enhancement can be maximized by manipulating material and geometric properties of the system.
3. Electromagnetic modeling enables relating the optical signal from sensors based on antenna-reactor complexes to physical and chemical phenomena occurring during catalysis.
4. Hot electron generation in antenna-reactor dimers is enhanced with respect to an isolated transition metal particle due to excitation and subsequent dephasing of localized surface plasmon resonance.

1.5 Publications included in the thesis

The main part of the thesis are four chapters devoted to the original results of the author, summarized in five publications, in which the author of the dissertation is the first author:

I Krzysztof M. Czajkowski, Tomasz J. Antosiewicz, "Electromagnetic Coupling in Optical Devices Based on Random Arrays of Dielectric Nanoresonators," Journal of Physical Chemistry C 124, (1), 896–905 (2020).

II Krzysztof M. Czajkowski and Tomasz J. Antosiewicz, "Effective dipolar polarizability of amorphous arrays of size-dispersed nanoparticles," Optics Letters 45, 12, 3220–3223 (2020).

III Krzysztof M. Czajkowski, Maria Bancerek, Tomasz J. Antosiewicz, "Multipole analysis of substrate-supported dielectric nanoresonator metasurfaces via the T-matrix method," Physical Review B 102, 085431 (2020).

IV Arturo Susarrey-Arce,* Krzysztof M. Czajkowski,* Iwan Darmadi, Sara Nilsson, Irem Tanyeli, Svetlana Alekseeva, Tomasz J. Antosiewicz, Christoph Langhammer, "A nanofabricated plasmonic core–shell-nanoparticle library," Nanoscale 11, 21207–21217 (2019). *equal contribution

V Krzysztof M. Czajkowski, Dominika Świtlik, Christoph Langhammer, and Tomasz J. Antosiewicz, "Effective Optical Properties of Inhomogeneously Distributed Nanoobjects in Strong Field Gradients of Nanoplasmonic Sensors," Plasmonics 13(6), 2423–2434 (2018).

1.6 Publications not included in the thesis

I M. Kuisma, B. Rousseaux, K.M. Czajkowski, T.P. Rossi, T. Shegai, P. Erhart, T.J. Antosiewicz, “Ultra-strong coupling of a single molecule to a plasmonic nanocavity: A first-principles study,” ACS Photonics, Article ASAP, doi:10.1021/acsphotonics.2c00066, (2022)

II K. M. Czajkowski et al., “Polarization-dependent mode coupling in hyperbolic nanospheres,” Nanophotonics 10(10), 2021, 2737–2751 (2021).

III A. Egel, K. M. Czajkowski et al., “SMUTHI: A python package for the simulation of light scattering by multiple particles near or between planar interfaces,” Journal of Quantitative Spectroscopy and Radiative Transfer 273, 107846 (2021).

IV M. Bancerek, K. M. Czajkowski, R. Kotyński “Far-field signature of subwavelength microscopic objects,” Optics Express 28(24), 36206–36218 (2020)

V J. Kierdaszuk, M. Tokarczyk, K. M. Czajkowski et al., “Surface-enhanced Raman scattering in graphene deposited on AlxGa1–xN/GaN axial heterostructure nanowires,” Applied Surface Science 475, 559–564 (2019).

VI K. M. Czajkowski, A. Pastuszczak, R. Kotyński, “Single-pixel imaging with sampling distributed over simplex vertices,” Optics Letters 44(5), 1241–1244 (2019).

VII K. M. Czajkowski, A. Pastuszczak, R . Kotyński “Real-time single-pixel video imaging with Fourier domain regularization,” Optics Express 26(16), 20009–20022 (2018).

VIII K. M. Czajkowski, A. Pastuszczak, R. Kotyński, “Single-pixel imaging with Morlet wavelet correlated random patterns,” Scientific Reports 8(1), 1–8 (2018).

IX K. M. Czajkowski, M. Schmid, “Durable and cost-effective neutral density filters utilizing multiple reflections in glass slide stacks,” IEEE Photonics Journal 9 (6), 1-11 (2017).

1.7 Thesis structure

The doctoral dissertation is divided into nine chapters. The first four chapters form a review of the literature related to the subject of the dissertation and the next four concern the author’s original results. The final chapter contains a summary and conclusions. The first chapter is an introduction to antenna-reactor complexes. The chapter presents the aim of the work, potential applications of the studied system and introduces the main research issues addressed in the thesis. The second chapter introduces the theoretical and numerical methods of describing optical properties and electronic structure of nanoparticles including classical electrodynamics and time-dependent density functional theory. The next chapter describes the state of the art of optical antennas. The purpose of this chapter is not only to present the antennas and their properties, but also to summarize various methods for describing the properties of plasmonic and dielectric nanoparticles including multipole expansion as a tool to interpret the properties of optical antennas. The last chapter of the literature review, Chapter 4, is devoted to multiple scattering in optical antenna systems. It presents the problem of describing the optical properties of antenna arrays and the phenomenon of multiple scattering, which makes the optical properties of nanoparticles in an array distinct from those of isolated nanoparticles. In this chapter three methods of describing these properties are presented: the T matrix method, the coupled dipoles/multipoles method and the effective dielectric permittivity method, which account for the phenomenon of multiple scattering in various ways. In addition, the current knowledge on the use of optical antenna arrays in flat optical devices, so-called meta-surfaces is presented.

Chapter 5 deals with the effective optical properties of amorphous arrays of optical antennas. The author proposed a method of describing the effective optical properties of amorphous matrices taking into account higher order multipole moments of both electrical and magnetic nature. The significant simplification resulting from this model enables analysis of influence of the multiple scattering on the optical properties of amorphous arrays. Numerous factors are taken into account, such as the presence of magnetic moments in dielectric antennas, dispersion of the antenna size or additional scattering channels related to the presence of the substrate. The chapter also describes shaping the optical properties by controlling the minimal distance between antennas. The analysis is discussed in the context of potential applications including sensitivity of the optical response to the external environment, as well as the ratio of scattering to absorption, which determines the possibility of generating hot carriers as a result of plasmon decay in the antenna-reactor system.

The next chapter, Chapter 6, containing the author's original results, concerns the absorption of light in the antenna-reactor system. It details a model of optical properties of the antenna-reactor system, taking into account the features of the experimental implementation of the system. Factors that can be controlled in the experiment, such as the material of the antenna as well as the thickness and material of the dielectric separator separating the antenna from the catalytic nanoparticles, are studied as a method of shaping the spectrum of the absorption enhancement.

Optical monitoring of physical and chemical changes during catalysis with the antenna-reactor complexes is the subject of Chapter 7 of this dissertation. In this dissertation, a novel model of effective permittivity has been proposed, making it possible to find the relationship between the optical signal from the sensor and phenomena occurring during catalysis without the need to simulate many realizations of the system. Various possible scenarios are studied including changes of the size distribution of transition metal nanoparticles due to sintering and changes in refractive indices and layer thicknesses of the core-shell nanoantenna due to adsorption of chemical species during catalysis.

Chapter 8, the final one containing author's results, is devoted to the study of the electronic structure of antenna-reactor complexes. While Chapter 6 provides understanding of the factors determining absorption of light in the complex, here the accompanying process of hot carrier generation is studied. It is this process that is the main part of the underlying mechanism behind the light-induced enhancement of catalytic activity of antenna-reactor complexes. In order to address the problem of finding the spatial and energy distribution of the carriers resulting from plasmon decay, time-dependent density functional theory based approach is used.

The final chapter of the dissertation presents the summary and discusses the conclusions obtained from the presented study of antenna-reactor complexes. The thesis is accompanied by two appendices. In Appendix A we present special functions used in this work and expressions for multipole coupling matrix coefficients used in the T-matrix method. In Appendix B we briefly describe the Python code that is available publicly and that implements the effective model describing the optical properties of amorphous arrays of nanoparticles that is presented in Chapter 5.

Chapter 2

Theory

In this chapter we are going to summarize two fundamental theories that describe light-matter interactions. Light is a form of electromagnetic radiation and it is treated as a classical electromagnetic field in this thesis. Matter, on the other hand, is described in a two-fold manner: using dielectric permittivity, a purely classical way of tackling the material description and using an ab-initio approach based upon time-dependent density functional theory. Both approaches are described in this chapter. The first part of the chapter is devoted to classical electrodynamics and the scattering problem that arises in the description of optical properties of nanoparticles with this theory. Special focus is devoted to multipole decomposition and numerical techniques of solving scattering problem. The second part introduces density functional theory and its extension towards the time-dependent hamiltonian, which is necessary to describe interaction of light with atomictically described matter.

2.1 Fundamentals of classical electrodynamics

Electromagnetic fields in classical physics are governed by the set of four Maxwell equations:

$$\nabla \cdot \vec{D} = \rho, \tag{2.1a}$$

$$\nabla \cdot \vec{B} = 0, \tag{2.1b}$$

$$\nabla \times \vec{E} = -\frac{\partial \vec{B}}{\partial t}, \tag{2.1c}$$

$$\nabla \times \vec{H} = \frac{\partial \vec{D}}{\partial t} + \vec{j}(\vec{r}, t), \tag{2.1d}$$

where $\vec{E}$ is the electric field, $\vec{H}$ is the magnetic field, $\vec{D}$ is the electric displacement, $\vec{B}$ is the magnetic induction, ρ is the total charge density and $\vec{j}$ is the current density. The current density $\vec{j}$ can be split into an induced conduction current density $\vec{j}_c$ and a source current density $\vec{j}_s$,

$$\vec{j} = \vec{j}_c + \vec{j}_s. \tag{2.2}$$

In macroscopic electrodynamics, the materials are described using three quantities: polarization ($\vec{P}$), magnetization ($\vec{M}$) and conductivity (κ)

$$\vec{D}(\vec{r},t) = \varepsilon_0 \vec{E}(\vec{r},t) + \vec{P}(\vec{r},t), \tag{2.3}$$

$$\vec{H}(\vec{r},t) = \mu_0^{-1} \vec{B}(\vec{r},t) - \vec{M}(\vec{r},t), \tag{2.4}$$

$$\vec{j}_c(\vec{r},t) = \kappa(\vec{r},t)\vec{E}(\vec{r},t). \tag{2.5}$$

The total current density may be introduced

$$\vec{j}_t = \vec{j}_c + \vec{j}_s + \frac{\partial \vec{P}}{\partial t} + \nabla \times \vec{M}, \tag{2.6}$$

where the first two terms are the current density itself, while the remaining two correspond to the polarization current density and the magnetization current density, respectively.

Both polarization and magnetization are typically expanded in powers of the corresponding fields. In this thesis, only linear materials are considered, hence, polarization and magnetization are linearly proportional to the fields $\vec{E}$ and $\vec{H}$. It is, therefore, useful to define electric (χ_e) and magnetic (χ_m) susceptability

$$\vec{P} = \varepsilon_0 \chi_e \vec{E}, \tag{2.7}$$

$$\vec{M} = \chi_m \vec{H}. \tag{2.8}$$

Oftenmost, time harmonic fields with a frequency ω and a time dependence $\vec{E}(\vec{r},\vec{t}) = \mathrm{Re}(\vec{E}(\vec{r})e^{-i\omega t})$ are considered. The set of Maxwell equations provided above can be then used in the frequency domain.

$$\nabla \times \vec{E} = i\omega \vec{B}, \tag{2.9}$$

$$\nabla \cdot \vec{D} = \rho, \tag{2.10}$$

$$\nabla \times \vec{H} = -i\omega \vec{D} + \vec{j}, \tag{2.11}$$

$$\nabla \cdot \vec{B} = 0. \tag{2.12}$$

In the presence of inhomogeneities boundary conditions have to applied in order to obtain a solution at the material boundary. The tangential fields must satisfy

$$\begin{aligned} \vec{n} \times \left(\vec{E}_i - \vec{E}_j\right) &= \vec{0}, \\ \vec{n} \times \left(\vec{H}_i - \vec{H}_j\right) &= \vec{j}_{\text{surf}}, \end{aligned} \tag{2.13}$$

at the material boundary with $\vec{j}_{\text{surf}}$ being the surface current density and $\vec{n}$ being the surface normal vector, while the normal ones should satisfy

$$\begin{aligned} \vec{n} \cdot \left(\vec{D}_i - \vec{D}_j\right) &= \kappa, \\ \vec{n} \cdot \left(\vec{B}_i - \vec{B}_j\right) &= 0. \end{aligned} \tag{2.14}$$

2.2 Material properties

2.2.1 Dielectric permittivity and refractive index

Polarization $\vec{P}$ in eq. 2.7 describes the response of matter to the applied electric field as shown in the previous section. By inserting eq. 2.7 to eq. 2.3 we obtain

$$\vec{D} = \varepsilon_0(1 + \chi_e)\vec{E}. \tag{2.15}$$

It is possible to substitute the current $\vec{j}_c$ in eq. 2.11 by including it as part of the displacement

$$\vec{D}_t = \varepsilon_0(1 + \chi_e)\vec{E} + \frac{i}{\omega}\vec{j}_c. \tag{2.16}$$

Using eq. 2.5 one can obtain

$$\vec{D}_t = \varepsilon_0 \varepsilon \vec{E} \tag{2.17}$$

with $\varepsilon = 1 + \chi_e + \frac{i\kappa}{\varepsilon_0 \omega}$. ε is called relative permittivity and it characterizes the material. Per analogy, the magnetic permeability is defined as $\mu = 1 + \chi_m$ and from eq. 2.4 and eq. 2.8

$$\vec{B} = \mu_0 \mu \vec{H}. \tag{2.18}$$

Note that, the total current is closely related to the total displacement as

$$\vec{j}_t = -i\omega \vec{D}_t. \tag{2.19}$$

Using Maxwell equations in the frequency domain and material equations the following general wave equation can be derived

$$\nabla \times \mu^{-1} \nabla \times \vec{E} - \frac{\omega^2}{c^2}\varepsilon \vec{E} = \mathrm{i}\omega\mu_0 \vec{j}_{\mathrm{s}}. \tag{2.20}$$

It is also useful to define a quantity called refractive index:

$$n = \sqrt{\varepsilon\mu}, \tag{2.21}$$

which expresses the ratio between the velocity of an electromagnetic wave in a material and in vacuum. In this work we consider nonmagnetic materials only, hence $\mu = 1$ and

$$n = \sqrt{\varepsilon}. \tag{2.22}$$

Notably, under these assumptions the wave equation 2.20 takes on the form of the vector Helmholtz equation

$$\nabla^2 \vec{E}(\vec{r}) - k^2 \vec{E}(\vec{r}) = \mathrm{i}\omega\mu_0\mu\vec{j}(\vec{r}), \tag{2.23}$$

with $k^2 = \frac{\epsilon\omega^2}{c^2}$.

The material properties depend upon many factors such as position, direction of the applied field, as well as time dependence of the incident field. The last phenomenon is called dispersion and leads to the time dependent permittivity

$$\vec{D}(\vec{r}, t) = \varepsilon_0 \iint \tilde{\varepsilon}\left(\vec{r} - \vec{r}', t - t'\right) \vec{E}\left(\vec{r}', t'\right) \mathrm{d}\vec{r}' \mathrm{d}t'. \tag{2.24}$$

Because of the fact that eq. 2.24 expresses a convolution, it is conveniently expressed in the Fourier domain as $\vec{D}(\omega) = \varepsilon(\omega)\vec{E}(\omega)$, which makes dispersion much easier to treat in the frequency domain and enables each frequency to be considered independently simply by accounting for the frequency dependent permittivity. Material anisotropy (dependence on direction of the applied field) and non-locality (dependence on the position) are not considered in this thesis.

2.2.2 Plane wave at a material interface

One of the fundamental solutions to Maxwell equations is a plane wave. It is obtained in the absence of sources (charges and currents) in a homogeneous or planar structure. Omitting the harmonic time dependence, the plane wave solution is

$$\vec{E} = E_0 \vec{\Psi}, \tag{2.25}$$

with

$$\vec{\Psi} = \vec{e}_{pol} e^{i\vec{k}\cdot\vec{r}} \tag{2.26}$$

being the PVWF (plane vector wave function). $\vec{k}$ is a wavevector defined as

$$\vec{k} = \frac{n\omega}{c}\hat{k}, \tag{2.27}$$

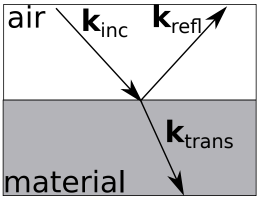

Figure 2.1: Schematic representation of reflection and transmission of a plane wave at an air-material interface.

where $\hat{k}$ determines the propagation direction, while $\vec{e}_{pol}$ is a polarization vector that determines the plane of field oscillation. Plane waves fulfill the condition

$$\vec{e}_{pol} \cdot \vec{k} = 0. \tag{2.28}$$

The magnetic field of a plane wave can be calculated as

$$\vec{H} = \sqrt{\frac{\varepsilon_0 \varepsilon}{\mu \mu_0}} (\hat{k} \times \vec{E}), \tag{2.29}$$

indicating that the magnetic field is perpendicular to the electric field as well as the propagation direction.

The essential application of plane waves is to study planar structures i.e. structures in which permittivity changes along a specified direction. As an example, we consider a case in which there is only a single material interface. The specific configuration is shown in Fig. 2.1.

An arbitrary incident plane wave can be decomposed into two polarizations: s (perpendicular, TE) and p (parallel, TM), which are treated separately. The incident field undergoes reflection and transmission. The amplitude of the reflected field is expressed as $E_r = E_0 r_{s/p}$, while the amplitude of the transmitted field is $E_t = E_0 t_{s/p}$.

It is convenient to express the wavevectors as

$$k_{z_{1,2}} = \sqrt{k_{1,2} - k_{||}}, \tag{2.30}$$

$$k_{||_{1,2}} = k_{1,2} \sin \theta_{1,2}, \tag{2.31}$$

where indices 1,2 number the media, while θ_1 and θ_2 are the angle of incidence and the angle of the transmitted wave, respectively. By imposing the boundary conditions (eq. 2.13 and eq. 2.14), it is found out that the parallel components of the wave vectors are convserved, hence,

$$k_1 \sin\theta_1 = k_2 \sin\theta_2. \tag{2.32}$$

The angle of the reflected wave remains unchanged, but its k_z is of opposite sign with respect to the incident wave wavevector. Also, the amplitudes of the reflected and transmitted plane waves are found for each polarization:

$$r^s = \frac{\mu_2 k_{z_1} - \mu_1 k_{z_2}}{\mu_2 k_{z_1} + \mu_1 k_{z_2}}, \tag{2.33}$$

$$r^p = \frac{\varepsilon_2 k_{z_1} - \varepsilon_1 k_{z_2}}{\varepsilon_2 k_{z_1} + \varepsilon_1 k_{z_2}}, \tag{2.34}$$

$$t^s = \frac{2\varepsilon_2 k_{z_1}}{\varepsilon_2 k_{z_1} + \varepsilon_1 k_{z_2}}, \tag{2.35}$$

$$t^p = \frac{2\varepsilon_2 k_{z_1}}{\varepsilon_2 k_{z_1} + \varepsilon_1 k_{z_2}} \sqrt{\frac{\mu_2 \varepsilon_1}{\mu_1 \varepsilon_2}}. \tag{2.36}$$

A useful spectroscopic quantity is reflectance defined as a ratio between reflected and incident intensities. For normal incidence,

$$R = \left| \frac{n_1 - n_2}{n_1 + n_2} \right|^2. \tag{2.37}$$

More complex planar media are beyond the scope of this thesis, but they can be treated with transfer matrix or scattering matrix formalisms.[28] It is also worth noting that due to orthogonality of PVWFs, an arbitrary field can be propagated through a planar structure using the proposed formalism via PVWF decomposition.

Figure 2.1 assumes that under these conditions the wave is incident from the medium with a lower refractive index (e.g. air) onto a higher refractive index material. Light bends towards the interface normal upon transmission. However, if light is incident from the optically denser medium, the opposite happens. Consequently, if the incidence angle in the dense medium is sufficiently large, it can happen that the transmitted beam cannot bend outwards any further and the wavevector becomes complex. This leads to a decay of the transmitted field. Such a field is called evanescent.

2.2.3 Dielectrics

Dielectrics are materials whose (valence) electrons are bound by a potential created by positively charged atomic cores limiting their mobility. A simple model of permittivity has been proposed by Lorentz and here we outline its basic ideas.

We assume that polarization arises from displacement of electrons from their equilibrium positions, provided that electrons are uncorrelated and thus can be treated independently,

$$\vec{P} = -Ne\vec{x}, \tag{2.38}$$

where we assume N electrons of charge $-e$. Based on this assumption, the polarization can be found using the following Newton equation for electron motion in the electric field,

$$\frac{d^2P}{dt^2} + \gamma\frac{dP}{dt} + \omega_0^2 P = \varepsilon_0\omega_p^2 E, \tag{2.39}$$

where ω_p is the plasma frequency defined as

$$\omega_p^2 = \frac{Nq^2}{m}, \tag{2.40}$$

and γ represents the material losses, while ω_0 is the resonant frequency of a particular electron. It is worth noting that the mass here is the effective mass of the electron in a given material.

The solution to the eq. 2.39 is

$$P = \frac{\varepsilon_0\omega_p^2}{(\omega_0^2 - \omega^2) - i\gamma\omega}E_0. \tag{2.41}$$

This leads to the following expression of the frequency-dependent permittivity

$$\varepsilon_{\text{Lorentz}} = 1 + \frac{\omega_p^2}{(\omega_0^2 - \omega^2) - i\gamma\omega}. \tag{2.42}$$

This permittivity can be decomposed into real and imaginary parts as

$$\epsilon_r(\omega) - 1 = \frac{\omega_p^2\left(\omega_0^2 - \omega^2\right)}{\left(\omega_0^2 - \omega^2\right)^2 + \omega^2\gamma^2}, \tag{2.43}$$

$$\epsilon_i(\omega) = \frac{\omega_p^2\gamma\omega}{\left(\omega_0^2 - \omega^2\right)^2 + \omega^2\gamma^2}. \tag{2.44}$$

These are plotted in Fig. 2.2a. If the frequency is lower than the resonance frequency, both the real and imaginary part of permittivity decrease with decreasing energy. This tendency applies also to the refractive index and is called normal dispersion. When the frequency is slightly larger than the resonance frequency ω_0, the tendency is reversed and the real and imaginary parts of permittivity decrease with increasing excitation energy. This phenomenon is called the anomalous dispersion. When the energy further increases, the tendency is reverted yet again and normal dispersion occurs.

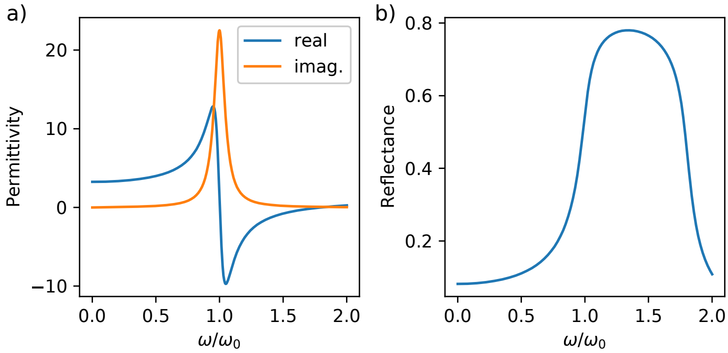

Figure 2.2: a) Real and imaginary parts of Lorentzian permittivity. b) Reflectance spectrum of Lorentzian dielectric.

Using eq. 2.37 reflectance spectra can be calculated for an air-Lorentzian dielectric interface (see Fig. 2.2b). At low frequencies dielectrics transmit light. With increasing frequency, reflectance increases, as do material losses (Fig. 2.2a). Above the resonance frequency ω_0, there is a purely reflective area of the spectrum with $\mathrm{Re}(\varepsilon) < 0$ called the reststrahlen band, but for sufficiently large frequencies the material is transmitting again.

2.2.4 Drude permittivity of metals

Metals differ from dielectrics due to the fact that there is no restoring force and electrons are free to move around the metal surface. In the absence of a restoring force $\omega_0^2 = 0$. Therefore, in metals the Lorentz model reduces to

$$\varepsilon_{\mathrm{Drude}} = 1 - \frac{\omega_p^2}{\omega^2 + i\Gamma\omega}. \tag{2.45}$$

An additional parameter ε_∞ is introduced into Drude model to correct for $\omega \gg \omega_p$

$$\varepsilon_{\mathrm{Drude}} = \varepsilon_\infty - \frac{\omega_p^2}{\omega^2 + i\Gamma\omega}. \tag{2.46}$$

This equation defines the Drude model of metal permittivity. The model is an idealization since in real metals interband transitions modify the material permittivity, $\varepsilon_{\mathrm{metal}} = \varepsilon_{\mathrm{Drude}} + \varepsilon_{\mathrm{interband}}$. Exemplary parameters of a Drude model used in this work to mimic silver in the IR-VIS range are $\varepsilon_\infty = 3$ with $\hbar\omega_p = 9.15$ eV and $\hbar\gamma = 0.133$ eV. A comparison with experimental data obtained by Johnson

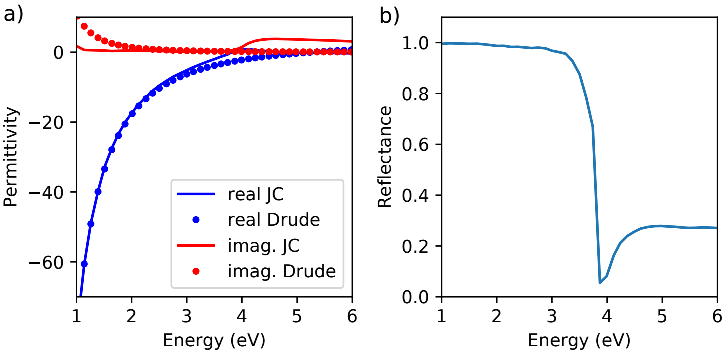

Figure 2.3: a) Real and imaginary parts of Drude permittivity. b) Reflectance spectrum of a Drude metal.

and Christy[29] is presented in Fig. 2.3. The deviation from Drude model is especially visible for high energies, where contribution from the interband transition cannot be modeled well by ε_∞.

2.3 Scattering problem

The problem of light-matter interaction at the nanoscale can be described as an electromagnetic scattering problem. The space is split into a bounded domain, which is the scatterer, and the external area, namely the host medium. The electromagnetic field is split into the external incident field that excites the system and the scattered field that is the result of light-matter interaction. The first one is a given while the other one is obtained using Maxwell equations, boundary conditions on the surface of the scatter and the far field condition called the Silver-Muller radiation condition.

We follow the general formulation of the scattering problem (transmission boundary-value problem) provided by Doicu et al.[30] Given incident fields $\vec{E}_{inc}$, $\vec{H}_{inc}$ as an entire solution to the Maxwell equations representing the external excitation, we find the scattered vector fields $\vec{E}_{scat}$, $\vec{H}_{scat}$ and internal $\vec{E}_{int}$, $\vec{H}_{int}$ satisfying the Maxwell equations and two transmission conditions at the scatterer boundary:

$$\vec{n} \times \vec{E}_{int} - \vec{n} \times \vec{E}_{scat} = \vec{n} \times \vec{E}_{inc}, \tag{2.47}$$

$$\vec{n} \times \vec{H}_{int} - \vec{n} \times \vec{H}_{scat} = \vec{n} \times \vec{H}_{inc}. \tag{2.48}$$

Additionally, the Silver-Muller radiation condition must be satisfied uniformly for all directions as $r \to \infty$. This condition can be formulated as

$$\frac{\vec{r}}{r} \times \sqrt{\mu}\vec{H}_{scat} + \sqrt{\varepsilon}\vec{E}_{scat} = O(1/r), \tag{2.49}$$

with ε being the permittivity of the scattering object and μ being its magnetic susceptibility.

2.3.1 Energy budget of a light scattering system

One of the key properties of a system is its energy budget. In fact, a typical measurement performed is a measurement of the far-field intensity as a function of wavelength and/or scattering angle. The far-field intensity is proportional to the power radiated by the system, rendering the energy budget an all-important aspect of light scattering in classical electrodynamics. Here, we show how to describe the energy budget and introduce meaningful quantities such as cross sections and efficiencies that are common observables obtained from the far field measurement.[31]

As a starting point, we use the fact that an electromagnetic field exerts a force on charged particles, which is called the Lorentz force,

$$\vec{F} = q(\vec{E} + \vec{v} \times \vec{B}). \tag{2.50}$$

This phenomenon leads to work being done in the system. The rate of this work is defined in classical mechanics as

$$\frac{dW}{dt} = \vec{F} \cdot \frac{d\vec{x}}{dt}. \tag{2.51}$$

The magnetic term vanishes, because the vector product yields a force that is perpendicular to velocity. Then the rate of work can be expressed as

$$\frac{dW}{dt} = q\vec{v} \cdot \vec{E} = \int \vec{j} \cdot \vec{E} dV. \tag{2.52}$$

Using Maxwell equations and vector algebra identities this equation can be converted to

$$-\frac{dW}{dt} = \int \left(\nabla \cdot \left(\vec{E} \times \vec{H} \right) + \vec{E} \cdot \frac{\partial \vec{D}}{\partial t} + \vec{H} \cdot \frac{\partial \vec{B}}{\partial t} \right) dV. \tag{2.53}$$

The first term is the divergence of the Poynting vector defined as

$$\vec{S} = \vec{E} \times \vec{H}. \tag{2.54}$$

The second term determines the time derivative of the energy density (u) change rate

$$\frac{\partial u}{\partial t} = \vec{E} \cdot \frac{\partial \vec{D}}{\partial t} + \vec{H} \cdot \frac{\partial \vec{B}}{\partial t}. \tag{2.55}$$

Based on these definitions the following conservation law arises from eq. 2.53,

$$-\frac{dW}{dt} = \nabla \cdot \vec{S} + \frac{\partial u}{\partial t}. \tag{2.56}$$

This expression simplifies assuming that the fields are harmonic in time and the media are linear. Then $\frac{\partial u}{\partial t} = 0$ and using eq. 2.52 it can be shown that the energy conservation (eq. 2.56) takes form

$$\int_{\partial V} \langle \vec{S} \rangle \cdot \vec{n} dA = -\frac{1}{2} \int_{V} \mathrm{Re}\left(\vec{j}^{*} \cdot \vec{E}\right) dV', \tag{2.57}$$

with the time averaged Poynting vector $\langle \vec{S} \rangle$ being

$$\langle \vec{S} \rangle = \frac{1}{2} \mathrm{Re}\left(\vec{E} \times \vec{H}^{*}\right). \tag{2.58}$$

Eq. 2.57 indicates that $\langle \vec{S} \rangle$ integrated over a suitably selected surface ∂V is equal to the average power dissipated within volume V. This is a powerful statement that enables us to consider surface instead of volume integrals and manipulate the surface ∂V almost arbitrarily.

Now we can proceed to the analysis of the energy budget of a scattering system interacting with an electromagnetic field. Outside the scatterer the electric field can be represented as

$$\vec{E} = \vec{E}_{scat} + \vec{E}_{inc} \tag{2.59}$$

and an analogous decomposition can be performed for the magnetic field. The Poynting vector can be then decomposed into

$$\vec{S} = \vec{S}_{inc} + \vec{S}_{scat} + \vec{S}_{ext}, \tag{2.60}$$

where

$$\vec{S}_{inc} = \frac{1}{2} \mathrm{Re}\left(\vec{E}_{inc} \times \vec{H}^{*}_{inc}\right), \tag{2.61}$$

$$\vec{S}_{scat} = \frac{1}{2} \mathrm{Re}\left(\vec{E}_{scat} \times \vec{H}^{*}_{scat}\right), \tag{2.62}$$

$$\vec{S}_{ext} = \frac{1}{2} \mathrm{Re}\left(\vec{E}_{scat} \times \vec{H}^{*}_{inc}\right) + \frac{1}{2} \mathrm{Re}\left(\vec{E}_{inc} \times \vec{H}^{*}_{scat}\right). \tag{2.63}$$

Assuming that the medium in which the scattering object is embedded is non-absorbing, we have $\vec{S}_{inc} = 0$. Then eq. 2.60 can be rewritten as

$$\vec{S}_{ext} = -\vec{S}_{scat} + \vec{S}. \tag{2.64}$$

Consequently, $W_{ext} = \int_{\partial V} \vec{S}_{ext} \cdot \vec{n} dA$ can be interpreted as power that is determined by the sum of $W_{scat} = -\int_{\partial V} \vec{S}_{scat} \cdot \vec{n} dA$, being the power scattered by the scatterer (the minus is added to make the quantity positive), and $W_{abs} = \int_{\partial V} \vec{S} \cdot \vec{n} dA$, which is the power absorbed by the scatterer. Because any of these quantities (in a non-absorbing host medium) do not depend on the shape of the integration surface as long as it is outside the scatterer, we can choose the integration surface arbitrarily. A convenient choice is to use a sphere situated at infinity. The electric field calculated at a distance from the scattering object approaching infinity is called the far-field. The far-field is approximately transverse,

$$\hat{r} \cdot \vec{E}_{scat} = 0, \tag{2.65}$$

while the magnetic field is given by

$$\vec{H}_{scat} = \frac{k}{\omega\mu} \hat{r} \times \vec{E}_{scat}. \tag{2.66}$$

This indicates that the rate of scattered power is proportional to the total radiated intensity

$$W_{scat} = \sqrt{\frac{\varepsilon}{\mu}} \int \left| E_{scat} \right|^2 d\Omega, \tag{2.67}$$

because

$$\hat{r} \cdot \left(\vec{E}_{scat} \times \vec{H}^*_{scat} \right) = \frac{k}{\omega\mu} \left| E_{scat} \right|^2. \tag{2.68}$$

Now that we have treated scattering, we focus on extinction. Because of the fact that extinction power depends on the incident field, a suitable far field representation is necessary. The incident field expanded into spherical waves in the far-field is equal to:[32]

$$\vec{E}_{inc}(\vec{r}) = \frac{2\pi i}{k} \left[\delta(\hat{k} + \hat{r}) \frac{e^{-ikr}}{r} - \delta(\hat{k} - \hat{r}) \frac{\mathrm{e}^{ikr}}{r} \right] \vec{e}_{pol}, \tag{2.69}$$

$$\vec{H}_{\mathrm{inc}}(\vec{r}) = \frac{2\pi i}{k} \left[\delta(\hat{k} + \hat{r}) \frac{e^{-ikr}}{r} - \delta(\hat{k} - \hat{r}) \frac{\mathrm{e}^{ikr}}{r} \right] \sqrt{\frac{\varepsilon_1}{\mu_0}} \hat{k} \times \vec{e}_{pol}. \tag{2.70}$$

Here, $\hat{r}$ is a unit vector in direction of $\vec{r}$. Using the second Green theorem W_{ext} can be expressed as

$$W_{\mathrm{ext}} = -\frac{1}{2} \int_S \vec{n} \cdot \mathrm{Re} \left\{ \vec{E}_{\mathrm{s}} \times \vec{H}^*_{\mathrm{e}} + \vec{E}^*_{\mathrm{e}} \times \vec{H}_{\mathrm{s}} \right\} \mathrm{d}S. \tag{2.71}$$

Assuming that the incident field is a plane wave in free space, after a considerable amount of algebraic manipulation

$$W_{\mathrm{ext}} = \frac{1}{2} \mathrm{Re} \left\{ \sqrt{\frac{\varepsilon}{\mu}} \frac{4\pi}{ik} \vec{e}_{pol} \cdot \vec{E}_{\mathrm{s}\infty}(\hat{k}) \right\}. \tag{2.72}$$

This result is among the key results of this section and it is the called the extinction theorem. It indicates that extinction is a consequence of incident and scattered fields interfering in the forward direction. Moreover, the extinction theorem shows that W_{ext} quantifies the amount of energy removed from the incident beam.

Finally, it is worth pointing out that in some numerical methods absorption is may be conveniently calculated by a volume integral over the scatterer volume rather than the surface located in the far field (eq. 2.19)

$$W_{abs} = -\int_V \frac{1}{2}\mathrm{Re}(\vec{j}^* \cdot \vec{E})dV' = \int_V \frac{\omega}{2}\mathrm{Im}(\vec{D}^* \cdot \vec{E})dV'. \tag{2.73}$$

For plane wave scattering it is useful to define a cross section as

$$C_v = \frac{W_v}{I_{inc}} \tag{2.74}$$

and its corresponding efficiency

$$Q_v = \frac{C_v}{g}, \tag{2.75}$$

where g is the geometrical cross-section of the particle ($g = \pi R^2$ for axisymmetric particles) and I_{inc} is the intensity of the incident field, while v stands for absorption, extinction or scattering.

The scattering cross section definition can be obtained by combining eq. 2.74 with eq. 2.67

$$C_{\text{scat}} = \frac{1}{|\vec{E}_0|^2}\int_\Omega \left|\vec{E}_{\text{s}\infty}\right|^2 \mathrm{d}\Omega. \tag{2.76}$$

It is also convenient to define the angle resolved scattering cross section called the differential scattering cross section

$$C_{\text{scat}}(\theta, \phi) = \frac{1}{|\vec{E}_0|^2}\left|\vec{E}_{\text{s}\infty}(\theta, \phi)\right|^2. \tag{2.77}$$

The extinction cross section is conveniently defined using the optical theorem (eq. 2.72)

$$C_{\text{ext}} = \frac{4\pi}{k_{\text{s}}|\vec{E}_0|^2}\,\mathrm{Im}\left\{\vec{E}_0^* \cdot \vec{E}_{\text{s}\infty}(\hat{k})\right\}. \tag{2.78}$$

2.3.2 Multipole expansion

Multipole decomposition is a key tool used in electromagnetic scattering. In this thesis it is used to decompose the scattered field into physically meaningful terms and to facilitate the description of systems of light scattering nanoparticles. It is also an exceptionally useful tool to formulate the scattering problems including multiple scatterers or complex environments such as e.g. planar media. At the same time, there are several misconceptions about multipole decomposition that have been clarified only recently. In this work, we use almost exclusively multipoles in the spherical basis as they lead to more compact expressions and they are rigorously established. In contrast, the Cartesian multipole formulation is far more intimidating mathematically (see e.g. Ref. 33), their interpretation is often oversimplified (even in classic textbooks such as Ref. 34) and may lead to ambiguity.[35] Nevertheless, for low multipolar orders Cartesian multipoles are used more often and hence they are also shown briefly in this subsection.

The multipole decomposition can be applied either to field or current density. The field expansion is defined as

$$\vec{E}(\vec{r}) = \sum_{l=1}^{\infty} \sum_{m=-l}^{l} b^{E}_{l,m} \vec{M}^{3}_{l,m}(\vec{r}) + b^{M}_{l,m} \vec{N}^{3}_{l,m}(\vec{r}), \tag{2.79}$$

where $b^{E}_{l,m}$ and $b^{M}_{l,m}$ are the electric and magnetic multipole moments, respectively, while $\vec{M}^{3}_{l,m}(\vec{r})$ and $\vec{N}^{3}_{l,m}(\vec{r})$ are vector spherical wave functions defined in Appendix A.

The induced current density and total electric field are related by

$$\vec{j} = \varepsilon_0 (\epsilon - \epsilon_s) \vec{E}. \tag{2.80}$$

It is therefore valid to pose the problem of how multipolar fields arise from corresponding current distributions and how the multipole moments of the fields are related to those of the current multipole decomposition.

We are going to perform the multipole decomposition in the Fourier domain (F denotes Fourier transform) following Alaee et al.,[36]

$$F[\vec{j}](\vec{p}) = \int \vec{j}(\vec{r}) \exp(i\vec{p} \cdot \vec{r}) d\vec{r}. \tag{2.81}$$

Then, the exact multipole decomposition of the induced current can be performed

$$F[\vec{j}](\vec{p}) = \sum_{l,m} b^{E,j}_{l,m} \vec{m}_{l,m}(\hat{p}) + i b^{M,j}_{l,m} \vec{n}_{l,m}(\hat{p}), \tag{2.82}$$

where subscript j indicates the current decomposition expansion coefficients and $\vec{m}_{l,m}$ and $\vec{n}_{l,m}$ denote vector spherical harmonics. Expansion coefficients are determined by

$$4\pi^3 q^{j}_{lm} = \int d\vec{p} \sum_{l',m'} \vec{Q}^{\dagger}_{l,m} Y_{l',m'}(\vec{p}) \int d\vec{r} \vec{j}(\vec{r}) Y^{*}_{l',m'} j'_{l}(kr), \tag{2.83}$$

where $j_l(kr)$ is the spherical Bessel function. q^j_{lm} stands either for $b^{E,j}_{lm}$ or $b^{M,j}_{lm}$, while $Q_{l,m}$ corresponds to $\vec{m}_{lm}(\hat{r})$ or $i\vec{n}_{lm}(\hat{r})$, respectively. Here, the induced current density is expressed as a spherical tensor,

$$\vec{j}(\vec{r}) = \begin{bmatrix} j^{-1} \\ j^0 \\ j^1 \end{bmatrix} = \begin{bmatrix} j^x + ij^y \\ \sqrt{2}j^z \\ -j^x + ij^y \end{bmatrix}, \tag{2.84}$$

and can be rewritten in Cartesian coordinates.

As shown by Alaee et al., the current and field multipole moments are related,[37]

$$a_{l,m} = -\frac{(i)^l}{\sqrt{(2\pi)^3}}\frac{Zk^2}{2}a^j_{l,m}, \qquad b_{l,m} = -\frac{(i)^l}{\sqrt{(2\pi)^3}}\frac{Zk^2}{2}b^j_{l,m} \tag{2.85}$$

with $Z = \sqrt{\frac{\mu}{\varepsilon}}$ being the impedance of the embedding medium. Clearly, both expansions are analogous and differ only by a system independent factor.

After tackling the multipole decomposition in the spherical basis, let us briefly review the Cartesian multipole formulation. Although one might argue that Cartesian multipoles are more physically meaningful and intuitive, spherical multipoles have plenty of useful properties and they carry the same physical information, albeit in a different basis. The current expansion in Cartesian coordinates in the high frequency approximation is given by

$$\begin{aligned}\vec{j}(\vec{r}) = -i\omega\vec{p}\delta(\vec{r}) + \frac{i\omega}{6}Q'\nabla\delta(\vec{r}) + [\nabla \times \vec{m}\delta(\vec{r})] \\ - \frac{i\omega}{6}O'[\nabla\nabla\delta(\vec{r})] - \frac{1}{2}\left[\nabla \times M'\nabla\delta(\vec{r})\right],\end{aligned} \tag{2.86}$$

with $\vec{p}$ being the electric dipole moment, $\vec{m}$ being the magnetic dipole moment, Q being the electric quadrupole moment, M being the magnetic quadrupole moment and O being the electric octupole moment.

The corresponding field is a sum of terms based on current multipole moments

$$\begin{aligned}\vec{E}_{\text{scat}}(\vec{n}) = \frac{k_0^2}{4\pi\varepsilon_0}\Bigg([\vec{n} \times [\vec{p} \times \vec{n}]] + \frac{1}{c}[\vec{m} \times \vec{n}] + \frac{ik_d}{6}[\vec{n} \times [\vec{n} \times Q\vec{n}]] \\ + \frac{ik_d}{2c}[\vec{n} \times (M\vec{n})] + \frac{k_d^2}{6}[\vec{n} \times [\vec{n} \times O(\vec{n}\vec{n})]]\Bigg).\end{aligned} \tag{2.87}$$

The extinction cross section (assuming x-polarized field) and scattering cross section can be expanded into contributions from individual multipoles as

$$C_{\text{ext}} = \frac{k_d}{\varepsilon_0\varepsilon_d\left|E_{0x}\right|^2}\,\text{Im}\left\{E^*_{0x}\left(p_x - \frac{ik_d}{6}Q_{xz} + \frac{1}{c}m_y - \frac{ik_d}{2c}M_{yz} - \frac{k_d^2}{6}O_{xzz}\right)\right\}, \tag{2.88}$$

$$\begin{aligned} C_{\text{scat}} = & \frac{k_0^4}{6\pi\varepsilon_0^2 \left|\vec{E}_{\text{inc}}\right|^2} |\vec{p}|^2 + \frac{k_0^4 \varepsilon_d \mu_0}{6\pi\varepsilon_0 \left|\vec{E}_{\text{inc}}\right|^2} |\vec{m}|^2 + \frac{k_0^6 \varepsilon_d}{720\pi\varepsilon_0^2 \left|\vec{E}_{\text{inc}}\right|^2} \sum_{\alpha\beta} |Q_{\alpha\beta}|^2 \\ & + \frac{k_0^6 \varepsilon_d^2 \mu_0}{80\pi\varepsilon_0 \left|\vec{E}_{\text{inc}}\right|^2} \sum_{\alpha\beta} |M_{\alpha\beta}|^2 + \frac{k_0^8 \varepsilon_d^2}{1890\pi\varepsilon_0^2 \left|\vec{E}_{\text{inc}}\right|^2} \sum_{\alpha\beta\gamma} |O_{\alpha\beta\gamma}|^2 . \end{aligned} \tag{2.89}$$

In this thesis we use Cartesian dipoles to describe scattered fields by small particles. Thus, it is useful to provide a transformation between spherical and Cartesian dipoles,

$$\begin{pmatrix} p_x \\ p_y \\ p_z \end{pmatrix} = c_E M \begin{pmatrix} b^E_{-1,1} \\ b^E_{0,1} \\ b^E_{1,1} \end{pmatrix}, \tag{2.90}$$

with M defined as

$$M = \begin{pmatrix} 1 & 0 & -1 \\ i & 0 & i \\ 0 & -\sqrt{2} & 0 \end{pmatrix} \tag{2.91}$$

and

$$c_E = \frac{\sqrt{6}\pi i \varepsilon_0}{k^3}. \tag{2.92}$$

The magnetic dipole obeys the same transformation rule

$$\begin{pmatrix} m_x \\ m_y \\ m_z \end{pmatrix} = c_M M \begin{pmatrix} b^M_{-1,1} \\ b^M_{0,1} \\ b^M_{1,1} \end{pmatrix}, \tag{2.93}$$

with

$$c_M = \frac{c_E}{\varepsilon_0}. \tag{2.94}$$

A derivation of this equation and general procedure is outlined in the literature.[36]

In scattering problems, the dipole moment $\vec{p}$ is proportional to the incident field

$$\vec{p} = \alpha_e \vec{E}_{inc}, \tag{2.95}$$

where α_e is the polarizability and is, in general, a 3x3 tensor. Using polarizability, the scattering and extinction cross-sections of a dipole are expressed as

$$C_{\text{ext}} = \frac{k_0}{\varepsilon_0} \operatorname{Im}(\alpha_e) \tag{2.96}$$

and

$$C_{\text{scat}} = \frac{k_0^4}{6\pi\varepsilon_0^2} |\alpha_e|^2 , \tag{2.97}$$

respectively. Analogously, the magnetic polarizability α_m is defined as

$$\vec{m} = \alpha_M \vec{H}_{inc}. \tag{2.98}$$

The extinction cross-section of a magnetic dipole is given by

$$C_{\text{ext}} = k_0 \, \text{Im}(\alpha_m). \tag{2.99}$$

2.3.3 Green function approach to scattering problem

As the first approach of solving the scattering problem, we would like to show the so-called volume integral equation. In order to derive this method it is first necessary to understand the concept of the Green function. The Green function is a solution to an inhomogeneous linear or differential equation with a delta function inhomogeneity that can be used to construct a solution of the equation with an arbitrary inhomogeneity by superposition. For example, given dyadic Green function for eq. 2.23 and current density $\vec{j}$ the electric field is

$$\vec{E}(\vec{r}) = \vec{E}_0(\vec{r}) + i\omega\mu\mu_0 \int_V G(\vec{r}, \vec{r'})\vec{j}(\vec{r'})dV' \tag{2.100}$$

Then, using Maxwell equations, the magnetic field can be determined as well,

$$\vec{H}(\vec{r}) = \vec{H}_0(\vec{r}) + i\omega\mu\mu_0 \int_V \nabla \times G(\vec{r}, \vec{r'})\vec{j}(\vec{r'})dV'. \tag{2.101}$$

The dyadic Green function for eq. 2.23 is

$$G = \left[\mathbb{1} + \frac{1}{k^2}\nabla\nabla\right] G_0(\vec{r}, \vec{r'}), \tag{2.102}$$

where

$$G_0(\vec{r}, \vec{r'}) = \frac{\exp(ik|\vec{r} - \vec{r'}|)}{4\pi|\vec{r} - \vec{r'}|} \tag{2.103}$$

is the Green function for the scalar Helmholtz equation.

By inserting eq. 2.103 into eq. 2.102, it is possible to obtain the explicit expression for the dyadic Green function,

$$G(\vec{r}, \vec{r'}) = \frac{\exp(ikR)}{4\pi R} \left[\left(1 + \frac{ikR - 1}{k^2R^2}\right)\mathbb{1} + \frac{3 - 3ikR - k^2R^2}{k^2R^2}\frac{\vec{R}\vec{R}}{R^2}\right], \tag{2.104}$$

where $R = |\vec{r} - \vec{r'}|$.

Now that we have established the general framework, it is useful to find propagators for selected multipoles. This will lead to a set of useful conclusions. The simplest example is the one for electric dipole, for which the current density is

$$\vec{j}(\vec{r}) = -i\omega\vec{p}\delta(\vec{r}). \tag{2.105}$$

Substiuting this current density into eq. 2.100, one can find that electric dipole propagator G^{EE} is

$$G^{EE}(\vec{r},\vec{r'}) = \frac{\exp(ikR)}{4\pi R}\left[\left(1+\frac{ikR-1}{k^2R^2}\right)\mathbb{1}+\frac{3-3ikR-k^2R^2}{k^2R^2}\frac{\vec{R}\vec{R}}{R^2}\right] \tag{2.106}$$

and

$$\vec{E}^p\left(\vec{r}\right) = \frac{k_0^2}{\varepsilon_0}G^{EE}\left(\vec{r},\vec{r}'\right)\vec{p}. \tag{2.107}$$

In a similar manner propagators of the other multipoles can be found. Here, we consider the magnetic dipole propagator

$$G^{EM} = \frac{i}{ck_0}\nabla\times G^{EE}. \tag{2.108}$$

It is useful to introduce vector $\vec{g}$ such that

$$\vec{g} = \frac{ikce^{ikR}}{4\pi\varepsilon_0 R}\left(\frac{ik}{R}-\frac{1}{R_{ij}^2}\right)(\vec{r}-\vec{r}'). \tag{2.109}$$

Then, G^{EM} can be evaluated as

$$G_{ij}^{EM} = \sum_{s=x,y,z}^{3}(\vec{g}\times\vec{\hat{s}})\otimes\hat{s}. \tag{2.110}$$

The electric field of amagnetic dipole is given by

$$\vec{E}^m(\vec{r}) = \frac{k_0^2}{\varepsilon_0}G^{EM}(\vec{r},\vec{r}')\vec{m}, \tag{2.111}$$

while its magnetic field is

$$\vec{H}^m(\vec{r}) = k_0^2G^{EE}(\vec{r},\vec{r}')\vec{m}. \tag{2.112}$$

The magnetic dipole propagator G^{EM} can be also used to obtain the magnetic field from the electric dipole

$$\vec{H}^p(\vec{r}) = -k_0^2G^{EM}(\vec{r},\vec{r}')\vec{p}. \tag{2.113}$$

2.4 Numerical methods in classical electrodynamics

2.4.1 Short note on FDTD/FEM method

The other class of methods that can be used to solve the scattering problem are those that use the differential representation of the Maxwell equations. In this work the finite-difference time-domain method (FDTD) and finite element method (FEM) are used to model light scattering by isolated antennas and antennas decorated with catalytic nanoparticles.

FDTD is the only method in this thesis that uses the time-domain formulation of the Maxwell equations (eqs. 2.1a-2.1d), albeit FEM can also be possibly formulated in the time domain. In order to discretize the Maxwell equations in the time domain, the central finite difference approximation is used. An important aspect of FDTD is a fact that that electric and magnetic fields are stored at different points in time and space providing additional stability and accuracy. This discretization is called the Yee lattice. Distinguishing between total and scattered fields in FDTD requires using the so-called total-field/scattered-field (TFSF) source. This leads to splitting the simulation space into two subdomains. In the first one in which the scatterer resides contains both the scattered and incident field. Thus, it is called the total field region. The second one is outside the first one and in this region only the scattered field is present. This approach makes it possible to find the amount of absorbed power using volume integral (eq. 2.73) as well as the scattered power using surface integral over a surface of a box spanning outside the source region (eq. 2.62). Absorption can equally be calculated using a surface integral that encloses the integral volume. In this thesis a commercial FDTD solver called Lumerical FDTD Solutions (Ansys) is used.

The very general and simple formulation of FDTD stands behind many strengths as well as weaknesses of the method. Some of the strengths of FDTD are:

- a broad spectral response can be obtained from one simulation using the Fourier transform;
- it is a versatile method with permittivity specified individually at each point of the simulation grid (linear, nonlinear and anisotropic materials are possible);
- high accuracy (unless dispersive materials are used);
- more degrees of freedom can be solved for than in FEM, because matrix inversion is not required;

- the method works well in parallel computing schemes (MPI, CUDA etc.).

Weaknesses of FDTD:

- dispersive materials need special treatment as they are defined in the time domain;
- the field is computed only in the grid points – other points are difficult to access (the far-field can be computed but it increases the cost substantially, it is very difficult in a non-homogeneous environment e.g. if scatterer is placed on a substrate).

In the finite element method (FEM) partial differential equations are converted into a system of linear equations by dividing the space into elements by constructing a mesh of the simulated object. At each element the solution is approximated by a piecewise function (e.g. linear), reducing the problem to finding the values of the solution at nodes of the mesh. Conversion to a linear system is typically performed by finding the weighted residual integral in the weak form and then by applying the piecewise function approximation. The solution is then obtained by direct (e.g. LU) or iterative (e.g. GMRES) linear equation solvers. In this work COMSOL with the Wave Optics module is used to solve the Helmholtz equation (eq. 2.23) in the frequency domain.

Strengths of FEM:

- the most accurate and versatile method;
- dispersion is treated in the frequency domain;
- the simulation grid can be highly non-uniform.

Weaknesses of FEM:

- meshing of the simulation domain requires expertise;
- solution takes a significant amount of time;
- iterative solvers tend to diverge around resonant frequencies of the system.

Since space is discretized in the FDTD method and FEM the spatial extent of the simulation must be specified, requiring careful truncation of the simulation volume. In some problems periodic boundary conditions can be applied. Other times, when the field decays sufficiently fast, hard wall boundaries can be used. Most often in scattering problems, however, these conditions do not apply and using hard wall boundaries is impractical and leads to artifacts. Therefore, there is a need for absorbing boundary conditions (ABC) that would not lead to artificial reflection from the simulation edge. The idea is realized in practice by a

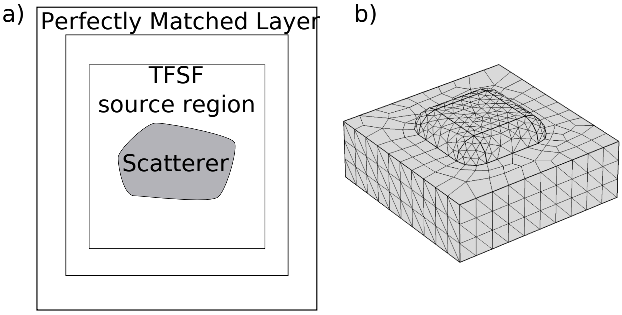

Figure 2.4: a) Schematic representation of an FDTD simulation of optical scattering. b) Example of an FEM mesh for a scatterer on a plane substrate.

using an absorbing perfectly matched layer (PML), which is engineered so that the wave is not reflected off the nonabsorbing-PML material boundary.[38] The modern approach to PMLs generally resolves around the idea of complex coordinate stretching. As a consequence of complex coordinate stretching all the field derivatives in the PML region are transformed so that the non-evanescent waves are turned into evanescent waves. At the same time, outside the PML region, the wave equation remains unchanged, hence, reflections are not present. This simple approach yields problems when the evanescent waves are to be absorbed by the PML as well. Then, additional coordinate stretching is used to increase the decay rate of evanescent waves.

2.4.2 T-matrix framework

In this thesis we also rely on the T-matrix method to solve a broad range of scattering problems. The T-matrix is a surface integral method which is used to solve the scattering problem by expanding the fields into vector spherical wave functions. A detailed derivation of the T-matrix method is outside the scope of this thesis and it can be found e.g. in Ref. 39. Most modern null-field methods support a variety of basis functions, but here we stick to the typical choice of VSWF. The incident field is expanded into regular vector spherical wave functions $\vec{M}^1_{lm}(\vec{r})$ and $\vec{N}^1_{lm}(\vec{r})$,

$$\vec{E}_{ext}(r) = \sum_{l=1}^{\infty} \sum_{m=-l}^{l} a^E_{lm} \vec{M}^1_{lm}(\vec{r}) + a^M_{lm} \vec{N}^1_{lm}(\vec{r}) \tag{2.114}$$

while the scattered field is expanded into radiating vector spherical wave functions,

$$\vec{E}_{scat}(r) = \sum_{l=1}^{\infty} \sum_{m=-l}^{l} b_{lm}^{E} \vec{M}_{lm}^{3}(\vec{r}) + b_{lm}^{M} \vec{N}_{lm}^{3}(\vec{r}). \tag{2.115}$$

The transition matrix (T-matrix) relates the expansion coefficients of the incident (a) and scattered fields (b) in terms of radiating vector spherical wave functions[30]

$$\begin{pmatrix} b^E \\ b^M \end{pmatrix} = \begin{pmatrix} T^{EE} & T^{EM} \\ T^{ME} & T^{MM} \end{pmatrix} \begin{pmatrix} a^E \\ a^M \end{pmatrix}. \tag{2.116}$$

If the incident field is a plane wave with wavevector $\vec{k}$, the VSWF coefficients are

$$a_{lm} = 4i^{n} \vec{e}_{pol} \cdot \vec{m}_{lm}^{*}(\hat{k}), \tag{2.117}$$

$$b_{lm} = -4i^{n+1} \vec{e}_{pol} \cdot \vec{n}_{lm}^{*}(\hat{k}). \tag{2.118}$$

The calculation of the T-matrix can be formulated as a matrix inversion problem,

$$\vec{T} = -\vec{Q}^{11}\left(k_{\mathrm{s}}, k_{\mathrm{i}}\right)\left[\vec{Q}^{31}\left(k_{\mathrm{s}}, k_{\mathrm{i}}\right)\right]^{-1}, \tag{2.119}$$

where the Q-matrices are defined as

$$Q^{pq}\left(k_1, k_2\right) = \left[\begin{array}{cc} \left(Q^{pq}\right)_{\nu\mu}^{11} & \left(Q^{pq}\right)_{\nu\mu}^{12} \\ \left(Q^{pq}\right)_{\nu\mu}^{21} & \left(Q^{pq}\right)_{\nu\mu}^{22} \end{array}\right] \tag{2.120}$$

with

$$\begin{aligned} \left(Q^{pq}\right)_{\nu\mu}^{11} = \frac{ik_1^2}{\pi} \int_S & \left[\vec{n}\left(\vec{r}'\right) \times \vec{M}_{\mu}^{q}\left(k_2 \vec{r}'\right)\right] \cdot \vec{N}_{\frac{\nu}{\nu}}^{p}\left(k_1 \vec{r}'\right) \\ & + \sqrt{\frac{\varepsilon_2}{\varepsilon_1}}\left[\vec{n}\left(\vec{r}'\right) \times \vec{N}_{\mu}^{q}\left(k_2 \vec{r}'\right)\right] \cdot \vec{M}_{\bar{\nu}}^{p}\left(k_1 \vec{r}'\right) \mathrm{d}S\left(\vec{r}'\right), \end{aligned} \tag{2.121}$$

$$\begin{aligned} \left(Q^{pq}\right)_{\nu\mu}^{12} = \frac{ik_1^2}{\pi} \int_S & \left[\vec{n}\left(\vec{r}'\right) \times \vec{N}_{\mu}^{q}\left(k_2 \vec{r}'\right)\right] \cdot \vec{N}_{\bar{\nu}}^{p}\left(k_1 \vec{r}'\right) \\ & + \sqrt{\frac{\varepsilon_2}{\varepsilon_1}}\left[\vec{n}\left(\vec{r}'\right) \times \vec{M}_{\mu}^{q}\left(k_2 \vec{r}'\right)\right] \cdot \vec{M}_{\bar{\nu}}^{p}\left(k_1 \vec{r}'\right) \mathrm{d}S\left(\vec{r}'\right), \end{aligned} \tag{2.122}$$

$$\begin{aligned} \left(Q^{pq}\right)_{\nu\mu}^{21} = \frac{ik_1^2}{\pi} \int_S & \left[\vec{n}\left(\vec{r}'\right) \times \vec{M}_{\mu}^{q}\left(k_2 \vec{r}'\right)\right] \cdot M_{\bar{\nu}}^{p}\left(k\,_1 \vec{r}'\right) \\ & + \sqrt{\frac{\varepsilon_2}{\varepsilon_1}}\left[\vec{n}\left(\vec{r}'\right) \times \vec{N}_{\mu}^{q}\left(k_2 \vec{r}'\right)\right] \cdot \vec{N}\frac{p}{\nu}\left(k_1 \vec{r}'\right) \mathrm{d}S\left(\vec{r}'\right) \end{aligned} \tag{2.123}$$

and

$$\begin{aligned}(Q^{pq})^{22}_{\nu\mu} = \frac{ik_1^2}{\pi} \int_S & \left[\vec{n}\left(\vec{r}'\right) \times \vec{N}^{q}_{\mu}\left(k_2\vec{r}'\right)\right] \cdot \vec{M}^{p}_{\bar{\nu}}\left(k_1\vec{r}'\right) \\ & + \sqrt{\frac{\varepsilon_2}{\varepsilon_1}} \left[\vec{n}\left(\vec{r}'\right) \times \vec{M}^{q}_{\mu}\left(k_2\vec{r}'\right)\right] \cdot \vec{N}^{p}_{\bar{\nu}}\left(k_1\vec{r}'\right) \mathrm{d}S\left(\vec{r}'\right), \qquad (2.124)\end{aligned}$$

where ε_1 and ε_2 are the permittivity of the host medium and the scatterer, respectively. In the equations presented above, ν and μ are (l, m) gathered into a single index. $\bar{\nu}$ is equal to ν with m replaced by $-m$. We calculate the T-matrices using the null-field method with discrete sources which is an efficient method of evaluating single particle scattering properties.

The strengths of the T-matrix approach are:

- possibility to exploit symmetries of the scatterer reduces computation time by orders of magnitude with respect to FDTD/FEM calculations;
- multipole decomposition is built inherently into the method and thus can be obtained without additional workload;
- it is a physically meaningful methodology for including multiple scattering between particles that scales up to over 1000 particles.

For these reasons the T-matrix method is used herein to describe of nanoantenna arrays.

The weaknesses of T-matrix method are:

- it is not as universal as other methods – arbitrary material anisotropy, structural inhomogeneity are difficult to attain;
- stability issues for particles that deviate significantly from spherical shape (e.g. elongated rods, structures with sharp features);
- the scattered field is valid only outside the smallest circumscribing sphere of the scatterer.

This last limitation is the most relevant for this work. There are two particular cases in which the scattered field validity is important. The first one is multiple scattering between two closely spaced nanoparticles. If their circumscribing spheres overlap the validity may be compromised. The other case is if the particle is embedded in a planar medium and its circumscribing sphere crosses one of the interfaces. Both cases are schematically represented in Fig. 2.5. At the same time, the use of the T-matrix approach is studied extensively as both are ubiquitous in nanophotonics. It has been shown that to some extent one

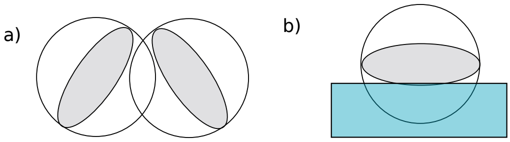

Figure 2.5: Examples of cases in which T-matrix method is not directly applicable: a) two closely spaced nanoparticles, b) flat particle on a plane substrate.

can anticipate that the fields will be valid inside the circumbscribing sphere of a particle given that the multipole truncation order is high and extended numerical precision should be used in such cases.[40]

In the T-matrix approach, the extinction cross section is given by

$$C_{\text{ext}} = -\frac{\pi}{k_{\text{s}}^2} \sum_{l=1}^{\infty} \sum_{m=-l}^{l} \text{Re}\left\{ b_{l,m}^{E} {a^{E}}^{*}_{l,m} + b_{l,m}^{M} {a^{M}}^{*}_{l,m} \right\}, \tag{2.125}$$

while the scattering cross section is

$$C_{\text{scat}} = \frac{\pi}{k_{\text{s}}^2} \sum_{l=1}^{\infty} \sum_{m=-l}^{l} \left| b_{l,m}^{E} \right|^2 + \left| g_{l,m} \right|^2 . \tag{2.126}$$

A useful quantity to describe the scattering process is the scattering-to-absorption ratio

$$SAR = \frac{C_{\text{scat}}(\lambda_{\text{res}})}{C_{\text{abs}}(\lambda_{\text{res}})} \tag{2.127}$$

2.5 Quantum description of matter interacting with classical light

The classical electrodynamics approach to light-matter interaction treats materials as continuous characterizing them by a position independent function $\varepsilon(\omega)$. However, it is possible to go beyond the treatment presented in the previous sections and consider the motion of electrons around the nuclei directly utilizing quantum mechanics. In this section the state-of-the-art approach to the electron dynamics in an electromagnetic field is presented.

2.5.1 Ground state of the electronic system

As a first step it is necessary to find the ground state of the electronic system under consideration. All the properties of the system in its ground state can be calculated from its wavefunction $\vec{\Psi}(\vec{r},t)$, which is the solution of the Schroedinger equation,

$$H(\vec{r},t)\vec{\Psi}(\vec{r},t) = -i\hbar\vec{\Psi}(\vec{r},t). \tag{2.128}$$

If the hamiltonian H is time-independent, then the Schroedinger equation takes form of an eigenvalue problem.

$$H(\vec{r})\vec{\psi}(\vec{r}) = E\psi(\vec{r}), \tag{2.129}$$

where E is the energy of the system. The time dependence can be restored using

$$\vec{\Psi}(\vec{r},t) = \vec{\psi}(\vec{r})e^{\frac{i}{\hbar}tH}. \tag{2.130}$$

The hamiltonian for the electronic system can be written as

$$H = T_e + V_{NN} + V_{ee} + V_{eN}, \tag{2.131}$$

where T_e is the kinetic energy of electrons, V_{NN} is the nucleus-nucleus interaction potential, V_{ee} is the electron-electron interaction potential, V_{eN} is the electron-nucleus interaction potential. Within the Born-Oppenheimer approximation used here, the positions of nuclei are treated as a parameter assuming that movement of the nuclei is much slower than that of electrons. While this hamiltonian is simple to write down, it is tremendously difficult to solve the corresponding Schroedinger equation.

2.5.2 Density functional theory

Solving the many-body Schroedinger equation in form of eq. 2.129 with the electronic hamiltonian (eq. 2.131) is a formidable task. With $3N$ dimensional wavefunctions its storage would require $B = q^{3N}$ bits, where q is number of bits per degree of freedom. A similar scaling is observed for the computational complexity of calculating wavefunctions with reasonable accuracy. This has been called the exponential wall by Walter Kohn[41] and it prevents solving the many-body problem for practical systems. It is, however, worth noting that certain methods such as configuration interaction and quantum Monte Carlo exist that enable wavefunction calculations for the many-body problem. Setting the capability of calculating wavefunctions aside, it is questionable whether the wavefunction is even needed. In fact, in a typical calculation we are interested in finding certain observables rather than the probabilities in position space and, as argued by Kohn, the wavefunction contains far more information than can be reasonably processed. This leads to the following question: is there a quantity that uniquely determines the system state which depends upon a smaller set of variables than a wavefunction? It turns out that a suitable quantity is the electron density given by

$$\rho(\vec{r}) = N \int \mathrm{d}^3\vec{r}_2 \cdots \int \mathrm{d}^3\vec{r}_N \Psi^* \left(\vec{r}, \vec{r}_2, \ldots, \vec{r}_N\right) \Psi \left(\vec{r}, \vec{r}_2, \ldots, \vec{r}_N\right). \tag{2.132}$$

The foundations of density functional theory (DFT) are based upon two theorems provided by Hohenberg and Kohn.[42] The first one states that there is a one-to-one correspondence between the density and external potential. This means that just like the wavefunction, the electron density determines uniquely all the system properties. One special property is energy. Based upon this it is possible to write an expression of energy as a density functional

$$E[\rho] = T_e[\rho] + E_{\text{int}}[\rho] + \int \mathrm{d}\vec{r}\, v_{ext}(\vec{r})\rho(\vec{r}), \tag{2.133}$$

where E_{int} is the electron-electron interaction energy and v_{ext} is the sum of the potential generated by the nuclei and any other external potential e.g. the electric field. The second Hohenberg and Kohn (HK) theorem states that the exact density of an interacting system can be found by minimization of energy. This theorem in principle provides a method of finding the density itself. At the same time, the functionals $T[\rho]$ and $E_{\text{int}}[\rho]$ in eq. 2.133 are unknown and therefore cannot be used for practical calculations. One particular system for which the kinetic energy functional can be calculated is a system of noninteracting electrons,

$$T_e[\rho] = \sum_{i=1}^{N} \int d\vec{r} \varphi_i^*(\vec{r}) \left(-\frac{\hbar^2}{2m}\nabla^2\right) \varphi_i(\vec{r}). \tag{2.134}$$

The most common and practical implementation of DFT is the Kohn-Sham method.[43] In this method the many-body problem is solved for a fictitious system of noninteracting electrons moving in an effective potential (v_{eff}). For this system eq. 2.133 reads

$$E[\rho] = T_e[\rho] + E_{\text{H}}[\rho] + E_{\text{xc}}[\rho] + \int \mathrm{d}\vec{r}\, v_{\text{ext}}(\vec{r})\rho(\vec{r}), \tag{2.135}$$

where $E_{\text{H}}[\rho]$ is Hartree energy defined as

$$E_{\text{H}}[\rho] = \frac{e^2}{2} \int d\vec{r} \int d\vec{r}^{prime} \frac{\rho(\vec{r})\rho\left(\vec{r}'\right)}{|\vec{r} - \vec{r}'|}. \tag{2.136}$$

The Hartree energy constitutes the majority of the interaction energy. However, a small part called the exchange-correlation energy remains undetermined.

There are several ways of approximating the exchange-correlation term, with the common ones being LDA and GGA.[44]

To sum up, in the Kohn-Sham method the following set of equations is solved self-consistently to find the ground state density, effective wavefunction and eigenvalues.

$$\left(\frac{\hbar^2}{2m}\nabla^2 + v_{eff}[\rho]\right)\phi_i = \varepsilon_i\phi_i, \tag{2.137a}$$

$$E[\rho] = T_s[\rho] + \int dr v_{ext}(r)\rho(r) + E_{HXC}[\rho], \tag{2.137b}$$

$$\rho(\vec{r}) = \sum_{i=1}^{N} |\psi_i(\vec{r})|^2 = \sum_i f_i |\psi_i(\vec{r})|^2, \tag{2.137c}$$

where $v_{eff} = v_{ext} + v_H + v_{XC}$ and $E_{HXC} = E_H + E_{xc}$.

The remaining difficulty, i.e. solving the Kohn-Sham equations, requires further approximations. The SIESTA code is used in this thesis to calculate the ground state Kohn-Sham equation solution.[45] The code uses the pseudopotential approximation. This approximation relies on the fact that the core electrons (those lying on the inner atomic shells) are chemically inert, have low corresponding eigenenergies and they lie close to the nuclei screening the nuclear potential. At the same time, they substantially increase the calculation cost. Therefore, it is justified to treat them effectively as a part of the potential and solve only for the electronic density of the remaining (typically valence) electrons. The choice of the pseudopotential should result in the following[44]

- for a given configuration all electron and pseudo valence eigenvalues should be equal;
- the wavefunctions should be the same above a chosen cutoff radius, while the logarithmic derivatives should agree at the cutoff radius;
- the total charge should be the same in the core region, leading to norm conservation.

The pseudopotentials fulfilling these rules (especially the last one) are called norm-conserving pseudopotentials.

In order to solve the differential equation, it is necessary to discretize it using a set of basis functions. While explicit spatial discretization is the most accurate, it leads to high computational cost rendering the method impractical for large systems. One choice that leads to a particularly compact basis are numerical atomic orbitals (NAOs). They are obtained by solving the Kohn-Sham hamiltonian for an isolated pseudoatom within the same approximations as for the full system under consideration. On top of vastly improved numerical convergence and computational cost, NAOs are also known for giving physical insight due to their locality.[45]

2.5.3 Time-dependent density functional theory

Density functional theory and the Kohn-Sham method can be applied to determine the ground state properties of a system. However, it is not applicable to finding the excited states and their dynamics upon time dependent stimuli such as laser pulses or electron beams. In such cases, a modified DFT version called time-dependent density functional theory (TDDFT) is necessary. TDDFT addresses the many-body problem with a time-dependent external potential and hence the time-dependent Schroedinger equation – eq. 2.128 in an analogous manner to ground state DFT. Analogously to the Hohenberg-Kohn theorems, the Runge-Gross theorems prove that there is a one-to-one correspondence between the time-dependent electron density and the time-dependent external potential.[46] The time-dependent Kohn-Sham equation reads

$$i\frac{\partial}{\partial t}\psi_i(\vec{r},t) = h_{\mathrm{Kohn-Sham}}(t)\psi_i(\vec{r},t) \tag{2.138}$$

with the time-dependent Hamiltonian

$$h_{\mathrm{Kohn-Sham}}(t) = -\frac{1}{2}\nabla^2 + \int \mathrm{d}\vec{r}'\,\frac{\rho\,(\vec{r}',t)}{|\vec{r}-\vec{r}'|} + v_{xc}[\rho](\vec{r},t) + v_{\mathrm{ext}}(\vec{r},t). \tag{2.139}$$

While it is possible to solve the time-dependent Kohn-Sham equation using explicit time propagation schemes such as the Crank-Nicolson algorithm, for the purpose of this work it is more useful to utilize the linear response (LR) approach in the frequency domain. This method is particularly useful when spectroscopic quantities are of interest. In linear response TDDFT, the assumption is that the time-dependent exciting potential is a weak perturbation of the ground state potential

$$v_{\mathrm{ext}}(\vec{r},t) = v_{\mathrm{ext}}(\vec{r}) + \delta v_{\mathrm{ext}}(\vec{r},t)\theta(t), \tag{2.140}$$

where $\theta(t)$ is the Heavyside theta function. Consequently, the induced density scales linearly with the external potential. Then

$$\rho(\vec{r},t) = \int dt' \int d^3\vec{r}\,'\chi(\vec{r},t,\vec{r}\,',t')v_{ext}(\vec{r}\,',t'), \tag{2.141}$$

where $\chi(\vec{r},t,\vec{r}\,',t')$ is the response function of the interacting system. We drop spatial variables and move to frequency domain

$$\delta\rho(\omega) = \chi(\omega)\delta v_{ext}(\omega). \tag{2.142}$$

We define the effective potential as

$$\delta v_{eff} = \delta v_{ext} + \delta v_{HXC}. \tag{2.143}$$

Then, we can reduce eq. 2.142 to

$$\delta\rho(\omega) = \chi_0(\omega)\delta v_{eff}(\omega). \tag{2.144}$$

The clear advantage of eq. 2.144 with respect to eq. 2.142 is that for the system of noninteracting electrons the response function $\chi_0(\omega)$ is given by

$$\chi_0(\omega) = \sum_{n,m}(f_n - f_m)\frac{\phi_n^*(\vec{r})\phi_m(\vec{r})\phi_m^*(\vec{r}\,')\phi_\rho(\vec{r}\,')}{\omega - (E_m - E_n) + i\varepsilon}. \tag{2.145}$$

By combining eqs. 2.142-2.144 it can be shown that

$$(1 - K\chi_0)\delta V_{eff} = \delta V_{ext}, \tag{2.146}$$

where $K = \frac{\delta v_{HXC}}{\delta n}$ is called the exchange-correlation kernel. This equation is called the Petersilka-Gossman-Gross equation and it is the fundamental equation of LR-TDDFT.

The ground state Kohn-Sham wavefunctions are produced as a linear combination of atomic orbitals (LCAO):

$$\phi_n(\vec{r}) = \sum_a X_n^a f^a(\vec{r} - \vec{r}_a), \tag{2.147}$$

where X_n^a is the expansion coefficient, f^a is the atomic orbital function, $\vec{r}_a$ is the position of the atom corresponding to the atomic orbital f_a. In eq. 2.145 products of wavefunctions appear. Thus, in order to obtain a compact representation of χ_0 it is essential to express orbital products compactly. This is achieved by using the product vertex ansatz following[47]

$$f_a f_b = V_\mu^{a,b} F^\mu, \tag{2.148}$$

where $V_\mu^{a,b}$ are the so-called vertex coefficients and F^μ are the dominant products. Such product basis can be formed in many ways. Here, we use the procedure outlined by Koval et al.[47] that enables reducing the dimensionality of the product basis by finding the dominant orbital products that contribute the most to the completeness of the product basis and re-expressing them using atom-centered product functions.

Thus, χ_0 can be expressed using the product vertex ansatz as

$$\chi_0(\vec{r}, \vec{r}\,', \omega) = \sum_{\mu,\nu} F^\mu(\vec{r})\chi^0_{\mu,\nu}(\omega)F^\nu(\vec{r}\,'), \tag{2.149}$$

where

$$\chi^0_{\mu,\nu}(\omega) = (f_n - f_m)\frac{(X^n_a V^{a,b}_\mu X^m_b)(X^m_c V^{c,d}_\nu X^n_d)}{\omega - (E_m - E_n) + i\varepsilon}. \tag{2.150}$$

This enables to rephrase eq. 2.146 as a linear equation system for the effective potential coefficients that can be solved numerically

$$\left[\delta_{\mu\nu} - K^{\mu\mu'}_{\mathrm{Hxc}}\chi^0_{\mu'\nu}(\omega)\right]\delta V^\nu_{\mathrm{eff}}(\omega) = \delta V^\mu_{\mathrm{ext}}(\omega). \tag{2.151}$$

The key observable studied in this work is the polarizability. The xx component of α is defined as

$$\alpha_{xx} = \int d^3\vec{r} d^3\vec{r}\,' x \chi(\vec{r}, \vec{r}\,', \omega) x'. \tag{2.152}$$

We also study the linear response density matrix $\rho^{(1)}$, which is basically the Kohn-Sham representation of the charge density,

$$\delta\rho(\mathbf{r}, \omega) = \sum_{i,j} \psi_i(\mathbf{r})\psi^*_j(\mathbf{r})\delta\rho^{(1)}_{ij}(\omega). \tag{2.153}$$

In this work we use PyNAO as an implementation of TDDFT. The details of the method can be found in.[47]

Chapter 3

Nanoantennas

The term nanoantennas was coined by Novotny to emphasize the analogy between interaction of light with small (subwavelength) objects and radio antennas. At the same time, the concept dates back to Edward Synge who wrote to Einstein about how a tiny particle could be able to convert propagating waves to a localized field interacting with surrounding matter.[48] In a similar manner to a classical antenna, a nanoantenna is able to directionally scatterer light from nearby and distant light sources. The key difference between the two is the relevant length scale.

Radio antennas utilize radio waves with wavelength on the order of meters, which correspond to frequencies at which metals can be approximated as perfect electric conductors. In contrast, nanoantennas are used for wavelengths ranging from UV to near infrared, approximately 300 - 2000 nm, where metals tend to have non-negligible dispersion. When shaped into nanoscale objects certain metals such as silver, gold and aluminium support localized surface plasmon resonances leading to deeply subwavelength localization of light and a set of unique physical properties. For exceptionally small nanoparticles, quantum effects can also be of interest. The localized surface plasmon resonance is shaped to a large extent by the nanoantenna size and geometry.[49] This aspect can be tailored almost arbitrarily due to substantial progress in fabrication techniques over recent decades. Freedom of designing optical properties with plasmonic resonances has led to a plethora of plasmonic devices. Recently, high-index dielectrics have been proposed as an alternative material platform for nanoantennas.[50] Especially semiconductor nanoantennas are considered in this thesis due to the fact they exhibit a rich amount of various multipolar resonances leading to interesting effects related to multiple scattering.

This chapter is structured as follows. First, the classical notion of resonance is revisited in the context of nanoantennas. Then, plasmonic and high-index dielectric nanoantennas are reviewed as material platforms for nanophotonics including their basic optical properties and selected applications. In the case of plasmonic nanoparticles, quantum effects and hot electron generation are emphasized. Finally, core-shell particles are discussed along with selected numerical aspects of theoretical investigation of nanoantennas.

3.1 Plasmonic nanoantennas

Plasmonic nanoantennas gained interest due to strongly enhanced electromagnetic fields and high scattering and absorption efficiencies resulting from localized surface plasmon resonances. Applications of plasmonic nanoparticles include, among many, refractometric sensing and plasmon enhanced catalysis described in more detail in the Introduction. Here, we briefly summarize other applications specific to plasmonic nanoparticles. The enhanced near fields may be used to enhance light-matter interactions in a variety of spectroscopic techniques including surface enhanced Raman spectroscopy, fluorescence and absorption spectroscopies.[51] Recent progress in sculpting the near-field of plasmonic nanoparticles enabled reaching the strong light-matter coupling regime.[52]

Plasmonic nanoparticles have found applications in photovoltaic devices enabling light management and sculpting of optical absorption in the active medium of a solar cell. Consequently, a reduced amount of active material may be used, reducing material costs, facilitating deposition of solar cells onto flexible substrates and integration into smart windows.[53] Examples of nanoparticle integration into solar cells can be found in all types of thin film devices including: chalcopyrate,[54] perovskite[55] and organic solar cells.[56] Miscellaneous applications of plasonic nanoantennas include structural colors,[57] thermoplasmonics (including radiative cooling),[58] superresolution imaging[59] among others. It is worth noting, that while in this work we focus on highly symmetric plasmonic nanoantennas (spheres, spheroids, disks, etc.), advanced light manipulation is possible by using complex antenna shapes including e.g. V-shaped antennas, split-ring resonators, or even more complex ones (dimers, trimers etc.).

The remaining part of this section is dedicated to a theoretical description of basic properties of plasmonic nanoantennas. Also, a brief review of concepts related to hot electron generation in plasmonic nanoantennas and quantum plasmonics is provided.

3.1.1 Polarizability of plasmonic spheres

Having outlined the general properties of nanoresonators we would like to study the electrodynamics of an optically small sphere, which is assume to be a model nanoresonator. In the limiting case of the sphere radius approaching zero one can treat the incident field as static. At the same time, to account for material dispersion, permittivity for a finite frequency will be used. Such an approximation is called quasi-static. In the limiting case of a static electric field there is no magnetic response, however the oscillating electric field induces a magnetic field and so for sufficiently large spheres a magnetic response should also be observed. For a static electric field, the wave equation reduces to the Poisson equation. It has the following analytical solution[34] which relates the internal field ($\vec{E}_{\text{int}}$) to the external one ($\vec{E}_{\text{ext}}$)

$$\vec{E}_{\text{int}} = \frac{3}{\epsilon + 2}\vec{E}_{\text{ext}}, \tag{3.1}$$

where ϵ is the relative permittivity of the material of the sphere.

In the quasi-static approximation the internal field is spatially uniform, while the field outside is equal to that of an induced dipole. The equation for the external field ($\vec{E}_{\text{out}}$) is given by

$$\vec{E}_{\text{out}} = \vec{E}_{\text{ext}} + \frac{3\vec{n}(\vec{n}\cdot\vec{p}) - \vec{p}}{4\pi\varepsilon_0}\frac{1}{r^3}. \tag{3.2}$$

The induced dipole moment is proportional to the polarizability (see eq. 2.95), which in the limit of a vanishingly small particle radius is equal to[31]

$$\alpha_{QS} = 3\varepsilon_0 V\frac{(\varepsilon - 1)}{(\varepsilon + 2)}. \tag{3.3}$$

The quasi-static polarizability approaches infinity if $\varepsilon + 2 = 0$, which is called Froelich condition. This implies that for small spheres the resonance can be observed only if the signs of the permittivities of the host and sphere media differ. This happens typically for metallic nanoparticles. For a Drude metal this equation can be written as

$$\frac{\alpha_{QS}}{4\pi\varepsilon_0 R^3} = \frac{\frac{(\varepsilon_\infty - 1)}{(\varepsilon_\infty + 2)}(\omega^2 + i\gamma\omega) - \tilde{\omega}_p^2}{(\omega^2 - \tilde{\omega}_p^2) + i\gamma\omega} \tag{3.4}$$

with

$$\tilde{\omega}_p = \frac{\omega_p}{\sqrt{\varepsilon_\infty + 2}}, \tag{3.5}$$

which for an electron gas ($\varepsilon_\infty = 1$) reduces to $\tilde{\omega}_p = \frac{\omega_p}{\sqrt{3}}$. Furthermore, eq. 3.4 stipulates that neither the resonance wavelength nor the width depend on size. This is characteristic for a material resonance, whose amplitude is proportional to the sphere volume.

As an example we show the intensity distribution for a 5 nm sphere made out of a Drude material mimicking silver in Fig. 3.1. The incident field propagates

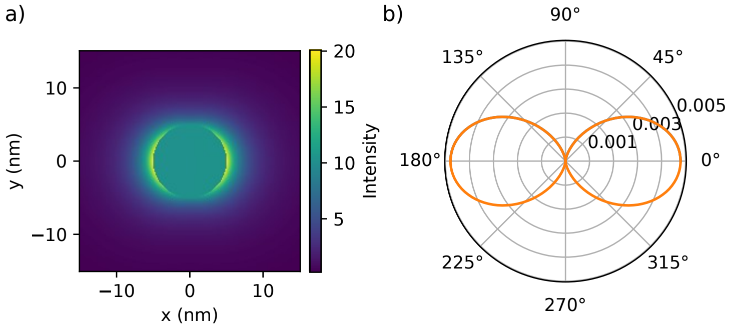

Figure 3.1: a) Electric field distribution in the vicinity of a 5 nm Drude sphere b) far-field distribution for the same sphere in x-z plane (0° corresponds to z direction).

along the z-axis, it is polarized in the x-direction and its wavelength matches the localized plasmon resonance condition eq. 3.5. The near field close to the sphere is enhanced mostly along the x-axis. The maximal enhancement is approximately 20. The far field calculated in the $x-z$ plane resembles a typical dipolar pattern. Its maximum is perpendicular to the polarization axis. In contrast, for the near field the maximum electric field is obtained along the polarization axis.

For increasingly larger spheres the resonance wavelength shifts towards the red and to describe this observation a different approximation is required. The polarization of a sphere can be approximately determined by a self-consistent calculation in which the depolarization field is determined by assigning an elementary dipole moment to a volume element inside the particle and integration of the generated field over the particle volume.[60] The resulting polarizability is then

$$1/\alpha_{mlwa} = 1/\alpha_{\text{QS}} - \frac{k^2}{4\pi\varepsilon_0 r} - \frac{2}{3}i\frac{k^3}{4\pi\varepsilon_0}. \tag{3.6}$$

The two terms which expand the result beyond the quasi-static approximation can be understood as follows. The first term corresponds to dynamic depolarization resulting from the fact that the field generated by elementary dipoles depends on the wavenumber in contrast to eq. 3.1. The second term is called radiative reaction. It is required in order to ensure energy conservation. The power dissipation via scattering requires work to be exerted on the oscillating charges. This intuitive result is called the modified long wavelength approximation (MLWA). It is worth noting that in order for MLWA to be valid the field inside the sphere has to be uniform.[61]

By substituting Eq. 3.3 into Eq. 3.6 the MLWA for spherical particles can be

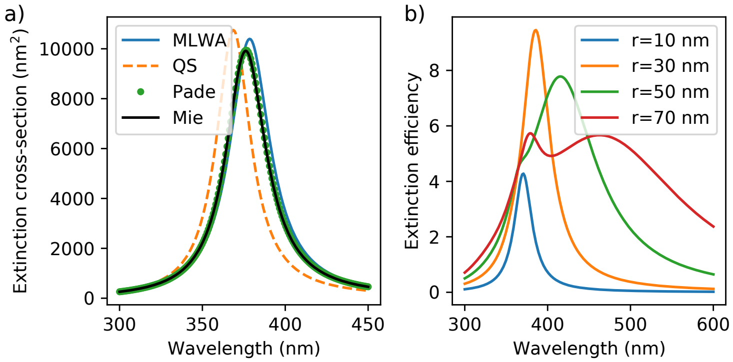

Figure 3.2: a) Extinction cross-section spectrum of a Drude sphere with 20 nm radius. Various approximate results are presented for comparison. b) Extinction efficiency spectra of Drude spheres with varying radii calculated with Mie theory.

obtained

$$\alpha_{\mathrm{mlwa}} = 4\pi\varepsilon_0 r^3 \frac{(\varepsilon-1)}{(\varepsilon+2-(\varepsilon-1)x^2 - i\frac{2x^3}{3}(\varepsilon-1))}, \tag{3.7}$$

with $x = kr$ being the size parameter. The resonance condition is now modified and it is observed at increasingly larger wavelengths as the size of the particle increases.

3.1.2 Mie theory

While the preceding approximations give physical insight into the properties of nanoresonators, they tend to be inaccurate for large particles. However, for spherical particles one can resort to use of Mie theory, which is an analytical solution for the scattering properties of a spherical particle. There are several routes towards Mie theory, but one that is especially convenient in the context of this thesis is by using the T-matrix approach. By invoking the orthogonality of vector spherical wavefunctions it is possible to perform the integrals analytically to obtain the elements of the Q matrices. Because the matrices are diagonal, the calculation of the T-matrix is simple and leads to analytical results. It is worth noting that while expressions cannot be explicitly evaluated without using numerical tools, they can be accurately approximated using e.g. Pade approximations. For the electric dipole, the approximate Mie coefficient is

$$a_1^P \approx -\frac{2}{3} i \frac{\varepsilon_1 - 1}{\varepsilon_1 + 2} \frac{x^3}{\left(1 - \frac{3}{5}\frac{\varepsilon_1-2}{\varepsilon_1+2}x^2 - \frac{2}{3}i\frac{\varepsilon_1-1}{\varepsilon_1+2}x^3\right)}. \tag{3.8}$$

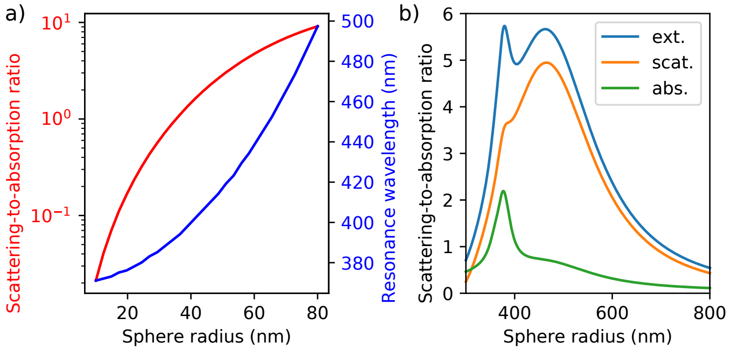

Figure 3.3: a) Resonance wavelength and scattering-to-absorption ratio of Drude spheres. b) Comparison of scattering, absorption and extinction spectra for Drude sphere with 70 nm radius.

The electric dipole polarizability of a sphere is proportional to the Mie coefficient and is equal to

$$\alpha_e = i\frac{6\pi\epsilon_0}{k_0^3}a_1. \tag{3.9}$$

A comparison of various approximations is presented in Fig. 3.2. Even at a relatively small size (20 nm radius) both the quasi-static approximation and the MLWA fail to exactly match the result from Mie theory, but the MLWA is a considerable improvement over the quasi-static approximation. The Pade approximation for this size matches the Mie theory result, but also fails if the size parameter is sufficiently large.

An example of scattering, absorption and extinction spectra for a Drude sphere with 70 nm radius are presented in Fig. 3.3. The electric dipole resonance for this sphere is relatively broad and predominantly scattering. The electric quadrupole is also present in the spectrum with a resonance at a shorter wavelength than that of the electric dipole. In contrast to the electric dipole resonance, the quadrupolar mode is mostly absorptive, which is typical for higher order resonances in nanostructures.

3.1.3 Shape related effects

In the quasistatic approximation, a spheroidal deviation of the shape from spherical can be accounted for by including a geometry-dependent dyadic L, which

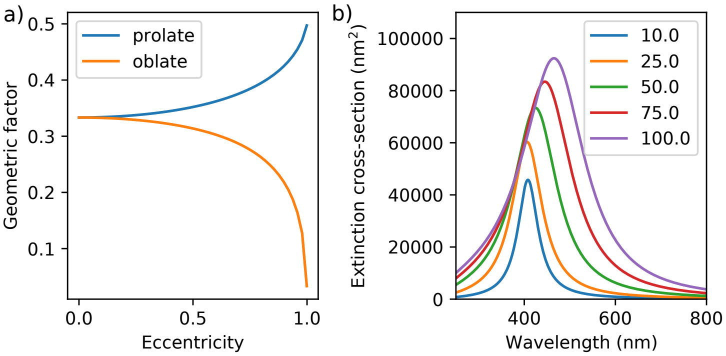

Figure 3.4: a) Geometric factor L_{xx} for oblate and prolate spheroid as a function of eccentricity, b) Drude spheroids with a fixed value of a semiaxis at 50 nm and varying b semiaxis.

leads to the following expression for the polarizability,[62]

$$\alpha(\omega) = \frac{4\pi a^2 c}{3}\varepsilon_0 \frac{\varepsilon(\omega) - 1}{1 + L[\varepsilon(\omega) - 1]}, \tag{3.10}$$

where a is the semi-axis in the $x - y$ plane and c is the distance from center to pole along z-axis. L is diagonal for spheroids with $L_x + L_y + L_z = 1$.

Typical shapes considered with this approach is are prolate and oblate spheroids. They differ by the symmetry axis, which is aligned with the major axis for prolate spheroids, while for oblate ones it is aligned with the minor axis. We assume that the symmetry axis is aligned with z, while the polarization of incident light is along x-axis. The geometric factor for a prolate spheroid is[31]

$$L_x = \frac{2e^2 - 1}{2e^2}\left(-1 + \frac{1}{2e}\ln\frac{1+e}{1-e}\right) \quad e^2 = 1 - \frac{a^2}{c^2}, \tag{3.11}$$

while for oblate spheroid it is

$$L_x = \frac{g(e)}{2e^2}\left[\frac{\pi}{2} - \tan^{-1} g(e)\right] - \frac{g^2(e)}{2}, \tag{3.12}$$

with

$$g(e) = \left(\frac{1-e^2}{e^2}\right)^{1/2} \tag{3.13}$$

and eccentricity e defined as

$$e^2 = 1 - \frac{c^2}{a^2}. \tag{3.14}$$

The geometric factor as a function of eccentricity is plotted in Fig. 3.4a. Eccentricity varies from zero to one and it determines the deviation of the spheroid shape from spherical (for $e = 0$ the spheroid reduces to a sphere). Because the internal field of a spheroid in the quasi-static limit is uniform, similarly to that of a quasi-static sphere, MLWA can be obtained in a similar manner to the case of a spherical particle[61] (see eq. 3.6). Extinction spectra obtained using MLWA for Drude spheroids with a fixed value of the a semiaxis at 50 nm and a varying b semiaxis are shown in Fig. 3.4b. With increasing elongation of the spheroid, the amplitude of the extinction cross section increases due to increasing volume, while the resonance wavelength is red shifted due to varying L.

An important shape related effect is generation of exceptionally large electric field enhancements in the vicinity of sharp features of plasmonic nanoparticles. These so-called hot-spots are sought after in many applications of plasmonics. Using chemical methods it is possible to synthesize a variety of nanoparticle shapes that support such hot-spots including star-shaped and prism-shaped nanoparticles.[63] A different route towards hot-spots is offered by placing a nanoparticle in a complex environment such as a metallic mirror forming the so-called nanoparticle-on-mirror system or another particle forming a nanoparticle dimer. Small gaps in these systems are where the hot spot is typically located. It is worth noting that when such gaps are atomically small they require quantum treatment, as a singular response may be obtained in a classical calculation in the limit of near-zero gap size.[64]

Finally, it is worth mentioning that for certain applications of nanoantennas symmetry breaking is required that may not be attainable with simple shapes such as sphere or a disk. The first class of shapes are V and L shapes that break symmetry in the $x - y$ plane making such antennas useful for polarization conversion. Hence such structures are representative for a large clase of so-called metasurfaces.[65] The second type are split ring resonators. Their shape enables obtaining a strong magnetic dipole moment in a plasmonic nanostructure that otherwise tends to support electric resonances only.[66] This feature is essential for tailoring the response of the magnetic part of the electromagnetic field.

3.1.4 Quantum aspects of plasmonics

The original motivation to analyze the plasmonic properties of metal nanoparticles using quantum mechanical calculations was the inconsistency of theoretical predictions with experimental results for nanoparticles smaller than 10 nm. In the classical quasi-static approximation the resonance position of a plasmonic nanoparticle does not depend on its size, while the intensity of the absorbed light is proportional to the volume. However, experiments have shown for sufficiently small nanoparticles a shift of the resonance toward higher energies with respect to the classical quasi-static result.[67] This effect was initially taken into account by adding a phenomenological term in the classical metal permittivity model associated with electron density extending beyond the metal surface (the so-called spill-out effect). Currently, many models have been proposed that include the results of quantum mechanical calculations in permittivity of the metal, often of a non-local nature.[68] It is also possible to determine light absorption spectra of nanoparticles directly from quantum mechanical calculations. In the case of plasmonic metal clusters with the number of atoms below 600 (sizes below 5 nm), one observes additional features in the optical spectra, the source of which are discrete electronic transitions.[69]

Another case, for which quantum mechanical effects are important in plasmonic nanostructures, occurs when the nanoparticles forming a system are at distances at which transport of charges is allowed by tunneling. A dimer composed of identical nanoparticles can be considered the simplest example. In the classical description of this system, as the gap shrinks and mutual coupling increases, its dipole resonance shifts towards lower energies, and in the case of very small distances higher-order modes appear. An important feature is also amplification of the electric field inside the cavity formed in this way, which classically can achieve unexpectedly high values when the nanoparticles are closer than 1 nm. This is the distance at which tunneling occurs, but it is not captured by the classical model.[70] Recent achievements related to the development of quantum mechanics computational methods now allow the determination of the optical properties of dimers in the tunneling regime. It turns out that the atomic structure of the studied nanoparticles is significant on this scale.[71] Advanced quantum mechanical calculations allow the tracking of nanojunction and nanocavity formation and the impact of the charge transport (including tunnel tranpsort) on the optical properties of nanostructures.[72] In the regime in which the tunnel transport does not occur, the effects associated with atomic structure can be partially taken into account by classical electrodynamics while maintaining a realistic atomic scale shape of nanoparticles.[73]

3.1.5 Hot electrons

Hot electrons are electrons with energies larger than that of thermally excited ones at given ambient temperature.[16] Such electrons may be generated in metals and semiconductors due to electron excitation by absorbed light. Metallic surfaces and nanoparticles typically reflect light efficiently without significant absorption. However, for plasmonic nanoparticles the scattering-to-absorption ratio decreases with nanoparticle size and if a nanoparticle's size is sufficiently small, absorption dominates over scattering. As we will show in the reminder of this thesis, non-radiative decay of plasmons in small nanoparticles leads to hot carrier generation.

The main applications of hot electrons generated in plasmonic nanoparticles are photocatalysis[74] and photodetectors.[75] In both cases, hot electrons increase the process efficiency and thus their generation is a subject of substantial research. Generation of hot carriers has been attributed as the mechanism behind several examples of plasmon mediated catalysis including hydrogen dissociation on Au nanoparticles,[5] photocatalytic water splitting on Au/TiO_2 films,[76] and CO oxidation.[77] Here, we outline the main results and concepts related to modelling of hot electron generation in plasmonic nanoparticles.

An early theoretical study of hot electron generation in plasmonic nanoparticles has been presented by Manjavacas et al.[78] In this work a free electron model has been used in which the incident electric field and the scattered electric field by a plasmonic nanoparticle are treated as classical fields. The electron dynamics in this model are obtained using Fermi's golden rule with initial and final (excited) states being determined by solving the Schroedinger equation for a spherical potential well. In order to include various plasmon decay mechanisms, a phenomenological decay time constant of 10 fs is introduced. Using this model, the authors calculate the number of generated hot carriers as a function of various system parameters including, among others, excitation frequency, nanoparticle diameter and carrier lifetime. They conclude that the optimal illumination wavelength is that matching the LSPR wavelength. Also, increasing nanoparticle size results in a larger number of generated carriers, but with lower energy. The same tendency is observed for increasing carrier lifetime.

Besteiro et al. have studied the impact of permittivity and particle shape on hot electron generation.[79] In his approach, the generation of hot electrons is a consequence of plasmon dephasing resulting from intra- (Drude) and interband transitions, as well as surface scattering (including hot spot regions). The results indicate that the latter dephasing mechanism enables quantum transitions of electrons to high energy states. The hot electron generation rate requires a combination of an enhancemed near field (a classical phenomenon) and efficient surface scattering described in a quantum mechanical manner. Similarily to Manjavacas et al., the authors observed that smaller nanoparticles tend to be more suitable for efficient hot electron generation. Also, nanoparticles with sharp features are favorable as they feature prominent plasmonic hot spots.[80]

Due to the fact that efficient hot electron generation necessiates small nanoclusters exhibiting quantum size effects, quantum approaches such as TDDFT[81,82] and GW[83] methods have been used to study plasmon dephasing leading to hot electron generation. The first approach to plasmon dephasing that describes the electronic system in a full quantum manner has been proposed by Jie Ma et al.[82] Using TDDFT with propagation in real time (RT-TDDFT), they have studied the evolution of electrons in small silver clusters (typically composed of 55 silver atoms) excited by a Gaussian pulse with a central frequency matching that of the plasmon resonance. In order to differentiate the electronic transitions corresponding to the plasmon resonance from single particle excitations characteristic of hot electron generation, the authors show that transition coefficients corresponding to single particle excitations vary slowly, so that the oscillation of the charge density matches the excitation frequency. At the same time, the plasmon is composed of rapidly oscillating transitions that are off-resonant and exhibit a collective behavior that cannot be described by a single particle excitation approximation. The results indicate that the electronic structure of the ground state is of critical importance when it comes to hot electron generation. In silver clusters, hot electrons are generated due to transitions to the LUMO from a plethora of states below the Fermi energy which are resonant excitations. When these states are artificially detuned from the plasmon frequency, the dipole amplitude exhibits Rabi oscillations between the collective mode and the plasmon, while the energy stored in each transition type does not change significantly in time. Interestingly, the authors have also shown that electron-phonon interactions do not influence significantly the plasmon dephasing process.

In a more recent work, Rossi et al.[81] analysed the linear response density matrix obtained using RT-TDDFT to study the impact of atomic structure on the process of hot electron generation. Using Voronoi decomposition of the induced charge density, they have been able to obtain spatially resolved energy distributions of occupation probability. The results indicate that the carrier energy distributions are dependent on both the shape and size of the atomic cluster. More importantly, they are also dependent on the presence of sharp features such as corners and edges that are regions of the most efficient hot carrier generation. Correct modeling of these kind of effects necessitates a quantum approach.

Here, we focus on the theoretical framework that was presented in the recent work by Rossi et al.,[81] because it provides useful information on plasmon formation and its subsequent dephasing. Furthermore, it gives the resulting hot electron generation from the linear response density matrix, which can be calculated using linear response TDDFT in frequency domain employing codes such as PyNAO described in the previous chapter. In the article 81, a dimensionless time-depedent density matrix is defined as

$$q_{ia}(t) = \frac{2\Re\delta\rho_{ia}^{(1)}(t)}{\sqrt{2\left(f_i - f_a\right)}}, \qquad p_{ia}(t) = -\frac{2\Im\delta\rho_{ia}^{(1)}(t)}{\sqrt{2\left(f_i - f_a\right)}}. \tag{3.15}$$

Decomposition of stored energy into contributions from resonant and non-resonant transitions is an indicator of plasmon formation and dephasing. The contribution from a particular ia Kohn-Sham transition to the stored energy is given by

$$E_{ia}(t) = \frac{1}{2}\left[p_{ia}(t)\dot{q}_{ia}(t) - q_{ia}(t)\dot{p}_{ia}(t) - v_{ia}(t)q_{ia}(t)\right], \tag{3.16}$$

where v_{ia} is the pulse potential represented in the Kohn-Sham orbital basis.

In order to find the hot electron distribution, occupation probabilities for electrons are necessary. It is defined as

$$P_a^{\mathrm{e}}(t) = \sum_i^{f_i > f_a} P_{ia}(t), \tag{3.17}$$

where P_{ia} is the transition probability determined using the density matrix,

$$P_{ia}(t) = \left| \frac{\delta \rho_{ia}^{(1)}(t)}{\sqrt{f_i - f_a}} \right|^2 . \tag{3.18}$$

This gives the electron energy distribution as

$$P_e(\epsilon) = \sum_a P_a^e \delta\left(\epsilon - \epsilon_a\right) = \frac{1}{2} \sum_{ia}^{f_i > f_a} \left(q_{ia}^2 + p_{ia}^2\right) \delta\left(\epsilon - \epsilon_a\right). \tag{3.19}$$

3.2 Dielectric nanoparticles

Plasmonics as a material platform for nanoantennas is hindered by certain limitations. The most important one is material losses, which are substantial even for noble metals in the visible range. Although these losses may be used for certain applications such as plasmonic heating or hot electron generation for catalysis, they are generally unwanted, causing Ohmic losses and reducing overall device efficiency. Another notable disadvantage is lack of a magnetic response for particles with simple geometries such as spheres or disks. Consequently, if manipulating the magnetic component of light is of interest, nanoantennas with complex shapes such as split ring resonators are necessary, increasing fabrication complexity. One promising alternative to plasmonics is the application of high index dielectrics or semiconductors such as silicon, germanium or gallium arsenide. In the near infrared range those materials are almost absorption free. Also, semiconductors are typically used in electronics facilitating the compatibility of nanoantennas with electronic devices. Lastly, high index dielectric nanoantennas support a plethora of multipolar resonances making them a valid platform for near arbitrary manipulation of light.

3.2.1 Magnetic response of a dielectric sphere

The key difference between dielectric and plasmonic nanoparticles is the presence of a strong magnetic response from high-index dielectric particles even in simple shapes such as spheres. In contrast, and as mentioned before, formation of a magnetic resonance in a plasmonic structure requires complex shapes. Although other approaches are possible (see e.g. a quasi-static description with radiative correction[84]), a simple description of the magnetic dipole can be obtained using a Pade approximant to the corresponding Mie coefficient,

$$b_1^P \approx -i\frac{\varepsilon_1 - 1}{45}\frac{x^5}{\left(1+\frac{1}{21}\left(5-2\varepsilon_1\right)x^2+\left[x^4\right]-i\frac{1}{45}\left(\varepsilon_1-1\right)x^5\right)}, \tag{3.20}$$

with the truncated term being

$$\left[x^4\right] = -\frac{\varepsilon_1^2+100\varepsilon_1-125}{2205}x^4. \tag{3.21}$$

Interestingly, eq. 3.20 leads to the following condition for magnetic dipole resonance

$$\varepsilon_1 = -2.07+\frac{10.02}{x^2}+1.42x^2-2ix\left(1.06-0.77x^2\right). \tag{3.22}$$

The polarizability of the magnetic dipole is calculated in a similar manner to that of electric dipole

$$\alpha_m = i\frac{6\pi}{k^3}b_1. \tag{3.23}$$

Observation of magnetic dipole resonances requires high refractive index or large size due to the x^5 proportionality of the corresponding Mie coefficient.

The presence of an additional resonance in the spectrum, especially of magnetic character, gives a much larger freedom to tailor the scattered field patterns of dielectric nanostructures. The scattering directionality has been extensively studied in recent years. It has been shown that scattering suppression in the forward or the backward direction, called the Kerker effect, can be obtained by multipolar interference. While, it is possible to achieve this effect by interference of higher order multipoles, here we focus on dipolar modes as they are dominant in the studied structures. The total scattered field in the far field approximation produced by the two (magnetic and electric) dipoles is[85]

$$\vec{E}_{s\infty} = \vec{E}^p_{s\infty}+\vec{E}^m_{s\infty} = \frac{k^2}{4\pi\epsilon_0}\left[\hat{r}\times\left(\vec{p}\times\hat{r}\right)+\frac{1}{c}\vec{m}\times\hat{r}\right]. \tag{3.24}$$

In spherical coordinates this equation can be reduced to

$$\vec{E}_{s\infty}(\theta,\phi) = \frac{k^2}{4\pi\epsilon_0}\left[\left(\frac{m_i}{c}+p_i\cos\theta\right)\cos\phi\hat{\theta}-\left(p_i+\frac{m_i}{c}\cos\theta\right)\sin\phi\hat{\phi}\right]. \tag{3.25}$$

Using equations 3.9 and 3.23, the scattered far field can be expressed in terms of Mie coefficients,

$$\vec{E}_{s\infty}(\theta,\phi) = \frac{3i}{2k}E_0\left[\left(b_1+a_1\cos\theta\right)\cos\phi\hat{\theta}-\left(a_1+b_1\cos\theta\right)\sin\phi\hat{\phi}\right]. \tag{3.26}$$

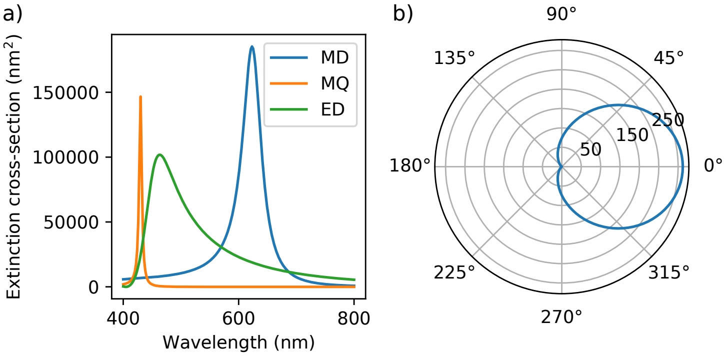

Figure 3.5: a) Multipole decomposed extinction spectrum of a high-index dielectric ($n = 4$) sphere with 75 nm. b) Differential scattering cross-section at 687 nm wavelength corresponding to Kerker condition.

In order to obtain the Kerker conditions for suppressing scattering, eq. 3.26 has to be analyzed in the forward and the backward scattering directions. In the forward direction ($\theta = 0$) this expression reduces to

$$\vec{E}_{s\infty}(\theta,\phi) = \frac{3i}{2k}E_0\left[(b_1 + a_1)\cos\phi\hat{\theta} - (a_1 + b_1)\sin\phi\hat{\phi}\right], \tag{3.27}$$

while in the backward direction ($\theta = \pi$) reduces to

$$\vec{E}_{s\infty}(\theta,\phi) = \frac{3i}{2k}E_0\left[(b_1 - a_1)\cos\phi\hat{\theta} - (a_1 - b_1)\sin\phi\hat{\phi}\right]. \tag{3.28}$$

Consequently, by tailoring the relative amplitude of the electric and magnetic dipole it is possible to suppress forward or backward scattering when

$$a_1 + b_1 = 0 \tag{3.29}$$

or

$$a_1 - b_1 = 0 \tag{3.30}$$

is fulfilled, respectively. These conditions, called the Kerker conditions,[85] can be fulfilled by a high-index dielectric sphere as shown in Fig. 3.5a. The corresponding scattering patterns are also presented Fig. 3.5b.

3.2.2 Silicon nanodisks

The useful aspect of dielectric photonics is manipulation of the multipolar resonances by simple tailoring of the geometrical parameters of the nanoresonator.

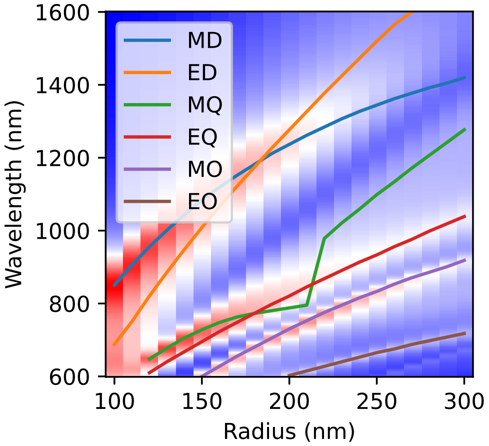

Figure 3.6: Extinction spectra of high-index dielectric ($n = 3.5$) nanodisks for a fixed height of 220 nm and varying radius immersed in a low-index dielectric ($n = 1.33$). Multipole resonance wavelength are marked with solid lines.

One particularly important example is the aspect ratio of nanodisks that enables the modification of the relative position of electric and magnetic dipole resonances.[86] When the aspect ratio ($AR = H/D$ with height H and diameter D) is close to unity, a spectrum reminiscent of that of a sphere is observed. As shown in Fig. 3.6 for very flat disks, the electric dipole resonance is observed for a larger wavelength than the one of the magnetic dipole resonance. The two resonances overlap once the aspect ratio approaches 0.76. This results in simultaneous fulfilling of the Kerker condition leading to suppressed backscattering and a strong resonant optical response.[86] Note, that other multipoles are also affected by aspect ratio modification.

Semiconductor nanodisks feature several traits making them a favorable nanoantennas for a variety of applications and observation of certain physical phenomena. Typically, they are used in the near infrared, a spectral region in which silicon exhibits simulatneously low losses and high refractive index. A broken crystalline structure symmetry of III-V semiconductors such as gallium arsenide enables highly efficient second harmonic generation that can be manipulated by forming nanoantennas out of these materials.[87] Other nonlinear processes e.g. third harmonic generation have also been realized and shaped using dielectric nanoantennas.[88,89] Similarly to plasmonic antennas, all dielectric nanoresonators can be also used to control emission from various light sources such as quantum dots or 2D materials.[90] Metasurfaces based on silicon nanodisks are excellent for enhancement of molecular circular dichroism due to the possibility of electric and magnetic dipole resonance overlap leading to preservation of light helicity upon scattering, while maintaining a strong optical response, which are the two factors essential for large enhancements.[91]

3.3 Core-shell particles

Core-shell nanoparticles are structures whose core, made of one material (in essence a single material nanoparticle), is coated by a layer of another material, the shell.[92] It is a subclass of heterogeneous nanoparticles that also includes alloy nanoparticles and Janus nanoparticles. The initial goal of obtaining core-shell nanoparticles was to physically separate the core nanoparticle from the environment or to chemically passivate the nanoparticle surface. Notable examples include a PMMA coating that is an effective gas barrier, but is permeable to hydrogen and hence can be used to form core-shell nanoparticles for catalytic or hydrogen storage applications.[93] For battery applications because, ZnO_2/TiO_2 particles have found use, because TiO_2 is a passivating layer that disables zinc ion migration to the solution.[94] At the same time, TiO_2 is a highly conductive layer that is simultaneously resistant to corrosion.

Core-shell nanoparticles combine the functionalities of the core and shell leading to enhanced tunability by adding more degrees of freedom or can even provide functionalities that cannot be achieved by homogeneous nanoparticles. For example, semiconductor core-shell nanoparticles enable bandgap engineering for tailored fluorescence. Magneto-plasmonic core-shell nanoparticles provide both magnetic and plasmonic properties.[95] At the same, the optical spectra of such nanoparticles are substantially affected by the fact that magnetic cores have very high dielectric permittivities.

The optical properties of core-shell particles are different with respect to those of particles discussed in previous sections. The properties of spherical core-shell particles can be evaluated analytically using extended Mie theory.[31] Theoretical analysis of optical properties of core-shell spheres has been provided by Tzarouchis et al.[96] with a rich numerical analysis in a follow-up paper.[97] The authors observe that the presence of an absorbing semiconductor shell around a plasmonic nanoparticle extends its absorption range. Both magnetic and electric resonances can be observed leading to the Kerker effect, but it is not possible to easily assign the resonances either to the core or the shell. The Kerker effect in core-shell nanoparticles can be much broader than in homogeneous spheres.[98] Large tunability of the relative spectral positions of multipoles in Ag-Si nanodisks has lead to efficient realization of electromagnetic anapoles.[99] It has been also observed that eccentricity of the core part can lead to even further tunability.[100] Notably, in addition to core-shell particles with dielectric shells, nanoparticles

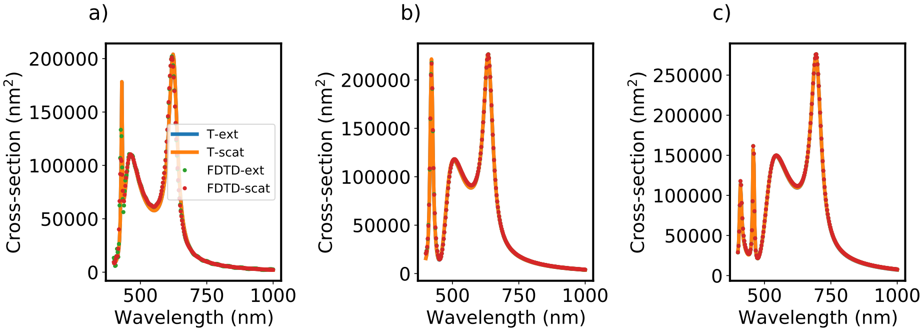

Figure 3.7: Comparison of cross-section spectra between T-matrix method (SMUTHI) and FDTD (Lumerical) for selected nanoparticle shapes with constant refractive index. a) sphere with radius of 75 nm, b) disk with radius of 75 nm and height of 120 nm, c) cube with edge length of 140 nm.

with plasmonic shells have also been realized. They are especially promising for nonlinear optical properties.[101,102] Finally, homogenization of multilayer heterogeneous nanoparticles leads to radial anisotropy that results in enhanced spectral and scattering tailoring.[103] A core-shell like system can also take form of silicon disks with air hole, with the resulting system being good for local enhancement of electromagnetic chirality.[104] In the case of eccentric holes these disks can be used for exciting anapoles or quasi-bound states in the continuum (quasi-BIC)[105] and act as efficient light trapping systems. Similarly, traditional core-shell particles have been considered as light trapping nanoparticles for photovolatic systems.[106]

3.4 Modeling of nanoantennas

In this section we briefly compare the results obtained with different methods described in the previous chapters. For dielectric particles FDTD and T-matrix methods are compared. For plasmonic nanoparticles further comparison is performed with FEM implemented in COMSOL Multiphysics. The T-matrix of an isolated particles is calculated using the null-field method implemented in SMUTHI code.[107] A key new feature in SMUTHI v1.0 is the NFMDS F2Py module developed by the author, which now enables simulation of arbitrarily shaped particles. The method is accurate, especially for dielectric nanoparticles. The main parameter that controls the numerical accuracy of the method is `lmax`, which is the multipole truncation order. The other two parameters (available for aspherical particles) that can be modified are `nint` (number of integration points) and `nrank` (NFMDS internal multipole truncation order).

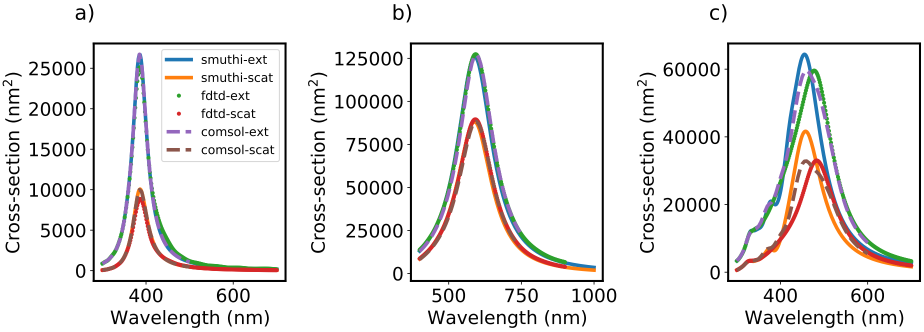

Figure 3.8: Comparison of cross-section spectra between T-matrix method (SMUTHI) and FDTD (Lumerical) for selected nanoparticle shapes with refractive index based upon Drude model with parameters mimicking silver. a) sphere with radius of 30 nm, b) disk with radius of 73.5 nm and height of 25 nm, c) cube with edge lenegth of 75 nm

Here we compare the results for three particles with varying shapes (sphere, disk, cube) for a constant refractive index of 4 and a Drude material mimicking silver presented in Figs 3.7 and 3.8, respectively. For dielectric particles, the comparison between the T-matrix result and spectra obtained with Lumerical FDTD Solutions shows very high accuracy of the T-matrix method. Even for a complicated geometry such as a cube, the agreement is excellent. Also, conservation of energy is satisfied accurately and therefore there is no difference between extinction and scattering cross-sections for non-absorptive material.

Simulations of plasmonic particles are, in general, more difficult to perform accurately due to regions of extraordinarily large field enhancement (hot-spots). To assure a fair comparison, we perform additional simulations with Comsol. For spheres, T-matrix reduces to an analytical solution based upon Mie theory. The results shown in Fig. 3.8a indicate that Comsol reproduces the analytical result better than FDTD. When we change the particle shape to a disk with radius of 73.5 nm and height of 25 nm, we can observe an excellent agreement between all of the tested methods. Notably, in this case NFMDS required a relatively large number of multipoles for the result to converge (on the order of 10). Finally, the comparison for cube-shaped particles indicates that numerical simulations of scatterers with sharp features are exceptionally difficult for plasmonic metals.

Chapter 4

Multiple scattering in optical antenna arrays

In the previous chapter we have focused on the properties of single nanoparticles due to the fact that, from a theoretical standpoint, they are much easier to describe. However, in practical situations nanoparticles are fabricated almost exclusively in the form of arrays or colloids. Also, when an optical experiment is being performed, the number of nanoparticles illuminated by a laser spot is on the order of hundreds of thousands. Therefore, this part of the thesis is dedicated to a literature review of particle arrays with a special focus on two dimensional ones.

4.1 Formulation of the multiple scattering problem

In this section we formulate the scattering problem for multiple particles following works by Egel et al. and Mackowski and Mischenko.[108,109] We assume that the system consists of N particles with positions $(r_1, ..., r_N)$ excited by external illumination $\vec{E}_{inc}$. A further condition that the circumscribing spheres of all particles do not overlap. For now, we also assume that the environment is free space. We will deal with the case of system of nanoparticles embedded in a layered medium later as a generalization of the results provided presently.

The total electric field is a sum of the incident field and the total scattered field

$$\vec{E}(\vec{r}) = \vec{E}_{inc}(\vec{r}) + \sum_i \vec{E}_{scat,i}(\vec{r}). \tag{4.1}$$

The field scattered by each particle $\vec{E}_{scat,i}(\vec{r})$ is expanded into VSWFs with their respective origin being the particle position $\vec{r}_i$

$$\vec{E}_{scat,i}(\vec{r}) = \sum_{l=1}^{\infty} \sum_{m=-l}^{l} b_{lm}^{E} \vec{M}_{lm}^{3}(\vec{r} - \vec{r}_i) + b_{lm}^{M} \vec{N}_{lm}^{3}(\vec{r} - \vec{r}_i). \tag{4.2}$$

In the multiple particle formulation, particles are no longer excited only by the external illumination. Instead, the exciting field ($\vec{E}_{exc}$) consists of the external illumination and the scattered field generated by all the other particles

$$\vec{E}_{exc}(\vec{r}_i) = \vec{E}_{inc}(\vec{r}_i) + \sum_{j \neq i} \vec{E}_{scat,j}(\vec{r}_i). \tag{4.3}$$

Each of these contributions can be expanded into regular VSWFs about the origin of the ith particle following eq. 2.114. The resulting expansions are related

$$\vec{a}^i = \vec{a}_{inc}^i + \sum_{j \neq i} \vec{a}_{scat,j}^i. \tag{4.4}$$

Here, $\vec{a}$ is a vector of the expansion coefficients of the exciting field, $\vec{a}_{inc}$ is a vector of the expansion coefficients of the incident field, and $\vec{a}_{scat,j}^i$ are the regular VSWF expansion coefficients of the scattered field from the jth particle around the position of the ith particle. Finding $\vec{a}_{scat,j}^i$ requires translation of the expansion origin to the ith particle and conversion of the radiating VSWF expansion to the regular VSWF expansion. This is performed by using the particle coupling operator W derived by Mackowski and Mishchenko[109]

$$\vec{a}_{scat,j}^i = W^{i,j} \vec{b}^j. \tag{4.5}$$

The formula for this operator is provided in Appendix A. The scattered field coefficients $\vec{b}^i$ are related to the exciting field expansion coefficients via the single particle T-matrix

$$\vec{b}^i = T^i \vec{a}^i. \tag{4.6}$$

In light of eq. 4.6, the fields scattered by a system of particles are determined by an interplay of the incident field, the properties of individual particles and their spatial distribution.

By inserting eq. 4.5 into eq. 4.6 we obtain the self consistent equation for the scattered field coefficients b^i including multiple scattering via the particle coupling operator W

$$\vec{b}^i = T^i(\vec{a}_{inc}^i + \sum_{j \neq i} W^{i,j} \vec{b}^j). \tag{4.7}$$

For optically small particles the dominant contribution to the optical response of the system comes from dipolar resonances. Then, it is useful to use the Cartesian multipole formulation. Eq. 4.3 is used as a starting point for the self-consistent system of equations for electric and magnetic dipole moments, but instead of a VSWF expansion, a Cartesian multipole expansion (eq. 2.86) is used in tandem with electric and magnetic dipole propagators (eqs 2.106 and 2.110). This way, we obtain the coupled electric and magnetic dipole model in a form proposed by Bendana et al.:[110]

$$\begin{pmatrix}\vec{p}\\ \vec{m}\end{pmatrix} = \frac{1}{\alpha^{-1} - A}\begin{pmatrix}\vec{E}_{ext}\\ \vec{H}_{ext}\end{pmatrix}, \tag{4.8}$$

where A is a block matrix

$$A = \begin{pmatrix}A^{EE} & A^{EM}\\ A^{ME} & A^{MM}\end{pmatrix}, \tag{4.9}$$

with $A^{EE}_{ij} = \frac{k_0^2}{\varepsilon_0}G^{EE}(\vec{r}_i, \vec{r}_j)$, $A^{EM} = \frac{k_0^2}{\varepsilon_0}G^{EM}(\vec{r}_i, \vec{r}_j)$, $A^{MM} = k_0^2 G^{EE}(\vec{r}_i, \vec{r}_j)$, $A^{ME} = -k_0^2 G^{EM}(\vec{r}_i, \vec{r}_j)$ and α is a block-diagonal matrix

$$\alpha = \begin{pmatrix}\alpha_e & 0\\ 0 & \alpha_m\end{pmatrix}. \tag{4.10}$$

The coupled electric-magnetic dipole equation (eq. 4.8) can be further simplified by omitting magnetic response. Then, in the so-caled coupled electric dipole approximation, eq. 4.8 reduces to

$$\vec{p}_i = \alpha_e(\vec{E}_{inc} + \sum_{i\neq j}^{N} A^{EE}_{ij}\vec{p}_j). \tag{4.11}$$

4.2 Introduction to metasurfaces

A metasurface is a two dimensional array of optical antennas designed to achieve a desired optical functionality by an abrupt change of the optical properties at the air-metasurface interface. In comparison to their three-dimensional analogues (called metamaterials), metasurfaces require a lesser fabrication effort, comprise of a smaller amount of material, thus limiting the cost and, perhaps most importantly, decrease propagation in the array, which limits losses.[111] Most typically, metasurfaces are used to introduce a phase gradient at the interface, which occurs by using either the generalized reflection law[111] or the Pancharatnam-Berry phase approach.[112] Phase gradients can be tailored in a way reminiscent of traditional diffractive elements to achieve flat counterparts of traditional bulk optical elements such as lenses[113] or holograms.[114] In contrast to traditional diffractive elements, metasurfaces enable much smaller resolution of phase gradients and provide control over polarization of light.[115] Here, we focus on effects related to multiple scattering in metasurfaces composed of resonant nanoantennas. Electromagnetic coupling that emerges as a consequence of multiple scattering leads to directional scattering effects, additional spectral features or substantial modifications of those existing in noninteracting system. Hence, electromagnetic coupling constitutes a substantial, but often neglected part of metasurface physics. Its state-of-the-art is summarized in this section and extended in the following chapter.

4.2.1 Electromagnetic coupling in periodic metasurfaces

In the first part of this chapter we will focus on periodic arrays, because this is the case which is most feasible for a theoretical analysis and significant literature is available. Also, metasurfaces are most typically arrays of antennas forming a rectangular grid. At the same time, many of the theoretical developments for periodic metasurfaces are applicable to random ones, which are then further developed in the latter chapters of the thesis.

A simple description of the optical properties of periodic nanoparticle arrays has been proposed in Jackson's textbook.[34] He assumed that multiple scattering is negligible and the particles forming the array are identical. Then, one can calculate the scattering spectrum by multiplying a single particle's angular spectrum by the so-called structure factor which depends only on the spatial distribution of the particles. The periodicity of the structure leads to narrow features in the angular spectrum of the array called Bragg peaks. This fact is often applied for analysis of X-ray scattering by crystals.

In arrays of resonant nanoantennas, multiple scattering leads to electromagnetic coupling, which cannot be neglected. Then, the electromagnetic response of the array comes from an interplay between the single particle response and the electromagnetic coupling determined by the spatial arrangement of antennas and the properties of incident illumination. In order to fully describe the optical properties of periodic arrays of small plasmonic nanoparticles, one can consider a dipole approach in which the particles are electromagnetically coupled (eq. 4.11). Assuming that the array is infinite, the polarization of each nanoparticle is identical and for normal incidence, the following equation for the effective polarizability is obtained[116]

$$(\alpha^*)^{-1} = \frac{1}{\alpha} - S, \tag{4.12}$$

where

$$S = \frac{1}{4\pi\varepsilon_0} \sum_{\text{dipoles}} e^{ikr} \left[\frac{(1-ikr)\left(3\cos^2\theta - 1\right)}{r^3} + \frac{k^2 \sin^2\theta}{r} \right]. \tag{4.13}$$

Here, the effective polarizability α_e^* is defined via relation

$$\langle \vec{p} \rangle = \alpha_e^* \vec{E}_{inc}. \tag{4.14}$$

The S term accounts for the electromagnetic coupling between nanoparticles. This term depends only on the spatial distribution of nanoparticles and the wavelength of incident light in the host medium.

As a consequence of radiative coupling the LSPR is modified. Namely, the spectral position of the resonance as well as, its width and amplitude change due to coupling. If the condition $nh > \lambda_0$, where n is environment refractive index, h is array pitch and λ_0 is the noninteracting LSPR wavelength, is fulfilled, then additional spectral features in the electromagnetic response of periodic metasurface can be observed.[116] Such features are called surface lattice resonances (SLR). They tend to be very narrowband compared to single-particle LSPR and come from an interplay between the resonant response of the antenna and diffraction on the periodic array. Due to their narrowband character, they have found applications in light-matter coupling[117] and sensing.[118]

The initial model has been only correct for small particles which can be addressed using the electric dipole model. Dielectric or large particles require including more multipoles. The first such attempt has been proposed by Evlyukin and others.[119,120] They have proposed to include the magnetic dipole into the analysis as it is an important resonance of high index nanoantennas. They have shown that there is no electric-magnetic dipole coupling hence the electric and magnetic response can be analyzed separately and the corresponding lattice sums are identical. Consequently, SLRs of electric or magnetic character can occur. These resonances as well as the modified single particle resonances can be tailored independently by adjusting the lattice period in horizontal and vertical direction due to the fact that each dipole type couples to a different orthogonal polarization of light.

By combining Mie theory with the multiple scattering equation using the multipole expansion (eq. 2.79), one can calculate the optical properties of periodic nanoparticle arrays including arbitrarily high multipole orders.[121] Notably, the general rules of multiple coupling in periodic arrays are provided.[121] Here, we summarize the results of this analysis.

Let us consider the associated Legendre polynomial part of the direct coupling matrix elements (eq. 10.10),

$$P_p^{|m_1 - m_2|}(\cos\theta), \tag{4.15}$$

where $p \in [|l_1 - l_2|, l_1 + l_2]$ and θ is the azimuthal angle. As a consequence of symmetry, interparticle coupling vanishes unless $m_1 = m_2$ and one can use the recurrence relation

$$P_{n+1}(\cos\theta) = \alpha \cos\theta P_n(\cos\theta) - \beta P_{n-1}(\cos\theta), \tag{4.16}$$

with $P_0 = \frac{\sqrt{2}}{2}$ and $P_1 = \sqrt{3/2}\cos\theta$ to evaluate these polynomials. As a consequence of the fact that we are analyzing a planar array, we set $\cos\theta$ to zero. Then only even values of p contribute to the overall result.

The other factor governing the occurrence of coupling between multipoles of given degrees are Wigner-3j symbols which enter W via a_5 (eq. 10.13) and b_5 (eq. 10.14) coefficients,

$$w^a(l_1, l_2, p) = \begin{pmatrix} l_1 & l_2 & p \\ 0 & 0 & 0 \end{pmatrix}, \tag{4.17}$$

which contribute to coupling between multipoles of the same type (i.e. electric and electric or magnetic and magnetic) and

$$w^b(l_1, l_2, p) = \begin{pmatrix} l_1 & l_2 & p-1 \\ 0 & 0 & 0 \end{pmatrix}, \tag{4.18}$$

which contributes to coupling between electric and magnetic multipoles.

Such Wigner-3j symbols vanish unless the sum of its top row is an even integer. Because the condition that stems from the Legendre polynomial part limits p to even numbers if $l_1 + l_2$ is even, then $w_a \neq 0$ and $w_b = 0$. Otherwise, if $l_1 + l_2$ is odd, $w_a = 0$ and $w_b \neq 0$.

This leads to the following conclusion: coupling between electric and magnetic multipoles can happen only if one of their orders is even and the other is odd. For such orders, no coupling between multipoles of the same types occur. Otherwise, only coupling between the same multipole types occurs. This is a generalization of previously known examples of multipole coupling selection rules.

4.2.2 Coupling related phenomena in periodic metasurfaces

Here, we briefly review coupling related phenomena in periodic metasurfaces: directional scattering and suppresion of reflection or transmission of light. As a starting point, we consider effective dipole polarizabilities (electric or magnetic) obtained using eq. 4.12. Light transmission is suppressed at each dipole resonance in a periodic metasurface if light absorption is neglible and the resonances are spectrally separated so that the contribution from the multipoles other than the one at resonance can be omitted.[122] Suppression of reflection by periodic metasurfaces is closely related to the Kerker effect. As shown by Evlyukhin et al.,[120] reflection of light for specular incidence does not occur if the electric and magnetic dipole polarizabilities are equal. This effect is called the lattice Kerker effect.[123] It can be generalized to higher order multipoles, but this case requires more complicated multipolar interference. The interference of dipole and quadrupoles in arrays of silicon cubes can lead to simultaneous suppression of both forward and backward scattering leading to the so-called lattice invisibility effect.[124]

4.3 Random heterogeneous metasurfaces

Random metasurfaces are relatively simple to fabricate and hence they have found several applications. Such metasurfaces can be formed, for instance, by self-assembly of colloidal nanoparticles on a substrate or laser ablation for dielectric nanoparticles.[84] One notable example is hole colloidal lithography (HCL),[125] a technique which uses electrostatic self-assembly of surface-charged particles (typically polystyrene nanospheres) in a refined way to gain control over the process. The minimal center-to-center distance can be controlled by experimental conditions of the process, e.g. electrolyte concentration, particle density or exposure time. Applications of random metasurfaces include photovoltaics,[126] heat management,[127] sensors[128] and lenses.[129] In this section we show how to numerically generate and characterize random arrays in terms of their spatial arrangement and optical properties.

In order to generate the positions of nanoparticles we simulate a process of random sequential adsorption (RSA).[130] It is especially useful due to the fact that the problem of finding the characteristics of random 2D arrays cannot be found analytically even by utilizing common approximations such as the Perckus Yevick approximation. Also, the method is suitable for finding densely packed distributions. In RSA, positions of the nanoparticles are sequentially drawn from a uniform random distribution. After each step, the newly drawn position is tested. If the new particle overlaps with any other nanoparticle, the particle is not accepted. Otherwise, it is appended to the particle list. This process physically corresponds to irreversible adsorption of particles on a surface.

While the basic algorithm itself is very simple, there are certain specific criteria to consider when forming an array using an RSA simulation. First of all, we aim to obtain the maximal surface coverage. In other words, we want to achieve an array for which it is not possible to adsorb another nanoparticle due to position overlap. At the same time, this is at odds with the fact that probability of successful adsorption rapidly decreases with the number of deposited particles.

To achieve saturation, it is prudent to cease adsorbing particles at random if the number of necessary trials to find a particle position that meets the acceptance conditions exceeds a predetermined value, here we typically used 100 000 as

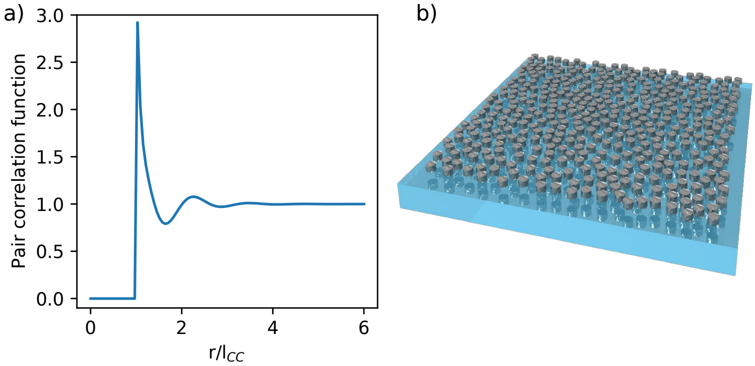

Figure 4.1: a) Pair correlation of an amorphous array. b) Schematic representation of an amorphous array of nanoparticles placed on a glass substrate.

the limit. We stop the RSA process and scan the adsorption area (space) for any possible remaining empty space which can be still occupied by particles. A particle is adsorbed whenever such empty space is found. The second aspect are boundary conditions. Here, we use periodic boundary conditions and modify the acceptance condition accordingly.

The pair correlation function is used as a way of characterizing the spatial distribution of nanoparticles in this work. It is proportional to the local density of nanoparticles measured at a certain distance from an arbitrarily selected reference particle. The pair correlation function can be found based upon the histogram of interparticle distance ($\eta(r)$), which is then adequately normalized[130]

$$g(r) = \frac{\eta(r)}{\sigma N v_{shell}(r)}, \tag{4.19}$$

with

$$v_{\text{shell}}\,(r) = \pi r^2 \left[\frac{(r+\Delta r/2)^2 - (r-\Delta r/2)^2}{r^2}\right]. \tag{4.20}$$

4.3.1 Amorphous metasurfaces

Publications I-III focus on the optical properties of a subclass of random nanoparticle arrays called amorphous arrays. The spatial distribution of particles in this type of random arrays is constrained by the fact that the center-to-center distance cannot be smaller than a certain threshold value l_{cc}, i.e. the minimal center-to-center distance. Herein, we parametrize l_{cc} by a dimensionless param-

Table 4.1: Values of fitted parameters of the pair correlation function, Equation 4.19, of the amorphous arrays generated using RSA.

a	a_0	a_1	b	b_0	b_1	d_1	e_1
1.016	1.054	17.53	0.7718	0.8675	1.624	0.7888	1.223

eter CC, which is l_{cc} normalized by the particle diameter,

$$l_{cc} = CC\,D. \tag{4.21}$$

An amorphous array with $CC = 1$ is equivalent to the so-called dense random packing, which is numerically generated by RSA as described in the previous section. In practice, larger values of CC are also considered, which in a simulation are obtained by scaling the positions of particles by the new CC value. Such arrays can be fabricated using e.g. HCL, in which CC may be controlled by experimental parameters such as concentration of the electrolyte used during the HCL process, particle density, adsorption time or surface charge.

We have generated a set of approx. 10 000 particles using RSA and calculated its PCF using eq. 4.19. The resulting PCF is presented in Figure 4.1 and is consistent with state-of-the-art results. The acceptance condition introduces a cut-off of the pair correlation function at the minimal center-to-center distance. At the minimal center-to-center distance the local density of particles is high, which is a consequence of short-range ordering. Then, the PCF quickly diminishes with a tendency to fluctuate. At sufficiently large distances from a reference particle, the array appears to be completely disordered. Thus, the local density is equal to the global (one particle) density and the pair correlation function at large distances is equal to one. This leads to a useful approximation of the PCF as a Heavyside theta function:

$$g(x) = \theta(x-1), \tag{4.22}$$

where $x = r/l_{cc}$ with l_{cc} being the minimal center-to-center distance. In order to obtain an accurate, but analytical representation of the PCF of an amorphous array we have fitted the following function to the numerical data

$$\begin{split} g(x) = \{[a\exp(-a_1(x-a_0)) + b\exp(-b_1(x-b_0))] \times \\ \sin(2\pi(x-d_1)/e_1) + 1\}\,\theta(x-1), \end{split} \tag{4.23}$$

the fitting parameters are given in Table 4.1.[14] In theoretical calculations it is useful to use an exponential representation of sine. Then the result can be represented as

$$g(x) = \left(\sum_j v_j e^{n_j x} + 1\right)\theta(x-1). \tag{4.24}$$

In the following subsections we deal with the optical properties of random metasurfaces. The first relevant works are those by Schwind[131] and Conley.[132] In these works the single scattering approximation is used. Angular scattering patterns obtained by the authors are distinct from the corresponding single particle patterns. Several maxima appear in the angular scattering patterns amorphous array, which are reminiscent of Bragg peaks for periodic arrays, but these features are substantially broader than Bragg peaks due to disorder. The presence of these maxima is a consequence of short range ordering. They appear at angles close to those obtained by scattering patterns generated by two particles separated by l_{cc}. A characteristic of short range ordering is also the lack of forward scattering for a broad range of frequencies and simultaneous strong backward scattering. In contrast, uncorrelated systems tend to scatter light in the forward direction.

Here, we focus on accounting for multiple scattering in order to describe resonant phenomena arising in amorphous arrays. While RSA among with other methods enables drawing large ensembles of nanoparticles, solving the multiple scattering equation (eq. 4.7) for such a system is a formidable task. Modern techniques such as the fast multipole method[133] or the GPU accelerated T-matrix[107] method enable studying arrays containing several thousands of particles, but due to large computation times they remain rather impractical for gaining intuition about physical phenomena in random metasurfaces. In this work they serve the purpose of a benchmark tool. Instead, for physical insight, we resort to two approximate methods: an effective medium theory and a film of dipole approximation, which are outlined here. Their extensions form a major contribution of the author and are presented in subsequent chapters of this thesis.

4.3.2 Effective medium theory

Effective medium theory describes a random ensemble of nanoparticles by replacing a heterogeneous distribution of permittivity that contains separate contributions from the particles and the background medium with a homogeneous and thus effective permittivity. While there are many various methods to obtain the effective permittivity, here we present the most common one, which is the Maxwell-Garnett approximation.

The considerations here follow those presented by Vadim Markel in his tutorial on the Maxwell-Garnett approximation.[134] First, we find the field from a dipole at the dipole position. The Green function approach cannot be applied directly, because as the position of the observation point approaches that of the dipole itself, the Green function becomes singular. This singularity, however, is integrable.[134] Here, we use a somewhat simpler mathematical argument. A model of the dipole will be a small sphere that scatters the electric field. The internal field is given by eq. 3.1

$$\vec{E}_{int} = \frac{3}{\varepsilon + 2}\vec{E}_{ext}. \tag{4.25}$$

The depolarization field of the sphere corresponding to the dipole itself is $E_{dep} = E_{int} - E_{ext}$. Hence,

$$\vec{E}_{dep} = \frac{-\varepsilon + 1}{\varepsilon + 2}\vec{E}_{ext}. \tag{4.26}$$

Using the quasi-static expression for polarizability, $\vec{E}_{dep}$ is expressed as

$$\vec{E}_{dep} = -\frac{1}{4\pi\varepsilon_0 r^3}\vec{p}. \tag{4.27}$$

When integrated over the sphere's volume, the field is given by

$$\int_{sphere} \vec{E}_{dep} dV = -\frac{1}{3\varepsilon_0}\vec{p}. \tag{4.28}$$

Finally, due to the point-like nature of the dipole, the internal field is given by

$$\vec{E}_d = -\frac{1}{3\varepsilon_0}\vec{p}\delta(\vec{r} - \vec{r_0}). \tag{4.29}$$

The effective medium permittivity can be related to polarization as (see eq. 2.7)

$$\vec{P} = \varepsilon_0(\varepsilon_{eff} - 1)\vec{E}. \tag{4.30}$$

The polarization can be defined using the dipole approximation as

$$\vec{P} = \sum_i \vec{p_i}\delta(\vec{r} - \vec{r_i}). \tag{4.31}$$

We approximate $\vec{p_i}$ as

$$\vec{p_i} = \alpha_e \vec{E}_{inc}, \tag{4.32}$$

which is valid for sparse isotropic particle ensembles. Next, we find volume averages of expressions eqs. 4.30 and 4.31 and use the condition that both averages must be equal to obtain the relation

$$N\alpha_e \vec{E}_{inc} = \varepsilon_0 V(\varepsilon - 1)\langle\vec{E}\rangle, \tag{4.33}$$

where N is the number of particles and V is the examined volume. In order to find the effective permittivity the average electric field $\langle\vec{E}\rangle$ must be calculated. This field is expressed as

$$\langle\vec{E}\rangle = \vec{E}_{inc} + \langle\sum_i \vec{E}_{scat}\rangle. \tag{4.34}$$

In the quasi-static approximation the regular part of $\vec{E}_{scat}$ vanishes upon averaging and only the singular part (see eq. 4.29) is retained, which yields

$$\langle \vec{E} \rangle = \vec{E}_{inc} - \frac{\sigma}{3\varepsilon_0}\vec{p} = \left(1 - \frac{\sigma\alpha_e}{3\varepsilon_0}\right)\vec{E}_{inc}, \tag{4.35}$$

where $\sigma = N/V$ is the number density. After inserting the average field described by eq. 4.35 into eq. 4.33 and algebraic manipulation, the Clausius-Mosotti relation is obtained

$$\alpha_e = \frac{\sigma}{3\varepsilon_0}\frac{\varepsilon_{eff} - 1}{\varepsilon_{eff} + 2}. \tag{4.36}$$

The most typical effective medium theory, the Maxwell-Garnett permittivity stems from the Clausius-Mosotti relation and it is obtained by substituting eq. 3.3 into eq. 4.36

$$\frac{\varepsilon_{eff} - 1}{\varepsilon_{eff} + 2} = f\frac{\varepsilon - 1}{\varepsilon + 2} \tag{4.37}$$

where $f = V_{incl}/V$ and is the volume fraction of inclusions.

The effective medium approach has been widely used to calculate the optical properties of nanoparticles in solar cells, nano- and microparticles in natural and artificial heterogeneous materials such as ice or ceramics. Also various effects can be accounted for in effective medium theory, such as electromagnetic chirality or nonlinearity. At the same time, we find this approach to be inadequate to describe complex electromagnetic coupling in amorphous arrays and thus use a different, more direct approach which is the film of dipoles model.

4.3.3 Optical properties of amorphous arrays

A starting point for the derivation of the film of dipoles model is a common approach to solving the coupled dipole equation (eq. 4.11) called the scattering series expansion. This series expansion is obtained by iterating eq. 4.11. The result is

$$\vec{p}_i = \alpha_{e,i}\left(\vec{E}_{inc,i} + \sum_{j\neq i} A^{EE}_{ij}\alpha_{e,j}\vec{E}_{inc,j} + \sum_{j\neq i} A^{EE}_{ij}\alpha_{e,j}\sum_{k\neq j} A^{EE}_{jk}\alpha_{e,k}\vec{E}_{inc,k} + ...\right). \tag{4.38}$$

The series can be interpreted as follows. Each term $A^{EE}_{ij}\alpha_{e,j}$ corresponds to a scattering event off particle j resulting with field generation at particle i. Then, subsequent terms contain increasing number of scattering events. First, there is just the incident field, then a single scattering enters the series, double scattering and so on. The scattering series expresses the idea of multiple scattering, but it has to be noted that it is more of a mathematical concept than a physical one. Also, while truncating the scattering series is often used (which is called the

Born approximation), the series may not be convergent if the particle coupling is sufficiently strong.

In order to perform statistical averaging of the scattering series, we resort to approximations. In triple scattering and other higher order terms of the scattering series, the same particle can be included more than once. As shown by Twersky[135] in the limit of an infinite number of particles, such terms do not contribute significantly to the series. Here, we utilize the Twersky approximation that removes scattering paths that include the same particle more than once

$$\vec{p}_i = \alpha_{e,i}\Big(\vec{E}_{inc,i} + \sum_{j\neq i} A_{ij}^{EE}\alpha_{e,j}\vec{E}_{inc,j} + \sum_{j\neq i} A_{ij}^{EE}\alpha_{e,j} \sum_{\substack{k\neq j\\ k\neq i}} A_{jk}^{EE}\alpha_{e,k}\vec{E}_{inc,k} + ...\Big). \tag{4.39}$$

The equation for the total polarization density can be now written as

$$\sum_i \vec{p}_i\delta(\vec{r}-\vec{r}_i) = \alpha_{e,i}(\vec{E}_{inc,i}\delta(\vec{r}-\vec{r}_i) + \sum_{j\neq i} A_{ij}^{EE}\alpha_{e,j}\vec{E}_{inc,j}\delta(\vec{r'}-\vec{r}_j) + \\ \sum_{j\neq i} A_{ij}^{EE}\alpha_{e,j} \sum_{\substack{k\neq j\\ k\neq i}} A_{jk}^{EE}\alpha_{e,k}\vec{E}_{inc,k}\delta(\vec{r}-\vec{r}_i) + ...). \tag{4.40}$$

Now we find the ensemble average of the exciting field in the limit of an infinite number of particles. We account only for pair correlations. Assuming that particles are identical and using the fact the spatial distribution of particles is isotropic, the exciting field can be expanded (within the self-avoiding approximation) as:

$$\langle\vec{E}_{exc}\rangle = \vec{E}_{inc} + \alpha_e\sigma\int dr' A^{EE}(\vec{r}-\vec{r}\,')g(\vec{r}-\vec{r}\,')\vec{E}_{inc}(\vec{r}\,') + \\ \alpha_e^2\sigma^2\int dr'\int dr''\phi(\vec{r}-\vec{r}\,')g(\vec{r}-\vec{r}\,')A^{EE}(\vec{r}\,'-\vec{r}\,'')g(\vec{r}-\vec{r}\,')\vec{E}_{inc}(\vec{r}\,'') + ... \tag{4.41}$$

We introduce the incident field of the form

$$\vec{E}_{inc}(\vec{r}) = \lim_{q\to 0}\vec{E}_0 e^{iqr}. \tag{4.42}$$

Then, we observe that each of the integrals is a Fourier transform (denoted as F) of a convolution and then,

$$\langle\vec{E}_{exc}\rangle = \sum_{l=0}^{\infty}\lim_{q\to 0}(\alpha_e\sigma F[gA^{EE}](\vec{q}))^l\vec{E}_0 \tag{4.43}$$

The sum in this equation can be evaluated as

$$\langle \vec{E}_{exc} \rangle = \left(1 - \alpha_e \sigma \lim_{q \to 0} F[gA^{EE}](\vec{q}) \right)^{-1} \vec{E}_0 \tag{4.44}$$

The effective polarizability, α_e^* is defined via the relation with the average polarization (eq. 4.14), while the exciting field is related to polarization by

$$\langle \vec{p} \rangle = \alpha_e \langle \vec{E}_{exc} \rangle. \tag{4.45}$$

Using eqs 4.14, 4.44 and 4.45, it is shown that

$$\alpha_e^* = \alpha_e \left(1 - \alpha_e S_{EE} \right)^{-1}, \tag{4.46}$$

with

$$S_{EE} = \sigma \lim_{q \to 0} F[g \frac{1}{2} Tr(A^{EE})](\vec{q}). \tag{4.47}$$

Note that the full A^{EE} operator is replaced by half of its trace due to spatial isotropy of the array. The result is reminiscent of that obtained for periodic nanoparticle arrays, but now the coupling term S is different

$$S_{EE} = \frac{1}{4\pi\varepsilon_0} \sigma \int_{l_{CC}}^{\infty} \int_0^{2\pi} g(r) e^{ikr} \left[\frac{(3\cos^2\theta - 1)(1 - ikr)}{r^3} + \frac{k^2 \sin^2\theta}{r} \right] r dr d\theta, \tag{4.48}$$

where $\sigma = 0.69/l_{cc}^2$ is the number density of particles in the array.

If we assume a Heavyside theta representation of the PCF, the coupling term is of a simple form

$$S_{EE} = \frac{1}{4\pi\varepsilon_0} \pi\sigma \frac{e^{ikl_{CC}}}{l_{CC}} (1 + ikl_{CC}), \tag{4.49}$$

with Figure 4.2 illustrating an oscillatory nature of the interaction term. By substituting Equation 4.49 into Equation 3.4, one can show that the effective polarizability is Lorentzian with

$$\frac{\alpha_e^*}{4\pi\epsilon_0 R^3} = \frac{1 - \bar{\omega}^2 \left(1 + s^2\right) - qf + i \left(\bar{\omega} \left(\bar{\gamma} + \frac{2}{3} s^3 \bar{\omega}^2 \right) + qg \right)}{\left(1 - \bar{\omega}^2 \left(1 + s^2\right) - qf\right)^2 + \left(\bar{\omega} \left(\bar{\gamma} + \frac{2}{3} s^3 \bar{\omega}^2 \right) + qg \right)^2}, \tag{4.50}$$

where $\bar{\omega} = \frac{\omega}{\omega_0}, \bar{\gamma} = \frac{\gamma}{\omega_0}, s = \frac{\omega_0 R}{c}$ with $\omega_0^2 = \frac{\omega_p^2}{3}$, a coupling strength $q = \pi\sigma_0 \left(R/\ell_{\mathrm{cc}}\right)^3$, $f(x) = \cos x - x \sin x, g(x) = \sin x + x \cos x$, and c is the speed of light. Functions $f(x)$ and $g(x)$ correspond to real and imaginary parts of $4\pi\varepsilon_0 S$, respectively.

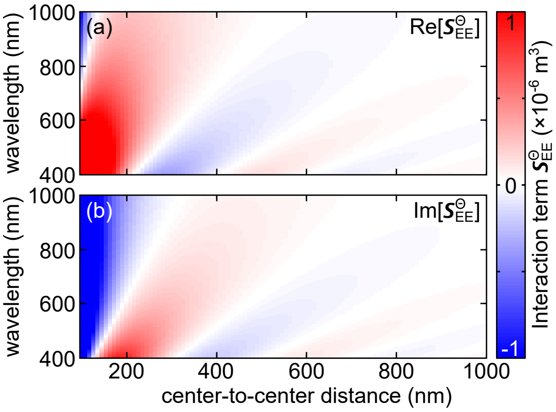

Figure 4.2: a) Real and b) imaginary part of dipolar coupling term for amorphous array of nanoparticles assuming that PCF may be approximated by Heaviside theta function. The real part is responsible for the modification of dipole resonance condition, while the imaginary part leads to modification of resonance width.

Based on this representation of the effective polarizability, it is possible to extract the resonant frequency of the interacting system ($\bar{\Omega}_{\mathrm{I}}$) with respect to the noninteracting system resonant frequency ($\bar{\Omega}_{\mathrm{N}}$)

$$\bar{\Omega}_{\mathrm{I}}/\bar{\Omega}_{\mathrm{N}} = \sqrt{1 - qf(k_{\mathrm{N}}l_{cc})}. \tag{4.51}$$

This indicates that $\mathrm{Re}(S) > 0$ results in the decrease of resonant frequency, while $\mathrm{Re}(S) < 0$ leads to a shift of the resonance frequency towards the blue. The corresponding resonance linewidth ($\bar{\Gamma}_{\mathrm{I}}$) normalized to its counterpart for the non-interacting system ($\bar{\Gamma}_{\mathrm{N}}$) is

$$\bar{\Gamma}_{\mathrm{I}}/\bar{\Gamma}_{\mathrm{N}} = 1 + 2\left(1 + s^2\right) Q_{\mathrm{N}} g(k_{\mathrm{N}}l_{cc}), \tag{4.52}$$

where Q_{N} is the quality factor of the individual particle. A positive value of $\mathrm{Im}(S)$ leads to increased linewidth with respect to the non-interacting, while the converse happens if $\mathrm{Im}(S)$ is negative. Figure 4.2 plots the values of the real and imaginary parts of S for a PCF that is given by the Heaviside theta function. This is presented in Fig. 4.3 in which $\bar{\Omega}_{\mathrm{I}}/\bar{\Omega}_{\mathrm{N}}$ and $\bar{\Gamma}_{\mathrm{I}}/\bar{\Gamma}_{\mathrm{N}}$ are plotted as a function of the minimal center-to-center distance normalized by the resonance wavelength of the non-interacting system.

In a similar fashion to resonance wavelength and linewidth, the resonance amplitude is modified as well. This modification affects scattering and absorption

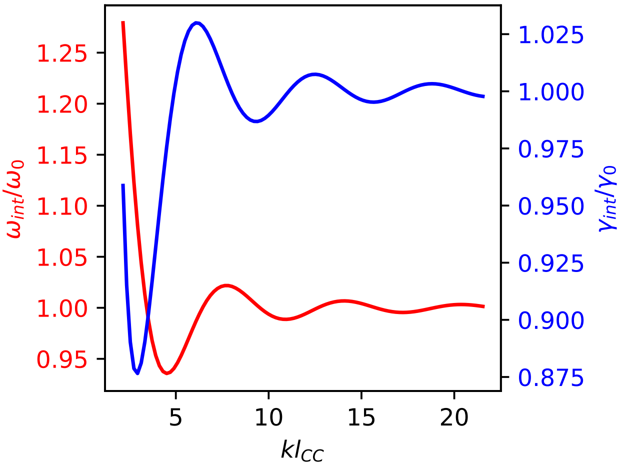

Figure 4.3: Resonance wavelength and linewidth of an amorphous array composed of metallic nanoparticles. We assume that the quality factor of the noninteracting system is 0.5, particle radius is 60 nm, while the non-interacting resonance wavelength is 350 nm.

cross sections at the resonance wavelength in differently, which in turn leads to a scattering-to-absorption ratio modification. Due to an oscillatory behaviour of the effective polarizability as a function of the center-to-center distance, the scattering-to-absorption ratio can be tailored for a specific application by tuning the amorphous array density.[12]

4.4 Substrate mediated multipole coupling

4.4.1 Substrate mediated coupling in isolated nanoantennas

Nanoantennas are typically fabricated using a deposition processes onto a dielectric substrate. Unless the structure is covered by an index matching superstrate, the substrate substantially affects the optical response of the system and therefore substrate mediated effects cannot be omitted in the analysis of light scattering by nanoantennas. One of the important effects related to the presence of a substrate is the so-called substrate induced bianisotropy.[136] The effect stems from the fact that otherwise uncoupled electric and magnetic dipole resonances of an antenna are coupled when placed on a planar substrate. This leads to a strong

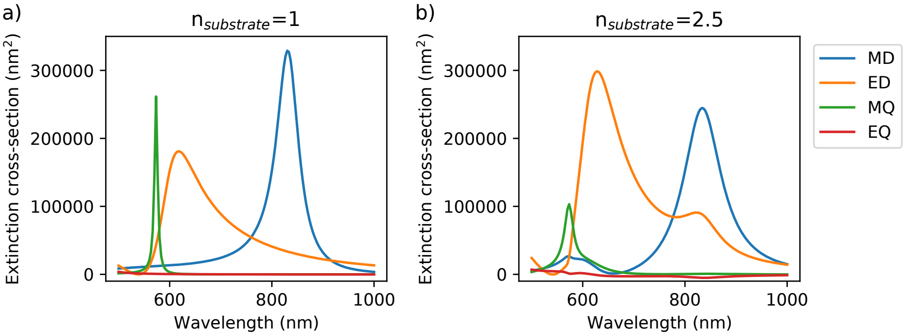

Figure 4.4: Multipole decomposed extinction spectra of high-index dielectric sphere ($n = 4$) with 100 nm radius a) in free space b) on a substrate.

magnetic response at the electric dipole resonance.[137] The sign and the strength of this response depends on the relative particle-substrate position as well as the substrate refractive index. In order to visualize this effect we plot multipole decompositions of extinction spectra for a high-index nanoparticle in free space and on a substrate in Fig. 4.4. A signature of substrate indcuded biansotropy is a significant increase of the electric dipole amplitude in the vicinity of magnetic dipole resonance. Notably, higher order multipoles can also couple via off-substrate reflection. One such example is a modified amplitude of the magnetic dipole near the magnetic quadrupole resonance. The general coupling rules are described later in the thesis. The effect resulting from substrate induced bianisotropy is a strong dependence of the magnetic and electric dipole spectral features on the polarization of incident light under oblique incidence.[138] Such a polarization-dependent effect can be used to manipulate chiral properties of light scattered by a nanostructure.[139]

The presence of the substrate modifies the fields generated by multipoles due to the fact that there is an additional off-substrate reflection and transmission of these fields, which does not occur during propagation in free space. Kerker conditions derived for free-space propagation are no longer valid when the structure is substrate-supported, yet it is still possible to suppress backward scattering and achieve highly unidirectional light scattering under modified conditions that account for the reflection of the scattered field off the substrate.[140] The near-field modification by the substrate is especially important for plasmonic nanostructures. The electromagnetic hot-spots are generally pushed into the substrate. As shown by Antosiewicz et al.,[141] this effect can be used to additionally enhance light-matter interactions in the vicinity of the substrate. We exemplify this by studying the case of a Drude disk placed on a substrate with a varying refractive

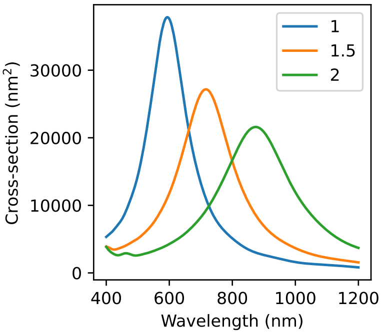

Figure 4.5: Extinction spectra of Drude disk (diameter of 150 nm, height of 25 nm) placed on a substrate with varying refractive index.

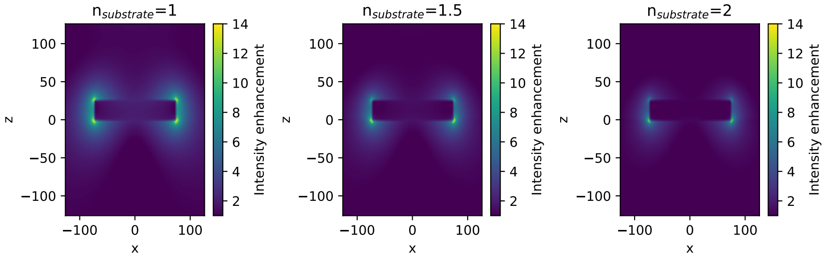

Figure 4.6: Electric field enhancement of Drude disk (diameter of 150 nm, height of 25 nm) placed a) in free space b) on glass substrate c) on a dielectric substrate with refractive index of 2.

index. The presence of the substrate redshifts the localized surface plasmon resonance as shown in Fig. 4.5. The effect of the substrate on the near field of the disk is presented in Fig. 4.6. With an increasing refractive index of the substrate, there is an increasing asymmetry between the top and bottom of the disk. The hot spots placed close to the substrate tend to be enhanced by its presence.

Nanostructures separated by a thin spacer from a metallic mirror have recently found application as an efficient platform for enhancing light-matter interactions. The system can be described as a one of two coupled dipoles: the first corresponding to the particle itself and the second being an image dipole which arises from multiple reflection of light off the substrate. Similarly, to the case of the gap in a plasmonic dimer, the field in the spacer is extremely confined. Even further enhancement is observed due to the formation of atomic scale features

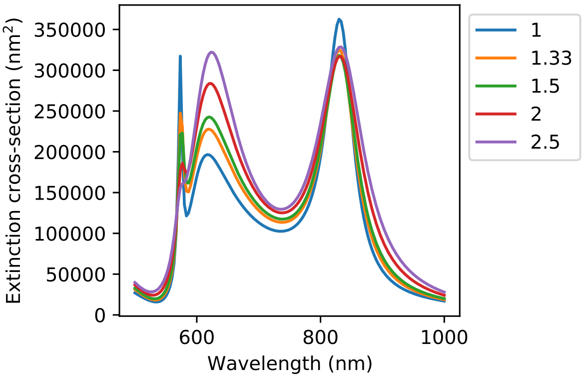

Figure 4.7: Extinction spectra of high-index dielectric sphere ($n = 4$) with 100 nm radius placed on a substrate with varying refractive index denoted in the plot legend.

on the particle surface, resulting in a so-called picocavity that has been used e.g. for extremely precise measurements of molecule position using Raman spectroscopy.[142] It is worth noting that while the case of a plasmonic nanoparticle on a mirror is more popular, systems comprised of dielectric nanoparticles have also been studied in the literature.[143]

As a consequence of light reflection off the substrate, multiple scattering of light between the substrate and the antenna occurs. From a theoretical standpoint this leads to a modification of the scattering coefficients of the system. The system's response becomes

$$\vec{b} = (T^{-1} - W_r)^{-1}\vec{a} \tag{4.53}$$

where W_r is the coupling matrix describing the multiple scattering process (see Appendix A). More details on the calculation of W_r and other properties are shown in the next section.

The most basic optical effect of placing a nanostructure on a substrate is the shape and position modification of the multipolar resonances in the optical spectra. As shown in Fig. 4.7, in case of a high-index dielectric nanoparticle, it is mostly the amplitudes of the peaks that are changed, while their positions remain almost identical to the free space case.

As shown in the second chapter, extra care must be taken when performing simulations with the T-matrix method for particles placed on a substrate. The calculation of the fields reflected off the substrate can be considered as a following process:

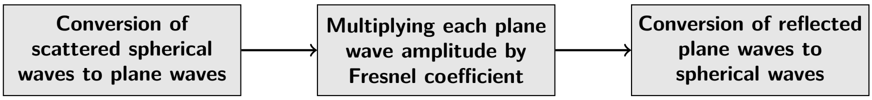

The equation for the coupling matrix element describing multiple scattering between particle and the substrate is given Appendix A (eq. 10.17). One of the main difficulties when evaluating the coupling matrix is an adequate choice of the integration contour for Sommerfeld integrals which convert spherical waves into plane ones. In SMUTHI, the T-matrix code used in this thesis, it is controlled by three parameters: `neff_res`, `neff_max`, `neff_imag`. There are two main issues to consider when choosing the parameter values. The first one is the convergence of the self-interaction term (where the in-plane distance between the particle and its image is zero). For spherical or tall particles (height larger than width) selecting the Sommerfeld integral truncation wavenumber (`neff_max`) somewhere above the highest refractive index in the simulation should result in accurate integration. For flat particles the truncation wavenumber should be selected with extra care and there are multiple articles on this issue.[144–147] Here, we adopt the method proposed by Egel et al.[146] and the adequate `neff_max` value can be obtained using the `jqsrt_contour` function in the `simobjects` module. To test the method we calculate the spectra of a single nanodisk with refractive index of 4, radius of 75 nm and height of 120 nm placed on a substrate with refractive index of 2. We vary the multipole truncation order l_{max} and n_{eff}^{max} to investigate their effect on the relative error with respect to a corresponding FDTD simulation result. Even for relatively low l_{max} of 3 and the default SMUTHI n_{eff}^{max} it is possible to observe qualitative agreement with FDTD (see Fig. 4.8a). However, to observe quantitative agreement similar to the one that was attainable when the substrate is not present one has to select the n_{eff}^{max} carefully. As shown in Fig. 4.8b, only choosing n_{eff}^{max} to follow the dependence proposed by Egel et al. one can see substantial improvement in accuracy by increasing l_{max}. In our work we have typically used $l_{max} = 5$ as it was a good balance between computation time and simulation accuracy.[146]

4.4.2 Multiple scattering in substrate supported nanoparticle arrays

The general many-particle scattering problem for flat particle layers is formulated in the T-matrix framework as follows[108]

$$\vec{b^S} = T^S\left(\vec{a^S} + \left[W_r^{S,S} + \sum_{S'\neq S}\left(W(\rho_{S,S'},\phi_{S,S'}) + W_r(\rho_{S,S'},\phi_{S,S'})\right)\right]\vec{b^{S'}}\right), \qquad (4.54)$$

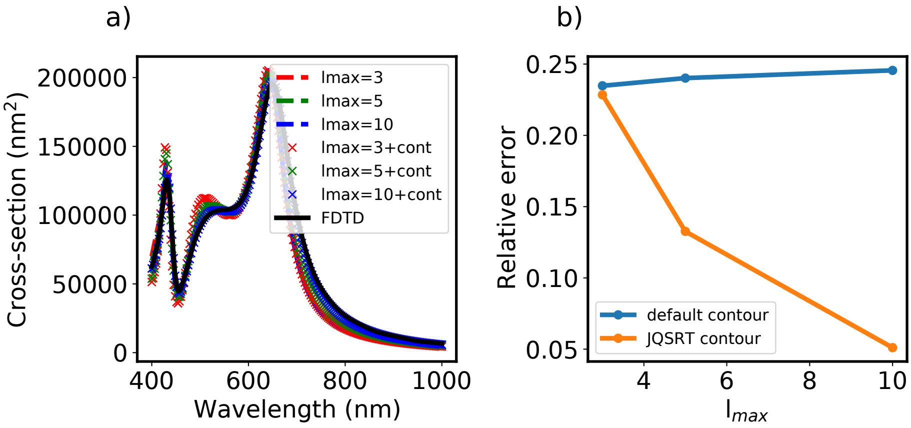

Figure 4.8: Comparison between SMUTHI and FDTD for a single nanodisk with radius of 75 nm and height of 120 placed on a substrate with refractive index of 2. a) Extinction spectra, b) mean relative error as a function of multipole truncation order l_{max} for two choices of plane wave truncation wavenumber. Only truncation at wavenumber proposed by Egel et al.[146] provides a decreasing simulation error with increasing l_{max}.

where $\vec{b}$ is the vector of scattering coefficients, $\vec{a}$ is the vector of the incident field expansion coefficients, W_r is the coupling matrix for substrate-mediated coupling, W is the coupling for direct interaction between particles and T is the T-matrix of the particle. Here, S indexes the particles, while the sum runs over all the particles other than the one with index S. Finally, ρ and ϕ denote polar coordinates of the particles. The resulting equation can be viewed as an extension of eq. 4.7. Equation 4.54 accounts for multiple scattering mediated by the layered system by including W_r which is defined for substrate-supported nanoparticle arrays in Appendix A (see eq. 10.15).

Chapter 5

Effective optical properties of amorphous arrays of optical antennas

5.1 Introduction

The aim of this chapter is to present a method of describing the optical properties of amorphous metasurfaces within the T-matrix framework and the mean-field approximation. In general, light scattering by random systems is difficult to tackle numerically because of the necessity to solve a problem with two distinct length scales: one related to the size of a single particle, which is on the order of $\lambda/4$ and one related to the size of the illumination spot which is at least on the order of a few microns. The idea behind the proposed method is that while each of the particles has a unique surrounding, which leads to a unique multiple light scattering process between the particle and its neighbours, selected macroscopic optical properties (e.g. extinction cross-section) are characterized only by the average of the scattering coefficients. To find the average scattering coefficients we use the mean-field approximation i.e. we map a many-body scattering problem to a one-body problem by replacing the scattered field from a given particle's neighbourhood with the average scattered field. This enables us to solve the scattering problem including almost arbitrarily high multipole orders and substrate-mediated interparticle coupling.

5.2 Film of multipoles model for amorphous arrays

5.2.1 General model

In order to derive the film of multipoles (FOM) model for amorphous arrays we start from a general multiple scattering equation for nanoparticles placed on a substrate (eq. 4.54). We separate coupling between different particles ($S \neq S'$, interparticle coupling) from substrate mediated self-interaction, because only interparticle coupling requires statistical averaging

$$\vec{b}^S = T^S \left(\vec{a}^S + \left(W^{S,RS} + \sum_{S'} \left(W^S(\rho_{S'}, \theta_{S'}) + W^{RS}(\rho_{S'}, \theta_{S'}) \right) \right) \vec{b}^S \right). \tag{5.1}$$

The procedure outlined in the previous chapter is applied to the dipolar analogue (eq. 4.40) of the formula presented above to obtain an effective polarizability (eq. 4.46). The discrete particle positions are replaced by a continuous distribution with a density described using the PCF,

$$\begin{aligned} \vec{b}^S = T^S \Big(\vec{a}^S + \Big(W^{S,RS} \\ + \int_0^\infty \rho d\rho \int_0^{2\pi} d\theta \Gamma(\rho/r_{cc}, \theta)(W^S(\rho,\theta) + W^{RS}(\rho,\theta))\sigma \exp(-\varepsilon\rho) \Big) \vec{b}^S \Big). \end{aligned} \tag{5.2}$$

Here, we multiply the integral function by an exponential decay with a small constant ε to obtain zero when the limit of the integral function as the interparticle distance approaches infinity is taken.

The equation can be further simplified by analyzing the angular integral. The coupling matrix can be factorized into radial and angular terms,

$$W(r,\theta) = W(r) \exp(i(m_2 - m_1)\theta). \tag{5.3}$$

Thus, the angular integral can be easily performed, leading to the following result:

$$\vec{b}^S = T^S \Big(\vec{a}^S + \Big(W^{S,RS} + \widetilde{W}^S + \widetilde{W}^{RS} \Big) \vec{b}^S \Big), \tag{5.4}$$

for $m_1 = m_2$ and zero elsewhere. $\widetilde{W}^S$ is defined as

$$\widetilde{W}^S = 2\pi \int_0^\infty \rho d\rho \Gamma(\rho/r_{cc}) W^S(\rho) \sigma \exp(-\varepsilon\rho) \tag{5.5}$$

and $\widetilde{W}^{RS}$ is defined as

$$\widetilde{W}^{RS} = 2\pi \int_0^\infty \rho d\rho \Gamma(\rho/r_{cc}) W^{RS}(\rho) \sigma \exp(-\varepsilon\rho). \tag{5.6}$$

Evaluation of the integrals in the definitions of $\widetilde{W}^{RS}$ and $\widetilde{W}^{S}$ is discussed in the following subsection. Eq. 5.4 can be solved for scattering coefficients b_s by matrix inversion

$$b^S = a^S\left((T^S)^{-1} - \left(W^{S,RS} + \widetilde{W}^S + \widetilde{W}^{RS}\right)\right)^{-1}. \tag{5.7}$$

5.2.2 Evaluation of the direct coupling integral

The efficiency of the semianalytical film of multipoles (FOM) outlined above stems from the reduced number of unknowns in the inverse problem by a factor equal to the number of particles. However, the FOM requires spatial integration to evaluate $\widetilde{W}^{RS}$ and $\widetilde{W}^{S}$. While the substrate-mediated coupling term contains Sommerfeld integrals and cannot be integrated analytically, it is possible to represent the direct coupling term using the incomplete gamma function and thus obtain an analytical result for this term, which can be easily evaluated numerically. The direct coupling term prior to statistical averaging is given by eq. 10.10 and the pair correlation function takes the form of eq. 4.24. Then, the direct part integral can be represented as

$$\widetilde{W}^{S,S'}_{n,n'} = 2\pi\sigma \int_0^\infty \rho d\rho \left(1 + \sum_j e^{-b_j\rho/l_{cc}}\right) \sum_{\chi=|l-l|'}^{l+l'} d^{S,S'}_{\chi,n} \sum_{\Lambda=0}^{\chi} c_{\chi,\Lambda} \frac{e^{ik\rho}}{(k\rho)^{\Lambda+1}}, \tag{5.8}$$

where

$$d_{\chi,n} = \mathrm{e}^{\mathrm{i}(m-m')\phi} \sum_{\chi=|l-l'|}^{l+l'} x_5\left(l, m\,|l', m'|\,\lambda\right) P_\chi^{|m-m'|}\left(\cos\theta\right). \tag{5.9}$$

The order of summation and integration is exchanged to obtain

$$\widetilde{W}^{S,S'}_{n,n'} = 2\pi\sigma \sum_{\chi=|l-l|'}^{l+l'} d^{S,S'}_{\chi,n} \sum_{\Lambda=0}^{\chi} \frac{c_{\chi,\Lambda}}{k^{\Lambda+1}} \left(\int_0^\infty d\rho \frac{e^{ik\rho}}{\rho^\Lambda} + \sum_j \int_0^\infty d\rho \frac{e^{ik\rho - b_j\rho/l_{cc}}}{\rho^\Lambda}\right). \tag{5.10}$$

The resulting integral is of the form

$$\int_a^\infty e^{-kx}x^{-n}dx = k^{n-1}\Gamma(1-n, ak), \tag{5.11}$$

where $\Gamma(1-n, ak)$ is the incomplete gamma function. Thus, the result is

$$\widetilde{W}^{S}_{n,n'} = 2\pi\sigma \sum_{\chi=|l-l|'}^{l+l'} d^{S,S'}_{\chi,n} \sum_{\Lambda=0}^{\chi} \frac{c_{\chi,\Lambda}}{k^{\Lambda+1}} \Big((-ik)^{\Lambda-1}\Gamma(1-\Lambda, -ikl_{cc}) + \sum_j (-ik + b_j/l_{cc})^{\Lambda-1}\Gamma(1-\Lambda, b_j - ikl_{cc})\Big). \tag{5.12}$$

Finally, to calculate these sums we make use of the following properties of Γ

$$\Gamma(1,x) = e^{-x}, \tag{5.13}$$

$$\Gamma(s+1,x) = s\Gamma(s,x) + x^s e^{-x}. \tag{5.14}$$

5.2.3 Electric and magnetic dipoles

The dipolar approximation of eq. 5.7 combined with a transformation to Cartesian multipoles enables us to obtain the mean-field analogue of the coupled electric and magnetic dipole method formulated in eq. 4.8 for amorphous arrays in free space. This model has been proposed by the author in Publication I. In this article we have used units such that $4\pi\varepsilon_0 = 1$ and $c = 1$. We adopt these units here (and whenever the model outlined here is used) as well. The reason behind this is that then the electric and magnetic polarizabilities have the same units (units of volume). Also, the electric and magnetic fields and coupling terms have the same units. This substantially facilitates the analysis of the effective magnetic and electric dipole moments and their comparison. Because of the fact that an amorphous array is approximately statistically isotropic (especially at long distance), the coupling terms for electric and magnetic dipoles are identical

$$S_{EE} = S_{MM} = \sigma \int_{l_{cc}}^{\infty} \int_0^{2\pi} \Gamma(r) e^{ikr} \left[\frac{(3\cos^2\theta - 1)(1 - ikr)}{r^3} + \frac{k^2 \sin^2\theta}{r} \right] r dr d\theta. \tag{5.15}$$

Due to this isotropy, the same multipole coupling rules apply to amorphous arrays in free space as in the case of periodic arrays. Thus, it can be shown that coupling between electric and magnetic dipoles vanishes by performing the angular integration of the following term

$$S_{EM} = \sigma \int_{l_{cc}}^{\infty} \int_0^{2\pi} \Gamma(r) \frac{k^2 e^{ikr}}{r} \left(\frac{ik}{r} - \frac{1}{r^2} \right) \cos\theta r dr d\theta = 0. \tag{5.16}$$

Consequently, each of the multipole moments can be solved for independently (in the dipole approximation) using an isolated nanoparticles magnetic/electric polarizability and the coupling term. Thus the following solution

$$\alpha_{m,e}^{eff} = \frac{1}{\alpha_{m,e}^{-1} - S_{EE}} \tag{5.17}$$

constitutes the film of dipoles (FOD) model.

5.3 Multipole coupling in amorphous arrays

5.3.1 Multipole coupling in amorphous arrays – rules

The selection rules presented in Chapter 3 for periodic arrays of nanoparticles are also valid for amorphous arrays treated using FOM if the particles are embedded in a homogenous environment. This is due to the fact that we assume in our model that the spatial distribution of nanoparticles is planar and isotropic. Also, we consider only the mean values of multipole moments. Consequently, two multipoles couple only if $m_1 = m_2$ and, as discussed earlier, coupling between electric and magnetic multipoles requires one of their orders (l) to be even and the other to be odd. For such orders, coupling between multipoles of the same types does not occur. Otherwise, only coupling between the same multipole types occurs. This is illustrated by an exemplary coupling matrix presented in Fig. 5.1a.

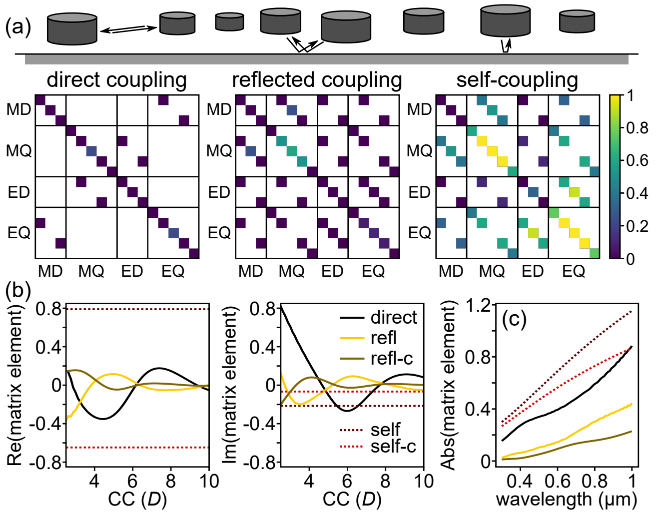

Figure 5.1: (a) Coupling matrices for different coupling channels: direct interparticle coupling (left), substrate-mediated interparticle coupling (center), and substrate-mediated self-coupling (right) calculated for $CC = 3.5$, $\lambda = 700$ nm with $D = 160$ nm and $H = 160$ nm. (b) Coupling matrix elements (real and imaginary parts) for $l = 1$ (dipole) at $\lambda = 700$ nm as a function of CC for direct coupling (direct), substrate-mediated interparticle coupling between the same dipole type (refl), and self-coupling. $-c$ in the label denotes cross coupling between electric and magnetic dipoles. (c) The magnitude of each coupling matrix element from (b) as a function of wavelength for CC fixed at 3.5D.

The presence of a substrate introduces additional channels of electromagnetic coupling via multiple scattering. Multipole coupling can occur between each particle and the substrate due to multiple reflection of scattered light by the substrate. We call this coupling type self-coupling. The other interaction type introduced by the substrate is substrate-mediated interparticle coupling. In this type of process part of the light scattered by a particle is reflected by the substrate and then becomes part of the exciting field for another particle. Substrate-mediated coupling obeys different multipole coupling selection rules than direct coupling as shown in Fig. 5.1a. In this case, the multipoles with the same order m can couple regardless of their type and degree. The minimal requirement that the spatial arrangement of particles needs to obey in order for these rules to apply is invariance of the spatial distribution with respect to the $\theta \rightarrow -\theta$ transformation.

Consequently, in the dipole approximation there are three possible multipole coupling scenarios: electric dipole – electric dipole, magnetic dipole – magnetic dipole and cross coupling between the two, which is manifested as substrate induced bianisotropy. We therefore study each coupling type for each multipole pair as a function of CC and wavelength for an amorphous array on a substrate ($n_{sub} = 2$) at $\lambda = 700$ nm in Fig. 5.1b,c. In general, substrate-mediated self-coupling constitutes the largest part of electromagnetic coupling, but with direct coupling being a comparable contribution. Substrate-mediated interparticle coupling is also an important contribution, but mostly for larger CC values. Each interparticle coupling type exhibits an oscillatory behavior as a function of CC, but reflected and direct contributions are phase shifted and have different magnitudes. Notably, cross coupling terms have a similar magnitude to coupling between identical multipole types, which means that if the electric dipole (ED) and the magnetic dipole (MD) are of similar magnitude, the two coupling types can both lead to substantial modifications of the optical properties or cancel each other out if the corresponding coupling terms have opposite signs.

5.3.2 Coupling in arrays embedded in homogeneous media

Forming an amorphous array out of high index dielectric nanoresonators leads to modification of nanoparticle multipole moments, which in the dipolar approximation is given by eq. 5.17. The interparticle coupling term, shown in Fig. 4.2 behaves in an oscillatory manner making the scaling parameter CC a useful handle for tailoring the optical response of the array. In Figs. 5.2 and 5.3 we present a comparison of sphere-based amorphous arrays modeled with the effective model and the exact solution of multiple scattering equation obtained using the MSTM code. Multiple scattering clearly affects the optical properties of the arrays. The effective model predicts accurately the impact of multiple scattering

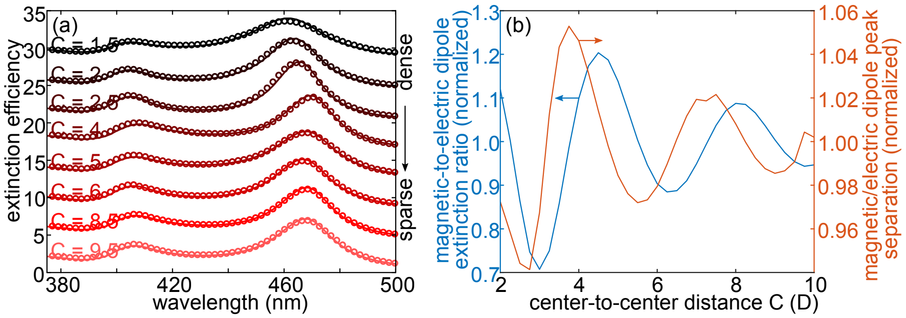

Figure 5.2: Comparison of exctinction efficiency spectra of amorphous arrays composed of D=100 nm Si nanospheres for FOD model (solid lines) and T-matrix method (circles). Each subsequent spectrum is shifted with respect to the previous one by four for enhanced readability. b) Extinction amplitude ratio and wavelength separation of electric and magnetic dipole resonances extracted from a) and normalized to their single particle counterparts. These properties are influenced by CC due to the fact that coupling term S is distinct at each resonance wavelength.

on both resonances. Due to the fact that the coupling term S is distinct at each resonance wavelength, each resonance is modified differently in comparison with the single particle counterparts. This results in an oscillatory behavior of the extinction amplitude ratio and wavelength separation of electric and magnetic dipole resonances.

In a typical experimental scenario, Si nanodisks are used to form amorphous

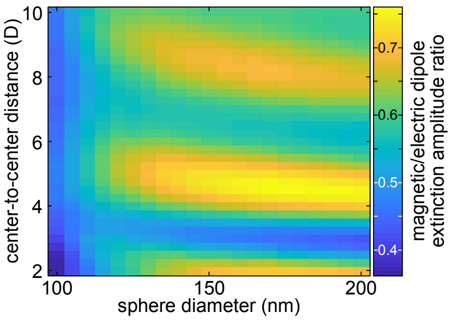

Figure 5.3: Extinction amplitude ratio of ED and MD resonances for amorphous arrays of Si nanospheres (D=100 nm) with varying diameter and CC.

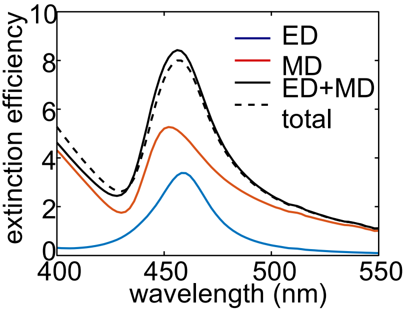

Figure 5.4: Multipole decomposition of extinction spectrum for a silicon nanodisk with D = 150 nm and H = 225 nm and comparison between sum of dipolar contributions and a total extinction efficiency.

arrays. The benchmark results for amorphous arrays of nanodisks and electric and magnetic polarizabilities of individual nanodisks used here are obtained using the T-matrix approach implemented with SMUTHI. The properties of a individual nanodisk with $D = 150$ nm and $H = 225$ nm are presented in Fig. 5.4. The aspect ratio is selected so that electric and magnetic dipole resonances overlap, while higher order multipoles do not contribute significantly.

In the case of an amorphous array of nanodisks with overlapping magnetic and electric resonances presented in Fig. 5.5, an oscillatory behavior of both

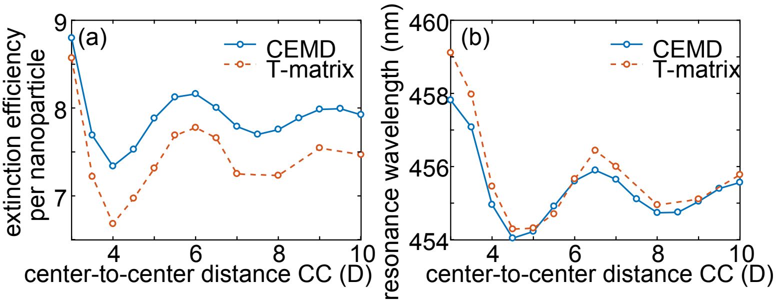

Figure 5.5: (a) Peak extinction efficiency per nanoparticle and (b) resonance positions for amorphous arrays composed of Si nanodisks with D = 150 nm and H = 225 nm. The results indicate good agreement between the FOD model and the T-matrix method.

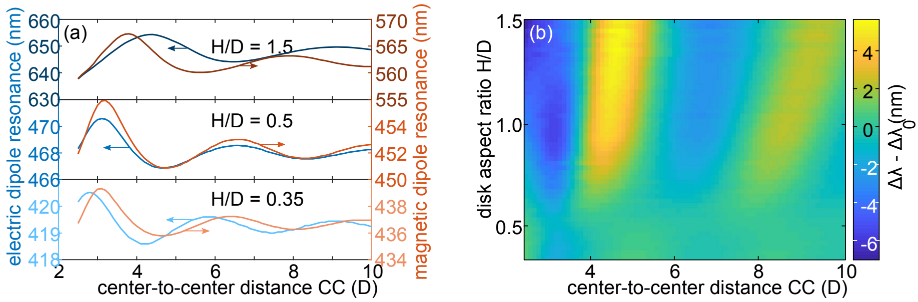

Figure 5.6: (a) Electric and magnetic dipole resonance wavelength of amorphous arrays of Si nanodisks with varying H/D ratio and fixed diameter of 130 nm. (b) Difference between wavelength separation of ED and MD resonances in amorphous arrays of Si nanodisks and corresponding single particle value as a function of the aspect ratio and CC.

resonance amplitude and wavelength properties is observed, similar to the one observed earlier for plasmonic particles (see Fig. 4.3), which is a consequence of the fact that the interaction is governed by the same term as in the case of the electric dipole mode in plasmonic particles. Good agreement between the effective model and explicit SMUTHI calculations is observed.

When the magnetic and electric resonance wavelengths are not equal, the interaction term for each moment separately is evaluated at a different wavelength for each resonance and hence electromagnetic coupling affects the resonances in a distinct manner. This enables manipulation of the array spectrum in terms of wavelength shift and amplitude ratio between the resonances not only using the particle geometry, but also by modifying the l_{cc} of the array. We show two examples of this kind of process in Fig 5.6. When the initial response separation is large, the properties can be manipulated to a larger extent as exemplified in nanodisk arrays. While the changes in spectral separation of the resonances are not large, they should still be accounted for when designing the array for a specific application, especially because the positions of individual resonances may change by tens of nanometers. At the same time, the change in the amplitude ratio is substantial and can be on the order of 30% with respect to the single particle value.

5.3.3 Coupling in substrate supported arrays

Substrate-mediated coupling is influenced by two factors. The first one is the substrate refractive index which enters the substrate mediated coupling term via

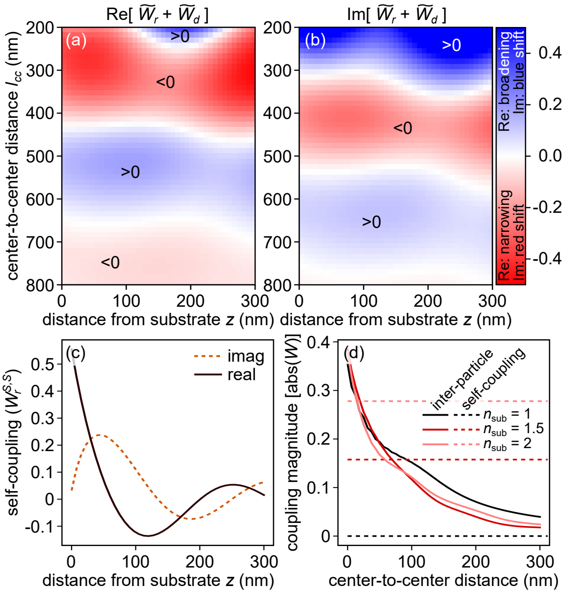

Figure 5.7: (a) Real and (b) imaginary parts of sum the of direct and substrate-mediated interparticle dipolar coupling matrix elements as a function of center-to-center distance and substrate-particle distance for amorphous array on a substrate ($n_{sub} = 2$) at $\lambda = 500$ nm. The colorbar indicates effects related to each part of this sum assuming that no other interparticle coupling occurs (higher order multipole coupling or dipolar cross-coupling). (c) Real and imaginary parts of the corresponding dipolar substrate mediated self-coupling term. (d) Comparison of interparticle and self-coupling in terms of dipolar coupling matrix element magnitude for varying refractive index of substrate as a function of l_{cc}.

the Fresnel reflection coefficients (see eq. 10.15). Here, we focus on the second factor which is the array-substrate distance. It contributes to the phase factor in eq. 10.15. Changing this distance determines (along with the wavelength of light in embedding the medium) the phase shift between the direct and the reflected scattered fields and thus changes interparticle coupling. We analyze this effect for magnetic dipole coupling terms calculated at free space resonance wavelength for a silicon nanodisk with height 100 nm and diameter 100 nm, which equals 500 nm (see Fig. 5.7). For dense arrays, the interparticle coupling can be modified to a large extent by manipulating the array-substrate distance. For instance, it is possible to change the sign of the real part of the dipolar coupling term or even to cancel it out. The imaginary part can also be modified substantially, but to

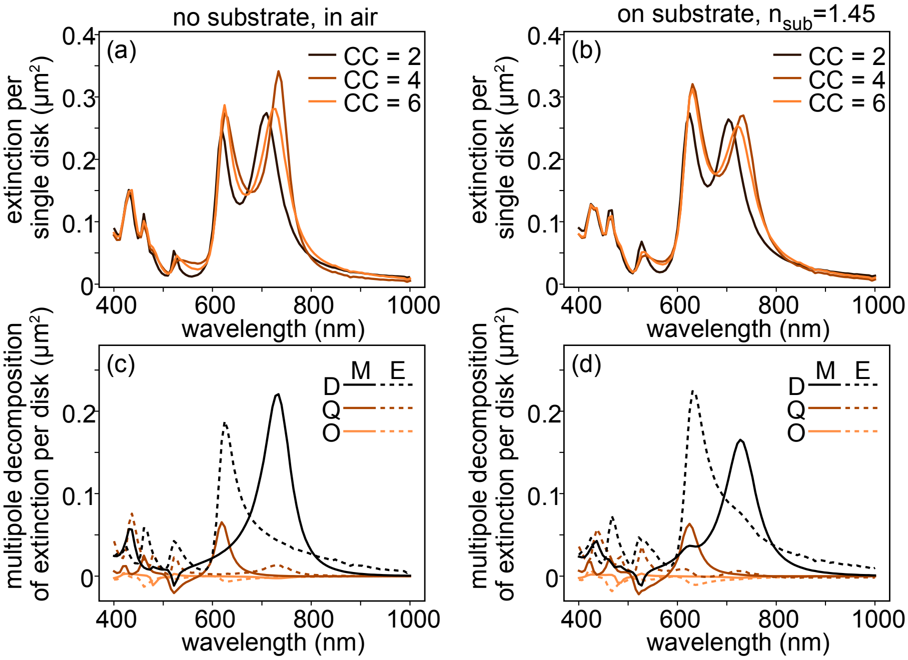

Figure 5.8: Extinction spectra of amorphous arrays of Si nanodisks embedded in varying environments: (a) in air, (b) on a substrate for three different *CC* values. (c,d) Multipole decomposition of extinction spectra presented in (a,b). The results indicate that while qualitatively the extinction spectra are similar, the unique multipole coupling effects in each environment affect how this extinction is split into multipoles.

a lesser degree. In contrast, the dipolar interparticle coupling in sparse arrays is not considerably influenced by the array-substrate distance. At the same time, it is also significantly smaller in comparison with the one obtained for dense arrays. It should be, however, noted, that the overall interparticle coupling in the array is determined not only by the dipolar term, but also by cross-coupling and higher-order terms, which are most often non-negligible.

Finally, we exemplify multipole coupling by considering an amorphous array of nanodisks of c-Si cylinders with D = 150 nm and H = 225 nm embedded in three different environments: in free space, on a substrate with a refractive index of 1.45 to mimic glass (see Fig. 5.8). The spectra for particles on a substrate are qualitatively similar to those obtained in free space with the largest

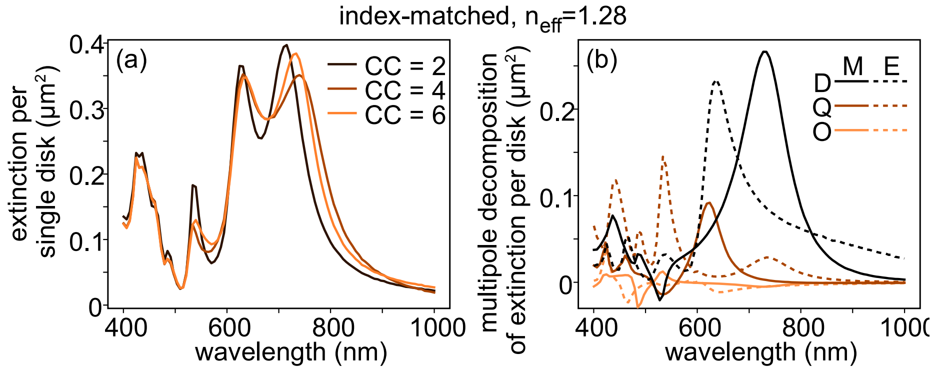

Figure 5.9: Extinction spectra of amorphous arrays of Si nanodisks embedded in varying environments: (a) in an index matched medium for three different CC values. (b) Multipole decomposition of extinction spectra presented in (a). The results indicate that while qualitatively the extinction spectra are similar, the unique multipole coupling effects in each environment affect how this extinction is split into multipoles.

difference being observed for $CC = 4$. For comparison, results for amorphous array embedded in an index matched medium with a refractive index of 1.28 are presented in Fig. 5.9. In this case, the dependence of the spectrum on the minimal center-to-center distance is distinct from the other two. Also, an increased extinction cross-section is observed when the particles are embedded in the indexed matched medium. Because of the fact that instead of accounting for off-substrate reflection, a simple phase shift has been applied, the multiple scattering effect on the array response is approximated poorly by using the index-matched medium.

Studying multipole decomposition of extinction spectra for each environment elucidates further differences between the impact that multiple scattering has on the optical response in each case. The two most prominent features typically correspond to magnetic and electric dipoles. Also, higher order multipoles with smaller amplitudes are observed. In each case, magnetic and electric quadrupole resonances overlap with the main dipolar peaks. The most prominent effect of the coupling between the electric and magnetic dipole is observed when the particles are placed on a substrate. It is not present in any of the other two cases without a substrate. A significant increase of the electric dipole contribution around the magnetic dipole resonance for a substrate-supported array is a clear indicator of this effect. A similar effect is observed at the electric dipole resonance wavelength. In this case the effect is more complex, because the resonance actually contains a considerable contribution from the magnetic quadrupole and a non-zero contribution from the electric quadrupole, which is due to a larger than unity H/D ratio. Consequently, all four multipoles couple together as indicated by an enhanced magnetic dipole and electric quadrupole response.

5.4 Density as a handle for applications

The capability to modify the optical response by manipulating the scaling parameter CC is useful to adjust the optical response to make it suitable for a specific application/optical device. In this section we look at three standout cases of devices based on amorphous arrays of dielectric nanoresonators: directional scatterers, refractometric sensors and solar energy harvesting devices.

5.4.1 Directional scattering

We start by investigating how to obtain directional scattering by amorphous arrays of high index dielectric nanoparticles featuring an electric and magnetic dipole response. As shown earlier in this thesis, directional scattering effects have been observed for isolated particles, as well as nanoparticles forming a periodic nanoparticle array. Here, we show using our FOD model that similar effects may be observed in random arrays. The backward to forward scattering cross-section ratio is given by

$$\frac{C_b}{C_f} = \left| \frac{\alpha_e^* - \alpha_m^*}{\alpha_e^* + \alpha_m^*} \right|^2 , \tag{5.18}$$

where α_e^* and α_m^* are obtained using eq. 5.17. Minimizing the numerator and denominator will lead to minimal backward and forward scattering, respectively, and thus to the lattice Kerker effects in the corresponding directions.

Using eq. 5.18, the lattice Kerker effects conditions are found for forward,

$$\frac{(\alpha_e + \alpha_m) - 2\alpha_e \alpha_m S_{EE}}{(1 - \alpha_m S)(1 - \alpha_e S_{EE})} = 0, \tag{5.19}$$

and backward scattering cross-sections,

$$\frac{\alpha_e - \alpha_m}{(1 - \alpha_m S)(1 - \alpha_e S_{EE})} = 0. \tag{5.20}$$

Then, the backward to forward scattering cross-section ratio is given by

$$\frac{C_b}{C_f} = \left| \frac{\alpha_e - \alpha_m}{(\alpha_e + \alpha_m) - 2\alpha_e \alpha_m S_{EE}} \right|^2 . \tag{5.21}$$

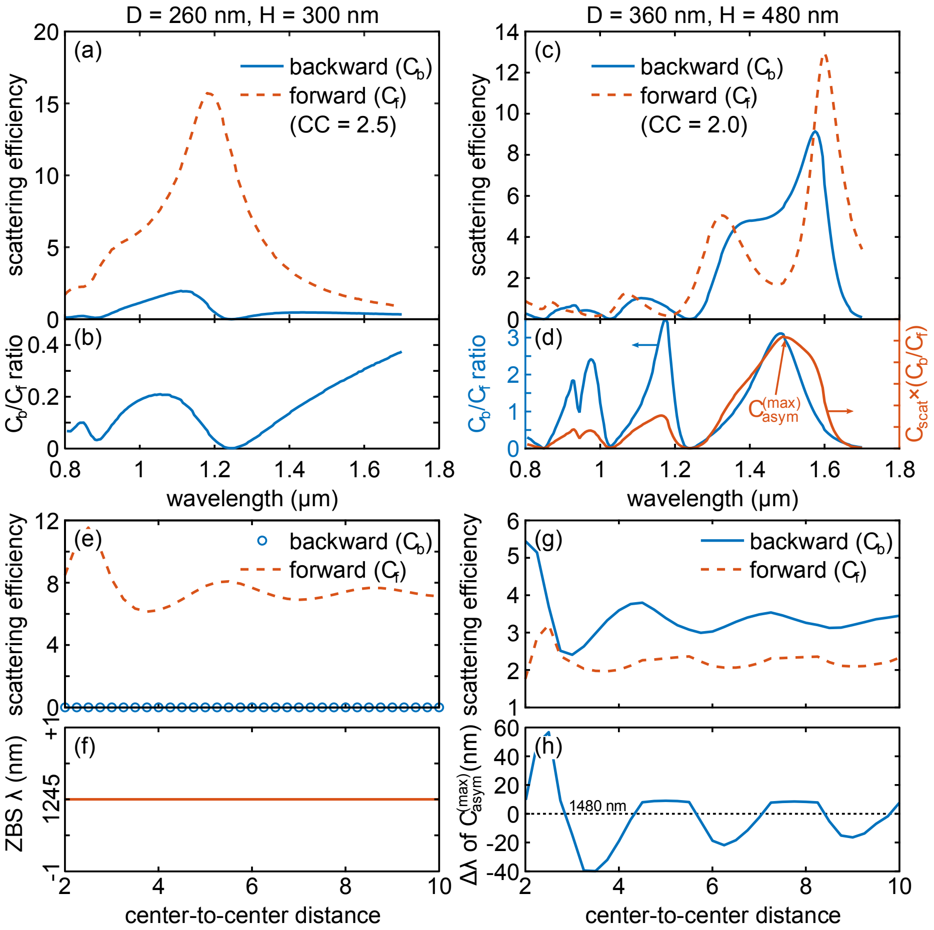

Figure 5.10: Analysis of forward and backward scattering of amorphous arrays of silicon nanodisks (left column: D = 260 nm, H = 300 nm; right: D = 360 nm, H = 480 nm) a), c) Forward and backward scattering efficiency spectra. b), d) Backward to forward scattering cross-section ratio. Additionally, this ratio multiplied by the total scattering cross section C_{asym} is plotted in d), which is a figure of merit used to maximize directionality towards backscattering, while maintaining high scattering efficiency. e), g) Backward and forward scattering efficiencies at 1245 nm in e) and 1480 nm in g) as a function of CC. f) Wavelength at which zero backward scattering occurs does not depend on CC value. h) In contrast, wavelength corresponding to maximum of C_{asym} varies as a function of CC.

In order to illustrate directional scattering effects we have selected two examples: Si nanodisks 260 nm in diameter and 300 nm in height, used to observe backward scattering suppression, and Si disks 360 nm in diameter and 480 nm in height to observe maximal backward scattering with a simultaneous significant suppression of forward scattering. The C_f and C_b spectra for amorphous arrays formed by those particles are presented in Fig. 5.10a,c, while corresponding backward to forward scattering cross-section ratios are presented in Fig. 5.10b,d. For the smaller disk, a lattice Kerker effect in the backward direction is observed at 1245 nm, while for the larger one forward scattering is near zero at approx. 1175 nm leading to a large backward to forward scattering cross-section ratio of about 3. At the same time, we find the second effect not to be important for practical applications, because despite forward scattering is indeed suppressed, the total scattering cross-section is also small, which means that the device would not be efficient. Therefore, we devise a different figure of merit for maximizing backscattering at suppressed forward scattering which is

$$C_{asym} = C_{scat}\frac{C_b}{C_f}. \tag{5.22}$$

This figure of merit is maximized at 1480 nm, where forward scattering efficiency is about 2, but backward scattering is over 5, which results in a large contrast in forward and backward scattering at a large overall scattering cross-section.

The lattice Kerker conditions given by eq. 5.20 and 5.19 lead to interesting consequences regarding directional scattering effects. The ZBS condition (eq. 5.20) does not depend on the interparticle coupling term. Instead, it only requires for single-particle electric and magnetic dipole polarizabilities to be equal. This is indeed confirmed in Fig. 5.10f. Simultaneously, the forward scattering cross-section at the wavelength fulfilling the ZBS lattice Kerker condition depends on the interparticle coupling term and in turn on CC as shown in Fig. 5.10e. In contrast, maximizing our figure of merit for maximal backscattering requires balancing both single particle polarizabilities, as well as, interparticle coupling. As shown in Fig. 5.10g observing a high figure of merit requires a dense array and the observed value depends significantly on CC. For CC of about 3, equal values of back- and forward scattering are observed. Also, the wavelength that corresponds to the maximum figure of merit depends on CC by virtue of eq. 5.19. This dependence is presented in Fig. 5.10h.

5.4.2 Sensing

We consider that the pinnacle of the applications presented here is refractometric sensing with high-index dielectric nanoparticles, which, in contrast to plasmonic counterparts, are not characterized by large intrinsic sensitivities. Instead, as

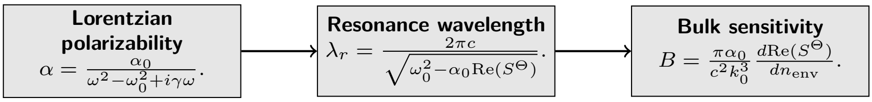

Figure 5.11: Schematic representation of the theoretical procedure used to obtain the bulk sensitivity of amorphous arrays of dielectric nanoparticles

we show here, the mechanism responsible for refractometric sensing of a bulk environment of the nanoparticles is in fact multiple scattering that may be introduced either by placing nanoparticles in an array or on a dielectric substrate. The theoretical procedure is outlined in Fig. 5.11.

As a starting point we use eq. 5.17, which has direct implications for refractive index sensing with an amorphous array of dielectric nanoparticles. We consider a dipole with polarizability α that can be modeled as a Lorentzian oscillator with amplitude α_0, resonance at λ_0 and damping 2γ,

$$\alpha = \frac{\alpha_0}{\omega^2 - \omega_0^2 + i\gamma\omega}. \tag{5.23}$$

We assume that these parameters do not depend on the refractive index of the nanoparticle environment (n_{env}) to show that even if the resonance of an individual nanoparticle is insensitive to change in the nanoparticle's environment, the sensitivity of an amorphous array to the refractive index can still be considerable. The effective polarizability of the array can be presented in the Lorentzian form using eqs 5.17 and 5.23,

$$\alpha^* = \frac{\alpha_0}{\omega^2 - \omega_0^2 + i\gamma\omega + \alpha_0 S_{EE}^{\Theta}}. \tag{5.24}$$

Here we use the Heaviside approximation for the PCF to obtain the coupling factor S_{EE}^{Θ}. Consequently, the polarizability of the amorphous array depends on the refractive index of the environment regardless of sensitivity of the individual particle due to the dependence of S_{EE}^{Θ} on the refractive index. From the denominator of eq. (5.24) we find that the resonance of the array appears at

$$\lambda_r = \frac{2\pi c}{\sqrt{\omega_0^2 - \alpha_0 Re(S_{EE}^{\Theta})}}. \tag{5.25}$$

We define bulk refractive index sensitivity, $B = \frac{d\lambda_r}{dn_{\mathrm{env}}}$, and evaluate the derivative for the resonance of amorphous array by utilizing eq. 4.49 to obtain the analytical formula

$$B = -\frac{2\pi^2 c\alpha_0\sigma l_{cc}^{-1}\left(k_0^2 l_{cc}^2 n\cos(k_0 l_{cc} n_{\mathrm{env}}) + 2k_0 l_{cc}\sin(k_0 l_{cc} n_{\mathrm{env}})\right)}{2(\omega_0^2 - \pi\alpha_0\sigma l_{cc}^{-1}(\cos(k_0 l_{cc} n_{\mathrm{env}}) - k_0 l_{cc} n_{\mathrm{env}}\sin(k_0 l_{cc} n_{\mathrm{env}}))^{3/2}}. \tag{5.26}$$

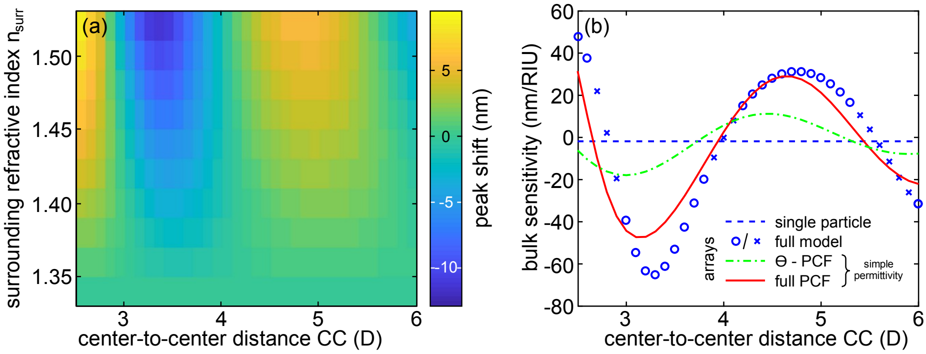

Figure 5.12: Refractometric sensing with amorphous arrays of $n = 4$ nanospheres with D=160 nm. (a) Resonance wavelength as a function of n_{env} and minimal-center-to-center distance CC. (b) Comparison of bulk sensitivity between isolated nanosphere and amorphous arrays. For amorphous arrays full FOD model is compared to approximations using Lorentzian polarizability and either complete or Heaviside theta part of PCF.

The denominator of the equation can be approximated by ω_0^3. Introducing $\beta = \pi^2\alpha_0 C_0 c^{-2}$ the formula can be rewritten as

$$B = -\frac{\beta}{k_0^2 l_{cc}^2}\left(k_0 l_{cc} n_{\mathrm{env}} \cos(k_0 l_{cc} n_{\mathrm{env}}) + 2\sin(k_0 l_{cc} n_{\mathrm{env}})\right). \qquad (5.27)$$

This result, although approximate, indicates that while the optical response of an isolated nanoparticle is not sensitive to the refractive index of the environment, multiple scattering is influenced by the phase difference between the incident and scattered fields and hence the entire system acts like an interferometer. The optical response depends on the wavelength in the surrounding medium and in turn on the refractive index of the environment. Indeed, as shown in Fig. 5.12a, the dependence of the magnetic dipole peak position as a function of the center-to-center distance is distinct for each n_{env} value. Also, note how eq. 5.27 indicates that bulk sensitivity B is a nonlinear function of n_{env}. Consequently, the parameters of the system have to be tuned to maximize sensitivity in a desired n range. At the same time, the examples provided in this work show that this nonlininearity is small enough to enable detecting changes that are observed in a typical sensing scenario ($\Delta n \ll 1$).

The concept of bulk sensitivity enhancement by forming the amorphous array is exemplified by comparing sensitivity of an isolated Mie sphere with refractive index of 4 and 160 nm diameter and an array of such spheres. An isolated particle has near zero sensitivity towards the refractive index of the environment

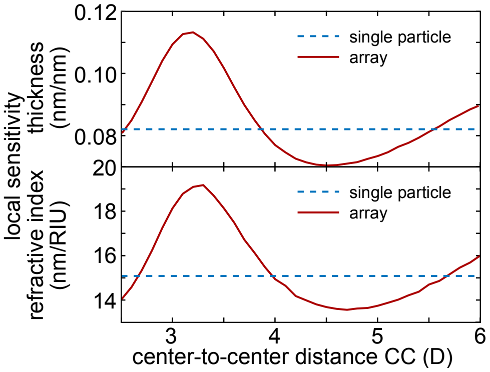

Figure 5.13: Refractometric sensing with amorphous arrays of $n = 4$ nanospheres with D=160 nm. Local sensitivity of an amorphous array and isolated particle obtained by considering nanospheres decorated with a thin layered of sensed material.

in the selected range of n_{env}, because the sphere itself is nondispersive and the magnetic dipole resonance is in general a geometric resonance i.e. it requires matching both refractive index and particle size to observe a resonance even for small particles. In turn, the magnetic dipole polarizability is suitable to be approximately described using eq. 5.24. When an amorphous array is formed out of Mie spheres, bulk sensitivity can be significant (despite the array being constructed of dielectric particles), that is reaching up to 65 nm/RIU (see Fig. 5.12b). As in case of any other property related to the optical response, we observe an oscillatory behavior of bulk sensitivity as a function of CC. The sign of bulk sensitivity can be positive or negative depending on CC choice, meaning that either a shift of the peak position towards red or blue will be observed, respectively. Also, due to this dependence on CC, the CC choice can lead to strong amplification, but when selected improperly to sensitivity suppression, as well. In Fig. 5.12b we compare the bulk sensitivity of an isolated Mie sphere with that of the amorphous array obtained using different approximations. While eq. 5.27 is good for qualitative explanation of the bulk sensitivity mechanism, it is insufficient to obtain quantitative agreement with the results obtaining by direct numerical calculation using eq. 5.17 and PCF in form of eq. 4.23. The agreement is vastly improved by considering the full PCF in eq. 5.27 instead of Heaviside theta, further justifying our use of Lorentzian polarizability and the proposed mechanism.

A different mechanism from which nanoresonator based sensors can benefit by multiple scattering in amorphous array is the enhancement of local sensitivity.

We model this case by considering core-shell particles in which the role of the core is played by the nanoresonator itself, while the shell is a thin layer of sensed material. As shown in Fig. 5.13 electromagnetic coupling in amorphous array may enhance the local sensitivity of the thin layer by up to 40%.

In addition to spherical high-index dielectric nanoresonators, we have also considered high-index dielectric nanodisks as suitable candidates for all-dielectric refractometric sensors and the impact of the electromagnetic coupling on their sensitivity. As shown earlier in this thesis, their optical response is far more tunable by selecting the particle aspect ratio and hence even an isolated particle can have non zero sensitivity. Thus, they have been considered as a candidate for refractometric sensor prior to our work (see the introduction chapter). Here, we have focused on understanding the bulk sensitivity mechanism. Despite, the fact the disk sensitivity towards n_{env} is non-zero, the main mechanism responsible for the observed sensitivity in amorphous arrays is also electromagnetic coupling. This is indicated by a strong dependence of the sensitivity on CC regardless of disk size as shown in Figs 5.14. Bulk sensitivity oscillates as a function of the sensed refractive index with an oscillation frequency determined by a scaling factor $k_0 l_{cc} n_{\mathrm{env}}$, which can be rationalized by eq. 5.27. This means that geometry of the nanodisk must be optimized to obtain maximal sensitivity and linear sensor response for a given analyte.

The geometric parameters of a nanodisk influence the bulk refractive index sensitivity of amorphous arrays formed with nanodisks by modifying the single particle sensitivity, resonance amplitude and scaling factor $k_0 l_{cc} n_{\mathrm{env}}$ that determines the phase relationship between incident and scattered fields. The FOD model enables efficient study of these effects. We choose the detected refractive index to be close to 1.33, which is the refractive index of water and find CC value maximizing bulk sensitivity as a function of aspect ratio and diameter of the nanodisks. The results are presented in Fig. 5.15a. The optimal CC values range from 2 to 5. This indicates that sufficiently dense arrays are required, so the impact of multiple scattering is substantially large. The optimal CC values tend to be especially low for nanodisks with small diameters and aspect ratios. The converse is true for nanodisks with large diameters and high aspect ratio. In Fig. 5.15b we show the maximal attainable bulk sensitivity for each nanodisk geometrical parameters. In general, its value increases with increasing aspect ratio and nanoparticle diameter.

As shown here, practical realization of refractometric sensors based on dielectric nanoresonators requires multipole coupling by multiple scattering. In publication I, this can be done by forming an amorphous array of nanoresonators and thus introduce intraarray coupling. Another way of introducing multiple scattering is to place a particle on a substrate and exploit self-coupling and substrate-mediated interparticle coupling as well. In Fig. 5.16a we consider

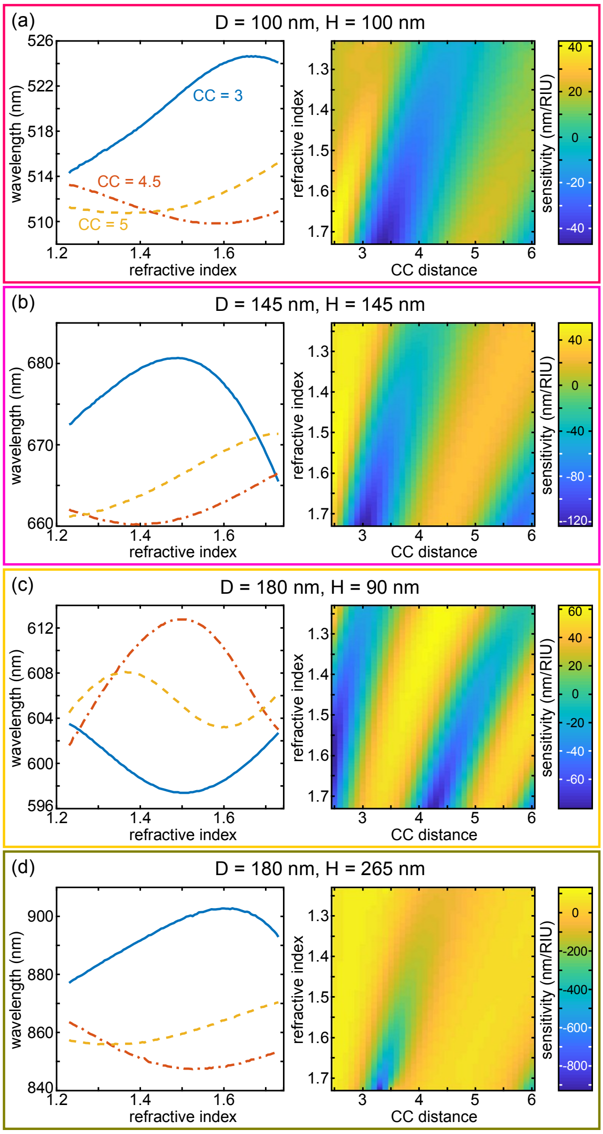

Figure 5.14: Impact of electromagnetic coupling on bulk refractive index sensitivity of amorphous arrays of Si nanodisks. (a-d) Line plots of resonance wavelength for selected CC values as a function of environment indicate that each nanoparticle geometry and CC combination leads to a distinct, nonlinear sensor response. Maps present bulk sensitivity plotted against n_{env} and CC.

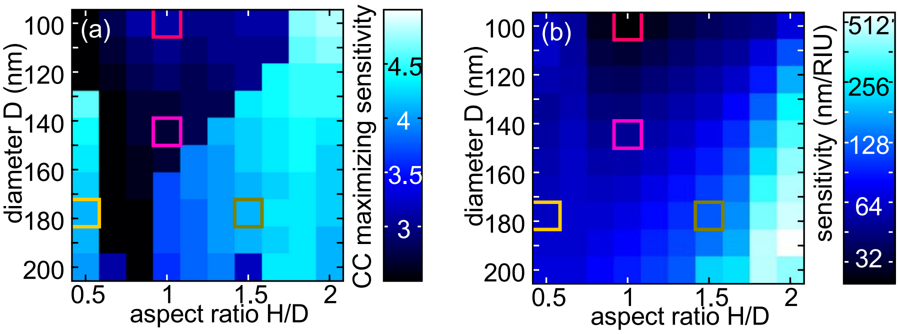

Figure 5.15: Impact of nanodisk geometry on bulk refractive index sensitivity of amorphous arrays of Si nanodisks. a) CC value maximizing bulk sensitivity for n_{env} of 1.33 (water) as a function of nanodisk geometry parameters. b) Bulk sensitivity values corresponding to CC selected in a).

an isolated particle placed on a substrate and study the impact of the substrate by modifying its refractive index. Indeed, the bulk sensitivity may be substantially amplified or suppressed by choosing the refractive index of the substrate adequately. Similarly, the sign of the bulk sensitivity is influenced by choice of the substrate material.

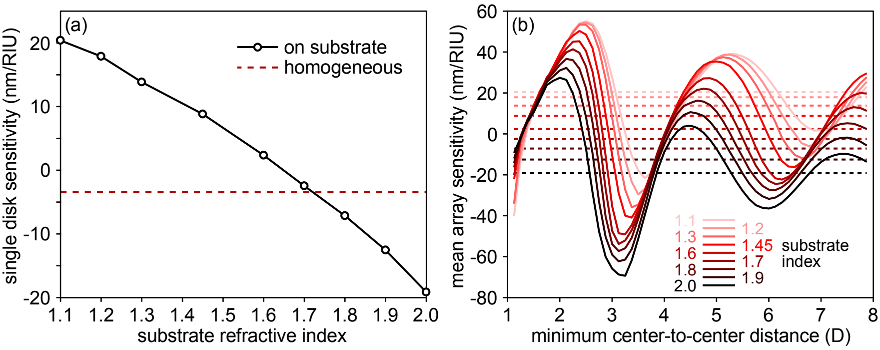

Figure 5.16: Bulk sensitivity of silicon nanodisks with $D = 160$ nm and $H = 160$ nm. a) Bulk sensitivity of an isolated nanodisk plotted against substrate refractive index. Bulk sensitivity in homogenous environment is added for comparison. b) Bulk sensitivity of amorphous array (solid lines) as a function of CC and isolated particles (dashed) lines. The result is averaged over n_{env} from 1.33 to 1.53.

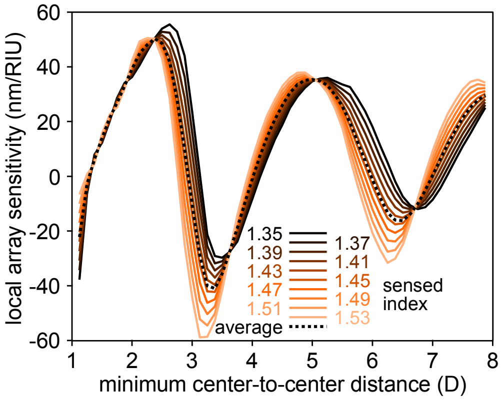

Figure 5.17: Bulk sensitivity of amorphoust arrays of silicon nanodisks with D = 160 nm and H = 160 nm without averaging over n_{env} for $n_{sub} = 1.45$ for a set of n values and corresponding average bulk sensitivity value.

When a substrate-supported amorphous array is used as a refractometric sensor, the sensitivity mechanism involves an interplay of all three coupling mechanisms. Substrate-mediated coupling depends not only on the refractive index of the antenna's environment via the scaling parameter CC, but also via the Fresnel reflection coefficients (see eq. 10.15 in Appendix A). As an extreme example, substrate-mediated coupling vanishes when the sensed medium has the same refractive index as the substrate. Perhaps, the most profound effect of the substrate is that it affects the limiting value when the array is diluted. Consequently, the sensitivity is shifted by a constant substrate dependent value regardless of CC choice. For substrate-supported arrays, the intraarray coupling leads to interference between reflected and direct scattered fields with phase relationship that is different than for an array in free space. This modified phase relationship manifests itself in sensitivity curves shown in Fig. 5.16b and hence, sensitivity maxima and minima as a function of CC depend on the choice of the substrate material. The response of the sensor is nonlinear with respect to the sensed refractive index in a similar manner to a free space array as shown in Fig. 5.17. While in general, the obtained sensitivity values for each refractive index of the environment are similar to the average one, the effect is especially pronounced with increasing CC value.

In conclusion, when designing all-dielectric refractometric sensors for monitoring changes of the bulk refractive index of the environment, different aspects of the system have to be accounted for. While it might seem that the most important factor is the nanoresonator geometry, in fact if simple shapes such as

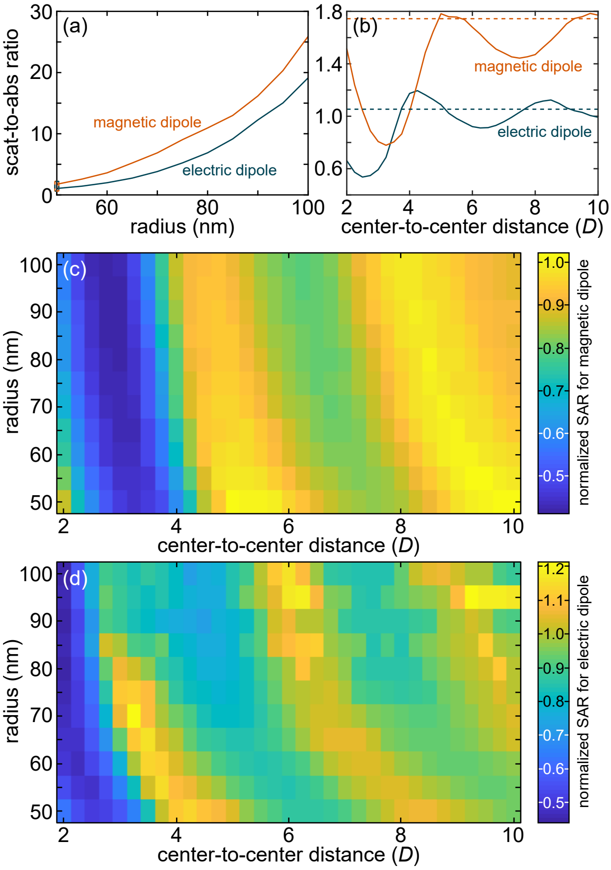

Figure 5.18: a) Scattering-to-absorption ratio (SAR) of isolated Si nanospheres. b) SAR for amorphous arrays composed of 100 nm diameter Si nanospheres (solid lines). Dashed lines indicated corresponding values for an isolated nanosphere. c), d) SAR for amorphous arrays of Si nanospheres plotted against particle radius and minimal center-to-center distance at magnetic and electric dipole resonance, respectively. SAR for an array is normalized in c) and d) to the single-particle counterpart.

spheres or disks are considered, the geometry is only important in determining the resonant frequency (frequencies) of the system. The key factors that may be manipulated to obtain an effective sensing device are the spatial arrangement of the nanoresonators and the substrate refractive index. They determine electromagnetic coupling, which is the main bulk sensing mechanism. The parameters should be selected in tandem as the resulting sensitivity stems from an interplay between various coupling channels.

5.4.3 Scattering to absorption ratio

The scattering to absorption ratio is an all important quantity for solar energy harvesting applications that, as discussed in the previous chapter, can be substantially modified by manipulating CC for plasmonic nanoparticles. Here, we focus on the case of high-index dielectrics, which exhibit both electric and magnetic resonance for which SAR may be manipulated. SAR for individual silicon nanospheres is shown in Fig. 5.18a. In general, SAR is relatively high for this type of nanoresonators and it rapidly increases with particle size, not only because that is the general tendency as shown by Antosiewicz et al.,[12] but also because with increasing particle size, the resonances are shifted towards larger wavelengths in which the intrinsic absorption of silicon is smaller. In contrast to the refractometric sensing example, here, the dominant factor determining SAR is still the single particle, but electromagnetic coupling is a factor that can be used to influence the SAR value. Multiple scattering in amorphous arrays embedded in a homogeneous material can substantially influence its SAR as indicated by the results presented in Fig. 5.18b. Specifically, SAR can be diminished by a factor of approximately 50% by appropriate choice of CC enabling reaching SAR below unity for small spheres. This minimum is almost independent on particle size and always reached for CC between 2 and 4 as shown in Fig. 5.18c for electric dipole resonance and Fig. 5.18d for magnetic dipole resonance. This effect may be promising for solar harvesting using silicon nanoresonator arrays as it enables maximizing absorption in the nanoparticles forming the arrays.

5.5 Optical properties of size dispersed amorphous arrays

FOD and FOM models enable modelling of amorphous arrays assuming that an array consists of identical particles. However, in practice, the arrays are oftenmost composed of nonidentical particles, as a result of experimental fabrication imperfections or a deliberate attempt to manipulate the optical response of the system. In this section we study the optical properties of size-dispersed amorphous nanoparticle arrays. To that end, we modify the minimal nanoparticle distance condition to $l_{cc} = CC(r_1 + r_2)$, where r_1 and r_2 are the nanoparticle radii. In turn, the condition may be different for each nanoparticle pair depending on nanoparticle sizes. The modified condition enables clustering of small particles around larger ones, which alters the nanoparticle spatial distribution. Thus, size

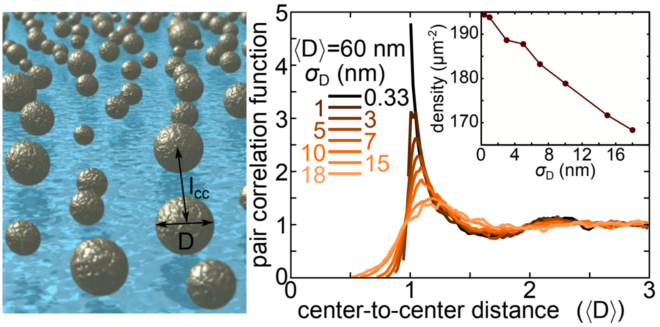

Figure 5.19: a) Schematic representation of amorphous array of size dispersed nanoparticles. b) Pair correlation function of amorphous array of size dispersed nanoparticles with mean diameter of 60 nm and varying diameter standard deviation. Inset - density varies with standard deviation of nanoparticle diameter.

dispersion influences optical properties in a two-fold manner: via modification of the average non-interacting nanoparticle polarizability and via modification of multiple scattering due to altered nanoparticle spatial distribution. We address both of these effects using a combined T-matrix and extended FOD model study.

5.5.1 Modified random sequential adsorption algorithm

The modified RSA algorithm is employed in order to generate amorphous random patterns consisting of size dispersed nanoparticles. We assume that an experimental nanoparticle diameter distribution is known and is a normal distribution with a mean value $\langle D\rangle$ and a standard deviation σ_D. The interparticle center-to-center distance of each nanoparticle pair with radii (r_1,r_2) is constrained by the $l_{cc} = CC(r_1 + r_2)$, which replaces the standard acceptance condition. The main difficulty that we tackle here is to assert that the constructed (modelled) nanoparticle size distribution is identical to that of the experimental one.

Naively, one could simply sample the experimental size distribution in order to obtain the nanoparticle sizes, which is a valid solution for sparse packings. However, as the number of adsorbed particles increases and the remaining space to be occupied by particles decreases, there is an increasing skew of the particle size distribution towards small nanoparticles and deviations from a normal distribution will be substantial. Instead of such a direct approach, we draw the nanoparticle sizes from a uniform sampling distribution with size range $[-3\sigma_D, 3\sigma_D]$. In order to obtain the target size distribution, we perform the following procedure. First, we generate a histogram of the desired size distribution. The total number of particles in the histogram is determined by $N = N_0\langle D\rangle^2(\sum_i D_i^2 x_i)^{-1}$, where x_i

is fraction of particles contained in ith histogram bin and D_i is the corresponding nanoparticle. Then, at each simulation step a particle size is drawn from a uniform distribution and its acceptance is determined by constraint $l_{cc} \geq CC(r_1+r_2)$ in a similar manner to standard RSA. Next, if the particle passes the spatial test, we check the number of particles in the histogram bin corresponding to the particle size. If it is larger than zero, we accept the particle and decrease the number of particles in the corresponding bin by one. Else, we reject the sample. Despite the fact that the size in this algorithm is no longer truly random, its histogram corresponds to the experimental one and it is randomly assigned to each particle.

Now we introduce the spatial characteristics of the arrays generated using the modified RSA algorithm. We calculate the PCF using the procedure outlined in Chapter 4. In Fig. 5.19 we present a pair correlation functions for amorphous arrays with varying size dispersion σ_D and $CC = 1$. Increasing σ_D leads to a decreased PCF in the vicinity of the mean particle diameter as a consequence of modified minimal center-to-center distance, which is now distinct for each pair of nanoparticle sizes. Also, the Heavyside theta is smoothed out, because particle pairs may have distances smaller than $\langle D \rangle$ if their diameters are both smaller than $\langle D \rangle$. With increasing size dispersion, the number density of the array decreases, which is required to maintain a Gaussian distribution of the particles.

5.5.2 Multiple scattering in size dispersed arrays

The description of an amorphous array of size dispersed nanoparticles can be approached within a film of dipoles framework in which each nanoparticle is described by an induced point dipole with polarizability α that depends on the material, size and shape of the nanoparticle. We discretize the nanoparticle size distribution and, consequently, their polarizability is determined by the average particle of given size α_e^*, which consists of the corresponding single particle value modified by interparticle coupling. In order to find α_e^*, we consider a set of equations describing the polarization of an average sphere of a given size assuming that the exciting field consists of the incident field $\vec{E}_{inc}$ and the scattered field from all other dipoles $\vec{E}_{scat}$ (the sum in the brackets of the following equation)

$$\vec{p}_i = \alpha_{e,i}^* \vec{E}_{inc} = \alpha_{e,i} \Big(\vec{E}_{inc} - \sum_{\text{dipole types}} \alpha_{e,j}^* S_{ij} \vec{E}_{inc} \Big). \tag{5.28}$$

Instead of summing over individual nanoparticles, we utilize the continuous film approach in which the retarded dipole potential is multiplied by the PCF and integrated over the entire 2D space:

$$S_{ij} = \frac{1}{4\pi\varepsilon_0} \sigma n_j \int_{l_{CC_{ij}}}^{\infty} \int_0^{2\pi} r dr d\theta e^{ikr} \left[\frac{(1-ikr)(3\cos^2\theta - 1)}{r^3} + \frac{k^2 \sin\theta}{r} \right] g_{ij}(r), \tag{5.29}$$

where σ is the nanoparticle number density, n_j is concentration of nanoparticles of j-th size, $l_{cc_{ij}}$ is the minimal center-to-center distance between nanoparticles of i-th and j-th size and $g_{ij}(r)$ is radial distribution function for nanoparticles of i-th and j-th size. We consider that each pair may have a different PCF, since in closely packed arrays small nanoparticles may cluster around larger ones resulting in a situation in which the average exciting field varies depending on nanoparticle size. For each pair of sizes a fitting procedure is performed with an analytical function that is integrable with the dipole potential in eq. 5.29, as shown in the previous subsection.

The equation set for the polarizability defined by eq. 5.28 written in matrix form is

$$\vec{\alpha}_e^* = \vec{\alpha}_e - \begin{pmatrix} \alpha_{e,1}S_{1,1} & \alpha_{e,1}S_{1,2} & \cdots & \alpha_{e,1}S_{1,N} \\ \alpha_{e,2}S_{2,1} & \alpha_{e,2}S_{2,2} & \cdots & \alpha_{e,2}S_{2,N} \\ \vdots & \vdots & \ddots & \vdots \\ \alpha_{e,N}S_{N,1} & \alpha_{e,N}S_{N,2} & \cdots & \alpha_{e,N}S_{N,N} \end{pmatrix} \vec{\alpha}_e^*. \tag{5.30}$$

The solution to the above equation is then obtained by matrix inversion:

$$\vec{\alpha}_e^* = \begin{pmatrix} 1+\alpha_{e,1}S_{1,1} & \alpha_{e,1}S_{1,2} & \cdots & \alpha_{e,1}S_{1,N} \\ \alpha_{e,2}S_{2,1} & 1+\alpha_{e,2}S_{2,2} & \cdots & \alpha_{e,2}S_{2,N} \\ \vdots & \vdots & \ddots & \vdots \\ \alpha_{e,N}S_{N,1} & \alpha_{e,N}S_{N,2} & \cdots & 1+\alpha_{e,N}S_{N,N} \end{pmatrix}^{-1} \vec{\alpha}_e. \tag{5.31}$$

As it can be seen in case when only a single type of dipoles is used to describe the nanoparticle properties this solution reduces down to the known solution for the average dipole polarizability in an infinite dipole array. We evaluate the total extinction spectrum as $C_{ext} = \frac{k}{\varepsilon_0}\sum_{i=dipole\,types} x_i \mathrm{Im}(\alpha_{e,i}^*)$ with x_i being the number fraction of nanoparticles of i-th size. The benefit of using eq. 5.31 instead of solving the coupled dipole equations with explicit nanoparticle positions is that instead of a set of equations for each particle, we reduce the problem dimensionality, which is given by the number of discretization bins.

In Fig. 5.20 we show the calculation results from our method and T-matrix method for $\langle D\rangle = 60$ nm and varying σ_D. Both methods are in good quantitative agreement. Thus, our method enables studying the optical properties of size-dispersed amorphous arrays of nanoparticles without the computational burden of T-matrix simulations with an explicit nanoparticle distribution. In subsequent paragraphs we describe main conclusions of this study.

Similarly to the case of mono-size-dispersed amorphous arrays, the size-dispersed ones tend to exhibit an oscillatory behavior of the optical properties as a function of the scaling parameter CC. Size dispersion modifies this behavior in a two-fold manner: by introducing nonidentical nanoparticle polarizabilities and by modifying the spatial arrangement of nanoparticles. As a representative example, in

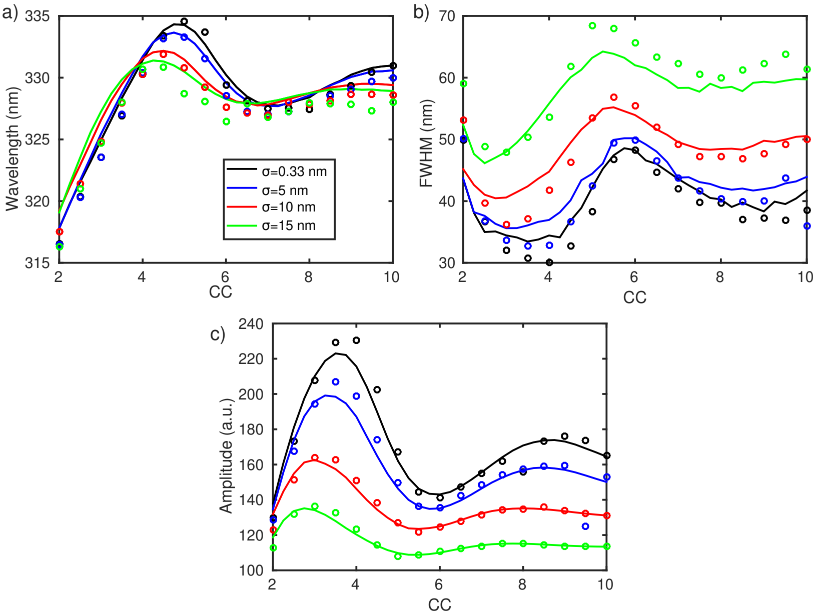

Figure 5.20: a) Localized plasmon resonance wavelength, b) width and c) amplitude as a function of CC parameter for size-dispersed amorphous nanoparticle arrays with $\langle D \rangle = 60$ nm and varying σ_D. Solid lines correspond to values obtained with our effective model, while circles denote the results of T-matrix calculations.

Fig. 5.20a we study the position of LSPR, which is known to be influenced by CC (see eq. 4.51). For small CC values ($CC < 3$), the arrays are sufficiently dense so that the interparticle coupling is contributes strongly to the optical response and the impact of size dispersion is almost negligible. With increasing CC the phase spread of the scattered field coming from particles of different sizes increases and the impact of interparticle coupling decreases. This is indicated by quicker damping of LSPR wavelength oscillations with CC in size-dispersed arrays than mono-dispersed ones. In the case of mono-dispersed arrays the oscillations are clearly visible up to $CC \approx 10$, while no clear trends may be observed for $CC \approx 6$ for $\sigma_D = 0.15$. Size dispersion affects the asymptotic LSPR position for sparsely distributed nanoparticles. The direction of this asymptotic LSPR shift for increasing size variation is related to the mean nanoparticle size. While for large nanoparticles (with mean diameter of 60 nm or more) increasing size dispersion leads to a decrease of the resonance wavelength, the presence of size variation in nanoparticle arrays with small mean diameters causes a redshift of the resonance wavelength. We relate this to the dependence of the extinction efficiency on nanoparticle size. Its value decreases with increasing nanoparticle diameters for diameters above 40 nm.

As expected, the extinction spectra are broadened by introducing size dispersion and above a diameter standard deviation of 10 nm the initial resonance width for the case of diluted arrays with an uniform nanoparticle size can no longer be retrieved by manipulating the array density (see Fig. 5.20b). The positions of local extrema of FWHM depend on the standard deviation of the nanoparticle diameter and they are shifted towards smaller CC values with increasing nanoparticle size variation. Global minima of the FWHM are observed for dense arrays with CC ranging from 2 to 4 depending on σ_D. This CC range might be optimal for spectral control of resonances because in that range LSPR wavelength changes rapidly with CC and the peak width is relatively small. The FWHM reaches its maximal value for CC between 5 and 6. At CC of about 7, the FWHM reaches its plateu that is determined by σ_D value.

The extinction amplitude is also affected by interparticle coupling as shown in Fig. 5.20c. In general, the amplitude decreases with increasing size dispersion and the magnitude of amplitude oscillations with CC becomes shallower with increasing size dispersion. In turn, for size dispersed arrays their LSPR amplitude is determined by the size distribution rather than the nanoparticle spatial arrangement. The maxima of extinction amplitude coincide with FWHM minima and vice versa.

5.5.3 Scattering-to-absorption ratio in size-dispersed arrays

Among the properties affected by size dispersion and interparticle coupling is the SAR at LSPR of the amorphous array. Size dispersion affects SAR even if interparticle coupling is negligible due to the presence of particles with different polarizabilities, as SAR of a nanoparticle is roughly proportional to the magnitude of the polarizability. At the same, interparticle coupling can modify SAR significantly and in size dispersed arrays it is also influenced by the standard deviation of the nanoparticle size. In Fig. 5.21 we present SAR as a function of CC for a broad set of $\langle D\rangle$ and σ_D. With increasing $\langle D\rangle$ SAR quickly increases which is a known effect shown previously.[12] For sparse arrays, SAR increases as size dispersion is increasingly pronounced. The impact of interparticle coupling is especially large for the smallest particles for which SAR can be modified by almost an order of magnitude and interparticle coupling influence decreases with increasing $\langle D\rangle$. Introducing size dispersion diminishes the amplitude of SAR oscillations and it shifts SAR maxima and minima towards denser arrays.

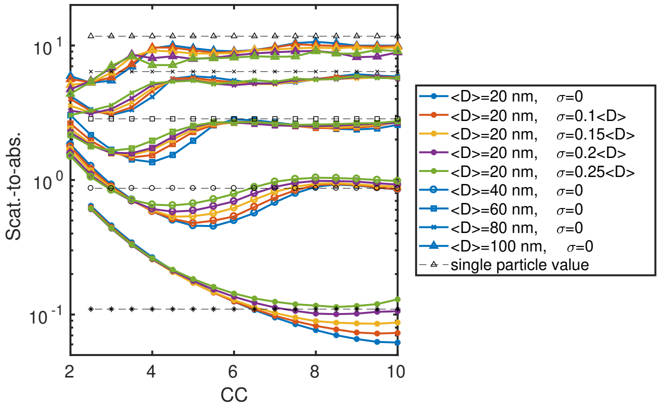

Figure 5.21: Scattering-to-absorption ratio of amorphous arrays of size-dispersed nanoparticles as a function of scaling parameter CC for selected values of mean diameter $\langle D\rangle$ and diameter standard deviation σ_D. Dashed lines indicate SAR for an isolated particle with $\langle D\rangle$ diameter.

The impact of interparticle coupling leads to an universal behavior of SAR as a function of the parameter kl_{cc} in monodispersed amorphous arrays of plasmonic nanoparticles. While the matrix equation eq. 5.31 does not allow for an

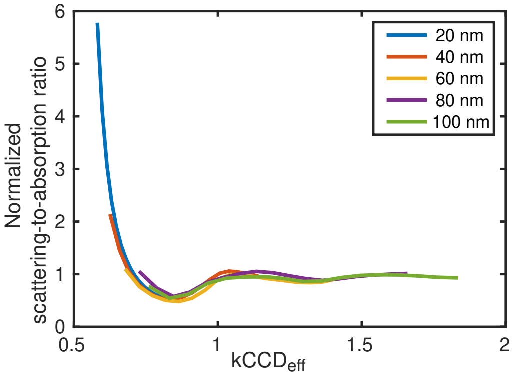

Figure 5.22: Universal scaling of scattering-to-absorption ratio (SAR) of amorphous arrays of size-dispersed nanoparticles normalized to SAR for isolated particles averaged over nanoparticle size distribution as a function of universal scaling parameter $kCCD_{eff}$ with $D_{eff} = \langle D\rangle + \sigma_D$.

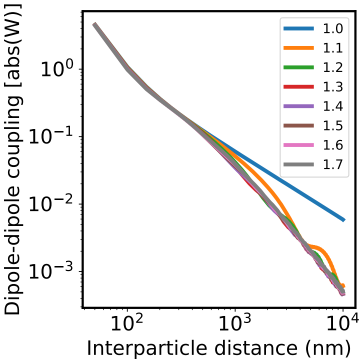

Figure 5.23: Dipole-dipole coupling matrix element as a function of interparticle distance for selected values of substrate refractive index.

analytical solution that could enable finding an analogous parameter for size-dispersed arrays, we have found out that SAR normalized to the SAR value for isolated particles averaged over the nanoparticle size dispersion indeed behaves universally with the scaling parameter $kCCD_{eff}$ with effective particle diameter $D_{eff} = \langle D \rangle + \sigma_D$. This effective particle diameter compensates for the phase shift introduced by size dispersion in SAR oscillations presented in Fig. 5.22. The relation between the universal scaling parameter and normalized SAR may be used to quickly estimate the resulting SAR for a specific application. It also marks the attainable limits of modifying SAR by tailoring the array density using the CC parameter.

5.6 Numerical aspects

In this section we summarize the numerical aspects of calculating the optical response of the amorphous arrays of nanoresonators using the FOM approach with a special focus on substrate supported arrays.

5.6.1 Sommerfeld integrals

Sommerfeld integrals appear both in the self-coupling as well as substrate-mediated interparticle coupling. While a well-known issue of choosing a suitable integration contour has been addressed in the previous chapter, the other issue, which is the long-distance value of the coupling matrix entries in the substrate-supported case is addressed here. In Fig. 5.23, we show how the absolute value of the dipole-dipole coupling matrix element depends on the distance for various refractive

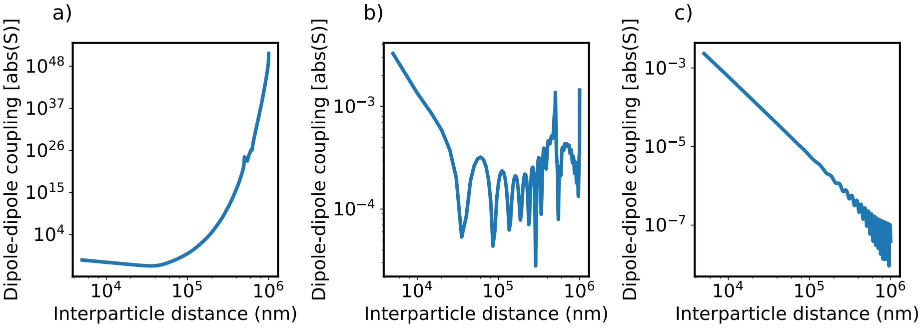

Figure 5.24: Dipole-dipole coupling matrix element as a function of interparticle distance for a substrate with refractive index of 2 for selected values of Sommerfeld contour resolution n_{eff}^{max} and deflection of the contour into imaginary plane n_{eff}^{imag}. a) $n_{eff}^{max} = 10^{-3}$, $n_{eff}^{imag} = 10^{-2}$, b) $n_{eff}^{max} = 10^{-3}$, $n_{eff}^{imag} = 10^{-4}$, c) $n_{eff}^{max} = 10^{-4}$, $n_{eff}^{imag} = 10^{-4}$

.

indices of the substrate. In general, we anticipate that the coupling magnitude will decrease with increasing distance. The asymptotic behavior of those terms is driven by the two other parameters n_{eff}^{imag} (deflection of the integration contour into the imaginary axis), n_{eff}^{res} (contour resolution).

Deflection into the imaginary axis is mainly necessary to address singularities of the coupling matrix that stem from the evanescent modes of the layered medium. Because for a simple two-layer medium there are no such modes (except for substrates made of noble metals, where SPPs are present) this can be safely set to a very low value. The contour resolution increases as n_{eff}^{res} decreases (it is simply an n_{eff} step). The n_{eff} and distance form a Fourier pair meaning that as the maximal interparticle under consideration increases the n_{eff}^{res} should decrease. On the other hand, decreasing n_{eff}^{res} increases simulation time. To show how the asymptotic values of the coupling matrix elements are affected by the choice of the aforementioned parameters, we have plotted selected results in Fig. 5.24. By default n_{eff}^{imag} is set to 10^{-2} and the resolution is set to 10^{-3}. As shown in Fig. 5.24a, in such a case after an initial decrease of coupling matrix element with distance, a rapid increase occurs leading to irrationally large coupling matrix magnitudes. This behavior is mitigated by setting n_{eff}^{imag} to a lower value of 10^{-4}. Then the result no longer has a tendency to grow rapidly, however still it does not behave monotonically (see Fig. 5.24b). To observe the expected behavior one has to set both the resolution and the deflection into the imaginary plane relatively low (see Fig. 5.24c).

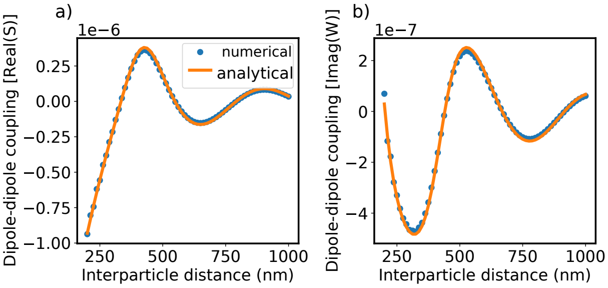

Figure 5.25: Comparison of dipole-dipole mean field integrals (for wavelength of 500 nm) obtained numerically and semi-analytically. a) real part, b) imaginary part.

5.6.2 Mean-field integral

The integral in eq. 5.6 is calculated by integrating the radial part of the coupling matrix calculated using the trapezoidal rule. There are three parameters related to this integral: `Nrho` (number of radial distances), `crit` (maximal distance under consideration), `smalleps` (value of ε in eq. 5.6). The main subtlety is the highly oscillating integral function, especially as the distance approaches infinity. In our previous work we have developed an analytical solution for the dipole-dipole coupling part in a homogeneous environment. To assert that the default choice of parameters (`Nrho` $= 20000$, `crit` $= 140CCD$, `smalleps` $= 10^{-4}$) is sufficiently accurate, we compare the analytical and numerical result of direct coupling integration for a varying minimal center-to-center distance between the nanoparticles at a fixed wavelength of 500 nm in Fig. 5.25. The results match closely, which leads to the conclusion that the numerical integration method with the selected parameters is indeed accurate.

5.6.3 Calculating scattered far-field

The simulation outcomes are average scattering coefficients of a particle in an array. The main useful quantity that can be accurately calculated using the FOD/FOM model is the extinction cross-section, which has been presented for amorphous arrays in several figures of this thesis. However, this is not the only quantity of interest when it comes to light scattering by amorphous arrays. Several quantities such as absorption and scattering cross-sections or far field intensity cannot be easily calculated using the model, because they are proportional to (depend on) the absolute value of the scattered field. This poses two issues. The first one is that we therefore need to consider the interference pattern formed

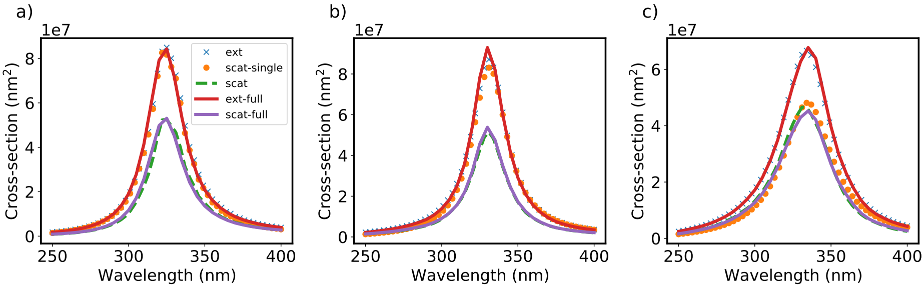

Figure 5.26: Comparison between various methods of obtaining cross-section spectra for amorphous arrays of plasmonic nanospheres of 30 nm radius with varying center-to-center distance a) $3D$ b) $4D$ c) $5D$, where D is the particle diameter. Solid lines indicate scattering and extinction cross-sections obtained with SMUTHI. Dashed lines indicate scattering cross-sections calculated using the interference procedure outlined in the main text, while dots indicate scattering cross-sections calculated using the FOM model without the interference procedure. Extinction cross-section obtained with FOM is marked by dots.

by the scattered fields of the particles. The second issue is that the mean value of any property that is proportional to the absolute value of the scattered field depends on the variance of scattering coefficients. While the latter is beyond the scope of this thesis, the first one can be addressed with the current model, although in a simplified manner.

To obtain the far-field interference pattern within the mean-field approximation, one can find the average scattering coefficients and then interfere the effective scattered fields from several point sources whose locations obey the spatial statistics of the simulated array. In case of an amorphous array, the simplest way to do this is to simulate the particle positions using random sequential adsorption algorithm.

To see how this works in practice, we propose three examples. The first one is an array of plasmonic nanospheres (30 nm radius) embedded in air. The plasmonic nanospheres tend to have large scattering cross-sections and therefore they exhibit strong interparticle coupling in arrays, especially in air. The second case is an array of dielectric nanodisks embedded in air, which is to be compared with the final example, which is the same array, but placed on a dielectric substrate with a refractive index of 2.

In Fig. 5.26 we present the results for three values of the minimal center-to-center distance: $CC = 3D$, $CC = 4D$, $CC = 5D$, where D is the particle diameter (60 nm). To test the accuracy we have calculated the result with SMUTHI

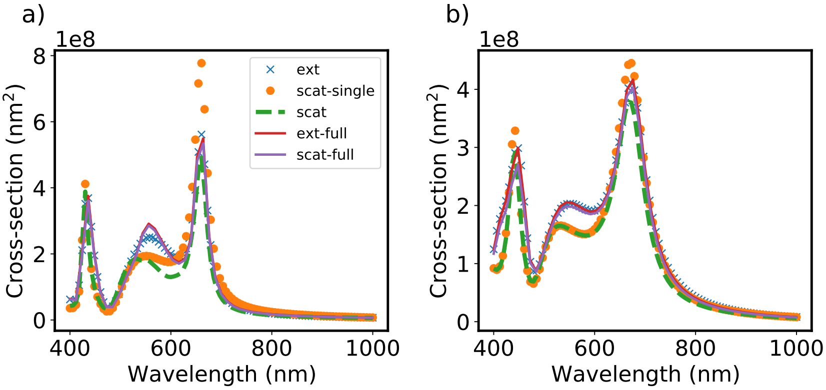

Figure 5.27: Comparison between various methods of obtaining cross-section spectra for amorphous arrays of dielectric nanodisks with radius of 75 nm and height of 120 nm. The minimal center-to-center distance is fixed at $3D$. a) no substrate b) dielectric substrate with refractive index of 2.

without any averaging procedure. Regardless of the center-to-center distance, the extinction spectrum calculated with the proposed method very accurately reproduces the one obtained with SMUTHI. For the scattering cross-section, the results obtained without considering the interference of the mean scattered fields are not accurate except for the largest center-to-center distance. In contrast, when the interference is accounted for, the accuracy is very high except for the largest center-to-center distance, where it is the same as the result obtained without taking the interference into account.

Lastly, we have performed similar tests for dielectric nanodisks at a fixed minimal center-to-center distance of $3D$ for the case without a substrate and with a substrate with refractive index of 2. The extinction spectrum is again reproduced most accurately. For dielectric particles, the scattering cross-section spectrum is far less accurately calculated than in plasmonic case. If interference is omitted, the error is very large for the case without the substrate. However, the spectra are very similar when the particles are placed on a substrate.

5.6.4 Outlook

The method proposed in this work can be efficiently used to predict the extinction cross-section spectra of amorphous arrays of nanoresonators on dielectric substrate. The agreement between the results obtained with the effective T-matrix method in comparison with other methods is satisfying. At the same time, there are still certain aspects to be improved. The stationary phase method could be used to mitigate the issue of far range substrate-mediated coupling. Also, it could be a good step forward to enable far-field calculations without resorting to numerically generated arrays, which is the limitation of the current code.

Chapter 6

Absorption of light in the antenna-reactor system

Nanoscale antenna-reactor systems may be used to mitigate the limited applicability of plasmonic metals such as silver or gold for plasmon mediated catalysis. This is achieved by incorporating a (non-noble) transition metal catalyst into the system and rational management of absorption enhancement. As shown in previous experimental studies, such absorption enhancement is correlated with the catalytic reaction rate.[9] The mechanism responsible for the observed absorption enhancement is electromagnetic coupling between a plasmonic nanoantenna and the adjacent palladium nanoparticles. In this chapter we discuss enhancing absorption in catalytic nanoparticles. We perform an extensive numerical study of the antenna-reactor system at the level of a single plasmonic nanoantenna decorated with catalytic nanoparticles and investigate factors that impact the absorption. In the publication IV this study has been complimented by experimental realization of the antenna-reactor system and an optical study.

6.1 Methods

Finite-difference time-domain (FDTD) simulations have been performed with Lumerical FDTD Solutions to study the role of shell and core properties in optical absorption enhancement within catalytic nanoparticles. An exemplary nanodisk with a diameter of 80 nm and height of 20 nm is chosen, while the shell thickness (unless otherwise mentioned) is 5 nm. We include tapering and rounding of the disk in our simulations with tapering angle of 20°, bottom rounding radius of 2 nm and top rounding radius of 5 nm, for consistency with experimental

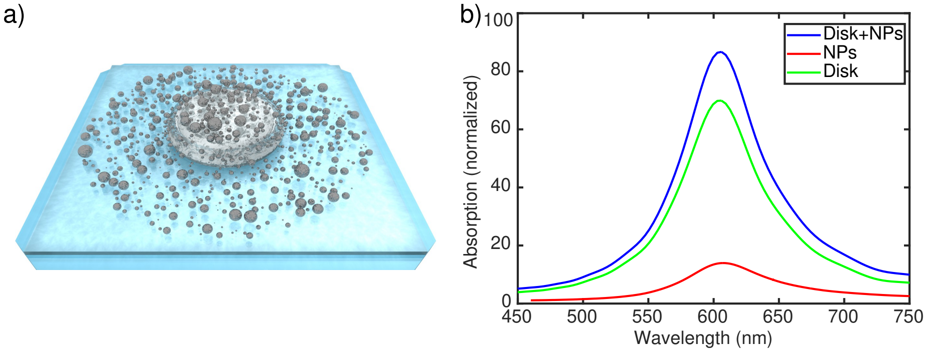

Figure 6.1: a) Schematic representation of antenna-reactor complex containing a core-shell plasmonic nanoantenna placed on a substrate and decorated with transition metal (palladium) particles. b) Optical absorption spectra of exemplary antenna-reactor complex including absorption in the entire system, in the plasmonic nanodisk and absorption in palladium nanoparticles.

conditions. Catalytic Pd nanoparticles are modelled as spheres with two Gaussian radius distributions depending on nanoparticle-disk center distance: 4.15 ± 2.7 nm diameter on top of the disk and away from the antenna and 2 ± 1.6 nm for particles at disk side wall. The equivalent thickness of Pd nanoparticle layer is 1 nm. This data is obtained from SEM/TEM images of experimental samples. For each core-shell antenna, we simulate several realizations of spatial distributions of catalytic nanoparticles. Pd nanoparticles are distributed within a circle with 200 nm diameter centered at the core-shell nanoparticle center by simulating a random sequential adsorption process assuming no overlap between palladium nanoparticles. An exemplary simulated system is schematically presented in Fig. 6.1a. Four different metals have been used as nanoantenna core material - Al, Ni, Au and Ag. The nanoantenna shell has refractive index of 1.68 (alumina). All material data has been taken from Palik.[148] The nanodisk and particles have been meshed with minimum mesh size of 0.5 nm. As the Pd nanoparticles do not have a plasmon resonance in the optical range for this size, this mesh size choice is adequate.

Total absorption is calculated by integrating the Poynting vector over a box containing both the core-shell and palladium nanoparticles. Absorption in the core-shell nanodisk is calculated as a difference between total absorption and absorption within the catalyst. In order to find the absorbed power in each palladium particle, we monitor the electric field in each particle and use eq. 2.73 to evaluate absorption. Absorption enhancement is defined as the ratio between absorption in palladium nanoparticles surrounding the core-shell nanodisk and

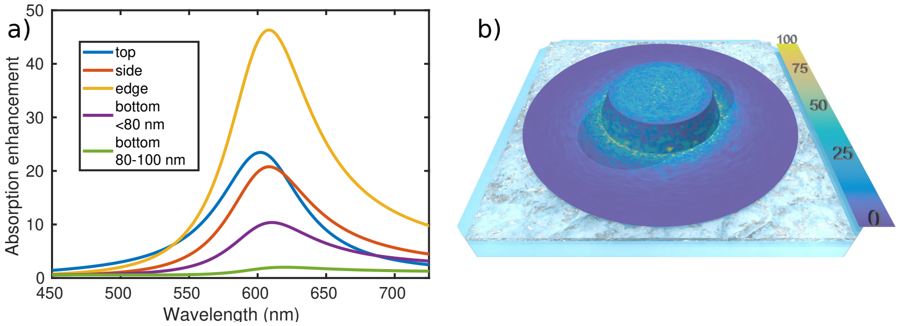

Figure 6.2: a) Relation between absorption enhancement and wavelength for a set of positions of nanoparticle in the system. b) The map of absorption enhancement within Pd nanoparticles. The wavelength of incident light is 600 nm to match the LSPR wavelength of the core-shell nanoantenna.

absorption in a layer with the same spatial distribution placed on a substrate without the antenna. In our simulations, we used a total field/scattered field source with 300x300 nm^2 size.

6.2 Spatial distribution of absorption enhancement

Calculation of absorption enhancement in individual Pd particles placed on a nanodisk enables studying its spatial distribution. Since we have a stochastic distribution of various sized particles, a large number of calculations is required for high quality enhancement vs. position map (see Fig. 6.2). The result is averaged azimuthally to obtain an unpolarized light radial distribution. It can be clearly seen that the absorption enhancement depends on the distance between the nanoparticle and disk center. The antenna can be split into zones with similar absorption enhancement: top of the disk, disk side-walls, disk edge, bottom of the disk (<80 nm from the disk center), rest of the simulation domain (>80 nm from the disk center). This enables an analysis of the dependence of the enhancement on the wavelength in each of the zones as presented in Fig. 6.2. Absorption in Pd nanoparticles reaches the maximal value in nanoparticles placed at the side-wall interface of the Ag core-shell particle and decreases with increasing distance from that position. The reason behind this is that the field enhancement distribution is maximized at the interface of the high refractive index support. High absorption enhancement values are also attainable at the upper rim of the nanoantenna, which is due to large field enhancement observed at sharp edges

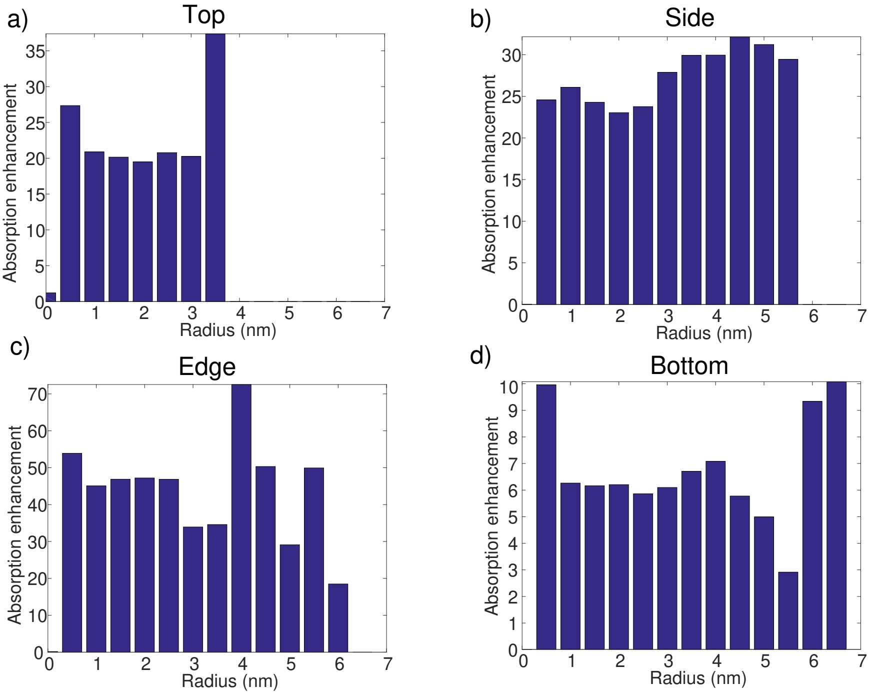

Figure 6.3: Absorption enhancement in Pd nanoparticles as a function of Pd nanoparticle radius for varying positions on the core-shell disk. The incident light wavelength is 600 nm to match the LSPR wavelength of the core-shell nanoantenna.

of the nanoantenna. Notably, the resonance wavelength of absorption is shifted from the value in Fig. 6.1b depending of the particle position.

As a result of performing calculations for a broad variety of Pd nanoparticle configurations, we can also analyze the dependence of the enhancement on particle radius as presented in Fig. 6.3. Regardless of the considered nanoparticle position, no clear relation between the absorption enhancement and nanoparticle radius has been observed within the examined nanoparticle radius range. Thus, we conclude that the absorption enhancement depends on the position rather than size for small Pd nanoparticles used in the simulation. This highlights the importance of the spatial distribution of the nanoparticles with respect to the nanoantenna core in the context of maximizing plasmon mediated catalysis effects and thus constitutes an important design rule for such systems.

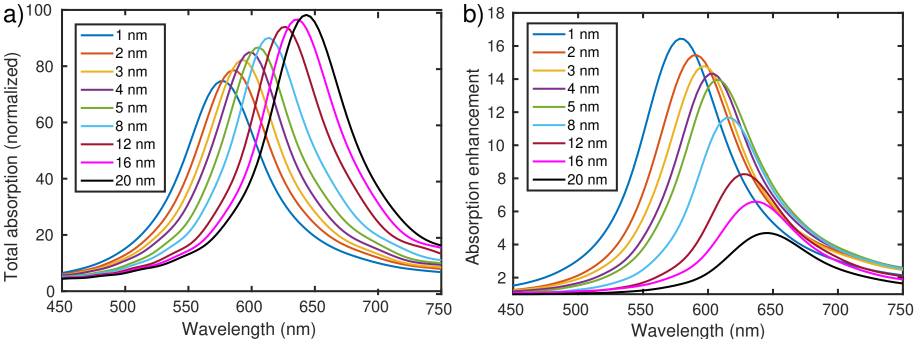

Figure 6.4: Absorption in the system as a function of wavelength for various Al_2O_3 shell thicknesses: (a) total absorption (b) absorption enhancement within the catalytic nanoparticles.

6.3 Absorption engineering

6.3.1 Influence of shell thickness

We have also analyzed how absorption within the catalyst and core-shell nanodisk depends on the properties of the nanodisk, as well as on the thickness of the nanodisk shell. Total absorption normalized to absorption within the catalyst layer without the nanodisk is presented in Fig. 6.4. The increase in shell thickness results in a resonance redshift and an increase in total absorption. Both of these effects occur due to increased antenna volume. This is accompanied by a decrease of energy absorbed within Pd nanoparticles at the resonance wavelength. The observed absorption enhancements range from the maximal value of 16 for a shell thickness of 1 nm down to 4 for a 20 nm thick shell. With increasing shell thickness, the distance between palladium nanoparticles and the antenna increases, diminishing the field intensity at the reactor particles. This effect leads to the observed decrease in absorption enhancement. As a consequence, a decrease of the splitting factor with increasing shell thickness is observed (the relation is plotted for 600 nm wavelength in Fig. 6.5). Tailoring the shell thickness is crucial when designing the antenna-reactor system. On one hand, optimizing optical absorption in catalytic nanoparticles promotes using thinner shells, while at the same time maintaining structural stability calls for increasing shell thickness.

6.3.2 Influence of disk material

The experimental method proposed by prof. Langhammer's group in publication IV enables using various materials for core layer of the nanoantenna. Here, we

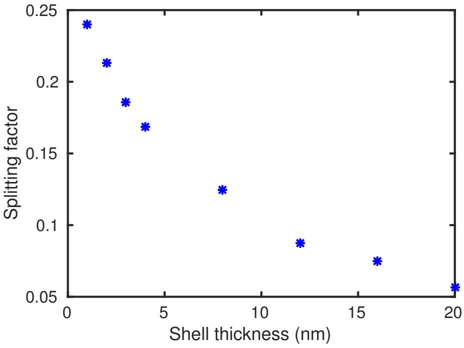

Figure 6.5: Splitting factor of absorption between Pd nanoparticles and core-shell nanodisk as a function of shell thickness.

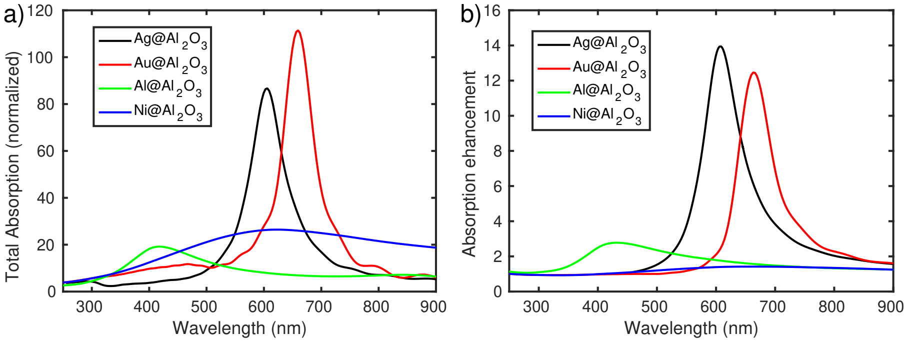

Figure 6.6: Comparison of (a) total absorption and (b) absorption enhancement in Pd nanoparticles in the systems containing nanodisks with various metals.

use plasmonic metals including Ag, Au, Al, and a non-plasmonic metal, Ni. Total absorption and absorption enhancement in nanoparticles for each tested metal is presented in Fig. 6.6. Systems containing silver and gold share similar properties, but absorption in the system with the Au disk is redshifted from the corresponding response of the system with silver. While the total absorption in system with the Au disk is increased with respect to silver disk, it is a consequence of parasitic absorption in the Au disk itself rather than the desired absorption enhancement in Pd nanoparticles.

Using other metals (Al and Ni) for the nanoantenna results in a substantial decrease in absorption enhancement. For aluminum, enhancement is still present, especially in the 400-450 nm wavelength range, where using silver or gold does

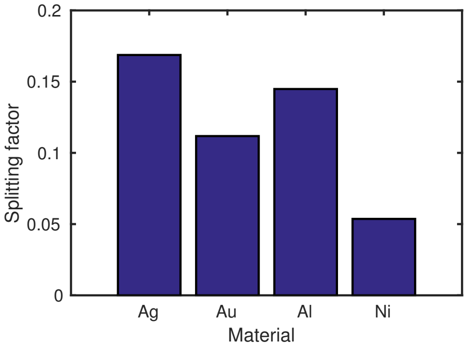

Figure 6.7: Splitting factor of absorption between Pd nanoparticles and core-shell nanodisk as a function of shell thickness.

not result in large enhancement factors. In contrast, barely any enhancement can be observed when Ni is used. Two effects contribute to decreased absorption enhancement. First, Al has larger losses than the other two (Au and Ag), which decreases the field enhancement. The second effect is related to the fact that the LSPR for Al disk occurs in UV range. In this range palladium nanoparticles exhibit higher absorption compared to the visible range. Absorption enhancement is a relative quantity and thus a larger amount of energy needs to be absorbed in palladium nanoparticles for the same enhancement to be seen in the UV range as in the visible.

For additional comparison, we examine the splitting factors for each disk material (see Fig. 6.7) at its resonance wavelength. It can be clearly seen that the silver disk enables obtaining the largest splitting factor. This is a direct consequence of overall lowest intrinsic losses in silver out of all plasmonic metals. Also note, that the splitting factor in Al is relatively large, despite the overall smaller absorption. On the other hand, the wavelength dependence of absorption in the system shown in Fig. 6.6, indicates that the metal choice shall depend on the wavelength range at which the device will operate, of course, it can be further tuned by changes in the antenna size.

6.3.3 Influence of antenna diameter

As shown in Chapter III, the nanoantenna size is an important factor determining the LSPR, influencing both the resonance wavelength as well as the electric field enhancement and extinction amplitude resulting in modified absorption in adjacent Pd nanoparticles in antenna-reactor complexes. In order to investigate the impact of the plasmonic core radius on absorption enhancement, we model

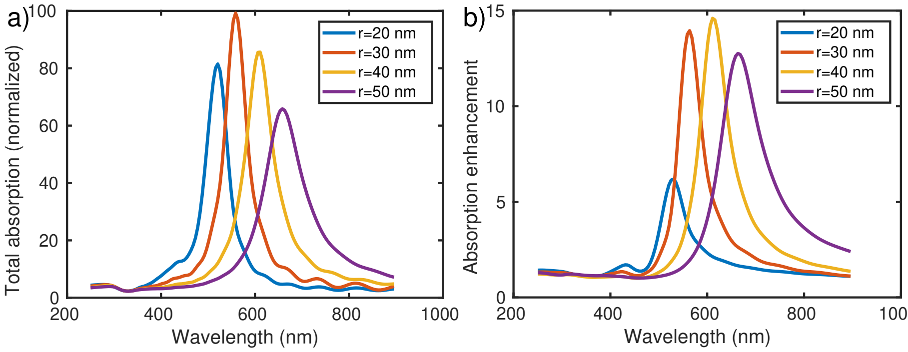

Figure 6.8: Comparison of (a) total absorption and (b) absorption enhancement in Pd nanoparticles in antenna-reactor complexes with nanoantenna containing silver core and varying core radius.

antennas with a varying core radius, while maintaining a fixed shell thickness of 5 nm. The results are presented in Fig. 6.8 for a silver core and in Fig. 6.9 for an aluminum core. The dependence of absorption enhancement on core radius is less pronounced when compared to other factors such as e.g. shell thickness. For Ag, initially, field enhancement increases with increasing radius leading to larger absorption in Pd. For large antenna sizes the depolarization field diminishes the attainable field enhancement and in turn absorption enhancement decreases with increasing radius. When an aluminum core is used, the intrinsic losses in the core

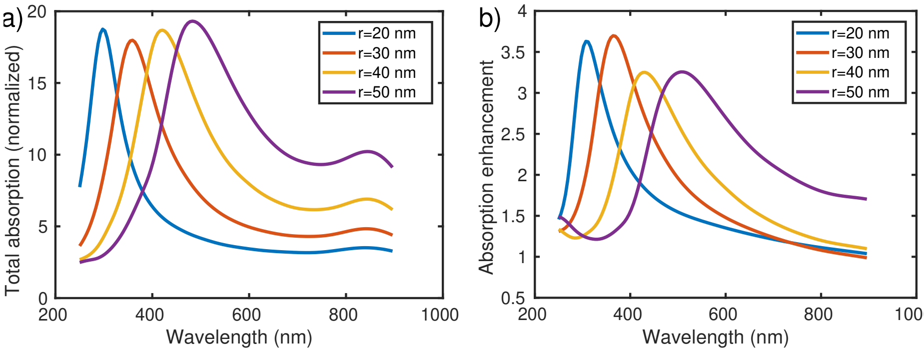

Figure 6.9: Comparison of (a) total absorption and (b) absorption enhancement in Pd nanoparticles in antenna-reactor complexes with nanoantenna containing aluminum core and varying core radius.

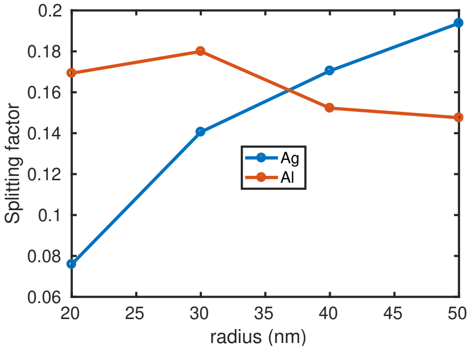

Figure 6.10: Splitting factor of absorption between Pd nanoparticles and core-shell nanodisk as a function of nanoantenna core radius for aluminum and silver core materials.

are substantially larger and they determine the response. Thus, large field and absorption enhancement are not possible and the dependence on antenna size is even weaker than for a silver core antenna. These trends are also observed in the splitting factor results presented in Fig. 6.10. A silver core antenna promotes a large splitting factor, which increases with nanoparticle radius, while a smaller, almost size-independent, value is observed when an aluminum core antenna is investigated.

6.4 Conclusions

We have studied the properties of plasmon mediated absorption and field intensity enhancement in catalytic nanoparticles decorating a core-shell nanodisk with a plasmonic metal core and alumina shell using FDTD simulations. The study enabled us to draw several conclusions regarding rational design of antenna-reactor complexes for enhanced absorption in transition metal nanoparticles. We have shown that the position of the nanoparticle with respect to the disk is an important factor for absorption enhancement in Pd nanoparticles. Additionally, the choice of disk material is essential for achieving high splitting factors and enhancement. The appropriate material should be chosen depending on the wavelength range in which the device should operate. The optimal one should support a strong LSPR, while minimizing the intrinsic losses. The optical response of the system is also influenced by the thickness of the dielectric shell separating the plasmonic disk from the catalytic nanoparticles. A smaller separation leads to increased energy absorption in the nanoparticles. On the other hand, the choice of shell thickness is also dictated by the experimental method. No significant dependence of the analyzed enhancements on catalyst nanoparticle size for nanoparticles with radius $<$10 nm has been observed, but one has to bear in mind that the absorption cross-section scales with nanoparticle volume. At the same time, choice of plasmonic nanoantenna radius is of considerable importance as it enables fine tuning of LSPR wavelength and at the same time influences both the splitting factor and maximal absorption enhancement.

Chapter 7

Optical monitoring of physical and chemical changes during catalysis with antenna-reactor complexes

Antenna-reactor complexes containing plasmonic nanoantennas and catalytic nanoparticles may not only be used as photocatalysts, but also as optical sensors probing chemical and physical processes occurring during catalysis. The main concepts of plasmonic sensing for material science, including catalysis, were reviewed in the Introduction Chapter of this thesis. In a typical sensing experiment, the LSPR wavelength shifts as physical or chemical phenomena occur leading to local modification of the refractive index in vicinity of the plasmonic sensor (or of the sensor itself). Here, we apply electromagnetic modelling to predict the LSPR wavelength shift of an antenna-reactor complex based sensor under modification of various parameters that may result from processes accompanying catalysis. Such a study provides valuable information on how to interpret experimentally observed sensor signals.

7.1 Sensing of core-shell nanoantenna physical and chemical changes during catalysis

In our work aluminum oxide is typically used as a material forming the nanoparticle shell. This material is known for its capability to adsorb nitrogen oxides (NO_x), which is an important process for removing of nitrogen oxides from the combustion engine exhaust gas using catalysts.[149–151] During NO_x uptake the structure of aluminum oxide films changes, altering their thickness as well as their chemical properties.[152,153] Such modifications change the optical properties of the shell which can be detected using a sensor based on an antenna-reactor complex. Here, we model the shift of the LSPR wavelength using the FDTD based approach outlined in Chapter 6. We assume that nitrogen uptake results in the increase of the shell thickness and a change of its refractive index due to chemical binding of NO_x. We also consider the possibility of electron extraction from or to the Au core of the nanoantenna, which we model as a change in the electron density of Au that affects the Drude part of the dielectric function.

Here, as a model of an antenna-reactor complex we use an Au core 80 nm in diameter and 20 nm in height and 2 nm Al_2O_3 layer ($n = 1.768$), as ditctated by accompanying experiments. The equivalent thickness of the Pd nanoparticle layer is 1 nm. The mean Pd nanoparticle diameter is 6 nm, while its standard deviation is equal to 0.85 nm. The palladium nanoparticle layer is modeled explicitly without homogenization. Statistical averaging of extracted quantities is performed over 20 FDTD simulations with different realizations of random drawing process are used for each considered system.

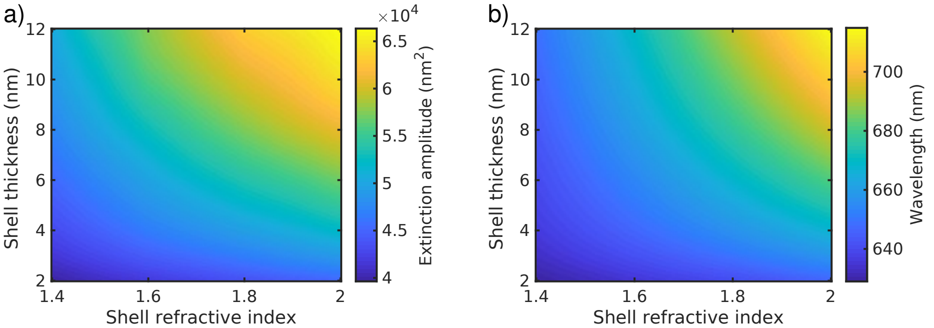

Figure 7.1: Influence of shell thickness and refractive index on optical properties of antenna-reactor complex containing silver core and palladium nanoparticle layer. a) Extinction amplitude and b) LSPR wavelength of antenna-reactor complex based sensor.

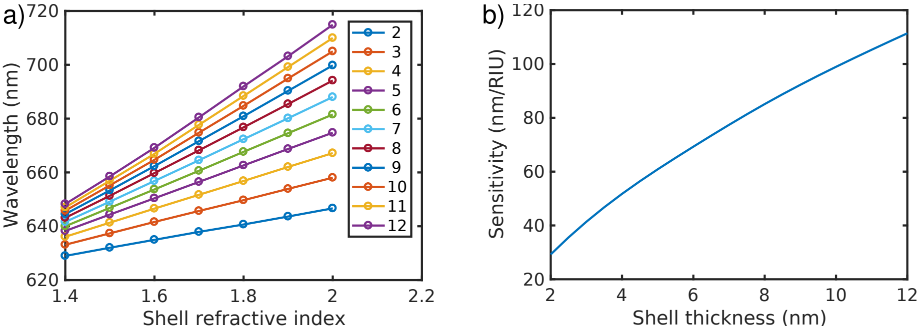

Figure 7.2: a) Linear dependence of LSPR peak wavelength of antenna-reactor complex based sensor on shell refractive index for varying shell thicknesses. b) Sensitivity of the sensor towards change in shell refractive index as a function of shell thickness.

In Fig. 7.1 we present the LSPR wavelength and extinction amplitude dependence on shell thickness and its refractive index. Both parameters affect the LSPR wavelength. Increase of shell thickness leads to a shift of the LSPR wavelength towards red and increase in extinction amplitude at the LSPR wavelength. Similar trends are observed for an increase of the refractive index of the shell, namely with an increasing refractive index of the shell both the wavelength and extinction amplitude increase. The impact of the modification of the refractive index of the shell is larger for thicker shells and vice versa. This means that based on either the LSPR wavelength or extinction amplitude alone one cannot differentiate between a change of the shell thickness and the change of its refractive index. Both quantities are correlated (i.e. they both grow with increase of either shell thickness or shell refractive index change), but, at least in principle, provided sufficient experimental accuracy, modification of shell thickness and refractive index can be resolved by simultaneous measurement of the LSPR wavelength and extinction amplitude.

The dependence of the LSPR peak wavelength on the refractive index of the shell is approximately linear as shown in Fig. 7.2a. Thus, if the shell thickness can be kept constant during a sensing process, the presented antenna-reactor complex could be a suitable sensor for detecting chemical changes at the shell surface that would lead to a modification of its refractive index. The sensitivity of the optical response towards a change of the shell refractive index is presented in Fig. 7.2b. Dependence of the LSPR wavelength on the refractive index of the shell for thicker shells manifests itself by an increase of sensitivity with increasing shell thickness. Sensitivity of up to 110 nm/RIU is attainable for a shell thickness of 12 nm, while the lowest value of 30 nm/RIU is observed for the thinnest shell

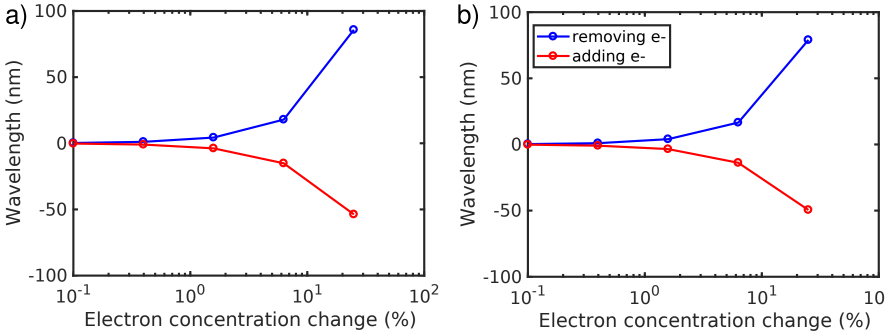

Figure 7.3: LSPR wavelength change upon modification of free electron concentration in golden shell of antenna-reactor complex based sensor for shell thickness of a) 12 nm b) 2 nm.

(2 nm thickness).

Adsorption of chemical species on the surface of the shell thickness may modify the electronic properties of the core due to electron extraction from or injection to gold by the adsorbed species. We model this process by modifying the Drude part of gold permittivity using the following procedure. We utilize experimental permittivity of gold from Palik[148] and split it into a frequency dependent interband and a Drude term. For small frequencies the interband term is small compared to the Drude term. Therefore, we fit the Drude model to that part of the permittivity function and use the fitted model to extract Drude model parameters. We assume that modification of carrier concentration affects only the Drude term and the interband remains unaffected. The interband term is extracted by subtraction of the Drude model within the entire frequency range. The modified gold permittivity is obtained as a sum of the interband term and the Drude term with modified parameters. Here, we assume that electron mobility is not affected by the presence of additional charge carriers or by carrier removal. Thus, the only change that occurs is the modification of the plasma frequency of gold, which is proportional to the square root of the carrier concentration. Thus,

$$\omega_{p,mod.} = \omega_p \sqrt{1 + \delta N}, \tag{7.1}$$

where $\omega_{p,mod.}$ and ω_p are, respectively, the modified and unmodified plasmon frequencies and δN is the fraction of added/removed electrons.

Modifying the carrier concentration in gold leads to an LSPR wavelength change as shown in Fig. 7.3. Because the plasma frequency of gold is increased by the presence of additional carriers, adding electrons to the gold core of the nanoantenna leads to a decrease of the LSPR wavelength. The converse happens if electrons are removed from the core. The observed LSPR wavelength shifts are larger when electrons are removed than when they are added, because the wavelength is inversely proportional to frequency. Considering that free electron concentration in gold is large, the change in carrier concentration required to observe a substantial LSPR wavelength shift is large. Approximately, a 1 nm shift is observed for a 4% change in carrier concentration. Due to an overall stronger optical response, the effect of free electron concentration modification is larger for nanoparticles with a thicker shell.

7.2 Gradient effective medium model

Antenna-reactor complexes contain randomly distributed small transition metal nanoparticles whose sizes are characterized by some distribution which evolves e.g. due to sintering during catalysis. Tackling such randomness requires significant effort in both time and computational resources, as one typically performs statistical averaging by explicit modeling of multiple different structural arrangements of particles in these random processes. An example of such an approach of studying antenna-reactor complexes is presented in the previous chapter. An alternative route, which does not require multiple simulations, uses the Maxwell-Garnett effective medium theory which was reviewed in Chapter 3. The effective medium theory assumes that the incident field is uniform and that the particles are distributed uniformly within the host medium. This is, however, not the case for nanoplasmonic sensors and antenna-reactor complexes that exhibit LSPR. Specifically, the electromagnetic field of the surface plasmon polariton or LSPR decays over distances which may be as small as tens of nanometers. Such strong field gradients require a different approach than the Maxwell-Garnett effective medium theory. To mitigate this issue and extend the applicability of the effective medium theory towards strong field gradients present in plasmonic nanosensors, we propose a gradient effective medium (GEM) model that incorporates a permittivity gradient with a spatial dependence determined by the inhomogeneous spatial distribution of nanoparticles.

7.2.1 Model derivation

The gradient effective medium model is based upon the Maxwell-Garnett effective medium model in which permittivity of the homogenized heterostructure is given by

$$\varepsilon_{eff} = \varepsilon_m \frac{2\delta(\varepsilon_i - \varepsilon_m) + \varepsilon_i + 2\varepsilon_m}{2\varepsilon_m + \varepsilon_i + \delta(\varepsilon_m - \varepsilon_i)}, \tag{7.2}$$

where ε_{eff} is the effective permittivity, δ is the volume fraction of inclusions, ε_i is permittivity of the inclusion and ε_m is the host permittivity.

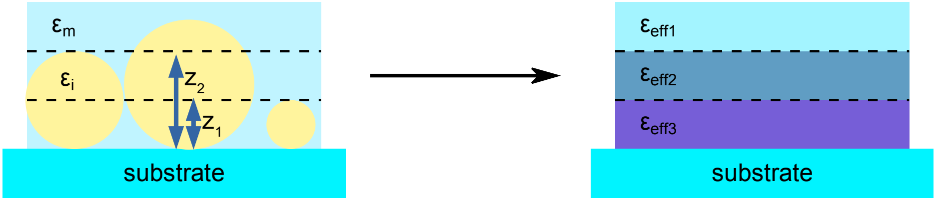

Figure 7.4: Schematic representation of the homogenization procedure in a gradient effective medium model. An explicit nanoparticle distribution is dissected into sublayers. Each sublayer contains a certain volume fraction of nanoparticle material and once homogenized it yields a distinct permittivity. As a result, we obtain a graded permittivity profile along the normal direction to the substrate that represents accurately nanoparticle mass distribution and enables modeling of nanoparticle layers in strong electric field gradients.

The GEM generalizes the MG model by homogenizing the nanoparticle layer into a set of sublayers each with a distinct permittivity value calculated using a generalized MG equation derived below. The homogenization procedure using the GEM is presented in Fig. 7.4. Each sublayer is characterized by a volume fraction δ just like in the MG model, but its evaluation requires accounting for the shape and inhomogeneous size distribution of nanoparticle. The volume fraction in a sublayer is calculated using the following parameters: number of parts, volume of each spherical segment in the sublayer and number of particles per area unit. The relation between the parameters and volume fraction stems from the fact that the volume fraction is simply a ratio of the total volume of spherical segments and the volume of the sublayer:

$$\delta_l = \frac{V_l}{V_{\text{sub}}} = \frac{\sum_i V_{\text{seg},i}^l N_i}{sh} = \frac{N_p}{H}\frac{N}{s}\sum_i V_{\text{seg},i}^l x_i \tag{7.3}$$

where V_l is the total volume of spherical segments in the l-th sublayer, V_{sub} is the volume of a sublayer, H is the nanoparticle layer height, N_p is the number of sublayers, s is the layer area, $V_{\text{seg},i}^l$ is the volume of a spherical segment of i-th size in l-th sublayer, x_i is the fraction of particles of i-th size and N is the total number of spheres; i indexes nanoparticle sizes.

By inserting eq. 7.3 into eq. 7.2 we obtain the following for equation for the permittvity of the sublayer

$$\varepsilon_{\text{eff},l} = \varepsilon_h \frac{2\frac{N_p}{H}\frac{N}{s}\sum_i V_{\text{seg},i}^l x_i\left(\varepsilon_i - \varepsilon_h\right) + \varepsilon_i + 2\varepsilon_h}{\varepsilon_i + 2\varepsilon_m + \frac{N_p}{H}\frac{N}{s}\sum_i V_{\text{seg},i}^l x_i\left(\varepsilon_i - \varepsilon_h\right)}. \tag{7.4}$$

To find the correct volume fraction of inclusions in each sublayer, it is necessary to calculate the volume of each spherical segment, which is defined as

$$V^l_{\mathrm{seg},i} = \frac{\pi}{6}(3r_1^2 + 3r_2^2 + h^2), \tag{7.5}$$

where r_1 is the radius of a circle created by an intersection of the segment with the bottom of the sublayer, r_2 is the radius of a circle created by an intersection of the segment with the top of the sublayer and h is the height of the layer. The i-th circle radius is given by

$$r_i^2 = R^2 - (z_i - R)^2, \tag{7.6}$$

where z_1 is the distance between the substrate and the bottom of the sublayer and z_2 is equal to between the substrate and the top of the sublayer.

The numerical implementation enables finding the correct value of the volume of a spherical segment in cases when both the top and the bottom of the sublayer do not intersect with the segment:

1. if the bottom of the sublayer is above the sphere, the segment volume equals zero
2. if the top of the sublayer is above the sphere, upper radius equals zero

7.2.2 Gaussian distribution of sphere quantity per surface area

In the GEM model the size distribution of the particles is quantified by the number of spheres per unit area ($\frac{N}{s}$) and x_i. While any distribution could be used to obtain x_i, here we use a Gaussian distribution of sphere radius. If sphere radii are normally distributed, the probability of a particular radius following between R_i and R_{i+1} is

$$x_i = \int_{R_i}^{R_{i+1}} \frac{1}{\sqrt{2\pi\sigma^2}} \exp\left(- \frac{(R-\mu)^2}{2\sigma^2}\right) dR. \tag{7.7}$$

For a sufficiently large number of spheres it can be assumed that this probability is equal to the fraction of spheres having their radius in the given range. The equivalent thickness defined as

$$h_{eq} = \frac{V_{sph}}{s} = \sum_i \frac{n_{cz_i}}{s} V_{sph_i} = \sum_i \frac{N}{s} x_i V_{sph_i} \tag{7.8}$$

and is used to quantify the volume fraction occupied by nanoparticles. It can be used to calculate $\frac{N}{s}$ present in eq. 7.4 as

$$\frac{N}{s} = \frac{h_{eq}}{\sum_i x_i V_{sph_i}}. \tag{7.9}$$

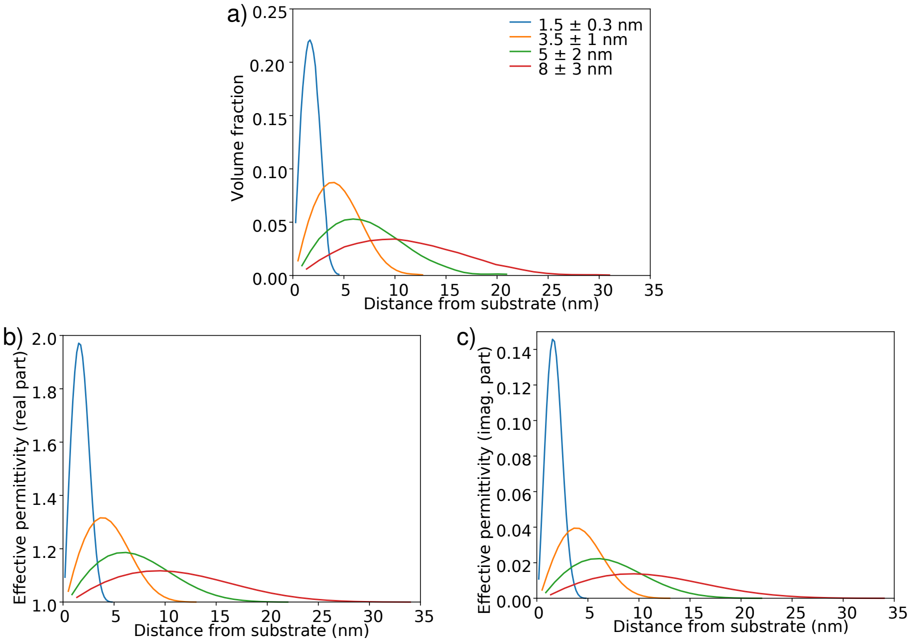

Figure 7.5: a) Volume fraction of palladium in nanoparticle layers placed on a substrate as a function of distance from substrate for selected radius distributions and b) real and c) imaginary parts of corresponding effective permittivity of nanoparticle layers obtained using GEM.

7.2.3 Numerical examples

Exemplary volume fraction distributions in the nanoparticle layer are shown in Fig. 7.5a with a given mean and standard deviation. The shape of these distributions is reflected in the effective dielectric function in the corresponding effective medium layers presented in Fig. 7.5b. The largest volume fraction corresponds to the sublayer containing the middle part of the spheres with the average radius value and decreases with increasing distance from that sublayer. Above that central sublayer, this decrease is slow due to the fact that those sublayers do not contain small particles whose contribution to both δ and the effective permittivity is confined to small distances (below the mean diameter). The effective permittivity follows those trends both in terms of its real and imaginary parts.

We assess the accuracy of the basic properties of the proposed GEM by benchmarking it against rigorous FDTD calculations with explicit nanoparticles for the case of substrate-supported Pd nanoparticle layers with random spatial and size

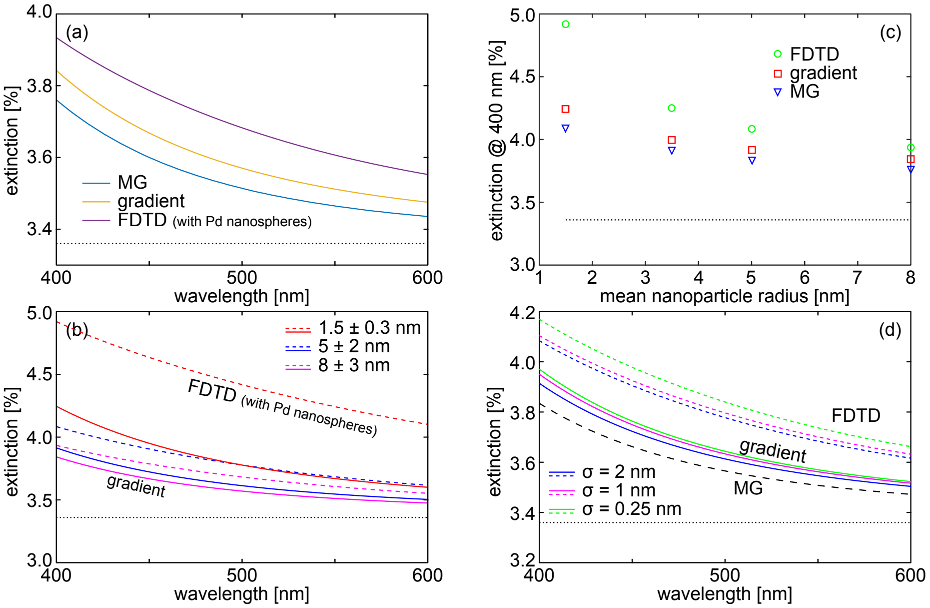

Figure 7.6: Comparison of light extinction by a flat layer of Pd nanoparticles placed on a substrate with n=1.45 obtained using GEM, Maxwell-Garnett effective medium and FDTD with explicit nanoparticles. a) Extinction spectrum of nanoparticle layer with $r = 8 \pm 3$ nm. b) Extinction spectrum of nanoparticle layers with selected radius distributions obtained with GEM and FDTD. c) Extinction at fixed illumination wavelength of 400 nm for varying mean nanoparticle radius. d) Extinction spectra for nanoparticle layer with fixed mean nanoparticle radius of 5 nm and varying radius standard deviation (σ). Extinction by bare substrate is marked by a black dashed line in all plots.

distributions. The substrate refractive index is equal to 1.45 to mimic glass. Here, no large field gradients are present, but still GEM could be useful to account for size distribution of the particles in the two-dimensional layers. The exemplary extinction spectra for Pd nanoparticle layers with $r = 8 \pm 3$ nm obtained using GEM, MG and FDTD are presented in Fig. 7.6a. In the studied wavelength range, the largest contribution comes from the substrate due to a small nanoparticle concentration and a low extinction efficiency of the nanoparticles. Reflection by the bare substrate results in extinction of 3.36%. FDTD calculations indicate that the nanoparticle layer increases extinction to about 3.8%. This modification is underestimated by both GEM and MG, but GEM is a better model even in this simple case.

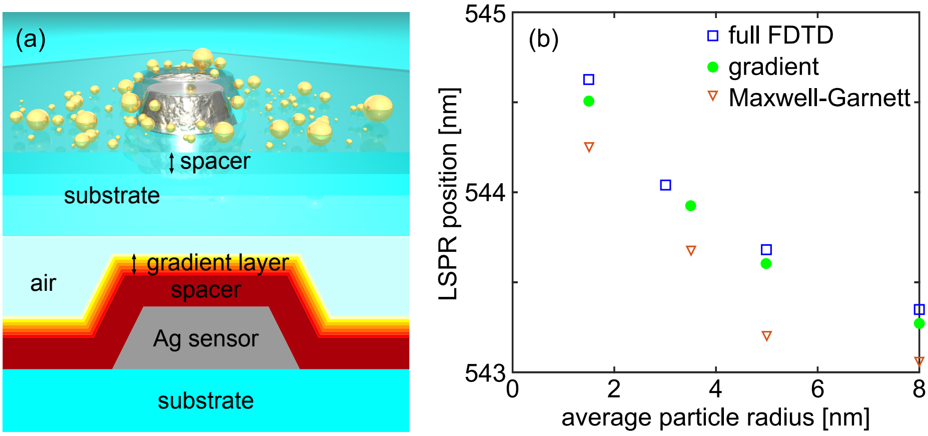

Figure 7.7: a) Schematic representation of the antenna-reactor complex based sensor (top) and its GEM-based model with homogenized palladium nanoparticle layer (bottom). b) LSPR peak wavelength of antenna-reactor complex based sensor as a function of average palladium nanoparticle radius calculated using various methods of treating palladium nanoparticle layer.

In Fig. 7.6b we show the impact of nanoparticle size on light extinction by the layer. Here, we start with an initial distribution of $r = 1.5 \pm 0.3$ nm and modify simultaneously the mean and standard deviation of the nanoparticle to mimic a hypothetical sintering process following Adibi et al.[22] During sintering the material (undergoing sintering) is redistributed from smaller to larger particles, however, the total amount of material is constant. Hence, the volume fraction of nanoparticles decreases as nanoparticles grow in size, due to an increase in layer height. Therefore, as the nanoparticle mean radius increases (for e.g. due to sintering during catalysis) the nanoparticle layer becomes more transparent to incident light. This tendency is present in the simulation results regardless of the approach. GEM underestimates the extinction regardless of the selected size distribution but to a lesser extent than MG. This underestimation is likely the result of neglecting interparticle coupling in simple effective medium models. Fig. 7.6c presents extinction for varying mean nanoparticle radius at a fixed wavelength of 400 nm. We observe that with increasing nanoparticle size (and simultaneous decrease in overall volume fraction) GEM becomes more accurate. This indicates that for a sparse sphere configuration multiple scattering is less prominent, which increases the model accuracy.

In the presented results, based on experimentally observed sintering,[21] the dispersion of nanoparticle size increases with increasing average size. Since the only parameter which depends on nanoparticle size and distribution in the Maxwell-Garnett formula is the volume fraction, the effective dielectric function does not depend on size dispersion. On the other hand, the gradient model takes size dispersion into account. Extinction spectra for selected values of nanoparticle size variance are shown in Fig. 7.6d. An increase of the standard deviation of nanoparticle radius results in decreased extinction. We see that GEM despite lacking the capability to match FDTD results quantitatively, reproduces the extinction decrease by introducing size dispersion. In gradient model, the layer is homogenized into multiple layers, hence with increasing size dispersion the bottom layers have a larger nanoparticle volume fraction in comparison with a gradient model multilayer based on a nanoparticle layer without size dispersion. Simultaneously, size dispersion results in increased layer height in a similar manner to increasing the mean nanoparticle sizes, leading to an overall smaller volume fraction of particles in the layer. This is the dominant effect which causes decreased extinction. Hence, the GEM offers an advantage to MG in describing an inhomogeneous nanoparticle distribution even for a small electric field gradient at substrate-nanoparticle layer interface. As we shall demonstrate subsequently, for large electric field gradients, the advantages of GEM over MG are even more apparent.

7.3 Sensing of Pd nanoparticle sintering

The gradient model can be used in FDTD simulations to model the effective properties of nanoparticle layers placed on nanoplasmonic sensors. In such sensors changes of the LSPR position with the distribution of nanoparticle size are typically less than 0.5 nm per 1 nm change of the average particle radius. This means that the simulations must be very precise to obtain correct and accurate results. However, when modelling explicit particle distributions in FDTD or FEM, several simulations are needed to find the average LSPR position for a given average nanoparticle size, since differences between two configurations (200x200 nm^2 surface area) drawn from the same ensemble can be up to 8 nm. Such repetition, especially with very fine meshes to capture the small sizes of sub-10 nm nanoparticles, are time and resource consuming. The GEM is thus a good alternative.

In Fig. 7.7a we present a schematic illustration of an antenna–reactor complex used as a sensor to monitor changes of the distribution of the Pd nanoparticles around the Ag sensing core. In the spirit of GEM, the Pd nanoparticle layer is thus converted to graded layers with an effective permittivity that is spatially dependent. The nanoantenna consists of a silver truncated cone with 25 nm in height and 30 nm in radius and separated from the environment by a 10 nm glass ($n = 1.48$) shell. In the GEM-based model, we homogenize the palladium

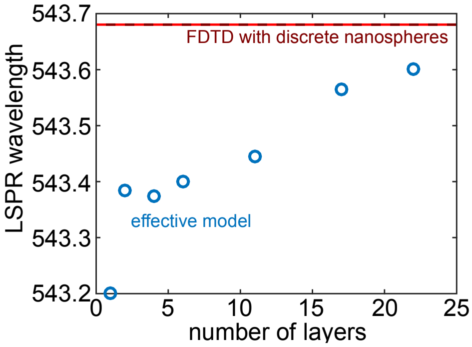

Figure 7.8: LSPR peak wavelength for antenna-reactor complex based sensor with Pd nanoparticle layer $r = 4 \pm 0.2$ nm calculated using GEM with varying number of sublayers. FDTD result is presented as a benchmark.

nanoparticle layer into 1 nm thick sublayers using our GEM approach. These GEM calculations are compared to simulations with explicit nanoparticles, whose results are averaged over 100 realizations of Pd nanoparticle size and position random drawing.

The LSPR wavelength as a function of the mean Pd nanoparticle radius is presented in Fig. 7.7b. The overall volume fraction in a nanoparticle layer is constant and equal to the ratio of the equivalent thickness and layer height. During sintering the nanoparticle size increases while the amount of the material is constant. Therefore, the height of the effective layer increases, while the equivalent thickness remains the same. As a result, the overall volume fraction of metal in the homogenized nanoparticle layer decreases during sintering. This in turn decreases the LSPR wavelength, which is adequately modeled regardless of the modeling approach (explicit, GEM or MG). However, MG substantially underestimates the LSPR wavelength, especially, for large mean nanoparticle radii. In contrast, GEM underestimates the result only by a small fraction of a nanometer. Thus, GEM can be used instead of explicit modeling of Pd nanoparticle layer to quantitatively predict the dependence of the LSPR wavelength of the sensor on the size distribution of the Pd nanoparticle layer.

In order to further discuss the accuracy of the GEM model, we present convergence of the obtained LSPR wavelength for an antenna-reactor-complex-based sensor with the number of layers used to homogenize the palladium nanoparticle layer covering the sensor. The results are shown in Fig. 7.8. Indeed, with an increasing number of layers the accuracy of GEM improves and is better than 0.1 nm when compared to the FDTD result with explicit nanoparticles when 22 effective sublayers with 1 nm thickness are used. Note, that for single sublayer

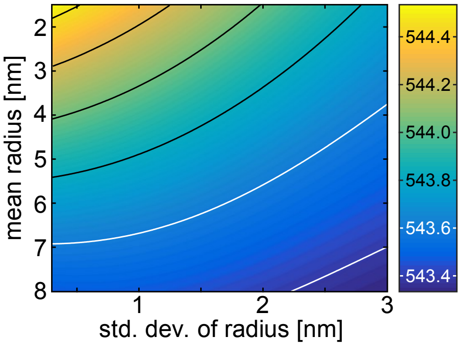

Figure 7.9: LSPR peak wavelength for antenna-reactor complex based sensor with Pd nanoparticle layer with varying nanoparticle size distribution obtained using GEM model. The obtained resonance wavelength depends on both average nanoparticle radius, as well as, its standard deviation.

the GEM and MG models are equivalent, but the observed error in the LSPR wavelength is about 0.5 nm.

The basic study of LSPR wavelength dependence on mean palladium nanoparticle radius has been presented earlier by Adibi et al.[22] Here, using the GEM model enables us to perform an extended study that accounts not only for mean radius, but also its standard deviation. Such an analysis would not only be impossible using MG, which cannot account for size dispersion, but also using an FDTD based approach with explicit nanoparticles, which would require more simulations than it is practically feasible. We calculate the LSPR wavelength for our sensor within a broad range of mean ($\mu_R \in [1.5, 8]$ nm) and standard deviation ($\sigma_R \in [0.3, 3]$ nm) values of palladium nanoparticles. In Fig. 7.9 we present the result of these calculations. A shift of the LSPR peak wavelength towards the blue is observed if either the mean or standard deviation of the Pd nanoparticle radius increase. Contour lines shown in the figure indicate that a given value of the LSPR wavelength corresponds to multiple (μ_R, σ_R) pairs. Thus, if the LSPR wavelength is the only measured quantity one cannot uniquely identify both parameters characterizing the nanoparticle size distribution. To that end, additional information must provided either based on prior knowledge of the nanoparticle size evolution during sensing or from other measurements.

Chapter 8

Electronic structure of antenna-reactor complexes

As discussed in Chapter 3, a nanoparticle based system, including ones with sizes or interparticle distances on the order of single nanometers, requires quantum mechanical treatment when discussing their optical and electronic properties. Specifically, hot electron related effects cannot be correctly accounted for in such system using classical electrodynamics. This is particularly relevant for photocatalysis by antenna-reactor systems when the characteristic sizes become sufficiently small. Therefore, in this chapter we address this issue by a time-dependent density functional theory (TDDFT) study of optical and electronic properties of antenna-reactor complexes, as well as isolated catalytic and plasmonic nanoclusters containing up to several hundreds of atoms. As a model antenna-reactor system, we have studied a nanocluster dimer comprised of silver and palladium nanoclusters. A schematic representation of such a dimer is shown in Fig. 8.1.

8.1 Methods

Icosahedral nanoclusters are modeled, because the icosahedron is the typically considered shape for small clusters in this kind of studies.[47,81] It has been also shown experimentally that charged Ag_{55} clusters constitute icosehdra.[154] The initial lattice constants are set to 3.9 Å for palladium and 4.0 Å for silver and ASE is used to generate the initial positions of atoms assuming an FCC crystalline structure for Pd and Ag. The final geometries are obtained by relaxation with molecular dynamics until forces acting on atoms are below 0.02 eV Å^{-1}. As input

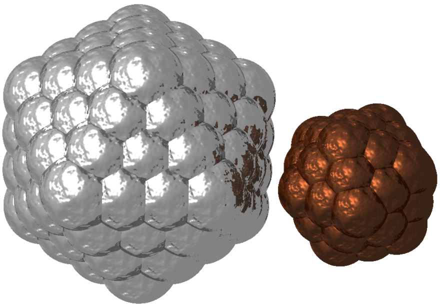

Figure 8.1: Schematic representation of Ag-Pd dimer, where larger cluster of atoms represents silver nanocluster, while smaller one represents palladium nanocluster.

for TDDFT modeling, the DFT ground state calculated with SIESTA is used.[45] The Wu-Cohen functional is employed for both Pd and Ag following Koval et al.[47] The optical response of nanoclusters to a δ-kick pulse is modeled using the iterative linear response TDDFT implementation (PyNAO) by Koval et al.[47] The LDA exchange correlation kernel is used in TDDFT calculations. We use Gaussian pulse excitation with a time dependence of the electric field given by

$$\mathcal{E}(t) = \mathcal{E}_0 \cos\left(\omega_0 \left(t - t_0\right)\right) \exp\left(-\left(t - t_0\right)^2 / \tau_0^2\right). \tag{8.1}$$

We set $\mathcal{E}_0 = 1$ a.u., $t_0 = 10$ fs, $\tau_0 = 5$ fs. ω_0 is set to match the plasmon resonance of the system found using the polarizability spectrum calculated with TDDFT, unless mentioned otherwise.

We obtain the density matrix describing the optical response to a Gaussian pulse by convolution of the linear response density matrix with the pulse electric field. Following Rossi et al.[81] we utilize such a density matrix to study the electron-hole contributions to electronic energy and temporal energetic distributions of the generated carriers. In PyNAO formalism the induced electron density is defined as

$$\delta\rho(\omega, \vec{r}) = \sum_{i,j} (f_i - f_j) \frac{\psi_i(\vec{r})\psi_j^*(\vec{r})\psi_j(\vec{r}\,')\psi_i^*(\vec{r}\,')}{\omega - (E_j - E_i)} \delta V_{eff}(\omega, \vec{r}\,'). \tag{8.2}$$

Hence,

$$\delta\rho_{i,j}^{(1)}(\omega) = (f_i - f_j) \frac{\psi_j(\vec{r}\,')\psi_i^*(\vec{r}\,')}{\omega - (E_j - E_i)} \delta V_{eff}(\omega, \vec{r}\,'). \tag{8.3}$$

Using the vertex product ansatz, the density matrix can be represented as

$$\delta\rho^{(1)}_{n,m}(\omega) = \frac{(f_n - f_m)(X^m_a V^{ab}_\mu X^n_b)}{\omega - (E_m - E_n) + i\varepsilon}\delta V^\mu_{eff}(\omega). \tag{8.4}$$

Finding the time-domain counterpart of the density matrix requires knowledge of its value at negative frequencies. In order to mitigate this difficulty, we calculate the inverse Fourier transform of each part (real and imaginary) in time individually using the properties of the Fourier transform

$$\mathrm{Re}(\delta\rho^{(1)}_{n,m}(t)) = F^{-1}\left[\frac{1}{2}(\delta\rho^{(1)}_{n,m}(\omega) + \delta\rho^{(1)}_{n,m}{}^{*}(-\omega))\right], \tag{8.5}$$

$$\mathrm{Im}(\delta\rho^{(1)}_{n,m}(t)) = F^{-1}\left[\frac{1}{2i}(\delta\rho^{(1)}_{n,m}(\omega) - \delta\rho^{(1)}_{n,m}{}^{*}(-\omega))\right]. \tag{8.6}$$

To evaluate $\delta\rho^{(1)}{}^{*}_{n,m}(-\omega)$ we utilize the property that the density matrix must be hermitian with

$$\delta\rho^{(1)}_{n,m}{}^{*}(-\omega) = \delta\rho^{(1)}_{m,n}(\omega). \tag{8.7}$$

After substituting eq. 8.4 into eqs 8.6 and 8.5 and algebraic manipulation, the real and imaginary part of the density matrix are

$$\mathrm{Re}(\delta\rho^{(1)}(t)) = F^{-1}\left[\frac{\Delta E}{a + ib}\Delta f(X^m_a V^{ab}_\mu X^n_b)\delta V^\mu_{eff}(\omega)\right], \tag{8.8}$$

$$\mathrm{Im}(\delta\rho^{(1)}(t)) = F^{-1}\left[-i\frac{\tilde{\omega}}{a + ib}\Delta f(X^m_a V^{ab}_\mu X^n_b)\delta V^\mu_{eff}(\omega)\right], \tag{8.9}$$

with $a = \omega^2 - \varepsilon^2 - \Delta E$, $b = 2\omega\varepsilon$, $\Delta E = E_m - E_n$. For real signals

$$F^{-1}[f(\omega)] = 2Re\left(\frac{1}{2\pi}\int_0^\infty f(\omega)e^{-i\omega t}\mathrm{d}\omega\right). \tag{8.10}$$

Hence, calculations at negative frequencies are unnecessary.

The remaining subtlety is treating the convolution of the delta-kick density matrix with a pulse to obtain the density matrix for a Gaussian pulse. This is due to the fact that we add a small imaginary part (ϵ) to each frequency in order to mimic dissipation of energy in the system, $\omega \to \tilde{\omega} = \omega + i\epsilon$. In order to perform the convolution, we use the following property

$$a * b = e^{dt}F^{-1}[F[ae^{-dt}]F[be^{-dt}]]. \tag{8.11}$$

Then,

$$\delta\rho^{(1)}(t) = e^{\epsilon t}F^{-1}[\delta\rho^{(1)}(\omega)E^{pulse}(\tilde{\omega})]. \tag{8.12}$$

The Fourier transform of the electric field of the pulse is given by

$$E^{pulse}(\omega) = \frac{\sqrt{\pi\tau^2}}{2} E_0 \exp(it_0\omega)(\exp(-1/4(\omega_0 - \omega)^2\tau^2) + \exp(-1/4(\omega_0 + \omega)^2\tau^2)), \quad (8.13)$$

where ω_0 denotes central frequency of the pulse, τ determines the pulse duration, t_0 is the central time of the pulse and E_0 is the pulse electric field amplitude.

This way we the obtain linear response density matrix, which is used to obtain the diagonal elements of the second order density matrix that determines the occupation change at each of the Kohn Sham states. In turn, these occupation changes determine the energetic and spatial distributions of hot electrons.

8.2 Small monometallic clusters

8.2.1 Silver clusters

The optical properties of silver clusters, which are dominated by an LSPR, are similar to those of larger plasmonic clusters that have been studied with classical electrodynamics. At the same time, TDDFT reveals effects that are not observed when using classical electrodynamics to describe such nanoparticles. Exemplary polarizability spectra of small icosahedral silver clusters are presented in Fig. 8.2a. The imaginary part of the polarizability is normalized to the number of atoms, as it is proportional to the absorption cross section (eq. 2.96). Because TDDFT does not account for retardation, a scattering cross-section is not expected. The smallest cluster (with 13 atoms) does not exhibit a clear plasmon peak. This stems from the fact that the number of atoms is too small to result in a collective excitation such as plasmon. Spectra of other clusters feature prominent plasmon peaks. The classical quasi-static polarizability (eq. 3.3) shows no dependence of the resonance condition on nanoparticle size as indicated in Chapter 3. The dependence of the LSPR wavelength on nanoparticle size captured by classical electrodynamics stems from retardation and depolarization, but TDDFT shows that other mechanisms are important once the nanoparticle is sufficiently small. Specifically, this dependence of the plasmon resonance on nanoparticle size stems from quantization of electronic states due to small nanoparticle size and electronic density spill-out.[155]

To further study the nature of plasmonic excitation in small clusters we present in Fig. 8.2b the Kohn-Sham decomposition of polarizability (its imaginary part) of Ag_{147} cluster at LSPR energy (3.36 eV) into contributions from individual Kohn-Sham (KS) transitions using a method proposed by Rossi et al.[156] The Kohn-Sham map is complimented by the density of states (DOS) plotted in Fig. 8.3. The results are in line with those obtained by Rossi et al.[156]

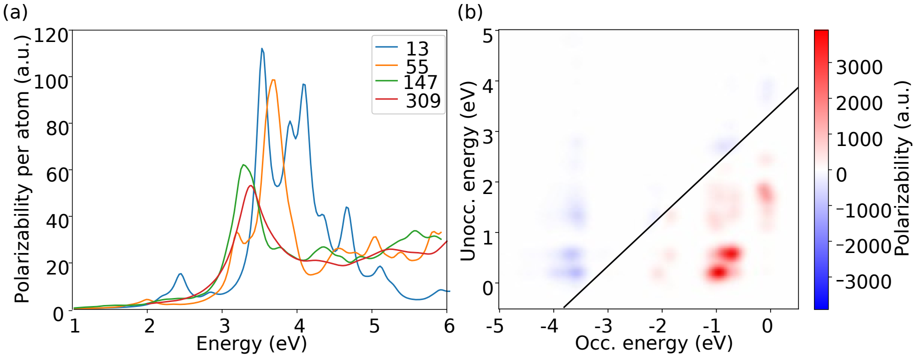

Figure 8.2: a) Imaginary part of polarizability calculated per atom for Ag icosahedral clusters with varying number of atoms (denoted in the legend). b) Kohn-Sham decomposition polarizability (imaginary part) into contributions from each electron-hole transition as a function of electron and hole energies for silver cluster with 147 atoms. The solid line marks the LSPR energy (3.36 eV). The hole and electron energies are given with respect to the Fermi level.

and indicate plasmon excitation in the system. The dominant KS transition contribution to the plasmon energy comes from low energy sp transitions with energies much lower than that of the plasmon. As these transitions tend to be close in terms of energy and are all coupled by the exchange-correlation kernel in a similar manner, they form a coherent collective excitation (plasmon).[157] Interaction between these transitions leads to increased energy of the plasmon with

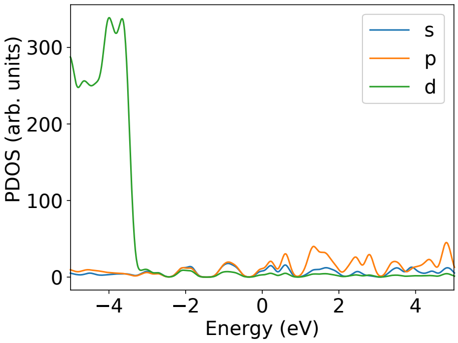

Figure 8.3: Density of states of Ag_{147} cluster ground state decomposed into contributions from s-,p-,d- and f states.

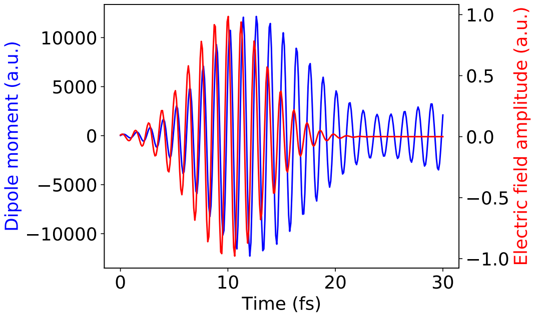

Figure 8.4: Electric field profile of a Gaussian pulse exciting the system plotted along with the dipole moment in Ag cluster with 147 atoms induced by this pulse. The pulse frequency is selected to match LSPR frequency of the cluster.

respect to the non-interacting spectrum peak. The large positive contribution from sp transitions is accompanied by significant negative contributions resulting from transitions from occupied d states to partially occupied sp states lying very close to the Fermi energy. The transition energy for these transitions is close to the plasmon energy. We will see that it is the presence of these partially occupied states and the transitions from d states to those states that determine hot electron generation in plasmonic particles.

Next, we investigate how these properties calculated in the frequency domain manifest themselves when the cluster is illuminated using a Gaussian pulse. The electric field profile of the pulse and resulting dipole moment of the Ag_{147} cluster are presented in Fig. 8.4. Both, the field profile and the induced dipole moment oscillate as a function of time. The time dependence of the dipole moment is similar to that of the pulse. However, the oscillation of the dipole moment is phase-shifted with respect to the pulse field, so that the dipole moment maximum is observed about 2 fs after maximal pulse field value. This phase lag is due to the plasmon excitation in silver particle. After the dipole moment maximum is reached its value decays due to plasmon dephasing until the oscillation amplitude reaches a plateau at about 20–30 fs.

Further insight into plasmon formation and its subsequent dephasing is provided by analyzing the energy stored in the system as a function of time decomposed into the contributions of Kohn-Sham electron-hole transitions. In Fig. 8.5 we show the histograms of stored energy in terms of the transition energy. The results for two time instances are presented: the initial one (at 0 fs) and after the pulse has decayed (at 30 fs). The initial distribution closely resembles the one obtained for the plasmon in the frequency domain. Most of the energy is stored in sp transitions with energies much lower than that of the plasmon. There is also

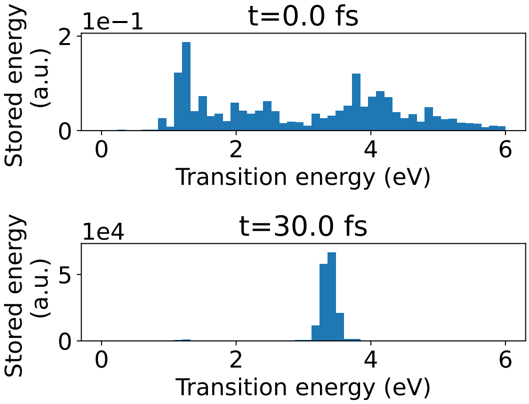

Figure 8.5: Histograms of stored energy in Ag_{147} cluster as a function of Kohn-Sham transition energy for two time instances: $t = 0$ fs (top), $t = 30$ fs (bottom).

energy stored in transitions from d states with energies above that of the plasmon. After 30 fs of time evolution, the energy stored from the system is several orders of magnitude larger than initially. The distribution of the stored energy is vastly different than initially. The final distribution is concentrated around the transition energy close to the one corresponding to the central frequency of the pulse.

The evolution of how the stored energy is distributed over Kohn-Sham transitions is a good indicator of plasmon dephasing. The stored energy as a function of time is plotted in Fig. 8.6, including a split into resonant and non-resonant parts. We obtain a result that is consistent with the literature.[81] The total energy stored in the electronic system grows as a function of time and reaches a plateau after the pulse decays. Non-resonant transitions (with energies outside $\omega_0 \pm \sqrt(2)/\tau$ range) that we attribute to the screened plasmon, contribute the most to the stored energy for the time corresponding to the dipole moment maximum. Afterwards, this contribution begins to decrease and vanishes after the pulse decays, at approx. 22 fs of propagation. A few femtoseconds later, a slight increase of the non-resonant transition contribution is observed. This is an indicator of plasmon revival that would occur after a long propagation due to a lack of dissipation in TDDFT.

The time domain approach proposed by Rossi et al.[81] enables us to calculate the hot electron distribution. In Fig. 8.7 we present the initial and final (after 30 fs) energy distribution of the occupation of electronic states for a silver cluster with 147 atoms. The initial occupations are small and are dominated by small

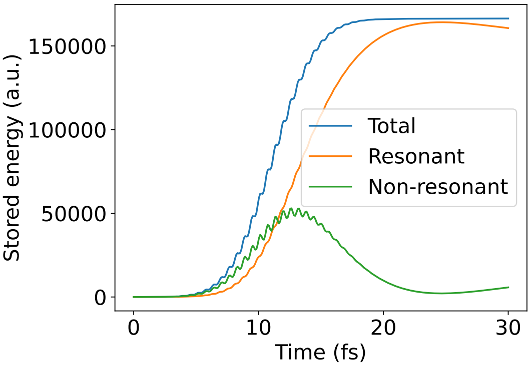

Figure 8.6: Decomposition of stored energy evolution in Ag_{147} cluster into resonant and non-resonant transitions. Total stored energy evolution is plotted for comparison.

energies close to the Fermi energy. After 30 fs a major increase of electron occupation is observed, and the energy distribution is also significantly modified. The contribution of electrons with energies close to the Fermi energy (¡1 eV) is no longer dominant. Instead, the most prominent contribution comes from electrons with energy of over 1 eV, which we will call hot electrons following Rossi et al.[81]

In order to further show that hot electron generation is related to plasmon decay and that it is caused by transitions resonant with the pulse, we compare the

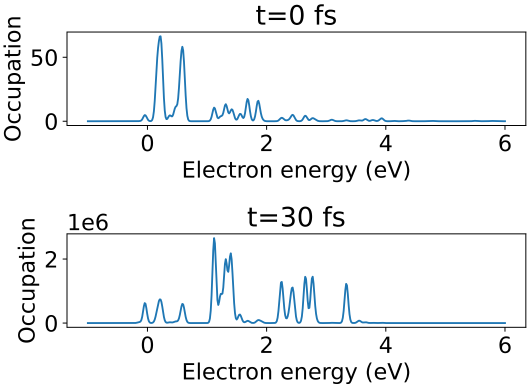

Figure 8.7: Initial ($t = 0$ fs) and final ($t = 30$ fs) occupation of electronic states in Ag_{147} cluster as a function of electron energy.

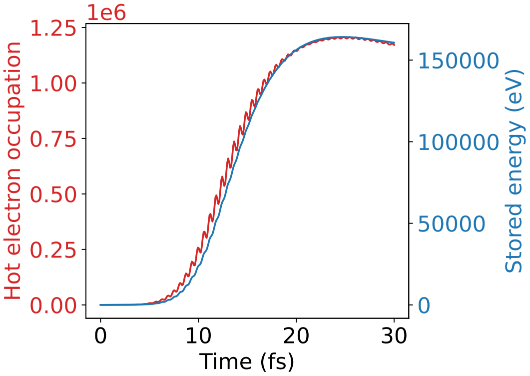

Figure 8.8: Integration of hot ($E > 1$ eV) electron occupation as a function of time. For comparison, we plot the time evolution of energy stored in resonant transitions, which is highly correlated with hot electron evolution.

evolution of occupation of electrons with energies of over 1 eV above the Fermi energy with the evolution of energy stored in resonant transitions in Fig. 8.8. Clearly, the two quantities are highly correlated and their evolution is very similar except for oscillations that are present in hot electron occupation evolution and are not present in stored energy evolution.

As a final part of this section devoted to the TDDFT study of silver clusters, we study the influence of transitions to partially occupied states on the hot electron generation process by comparing simulations of an Ag_{55} cluster with and without accounting for these transitions. The impact of this modification is clearly seen when comparing Kohn-Sham transition maps of stored energy in both scenarios (see Fig. 8.9). Initially (for $t = 0$ fs), the maps are in qualitative agreement except for the lack or presence of partially occupied states contributions. This seemingly minor modification leads to an entirely different time evolution when the system is excited with a Gaussian pulse. For the unmodified simulation, the plasmon decays predominantly into transitions with energies in resonance with the pulse and into partially occupied states. Due to removal of these the transitions in the modified simulations, the plasmon does not decay in the modified simulation and final Kohn-Sham transition map resembles qualitatively the initial map. This is in line with results observed in the literature,[82] where a similar effect has been observed by modifying silver's pseudopotential.

These observations are further confirmed by analyzing the evolution of the decomposition of stored energy in an Ag_{55} cluster into resonant and non-resonant transitions presented in Fig. 8.10. If the modification is not applied to the system, the energy evolution is very similar to the one observed for the larger silver cluster.

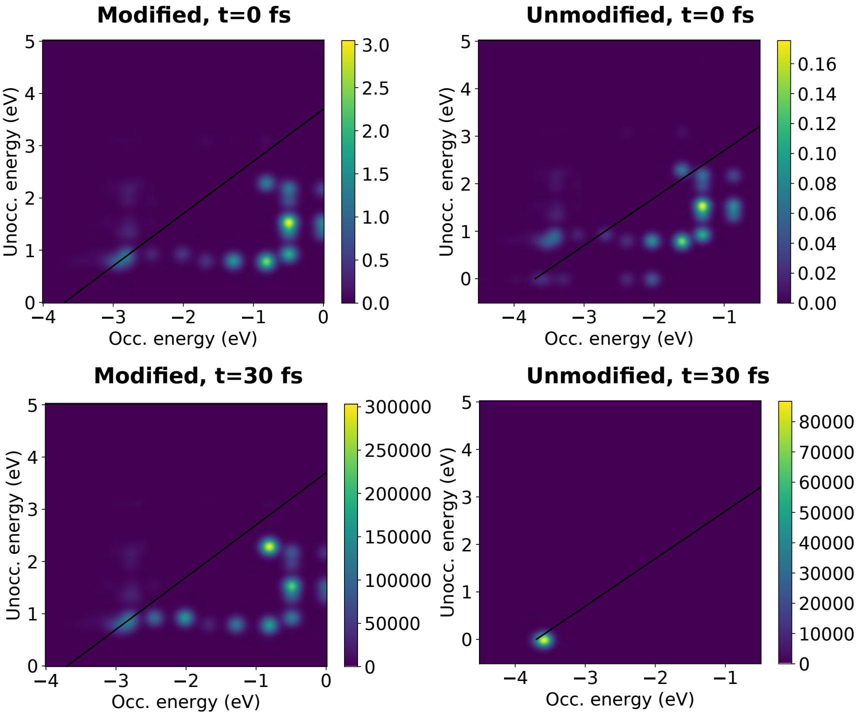

Figure 8.9: Kohn-Sham transition maps of stored energy in Ag_{55} cluster for two time instances: $t = 0$ fs (top), $t = 30$ fs (bottom). We compare simulation with (unmodified) and without transitions to partially occupied states.

Initially, non-resonant transitions that form the plasmon constitute a dominant contribution to stored energy. Once the pulse decays, the plasmon dephases, resonant transitions dominate and hot electrons are generated. In contrast, with no partially occupied states under consideration, the plasmon does not decay and resonant transitions never contribute more than non-resonant ones.

8.2.2 Palladium clusters

We study palladium clusters in a similar manner to that presented for silver in the previous subsection. In Fig. 8.11a spectra of the imaginary part of the polarizability are plotted for small icosahedral palladium clusters. In contrast to silver clusters, we add a so-called ghost atom layer. This is necessary for TDDFT simulations of isolated Pd clusters to converge. While silver clusters exhibited a

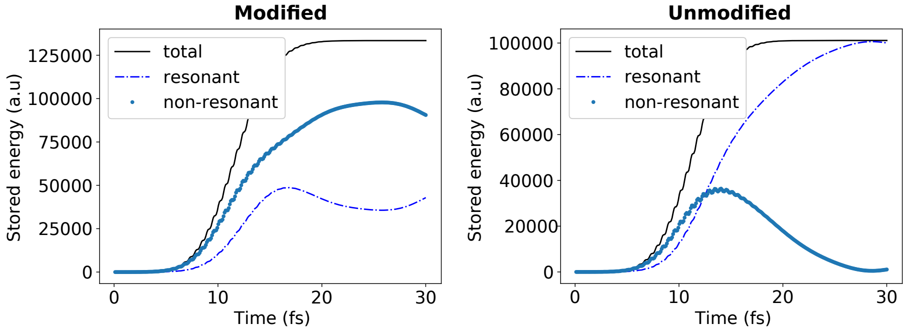

Figure 8.10: Decomposition of stored energy evolution in Ag_{55} cluster into resonant and non-resonant transitions. Total stored energy evolution is plotted for comparison. We compare simulation with (unmodified) and without transitions to partially occupied states.

clear LSPR peak in their spectrum, palladium does not support a LSPR in the studied excitation energy range. In general, the polarizability of small Pd clusters increases with increasing energy and does not significantly depend on particle size. The exception are small clusters such as Pd_{13}. Its spectrum oscillates due to a

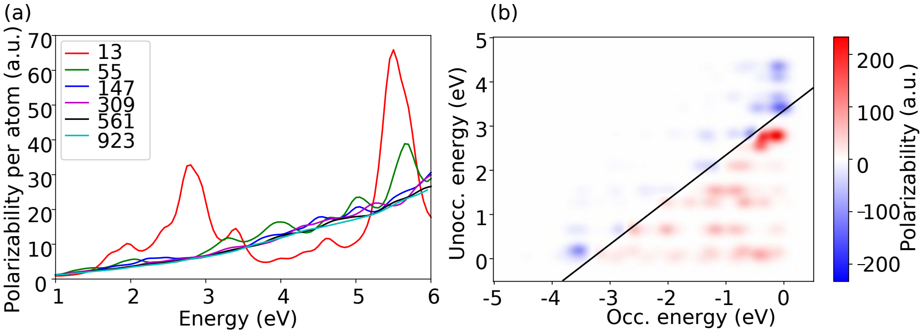

Figure 8.11: a) Imaginary part of polarizability calculated per atom for Pd icosahedral clusters with varying number of atoms (denoted in the legend). b) Kohn-Sham decomposition polarizability (imaginary part) into contributions from each electron-hole transition as a function of electron and hole energies for palladium cluster with 55 atoms. The excitation energy is 3.36 eV, which corresponds to LSPR energy of Ag_{147} cluster. Transitions with this energy are marked using a solid line.

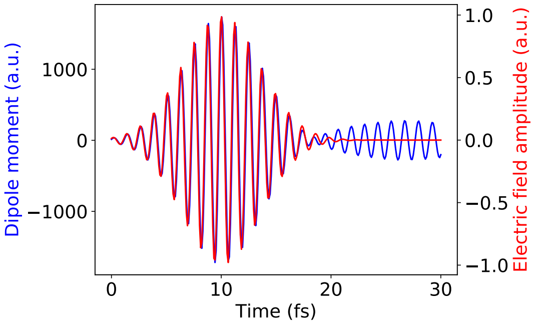

Figure 8.12: Induced dipole moment in Pd_{55} icosahedral cluster plotted with the electric field profile of a Gaussian pulse exciting the particle. The pulse parameters are selected as in Fig. 8.4.

large impact of atomic excitations on the optical properties. These oscillations diminish and eventually vanish with increasing number of atomic shells. For a large number of atoms, the spectrum resembles qualitatively the one obtained using FDTD (see Fig. 7.6 for comparison).

The Kohn-Sham decomposition map for the polarizability of Pd_{55} is presented in Fig. 8.11b. Despite using the same excitation energy it differs from the one obtained for the silver cluster (see Fig. 8.2b), due to lack of collective plasmon behavior observed for the silver cluster. Instead, the dominant contribution to polarizability comes predominantly from transitions that are close to the excitation energy. Other transitions that contribute to the polarizability are several transitions below the excitation energy, which do not posess their respective counterparts at high excitation energies like in the case of the silver cluster.

The non-plasmonic character of optical excitations in the palladium cluster is also represented in the dipole moment induced by a Gaussian pulse (see Fig. 8.12). The pulse parameters are chosen to be the same as in the case of the silver cluster for an adequate comparison. In contrast to the silver cluster, the induced dipole moment follows the Gaussian pulse field profile and no phase shift of the resulting dipole moment oscillations are observed. This indicates that the particle is excited with an energy different from its optical resonance (below the resonance).

In Fig. 8.13 we present the evolution of energy stored in the electronic system, as well as the resonant and non-resonant contributions to this energy for the Pd_{55} cluster. Qualitatively, it is similar to the evolution of stored energy obtained for the silver cluster due to an increase of stored energy over time and decay of the contribution of non-resonant transitions with the decay of the exciting pulse.

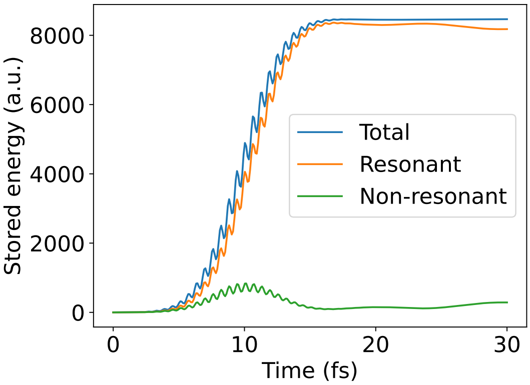

Figure 8.13: Decomposition of stored energy evolution in the Pd_{55} cluster into resonant and non-resonant transitions. Total stored energy evolution is plotted for comparison.

However, a considerable difference distinguishing a plasmonic silver cluster from a transition metal cluster such as Pd_{55} is the fact that for the latter resonant transitions dominate over non-resonant transitions regardless of the time instance. In contrast, for the silver cluster, initially it is the non-resonant transitions that contribute the most to the stored energy, due to efficient plasmon excitation in this system.

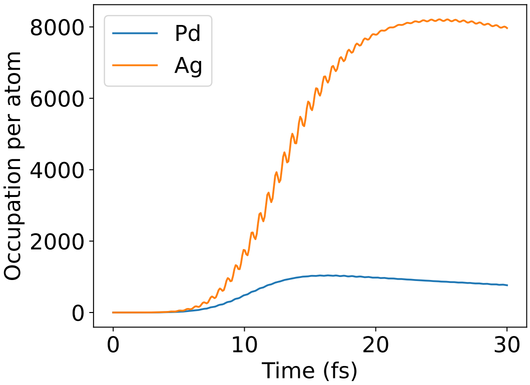

Figure 8.14: Time evolution of integrated hot electron occupation per number of atoms in Ag_{147} cluster and single Pd_{55} cluster.

Despite the fact that palladium clusters do not support a LSPR like silver clusters do, it is still possible to excite high energy electrons in Pd_{55}. In Fig. 8.14 we compare the evolution of hot electron occupation for Ag_{147} and Pd_{55}. We normalize the results by the number of atoms to account for the fact that occupation is proportional to number of atoms in the system. Clearly, hot electron generation is more efficient for the plasmonic particle. The maximal occupation per atom is over 10 times larger for the silver cluster than for the palladium cluster.

8.3 Silver-palladium dimers

After establishing the basic properties of individual silver and palladium clusters constituting antenna-reactor complexes studied in this work, we study the properties of dimers consisting of silver and palladium clusters. Four different dimer configurations are considered: face-to-face, tip-to-tip, face-to-tip and tip-to-face. The first part of the configuration name refers to silver, while the other one refers to palladium. These configurations are visualized in Fig. 8.15. We define the gap size as the distance between closest points of the clusters' surfaces assuming spherical atoms with covalent radii of silver (1.45 Å) and palladium (1.39 Å) atoms taken from ASE.

An exemplary spectrum of such a dimer is presented in Fig. 8.16. The tip-to-face configuration is used and the gap size is 0.7 Å. Spectra of isolated clusters are plotted along with the sum of polarizabilities of isolated clusters. As a result of coupling between the clusters, the polarizability is enhanced compared to a simple sum of the individual polarizabilities. The enhancement is especially pronounced

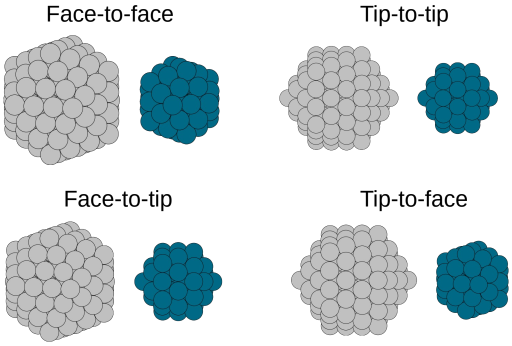

Figure 8.15: Schematic $Ag_{147}Pd_{55}$ dimer in various configurations analyzed in this chapter.

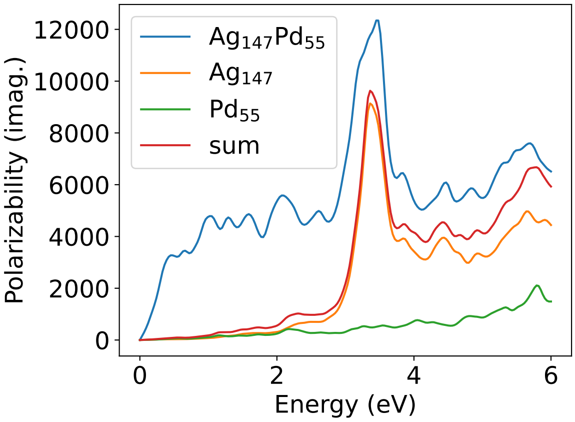

Figure 8.16: Spectrum of $Ag_{147}Pd_{55}$ dimer in tip-to-face configuration and with gap size of 0.7 Å. Also plotted are the spectra of isolated silver and palladium clusters and the sum of isolated clusters spectra.

for energies below the plasmon resonance energy.

Spectra of dimers in each of the four configurations and varying size of the gap are presented in Fig. 8.17. Depending on the particular configuration, the impact of gap size, and in turn intercluster coupling, on the optical properties varies significantly. When a gap size of 3 Å is used, the spectra for each dimer configuration are very similar. The main LSPR peak is observed at 3.45 eV (compare to silver with 3.36 eV) and the corresponding polarizability value is about 14000 a.u.

In contrast, for gap sizes below 3 Å the differences between cluster configurations manifest themselves in the optical spectra. The most notable changes are observed for the face-to-face configuration. The plasmon peak is broadened asymmetrically as the gap size decreases. The polarizability for energies below the plasmon resonance is enhanced, while for higher energies the polarizability remains almost unchanged. The energy corresponding to the LSPR is shifted towards lower energies with decreasing gap size.

When the dimer is oriented in the tip-to-tip configuration, the modification of the LSPR peak is the least prominent. The peak position and amplitude remain almost unmodified as the gap size is decreased. Asymmetric broadening is observed, similar to the one for the face-to-face configuration, but the observed enhancement of the polarizability below the LSPR energy is much smaller. Furthermore, an additional spectral peak is present at low energies for dimers in the tip-to-tip configuration.

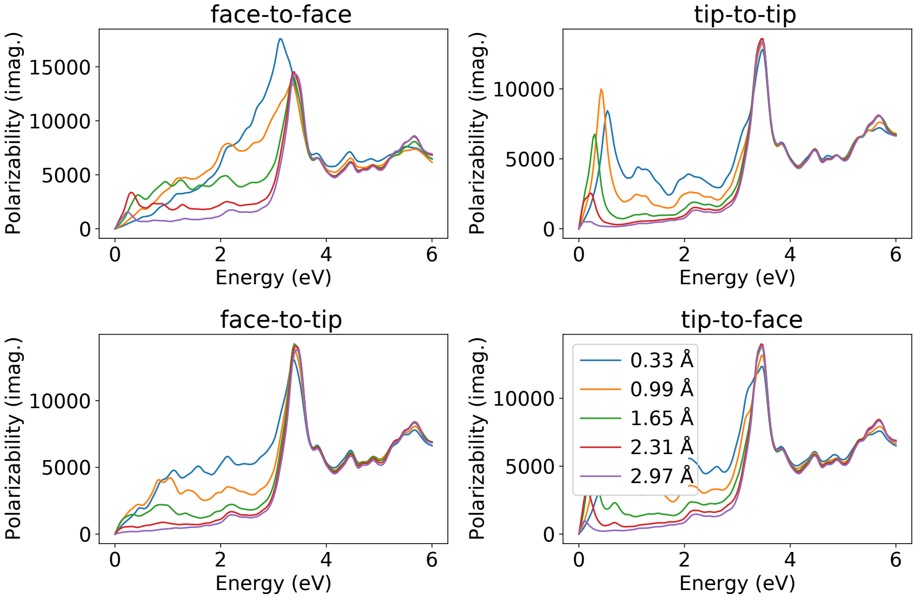

Figure 8.17: Spectra of $Ag_{147}Pd_{55}$ dimers with varying configurations and gap sizes. Configuration is indicated by the sub-figure title, while gap size is given in the legend.

The remaining dimers contain particles in opposing configurations. For both the tip-to-face and face-to-tip configurations, the main LSPR peak is not substantially modified, except for the asymmetric broadening, which is larger than that observed for the tip-to-tip configuration, especially for the face-to-tip configuration. The additional low energy spectral feature observed for the tip-to-tip configuration is also observed for dimers in the tip-to-face configuration, but its peak amplitude is considerably smaller in this case.

In order to rationalize the observed optical response of the dimers with varying configurations and gap sizes, we analyze the induced density for selected gap sizes and face-to-face configuration. The results are presented in Fig. 8.18. For gap sizes above 0.33Å each particle has its own plasmon represented as an electron density of opposing sign at the opposite sides of each icosahedron. This resembles a bonding dimer plasmon observed in dimers of identical particles.[70] Also, dipoles located at atomic coordinates are visible, which are known to be the result of d-electron screening of the plasmon.[69] For the smallest selected gap size (0.33Å), the electron density is also located in the gap indicating that in this case charge transfer between both clusters occurs and the efficiency of coupling

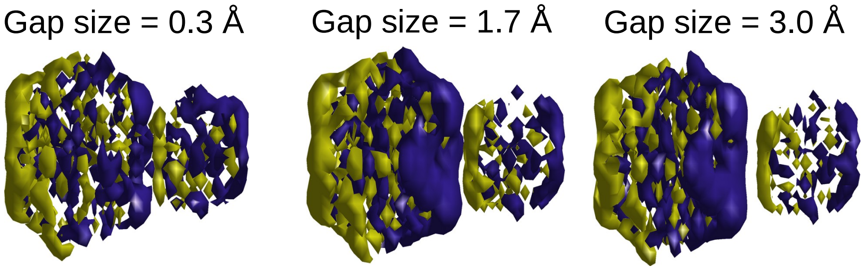

Figure 8.18: Imaginary part of $\delta\rho(r,\omega)$ for Ag-Pd dimer in face-to-face configuration for selected excitation energies and intercluster distance. Electric field is applied horizontally.

is large. Furthermore, screening appears to be more prominent for such a small gap size. This type of tunneling and screening effect, when diminishing the gap size, is known for dimers composed of identical particles.[70]

The optical study presented above is complimented by a time domain study, which captures plasmon dephasing and hot electron generation in $Ag_{147}Pd_{55}$ dimers. The initial and final histograms of the decomposition of stored energy into transitions with varying energy are presented for a dimer in the face-to-face configuration and 0.3 Å gap size in Fig. 8.19. The results resemble closely the ones obtained for the isolated silver cluster, which is a result of the plasmonic nature of the observed excitations. The initial distribution contains mostly contributions from transition energies that are outside the resonance energy of the coupled

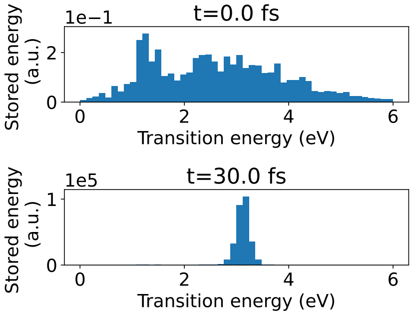

Figure 8.19: Histograms of stored energy in $Ag_{147}Pd_{55}$ dimer in face-to-face configuration and gap size of 0.3 Å as a function of Kohn-Sham transition energy for two time instances: $t = 0$ fs (top), $t = 30$ fs (bottom).

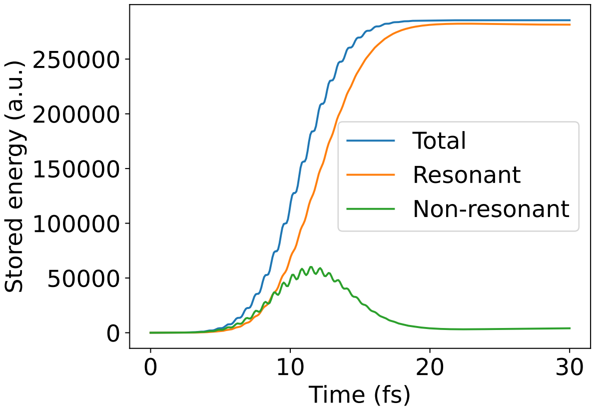

Figure 8.20: Energy stored in the electrons of $Ag_{147}Pd_{55}$ in face-to-face configuration and gap size of 0.3 Å decomposed into resonant and non-resonant contributions.

system, while the final one peaks at the plasmon energy and is much narrower than the initial one as a result of plasmon dephasing.

Plasmon formation and dephasing is further elucidated by analyzing the stored energy split into resonant and non-resonant contributions (see Fig. 8.20). In a similar manner to the case of a silver nanocluster, initially, as the pulse field increases, the non-resonant contributions to the stored energy are larger than the resonant ones, due to plasmon excitation. This excitation dephases and resonant contributions, which can be attributed to hot electron generation, become dominant. Due to the presence of the palladium cluster, the resonant transitions are more prominent and constitute a larger part of the system's energy than for an isolated plasmonic nanocluster.

The observed plasmon dephasing leads to efficient hot electron generation in our model antenna-reactor system. The observed hot electron occupations are larger than the ones observed for transition metal clusters. Enhancement of hot electron occupation, compared to an isolated Pd_{55} cluster, depends on the configuration and gap size of the dimer as shown in Fig. 8.21. In the considered gap size range, the observed enhancement does not change significantly within the gap size range that we consider, with the exception of the face-to-face configuration and the dimer configuration is the key factor. The observed hot electron generation enhancement is the largest for the face-to-face configuration and the smallest gap size. For this case, judging by the spectra and observed density isosurfaces, the two clusters are coupled the most efficiently. Hot electron gener-

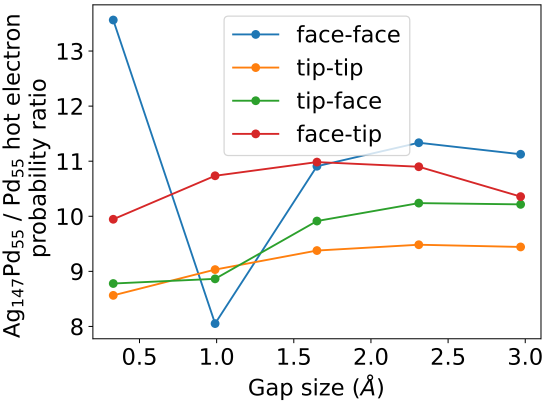

Figure 8.21: Hot electron generation probability ratio between $Ag_{147}Pd_{55}$ and individual Pd_{55} cluster. We account for the fact that dimer contains more atoms than palladium cluster by scaling down the observed enhancement, accordingly.

ation efficiency decreases if the silver cluster is in the tip configuration and it is the lowest for tip-to-tip configuration.

Chapter 9

Conclusions

In this thesis we have provided a comprehensive study of the antenna-reactor system using a multi-scale approach that treats the system at each physically relevant length scale ranging from the macroscopic scale, at which multiple antennas are electromagnetically coupled, through the single antenna level, at which transition metal particles are coupled to the optical antenna, down to the atomistic scale, at which quantum phenomena enable hot electron generation in the coupled antenna-reactor system. An antenna-reactor complex consists of an optical nanoantenna and non-noble transition metal nanoparticles. The optical antenna is used to focus visible light in nanoscale volumes typically smaller than the nanoantenna which is possible due to their capability to support strong optical resonances in this wavelength range. Transition metal nanoparticles are used due to their strong catalytic activity. Such a coupled system provides substantial enhancement of the optical response of transition metal nanoparticles. This thesis studies the electromagnetic coupling between the antenna-reactor complex components and has been motivated by several prospect applications of antenna-reactor complexes for material science outlined in the Introduction. We have focused on enhanced absorption and hot electron generation for photocatalysis, senstivity of optical properties towards changes occurring in bulk and nanoscale environments, and on the tunability of the optical response by manipulating the system parameters at various scales.

Each length scale unravels different physical phenomena and thus requires significantly different methodology, as outlined in Chapters 2-4 of this thesis. At the macroscopic level, an accurate description of multiple scattering of the electromagnetic field between antennas and between antennas and their environment must be provided. To that end, we have used the T-matrix approach – a state-of-the art method for this kind of problem. The novel and extensive description of the effective optical properties of amorphous arrays of optical nanoantennas within the T-matrix framework has been provided in Chapter 5. In amorphous arrays, in contrast to periodic ones, the optical properties of each particle are distinct, due to a unique spatial distribution of neighboring nanoparticles. At the same time the macroscopic response is well-defined and can be calculated by considering average multipole moments of nanoparticles in the array. Here, we have proposed an effective method that enables calculating such average multipole moments including multiple scattering effects. The method uses the pair correlation function as a description of the nanoparticle spatial distribution and multipole moments of isolated nanoparticles to characterize the single particle optical response. This approach significantly reduces the necessary computational effort as there is no need to solve self-consistently for multipole moments of each nanoparticle, which is a formidable task requiring solution of a large-scale inverse problem. Also, the semi-analytical nature of the proposed method has enabled us to obtain substantial physical insight into the properties of amorphous arrays of optical nanoantennas. We have emphasized the optical properties that are relevant for the prospect applications of amorphous arrays such as directional scattering, sensitivity of resonance wavelengths towards bulk and local refractive index change and scattering-to-absorption ratio. For each of the aforementioned properties we have proposed simple analytical formulas that provide useful guidelines for designing devices based on amorphous arrays of nanoparticles. The other aspect, in which our effective approach to calculating the optical properties of random/amorphous arrays of nanoantennas is superior to other methods of tackling this kind of scattering problems, is its generality and flexibility. We have shown that the presented formalism is able to account for various type of resonances occurring in optical antennas of both electric and magnetic origin and of high multipole order, in contrast to earlier approaches that relied on the electric dipole approximation. Two substantial improvements of our initial method have been also presented. The first one enables treating substrate mediated multiple scattering that provides additional multiple scattering via off-substrate reflection. In practical applications, amorphous arrays are fabriacted almost exclusively on dielectric substrates and careful balancing of both direct and substrate-mediated coupling channels is necessary. Such optimization is possible using the proposed approach. The second extenstion of the initial model introduces size dispersion of nanoparticles into consideration and treats it by introducing separate effective polarizability for each nanoparticle size.

At the single antenna level, we have studied electromagnetic coupling between the nanoantenna and transition metal nanoparticles using the finite-difference-time-domain method. The main difficulty in modeling an antenna-reactor system at this length scale is accurate description of the transition metal nanoparticle layer, due to the fact that it is random in terms of spatial and size distribution. We explore two different methods of tackling this issue. We model the transition metal nanoparticle layer either by explicit modeling of nanoparticles as nanospheres or by using a gradient effective medium model developed by the author specifically to account for the size inhomogeneity of transition metal nanoparticles and strong field gradients exhibited by plasmonic nanoparticle based sensors. In each case, the size and position distributions were based on electron microscopy images of experimental samples. The gradient effective medium model extends the Maxwell-Garnett model by introducing a spatially dependent effective permittivity.

The smallest length scale modeled in this thesis is the atomic scale treated using frequency-domain linear response time-dependent density functional theory. Except for polarizability spectra and their decomposition into Kohn-Sham transition contributions, which are a well-established analysis method for plasmonic excitations with TDDFT, the author has developed a method to obtain the linear response in time domain, which enables the implementation of hot carrier analysis tools previously developed for real-time TDDFT. This method has been used to study the optical response of isolated palladium and silver clusters, as well as, palladium-silver dimers, which constitute a model antenna-reactor system. To date, this is the first study of the optical properties of antenna-reactor complexes using the quantum mechanical approach.

This complex methodology has enabled us to prove the theses presented in the Introduction chapter. The first one has been formulated as follows.

- Nanoparticle density is a valuable parameter enabling tailoring the optical response of amorphous array of nanoantennas for prospective applications.

In Chapter 5 we have shown an extensive study of the optical properties of amorphous arrays of nanoantennas. The effective model proposed by the author enables formulation of several analytical formulas describing the dependence of figures of merit relevant for prospect applications on the spatial distribution of nanoparticles and single particle properties. The minimal center-to-center distance, which is characterized in our models by a dimensionless length scaling parameter CC, is a crucial parameter determining contribution of multiple scattering to the optical response of the array. The CC parameter determines the nanoparticle number density in amorphous arrays and can be controlled in experimental fabriaction processes. It enters all the proposed formulas making it a useful handle for optimization of devices based on amorphous arrays of nanoparticles including sensors, directional antennas and light absorbers. Especially, in the case of sensors made of dielectric nanoparticles, we have shown that significant sensitivity may be observed by optimizing CC even if isolated dielectric nanoparticles are not sensitve to bulk environment refractive index changes. If the array is supported by a dielectric substrate, direct and substrate mediated interparticle coupling channels are affected by CC. Here, CC must be optimized in tandem with substrate reflectivity for obtaining the optimal optical response for any desired application. A generalization of the CC parameter towards size dispersed nanoparticle arrays has been proposed and we have shown that the optical response of an amorphous array of size-dispersed nanoparticles can be manipulated by CC also in this case.

- Antena-reactor complexes, including plasmonic core-shell nanoantennas, enable significant light absorption enhancement in transition metal nanoparticles; this enhancement can be maximized by manipulating material and geometric properties of the system.

Using extensive FDTD based modeling we have studied the optical properties of antenna-reactor complexes containing plasmonic core-shell nanoantennas decorated by a layer of transition metal nanoparticles. The results of this study have been presented in Chapter 6 and in Publication IV, which is complimented by experimental results that have been obtained in the group of prof. Langhammer. Our models predict that significant enhancement of light absorption in transition metal nanoparticles can be obtained, which, however, requires a careful selection of materials and geometric parameters of the nanoantenna. By studying the impact of these parameters, we have determined several guidelines for maximizing the observed absorption enhancement.

- Electromagnetic modelling enables relating the optical signal from sensors based on antenna-reactor complexes to physical and chemical phenomena occurring during catalysis.

One of the primary applications of antena-reactor complexes is sensing of physical and chemical phenomena occurring during catalysis. In Chapter 7 we have modelled the optical response to modification of various parameters of the system, which might be altered during catalysis. We have shown that time evolution of nanoparticle size distribution due to sintering can be related to the LSPR wavelength shift of the sensor. At the same time, an additional signal is required to distinguish changes of both the mean and standard deviation of the nanoparticle radius. Modification of the plasmonic response of the system might be also due to adsorption of chemical species at the antenna surface. We have studied various effects related to this phenomenon and have concluded, that both modification of the dielectric shell thickness and refractive index, which may occur due to adsorption, can be monitored using an antena-reactor complex based sensor by measuring the LSPR wavelength and amplitude.

- Hot electron generation in antenna-reactor dimers is enhanced with respect to an isolated transition metal particle due to excitation and subsequent dephasing of localized surface plasmon resonance.

In Chapter 8 we have used TDDFT to study the optical response of clusters and dimers of silver and palladium containing up to a few hundred atoms. Small plasmonic clusters are known for hot electron generation upon light excitation, which is governed by phenomena occuring at the atomic scale. Here, we have provided a comparison of plasmonic (silver) and transition (palladium) metal clusters in terms of plasmonic excitations and hot electron generation. We have shown that both clusters support hot electron generation, which is however much more efficient in the plasmonic metal cluster. Plasmon dephasing that determines hot electron generation in the plasmonic system is requires the presence of partially occupied states to which the plasmon may decay to. When silver and palladium clusters form a dimer, their optical properties depend strongly on their configuration and distance. Hot electron generation is more efficient in the dimer than in individual palladium clusters by a factor of about ten. The process is the most effective if the clusters are in the face-to-face configuration and the gap size is small.

The results constituting this thesis have provided substantial insight into physical phenomena occurring in antenna-reactor complexes. These phenomena have been always studied in the context of prospect applications. Also, the study required implementing novel tools for studying multiple scattering of light in disordered systems of nanoparticles and for studying plasmon exictiations with frequency domain TDDFT. The developed methods might be useful for studying various nanophotonic systems beyond antenna-reactor complexes which were the subject of this thesis.

Chapter 10

Appendix A: maths

In this Appendix we provide the definitions of mathematical functions and coupling matrix elements. In literature there are various normalization and units conventions. Here, we follow those provided by Wriedt and Doicu in their textbook on light scattering by systems of particles[30] and by Amos Egel in his recent work about light scattering by nanoparticles embedded in layered media.[108]

10.1 Vector spherical wave functions

In the T-matrix method the electric and magnetic fields are expanded in regular (with upper index 1) and radiating (with upper index 3) vector spherical wave function defined as

$$\vec{M}^{1,3}_{l,m}(k\vec{r}) = z_l^{1,3}(kr)\vec{m}_{l,m}(\theta,\varphi) \tag{10.1}$$

$$\vec{N}^{1,3}_{l,m}(k\vec{r}) = \sqrt{\tfrac{n(n+1)}{2}}\,\frac{z_l^{1,3}(kr)}{kr}Y_{l,m}(\theta,\varphi)\vec{e}_r + \frac{\left[krz_l^{1,3}(kr)\right]'}{kr}\vec{n}_{l,m}(\theta,\varphi), \tag{10.2}$$

where $z_l^{1,3}$ denotes spherical Bessel function for regular and spherical Hankel function for radiating VSWF, $Y_{l,m}$ is scalar spherical harmonic, while $\vec{n}_{l,m}$ and $\vec{m}_{l,m}$ are vector spherical harmonics (VSH). VSH are defined as

$$\vec{m}_{l,m}(\theta,\phi) = \frac{c_{l,m}}{\sqrt{2n(n+1)}}\left[im\frac{P_l^{|m|}(\cos\theta)}{\sin\theta}\hat{\theta} - \frac{d}{d\theta}P_l^{|m|}(\cos\theta)\hat{\phi}\right]e^{im\phi} \tag{10.3}$$

and

$$\vec{n}_{l,m}(\theta,\phi) = \frac{c_{l,m}}{\sqrt{2n(n+1)}}\left[\frac{d}{d\theta}P_l^{|m|}(\cos\theta)\hat{\theta} + im\frac{P_l^{|m|}(\cos\theta)}{\sin\theta}\hat{\phi}\right]e^{im\phi}, \tag{10.4}$$

where $c_{l,m}$ is a normalization constant,

$$c_{l,m} = \sqrt{\frac{2l+1}{2} \cdot \frac{(l-m)!}{(l+m)!}} \tag{10.5}$$

and P_l^m signifies the associated Legendre polynomial. $Y_{l,m}$ is defined as

$$Y_{l,m}(\theta,\varphi) = c_{l,m} P_l^{|m|}(\cos\theta) e^{im\phi}. \tag{10.6}$$

Here, we recall certain useful properties of VSH and VSWF. N and M are related by

$$\vec{N}_{l,m}^{1,3}(k\vec{r}) = \frac{1}{k} \nabla \times \vec{M}_{l,m}^{1,3}(k\vec{r}). \tag{10.7}$$

VSH satisfy the following orthogonality relations

$$\begin{aligned} &\int_0^{2\pi} \int_0^{\pi} \vec{m}_{l,m}(\theta,\varphi) \cdot \vec{m}^*_{m'l'}(\theta,\varphi) \sin\theta \mathrm{d}\theta \mathrm{d}\varphi = \\ &\qquad = \int_0^{2\pi} \int_0^{\pi} \vec{n}_{l,m}(\theta,\varphi) \cdot \vec{n}^*_{m'l'}(\theta,\varphi) \sin\theta \mathrm{d}\theta \mathrm{d}\varphi = \pi \delta_{mm'} \delta_{nn'} \end{aligned} \tag{10.8}$$

and

$$\int_0^{2\pi} \int_0^{\pi} \vec{m}_{l,m}(\theta,\varphi) \cdot \vec{n}^*_{m'l'}(\theta,\varphi) \sin\theta \mathrm{d}\theta \mathrm{d}\varphi = 0. \tag{10.9}$$

10.2 Direct and substrate-mediated coupling matrix elements

The direct coupling matrix element between multipoles n and n' of S-th and S'-th nanoparticle is

$$W_{n,n'}^{S,S'} = \mathrm{e}^{\mathrm{i}\left(m-m'\right)\phi} \sum_{\chi=|l-l'|}^{l+l'} x_5\left(l,m\left|l',m'\right|\lambda\right) h_\chi^{(1)}(kr) P_\chi^{\left|m-m'\right|}(\cos\theta), \tag{10.10}$$

where x_5 represents a_5 or b_5 coefficient

$$x_5 = \left\{ \begin{array}{ll} a_5, & \text{for } \tau = \tau' \\ b_5, & \text{for } \tau \neq \tau' \end{array} \right\} \tag{10.11}$$

and $h_l^{(1)}(x)$ is a spherical Hankel function

$$h_l^{(1)}(x) = \sum_{m=0}^{l} c_{l,m} \frac{e^{ix}}{x^{m+1}}. \tag{10.12}$$

a_5 and b_5 coefficients are defined as

$$\begin{aligned} a_5\left(l,m\left|l',m'\right|p\right) =& i^{\left|m-m'\right|-\left|m\right|-\left|m'\right|+l'-l+p}(-1)^{m-m'} \\ & \times\sqrt{\frac{\left(2l+1\right)\left(2l'+1\right)}{2l(l+1)l'\left(l'+1\right)}} \\ & \times\left(l(l+1)+l'\left(l'+1\right)-p(p+1)\right)\sqrt{2p+1} \\ & \times\left(\begin{array}{ccc} l & l' & p \\ m & -m' & -\left(m-m'\right) \end{array}\right)\left(\begin{array}{ccc} l & l' & p \\ 0 & 0 & 0 \end{array}\right), \end{aligned} \tag{10.13}$$

$$\begin{aligned} b_5\left(l,m\left|l',m'\right|p\right) =& i^{\left|m-m'\right|-\left|m\right|-\left|m'\right|+l'-l+p}(-1)^{m-m'}\sqrt{\frac{\left(2l'+1\right)\left(2l+1\right)}{2l(l+1)l'\left(l'+1\right)}} \\ & \times\sqrt{\left(l+l'+1+p\right)\left(l+l'+1-p\right)} \\ & \times\sqrt{\left(p+l-l'\right)\left(p-l+l'\right)\left(2p+1\right)} \\ & \times\left(\begin{array}{ccc} l & l' & p \\ m & -m' & -\left(m-m'\right) \end{array}\right)\left(\begin{array}{ccc} l & l' & p-1 \\ 0 & 0 & 0 \end{array}\right), \end{aligned} \tag{10.14}$$

respectively.

Substrate mediated coupling term is given by the following equation

$$\begin{aligned} W^{S,S'}_{r,n,n'} = \frac{2}{\pi}\sum_j\int\frac{d^2\vec{k_{||}}}{k_z k}e^{i(m'-m)\phi_{S,S'}}e^{i\vec{k_{||}}\cdot(\vec{r_S}-\vec{r_{S'}})} \\ \times r_j(k_z)B^{\dagger}_{n,j}(k_z/k)B_{n',j}(-k_z/k)e^{ikz_S}, \end{aligned} \tag{10.15}$$

where $k_{||}$is the in-plane wave vector and k_z is the wave vector component perpendicular to the substrate. j corresponds to summation over plane wave TE and TM polarizations. $B^{\dagger}$ is B with all explicit i substitued by $-i$. B is defined as

$$\begin{aligned} B_{n,j}(x) = \frac{1}{i^{l+1}}\frac{1}{\sqrt{2l(l+1)}}\left(i\delta_{j,1}+\delta_{j,2}\right)\sqrt{1-x^2}\times \\ \times\left(\delta_{\eta j}\frac{\partial P_l^{|m|}(x)}{\partial x}+\left(1-\delta_{\eta j}\right)m\frac{P_l^{|m|}(x)}{1-x^2}\right). \end{aligned} \tag{10.16}$$

Substrate mediated coupling reduces to

$$W^{S,S}_{r,n,n'} = \frac{2}{\pi}\sum_j\int\frac{d^2\vec{k_{||}}}{k_z k}r_j(k_z)B^{\dagger}_{n,j}(k_z/k)B_{n',j}(-k_z/k)e^{ikz_S}, \tag{10.17}$$

if $S = S'$. Such coupling term is called self-coupling term.

Chapter 11

Appendix B: code

11.1 Code

The code is implemented on top of SMUTHI – light scattering by multiple particles in thin-film systems code. It also requires joblib and pycuda for CPU/GPU parallel execution, respectively. The code along with SMUTHI v1.0 is stored at `https://gitlab.com/nanophotonics_fuw/amosmuthi`. The version of the code described in this thesis is v0.2.

11.1.1 Installation

There are two ways to use the code. One way is to create a singularity image from recipe in recipes folder or use a pre-built image. The other way is to create a virtual environment and install using pip. The installation using pip is a two-step process. First install SMUTHI by going to `smuthi` folder and typing

```
pip install .
```

in the linux terminal. Note, you don't have to install numpy, scipy etc. The SMUTHI installer will install this for you. Then go to the main package folder and type the same command. It installs the `amosmuthi` package and joblib for you. The code is untested on GPU and hence, such usage is outside the report scope, but it should be possible by using standard SMUTHI GPU functions.

11.1.2 Code usage

The code usage has changed a lot since initial version used for Ref. 158. There are two reasons for those changes: first, the code is adopted API for v1.0 of

Smuthi and second, to give the control about all the simulation details to the user. The code now adopts the object-oriented and “we like typing” philosophy. Consequently, it is developed assuming that it is more important to have human-readable, expressive way of building simulations than it is to be concise. The advantage of being compatible with v1.0 of SMUTHI is that the user can simulate arbitrarily shaped particles and that the new API is more expressive. The examples are discussed in the Appendix.

11.1.3 Code structure

The main part of the package is extendedsim module, which implements three classes:

- `EffectiveSimulation` – a generic class for simulations of 2D nanoparticle arrays within the mean-field approach;
- `PeriodicArraySimulation` – use for periodic arrays;
- `AmorphousArraySimulation` – use for amorphous arrays.

The advantage of the object oriented approach is that if any new array type is to be implemented one just has to create a new class inheriting from the `EffectiveSimulation` and implement adequate `calculate_integrals` method that will calculate the effective interparticle coupling term. The second notable module is a modified SMUTHI module called `particle_coupling_amo`, which prepares the radial part of coupling matrix including Sommerfeld integrals. Three remaining modules analysis, utils and materials implement features that are useful, but currently are unavailable in the official SMUTHI release. Those include: various material models (reading from CSV file, Drude model), multipole decomposition of extinction cross-section, azimuthally averaged differential scattering cross-section, finding resonant frequencies.

Bibliography

[1] Rothenberg, G. *Catalysis concepts and green applications*; Wiley, 2017.

[2] Ma, Z.; Zaera, F. *Heterogeneous Catalysis by Metals*; John Wiley and Sons, Ltd, 2006.

[3] Christopher, P.; Xin, H.; Linic, S. *Nature Chemistry* **2011**, *3*, 467–472.

[4] Kale, M. J.; Avanesian, T.; Christopher, P. *ACS Catalysis* **2014**, *4*, 116–128.

[5] Mukherjee, S.; Libisch, F.; Large, N.; Neumann, O.; Brown, L. V.; Cheng, J.; Lassiter, J. B.; Carter, E. A.; Nordlander, P.; Halas, N. J. *Nano Letters* **2013**, *13*, 240–247.

[6] Avanesian, T.; Christopher, P. *Journal of Physical Chemistry C* **2014**, *118*, 28017–28031.

[7] Stasieńko, S.; Krajczewski, J.; Wojtysiak, S.; Czajkowski, K.; Kudelski, A. *Colloids and Surfaces A: Physicochemical and Engineering Aspects* **2014**, *443*, 102–1084.

[8] Zhang, C.; Zhao, H.; Zhou, L.; Schlather, A. E.; Dong, L.; McClain, M. J.; Swearer, D. F.; Nordlander, P.; Halas, N. J. *Nano Letters* **2016**, *16*, 6677–6682.

[9] Swearer, D. F.; Zhao, H.; Zhou, L.; Zhang, C.; Robatjazi, H.; Martirez, J. M. P.; Krauter, C. M.; Yazdi, S.; McClain, M. J.; Ringe, E.; Carter, E. A.; Nordlander, P.; Halas, N. J. *Proceedings of the National Academy of Sciences of the United States of America* **2016**, *113*, 8916–8920.

[10] Antosiewicz, T. J.; Wadell, C.; Langhammer, C. *Advanced Optical Materials* **2015**, *3*, 1591–1599.

[11] Li, K.; Hogan, N. J.; Kale, M. J.; Halas, N. J.; Nordlander, P.; Christopher, P. *Nano Letters* **2017**, *17*, 3710–3717.

[12] Antosiewicz, T. J.; Tarkowski, T. *ACS Photonics* **2015**, *2*, 1732–1738.

[13] Antosiewicz, T. J.; Apell, S. P.; Zäch, M.; Zorić, I.; Langhammer, C. *Physical Review Letters* **2012**, *109*, 247401.

[14] Antosiewicz, T. J.; Apell, S. P. *Optics Express* **2014**, *22*, 2031.

[15] Antosiewicz, T. J.; Apell, S. P. *RSC Advances* **2015**, *5*, 6378–6384.

[16] Brongersma, M. L.; Halas, N. J.; Nordlander, P. *Nature Nanotechnology* **2015**, *10*, 25–34.

[17] Anker, J. N.; Hall, W. P.; Lyandres, O.; Shah, N. C.; Zhao, J.; Van Duyne, R. P. *Nature Materials* **2008**, *7*, 442–453.

[18] Mauriz, E.; Dey, P.; Lechuga, L. M. *Analyst* **2019**, *144*, 7105–7129.

[19] Lopez, G. A.; Estevez, M. C.; Soler, M.; Lechuga, L. M. *Nanophotonics* **2017**, *6*, 123–136.

[20] Larsson, E. M.; Langhammer, C.; Zoric, I.; Kasemo, B. *Science* **2009**, *326*, 1091–1094.

[21] Larsson, E. M.; Millet, J.; Gustafsson, S.; Skoglundh, M.; Zhdanov, V. P.; Langhammer, C. *ACS Catalysis* **2012**, *2*, 238–245.

[22] Tabib Zadeh Adibi, P.; Mazzotta, F.; Antosiewicz, T. J.; Skoglundh, M.; Grönbeck, H.; Langhammer, C. *ACS Catalysis* **2015**, *5*, 426–432.

[23] Syrenova, S.; Wadell, C.; Nugroho, F. A.; Gschneidtner, T. A.; Diaz Fernandez, Y. A.; Nalin, G.; Świtlik, D.; Westerlund, F.; Antosiewicz, T. J.; Zhdanov, V. P.; Moth-Poulsen, K.; Langhammer, C. *Nature Materials* **2015**, *14*, 1236–1244.

[24] Tseng, M. L.; Jahani, Y.; Leitis, A.; Altug, H. *ACS Photonics* **2021**, *8*, 47–60.

[25] Yavas, O.; Svedendahl, M.; Dobosz, P.; Sanz, V.; Quidant, R. *Nano Letters* **2017**, *17*, 4421–4426.

[26] Bosio, N.; Šípová-Jungová, H.; Länk, N. O.; Antosiewicz, T. J.; Verre, R.; Käll, M. *ACS Photonics* **2019**, acsphotonics.9b00434.

[27] Offermans, P.; Schaafsma, M. C.; Rodriguez, S. R.; Zhang, Y.; Crego-Calama, M.; Brongersma, S. H.; Gómez Rivas, J. *ACS Nano* **2011**, *5*, 5151–5157.

[28] Born, M.; Wolf, E.; Bhatia, A. B. *Principles of optics*; Cambridge University Press, 2019.

[29] Johnson, P. B.; Christy, R. W. *Physical Review B* **1972**, *6*, 4370.

[30] Doicu, A.; Wriedt, T.; Eremin, Y. *Light scattering by systems of particles: Null-field method with discrete sources: Theory and programs*; Springer, 2006.

[31] Bohren, C. F.; Huffman, D. R. *Absorption and Scattering of Light by Small Particles* **1998**,

[32] Mishchenko, M. I.; Hovenier, J. W.; Travis, L. D. *Light scattering by nonspherical particles : theory, measurements, and applications*; Academic Press, 2000.

[33] Radescu, E.; Vaman, J.; Georgeta, *Progress In Electromagnetics Research B* **2012**, *36*, 89–111.

[34] Jackson, J. D. *Classical electrodynamics*; John Wiley & Sons, 1963.

[35] Evlyukhin, A. B.; Fischer, T.; Reinhardt, C.; Chichkov, B. N. *Physical Review B* **2016**, *94*, 205434.

[36] Alaee, R.; Rockstuhl, C.; Fernandez-Corbaton, I. *Optics Communications* **2018**, *407*, 17–21.

[37] Alaee, R.; Rockstuhl, C.; Fernandez-Corbaton, I. *Advanced Optical Materials* **2019**, *7*, 1800783.

[38] Johnson, S. G. *arXiv* **2021**, *2108.05348*.

[39] Doicu, A.; Mishchenko, M. I. *Physics Open* **2020**, *5*, 100020.

[40] Schebarchov, D.; Le Ru, E. C.; Grand, J.; Auguié, B. *Optics Express* **2019**, *27*, 35750.

[41] Kohn, W. *Reviews of Modern Physics* **1999**, *71*, 1253.

[42] Hohenberg, P.; Kohn, W. *Physical Review* **1964**, *136*, B864.

[43] Kohn, W.; Sham, L. J. *Physical Review* **1965**, *140*, A1133.

[44] Kohanoff, J. *Electronic Structure Calculations for Solids and Molecules: Theory and Computational Methods* **2006**, *9780521815918*, 1–348.

[45] Soler, J. M.; Artacho, E.; Gale, J. D.; García, A.; Junquera, J.; Ordejón, P.; Sánchez-Portal, D. *Journal of Physics: Condensed Matter* **2002**, *14*, 2745.

[46] Runge, E.; Gross, E. K. *Physical Review Letters* **1984**, *52*, 997.

[47] Koval, P.; Marchesin, F.; Foerster, D.; Sánchez-Portal, D. *Journal of Physics Condensed Matter* **2016**, *28*, 214001.

[48] Deutsch, B.; Novotny, L.; Bharadwaj, P. *Advances in Optics and Photonics* **2009**, *1*, 438–483.

[49] Yu, R.; Liz-Marzán, L. M.; García De Abajo, F. J. *Chemical Society Reviews* **2017**, *46*, 6710–6724.

[50] Jahani, S.; Jacob, Z. *Nature Nanotechnology* **2016**, *11*, 23–36.

[51] Yu, H.; Peng, Y.; Yang, Y.; Li, Z.-Y. *npj Computational Materials* **2019**, *5*, 1–14.

[52] Chikkaraddy, R.; De Nijs, B.; Benz, F.; Barrow, S. J.; Scherman, O. A.; Rosta, E.; Demetriadou, A.; Fox, P.; Hess, O.; Baumberg, J. J. *Nature* **2016**, *535*, 127–130.

[53] Enrichi, F.; Quandt, A.; Righini, G. C. *Renewable and Sustainable Energy Reviews* **2018**, *82*, 2433–2439.

[54] Yin, G.; Steigert, A.; Andrae, P.; Goebelt, M.; Latzel, M.; Manley, P.; Lauermann, I.; Christiansen, S.; Schmid, M. *Applied Surface Science* **2015**, *355*, 800–804.

[55] Moakhar, R. S.; Gholipour, S.; Masudy-Panah, S.; Seza, A.; Mehdikhani, A.; Riahi-Noori, N.; Tafazoli, S.; Timasi, N.; Lim, Y.-F.; Saliba, M. *Advanced Science* **2020**, *7*, 1902448.

[56] Ciesielski, A.; Czajkowski, K. M.; Switlik, D. *Solar Energy* **2019**, *184*, 477–488.

[57] Dean, N. *Nature Nanotechnology* **2015**, *10*, 15–16.

[58] Baffou, G.; Cichos, F.; Quidant, R. *Nature Materials* **2020**, *19*, 946–958.

[59] Willets, K. A.; Wilson, A. J.; Sundaresan, V.; Joshi, P. B. *Chemical Reviews* **2017**, *117*, 7538–7582.

[60] Wokaun, A.; Meier, M. *Optics Letters* **1983**, *8*, 581–583.

[61] Moroz, A. *Journal of the Optical Society of America B* **2009**, *26*, 517.

[62] Zorić, I.; Zäch, M.; Kasemo, B.; Langhammer, C. *ACS Nano* **2011**, *5*, 2535–2546.

[63] Krajczewski, J.; Michałowska, A.; Kudelski, A. *Spectrochimica Acta Part A: Molecular and Biomolecular Spectroscopy* **2020**, *225*, 117469.

[64] de Abajo, F. J. G.; Bryant, G. W.; Romero, I.; Aizpurua, J. *Optics Express* **2006**, *14*, 9988–9999.

[65] Wiecha, P. R.; Black, L.-J.; Wang, Y.; Paillard, V.; Girard, C.; Muskens, O. L.; Arbouet, A. *Scientific Reports* **2017**, *7*, 1–11.

[66] Hein, S. M.; Giessen, H. *Physical Review Letters* **2013**, *111*, 026803.

[67] Scholl, J. A.; Koh, A. L.; Dionne, J. A. *Nature 2012 483:7390* **2012**, *483*, 421–427.

[68] Monreal, R. C.; Apell, S. P.; Antosiewicz, T. J. *Optics Express* **2014**, *22*, 24994–25004.

[69] Kuisma, M.; Sakko, A.; Rossi, T. P.; Larsen, A. H.; Enkovaara, J.; Lehtovaara, L.; Rantala, T. T. *Physical Review B - Condensed Matter and Materials Physics* **2015**, *91*, 115431.

[70] Esteban, R.; Borisov, A. G.; Nordlander, P.; Aizpurua, J. *Nature Communications* **2012**, *3*, 1–9.

[71] Barbry, M.; Koval, P.; Marchesin, F.; Esteban, R.; Borisov, A. G.; Aizpurua, J.; Sánchez-Portal, D. *Nano Letters* **2015**, *15*, 3410–3419.

[72] Marchesin, F.; Koval, P.; Barbry, M.; Aizpurua, J.; Sánchez-Portal, D. *ACS Photonics* **2016**, *3*, 269–277.

[73] Urbieta, M.; Barbry, M.; Zhang, Y.; Koval, P.; Sánchez-Portal, D.; Zabala, N.; Aizpurua, J. *ACS Nano* **2018**, *12*, 585–595.

[74] Mascaretti, L.; Naldoni, A. *Journal of Applied Physics* **2020**, *128*, 041101.

[75] Li, W.; Valentine, J. G. *Nanophotonics* **2017**, *6*, 177–191.

[76] Hou, B.; Shen, L.; Shi, H.; Kapadia, R.; Cronin, S. B. *Physical Chemistry Chemical Physics* **2017**, *19*, 2877–2881.

[77] Kale, M. J.; Avanesian, T.; Xin, H.; Yan, J.; Christopher, P. *Nano Letters* **2014**, *14*, 5405–5412.

[78] Manjavacas, A.; Liu, J. G.; Kulkarni, V.; Nordlander, P. *ACS Nano* **2014**, *8*, 7630–7638.

[79] Besteiro, L. V.; Kong, X.-T.; Wang, Z.; Hartland, G.; Govorov, A. O. *ACS Photonics* **2017**, *4*, 2759–2781.

[80] Santiago, E. Y.; Besteiro, L. V.; Kong, X.-T.; Correa-Duarte, M. A.; Wang, Z.; Govorov, A. O. *ACS Photonics* **2020**, *7*, 2807–2824.

[81] Rossi, T. P.; Erhart, P.; Kuisma, M. *ACS Nano* **2020**, *14*, 9963–9971.

[82] Ma, J.; Wang, Z.; Wang, L.-W. *Nature Communications* **2015**, *6*, 1–11.

[83] Román Castellanos, L.; Hess, O.; Lischner, J. *Communications Physics* **2019**, *2*, 1–9.

[84] Zywietz, U.; Evlyukhin, A. B.; Reinhardt, C.; Chichkov, B. N. *Nature Communications* **2014**, *5*, 3402.

[85] Paniagua-Dominguez, R.; Luk'yanchuk, B.; Kuznetsov, A. I. *Dielectric Metamaterials: Fundamentals, Designs, and Applications* **2020**, 73–108.

[86] Staude, I.; Miroshnichenko, A. E.; Decker, M.; Fofang, N. T.; Liu, S.; Gonzales, E.; Dominguez, J.; Luk, T. S.; Neshev, D. N.; Brener, I.; Kivshar, Y. *ACS Nano* **2013**, *7*, 7824–7832.

[87] Timofeeva, M.; Bouravleuv, A.; Cirlin, G.; Shtrom, I.; Soshnikov, I.; Escalé, M. R.; Sergeyev, A.; Grange, R. *Nano Letters* **2016**, *16*, 6290–6297.

[88] Wang, L.; Kruk, S.; Koshelev, K.; Kravchenko, I.; Luther-Davies, B.; Kivshar, Y. *Nano Letters* **2018**, *18*, 3978–3984.

[89] Melik-Gaykazyan, E. V.; Shcherbakov, M. R.; Shorokhov, A. S.; Staude, I.; Brener, I.; Neshev, D. N.; Kivshar, Y. S.; Fedyanin, A. A. *Philosophical Transactions of the Royal Society A: Mathematical, Physical and Engineering Sciences* **2017**, *375*, 20160281.

[90] Staude, I.; Pertsch, T.; Kivshar, Y. S. *ACS Photonics* **2019**, *6*, 802–814.

[91] Solomon, M. L.; Hu, J.; Lawrence, M.; García-Etxarri, A.; Dionne, J. A. *ACS Photonics* **2018**, *6*, 43–49.

[92] Mélinon, P.; Begin-Colin, S.; Duvail, J. L.; Gauffre, F.; Boime, N. H.; Ledoux, G.; Plain, J.; Reiss, P.; Silly, F.; Warot-Fonrose, B. *Physics Reports* **2014**, *543*, 163–197.

[93] Jeon, K.-J.; Moon, H. R.; Ruminski, A. M.; Jiang, B.; Kisielowski, C.; Bardhan, R.; Urban, J. J. *Nature Materials* **2011**, *10*, 286–290.

[94] Lee, S.-H.; Yi, C.-W.; Kim, K. *Journal of Physical Chemistry C* **2010**, *115*, 2572–2577.

[95] Levin, C. S.; Hofmann, C.; Ali, T. A.; Kelly, A. T.; Morosan, E.; Nordlander, P.; Whitmire, K. H.; Halas, N. J. *ACS Nano* **2009**, *3*, 1379–1388.

[96] Tzarouchis, D. C.; Sihvola, A. *IEEE Transactions on Antennas and Propagation* **2018**, *66*, 323–330.

[97] Seyedheydari, F.; Conley, K. M.; Thakore, V.; Karttunen, M.; Sihvola, A.; Ala-Nissila, T. *Journal of Physics Communications* **2021**, *5*, 015002.

[98] Li, Y.; Wan, M.; Wu, W.; Chen, Z.; Zhan, P.; Wang, Z. *Scientific Reports* **2015**, *5*, 1–12.

[99] Kiselev, A.; Ray, D.; Martin, O. J. F.; Kiselev, A.; Martin, O. J. F. *Optics Express* **2021**, *29*, 24056–24067.

[100] Barreda, Á. I.; Gutiérrez, Y.; Sanz, J. M.; González, F.; Moreno, F. *Scientific Reports* **2017**, *7*, 1–10.

[101] Sakthisabarimoorthi, A.; Martin Britto Dhas, S. A.; Jose, M. *Journal of Materials Science: Materials in Electronics* **2018**, *30*, 1677–1685.

[102] E., S.; T., A.; D., N. R.; K., C. *Journal of Molecular Liquids* **2021**, *333*, 115935.

[103] Liu, W. *Optics Express* **2015**, *23*, 14734–14743.

[104] Mohammadi, E.; Tavakoli, A.; Dehkhoda, P.; Jahani, Y.; Tsakmakidis, K. L.; Tittl, A.; Altug, H. *ACS Photonics* **2019**, *6*, 1939–1946.

[105] Evlyukhin, A. B.; Tuz, V. R.; Volkov, V. S.; Chichkov, B. N. *Physical Review B* **2020**, *101*, 205415.

[106] Chen, F.-X.; Wang, X.-C.; Xia, D.-L.; Wang, L.-S. *AIP Advances* **2015**, *5*, 097129.

[107] Egel, A.; Czajkowski, K. M.; Theobald, D.; Ladutenko, K.; Kuznetsov, A. S.; Pattelli, L. *Journal of Quantitative Spectroscopy and Radiative Transfer* **2021**, *273*, 107846.

[108] Egel, A.; Lemmer, U. *Journal of Quantitative Spectroscopy and Radiative Transfer* **2014**, *148*, 165–176.

[109] Mackowski, D. W.; Mishchenko, M. I. *Journal of the Optical Society of America A* **1996**, *13*, 2266.

[110] Bendana, X. M.; García de Abajo, F. J.; Podosenov, S. A.; Sokolov, A. A.; Al, S. V. *Optics Express* **2009**, *17*, 18826–18835.

[111] Yu, N.; Capasso, F. *Nature Materials* **2014**, *13*, 139–150.

[112] Huang, L.; Chen, X.; Mühlenbernd, H.; Li, G.; Bai, B.; Tan, Q.; Jin, G.; Zentgraf, T.; Zhang, S. *Nano Letters* **2012**, *12*, 5750–5755.

[113] Chen, W. T.; Zhu, A. Y.; Sanjeev, V.; Khorasaninejad, M.; Shi, Z.; Lee, E.; Capasso, F. *Nature Nanotechnology* **2018**, *13*, 220–226.

[114] Huang, L.; Chen, X.; Mühlenbernd, H.; Zhang, H.; Chen, S.; Bai, B.; Tan, Q.; Jin, G.; Cheah, K. W.; Qiu, C. W.; Li, J.; Zentgraf, T.; Zhang, S. *Nature Communications* **2013**, *4*, 1–8.

[115] Scheuer, J. *ACS Photonics* **2020**, *7*, 1323–1354.

[116] Auguié, B.; Barnes, W. L. *Physical Review Letters* **2008**, *101*, 143902.

[117] Väkevaäinen, A. I.; Moerland, R. J.; Rekola, H. T.; Eskelinen, A.-P.; Martikainen, J.-P.; Kim, D.-H.; Törmä, P. *Nano Lett* **2014**, *14*, 1721–1727.

[118] Špačková, B.; Homola, J. *Optics Express* **2013**, *21*, 27490–27502.

[119] Evlyukhin, A. B.; Reinhardt, C.; Zywietz, U.; Chichkov, B. N. *Physical Review B* **2012**, *85*, 245411.

[120] Evlyukhin, A. B.; Reinhardt, C.; Seidel, A.; Luk'yanchuk, B. S.; Chichkov, B. N. *Physical Review B* **2010**, *82*, 045404.

[121] Stefanou, N.; Yannopapas, V.; Modinos, A. *Computer Physics Communications* **1998**, *113*, 49–77.

[122] Babicheva, V. E.; Evlyukhin, A. B. *Journal of Applied Physics* **2021**, *129*, 040902.

[123] Babicheva, V. E.; Evlyukhin, A. B. *Laser & Photonics Reviews* **2017**, *11*, 1700132.

[124] Terekhov, P. D.; Babicheva, V. E.; Baryshnikova, K. V.; Shalin, A. S.; Karabchevsky, A.; Evlyukhin, A. B. *Physical Review B* **2019**, *99*, 045424.

[125] Fredriksson, H.; Alaverdyan, Y.; Dmitriev, A.; Langhammer, C.; Sutherland, D.; Zäch, M.; Kasemo, B. *Advanced Materials* **2007**, *19*, 4297–4302.

[126] Zhang, Y.; Xu, Y.; Chen, S.; Lu, H.; Chen, K.; Cao, Y.; Miroshnichenko, A. E.; Gu, M.; Li, X. *ACS Applied Materials and Interfaces* **2018**, *10*, 16776–16782.

[127] V. Besteiro, L.; Kong, X.-T.; Wang, Z.; Rosei, F.; Govorov, A. O. *Nano Letters* **2018**, *18*, 3147–3156.

[128] Nugroho, F. A. A.; Frost, R.; Antosiewicz, T. J.; Fritzsche, J.; Langhammer, E. M.; Langhammer, C. *ACS Sensors* **2017**, *2*, 119–127.

[129] Kanté, B.; Nasari, H.; Dupré, M. *Optics Letters* **2018**, *43*, 5829–5832.

[130] Torquato, S. *Random Heterogeneous Materials*; Interdisciplinary Applied Mathematics; Springer New York: New York, NY, 2002; Vol. 16.

[131] Schwind, M.; Miljković, V. D.; Zäch, M.; Gusak, V.; Käll, M.; Zorić, I.; Johansson, P. *ACS Nano* **2012**, *6*, 9455–9465.

[132] Conley, G. M.; Burresi, M.; Pratesi, F.; Vynck, K.; Wiersma, D. S. *Physical Review Letters* **2014**, *112*, 143901.

[133] Markkanen, J.; Yuffa, A. J. *Journal of Quantitative Spectroscopy and Radiative Transfer* **2017**, *189*, 181–188.

[134] Markel, V. A. *Journal of the Optical Society of America A* **2016**, *33*, 1244.

[135] Twersky, V. *Journal of the Optical Society of America A* **1962**, *52*, 145–171.

[136] Albooyeh, M.; Alaee, R.; Rockstuhl, C.; Simovski, C. *Physical Review B* **2015**, *91*, 195304.

[137] Miroshnichenko, A. E.; Evlyukhin, A. B.; Kivshar, Y. S.; Chichkov, B. N. *ACS Photonics* **2015**, *2*, 1423–1428.

[138] Sinev, I.; Iorsh, I.; Bogdanov, A.; Permyakov, D.; Komissarenko, F.; Mukhin, I.; Samusev, A.; Valuckas, V.; Kuznetsov, A. I.; Luk'yanchuk, B. S.; Miroshnichenko, A. E.; Kivshar, Y. S. *Laser & Photonics Reviews* **2016**, *10*, 799–806.

[139] Nechayev, S.; Barczyk, R.; Mick, U.; Banzer, P. *ACS Photonics* **2019**, *6*, 1876–1881.

[140] Pors, A.; Andersen, S. K. H.; Bozhevolnyi, S. I. *Optics Express* **2015**, *23*, 28808–28828.

[141] Antosiewicz, T. J.; Wadell, C.; Langhammer, C. *Advanced Optical Materials* **2015**, *3*, 1591–1599.

[142] Benz, F.; Schmidt, M. K.; Dreismann, A.; Chikkaraddy, R.; Zhang, Y.; Demetriadou, A.; Carnegie, C.; Ohadi, H.; De Nijs, B.; Esteban, R.; Aizpurua, J.; Baumberg, J. J. *Science* **2016**, *354*, 726–729.

[143] Sugimoto, H.; Fujii, M. *ACS Photonics* **2018**, *5*, 1986–1993.

[144] Schebarchov, D.; Ru, E. C. L.; Grand, J.; Auguié, B. *Opt. Express* **2019**, *27*, 35750–35760.

[145] Egel, A.; Theobald, D.; Donie, Y.; Lemmer, U.; Gomard, G. *Opt. Express* **2016**, *24*, 25154–25168.

[146] Egel, A.; Eremin, Y.; Wriedt, T.; Theobald, D.; Lemmer, U.; Gomard, G. *Journal of Quantitative Spectroscopy and Radiative Transfer* **2017**, *202*, 279–285.

[147] Theobald, D.; Egel, A.; Gomard, G.; Lemmer, U. *Phys. Rev. A* **2017**, *96*, 033822.

[148] Palik, E. D. *Handbook of optical constants of solids*; Elsevier, 2012.

[149] Bögner, W.; Krämer, M.; Krutzsch, B.; Pischinger, S.; Voigtländer, D.; Wenninger, G.; Wirbeleit, F.; Brogan, M. S.; Brisley, R. J.; Webster, D. E. *Applied Catalysis B: Environmental* **1995**, *7*, 153–171.

[150] Takahashia, N.; Shinjoh, H.; Iijima, T.; Suzuki, T.; Yamazaki, K.; Yokota, K.; Suzuki, H.; Miyoshi, N.; Matsumoto, S. I.; Tanizawa, T.; Tanaka, T.; Tateishi, S. S.; Kasahara, K. *Catalysis Today* **1996**, *27*, 63–69.

[151] Ji, Y.; Bai, S.; Crocker, M. *Applied Catalysis B: Environmental* **2015**, *170-171*, 283–292.

[152] Staudt, T.; Desikusumastuti, A.; Happel, M.; Vesselli, E.; Baraldi, A.; Gardonio, S.; Lizzit, S.; Rohr, F.; Libuda, J. *Journal of Physical Chemistry C* **2008**, *112*, 9835–9846.

[153] Olsson, L.; Fridell, E.; Skoglundh, M.; Andersson, B. *Catalysis Today* **2002**, *73*, 263–270.

[154] Schooss, D.; Blom, M. N.; Parks, J. H.; Issendorff, B. V.; Haberland, H.; Kappes, M. M. *Nano Letters* **2005**, *5*, 1972–1977.

[155] Carmina Monreal, R.; Antosiewicz, T. J.; Apell, S. P. *New Journal of Physics* **2013**, *15*, 083044.

[156] Rossi, T. P.; Kuisma, M.; Puska, M. J.; Nieminen, R. M.; Erhart, P. *Journal of Chemical Theory and Computation* **2017**, *13*, 4779–4790.

[157] Guidez, E. B.; Aikens, C. M. *Physical Chemistry Chemical Physics* **2014**, *16*, 15501–15509.

[158] Czajkowski, K. M.; Bancerek, M.; Antosiewicz, T. J. *Phys. Rev. B* **2020**, *102*, 085431.